

The hadronic contribution to the running of the electromagnetic coupling and the electroweak mixing angle

Dissertation
zur Erlangung des Grades
„Doktor der Naturwissenschaften“
am Fachbereich Physik, Mathematik und Informatik
der Johannes Gutenberg-Universität
in Mainz

Miguel Teseo San José Pérez
geb. in Logroño

Mainz, den 20. Juni 2022

Miguel Teseo San José Pérez

The hadronic contribution to the running of the electromagnetic coupling and the electroweak mixing angle

Tag der Promotionsprüfung: Donnerstag, 09. Juni 2022

Kommissionsmitglieder:

Peter van Loock

Hartmut Wittig

Pedro Schwaller

Achim Denig

Jairo Sinova

Abstract

The electromagnetic coupling and the electroweak mixing angle are two quantities used in precision Standard Model tests and probes of new physics. However, their dependence on the energy suffers from uncertainties at low momenta, induced by hadronic effects. In this work, we study the latter in the space-like energy range $0 - 10 \text{ GeV}^2$, employing a lattice regularisation of isosymmetric quantum chromodynamics, which allows us to access the confining regime of the strong coupling constant. One may compute the hadronic contribution to the electromagnetic coupling and the electroweak mixing angle from vacuum polarisation functions. For the first case, we use two electromagnetic currents, while for the second, we require the mixing of an electromagnetic current with the vector component of a weak neutral current. We employ the time-momentum representation to compute both vacuum polarisation functions. We use a set of seventeen Monte Carlo simulations based on CLS ensembles with a $N_f = 2 + 1$ $\mathcal{O}(a)$ -improved Wilson fermion action and a tree-level improved Lüscher-Weisz gauge action. The simulations include the charm quark at the quenched level, and we include both quark-connected and quark-disconnected diagrams. Our simulations possess pion masses that span from $\sim 420 \text{ MeV}$ to $\sim 130 \text{ MeV}$, slightly below the physical pion mass, and include four different lattice spacings, 0.086 fm , 0.076 fm , 0.064 fm and 0.050 fm . This wide set allows us to combine extrapolating to the continuum limit and interpolating the physical pion and kaon masses in a single, correlated fit. Since improvement and renormalisation mix the various contributions to the vacuum polarisation function to $\mathcal{O}(a)$, we rearrange the flavour components in a $\text{SU}(3)$ -flavour basis. Autocorrelations in our two-point functions are studied and removed using a combination of binning and Ulli Wolff's Γ -method, and we employ bootstrap sampling to carry the statistical uncertainty and data correlations through the entire analysis. The signal-to-noise ratio is improved using a bounding procedure, which we compare with the more straightforward single-exponential fit and find the former more reliable for our ensembles with lighter pion mass. We remove the lattice infrared cut-off —the simulation spatial size— adding the difference between finite and infinite volumes, which we estimate using two different methods, the so-called Hansen-Patella and Meyer-Lellouch-Lüscher procedures. We find both methods to give compatible results. Finally, we cross-check the finite-volume correction by comparing ensembles with the same simulation parameters but different volumes. We perform a correlated extrapolation to the physical point of the various components for a dense set of momenta and establish that below 7 GeV^2 our fit functions describe the lattice artefacts correctly. We give the running with the energy of the electromagnetic coupling and the electroweak mixing angle using Padé approximants.

Contents

1	General Introduction	1
2	QCD in the continuum	5
2.1	Action in the continuum	5
2.1.1	Fermion action	5
2.1.2	Gluon action	7
2.1.3	θ -term	7
2.2	Gauge transporter	8
2.3	Path integral quantisation	8
2.4	Strong running coupling α_s	9
2.5	Global symmetries	11
3	QCD on the lattice	13
3.1	$\mathcal{O}(a)$ -improved Wilson fermion action	13
3.1.1	Naive lattice fermion action	14
3.1.2	Wilson fermion action	15
3.1.3	$\mathcal{O}(a)$ improvement	16
3.1.4	Other fermion discretisations	17
3.2	Tree-level Lüscher-Weisz gauge action	18
3.3	Feynman integration	20
3.3.1	Integration measure	20
3.3.2	Importance sampling	21
3.4	Hybrid Monte Carlo	23
3.4.1	Dynamical up and down quarks	25
3.4.2	Dynamical strange quark	27
3.4.3	Re-weighting	28
3.4.4	Boundary conditions	29
3.5	Scale setting	30
4	The electromagnetic coupling	33
5	The electroweak mixing angle	39
6	The hadronic vacuum polarisation	43
6.1	Renormalisation and $\mathcal{O}(a)$ improvement	44
6.1.1	$\mathcal{O}(a)$ improvement	45
6.1.2	Renormalisation	46

6.1.3	The vector current	47
6.2	The time-momentum representation	52
7	Implementation of the mesonic two-point functions	55
7.1	Quark-connected two-point functions	55
7.1.1	Point sources	56
7.1.2	Stochastic sources	58
7.1.3	Tuning the charm-quark mass	60
7.2	Quark-disconnected two-point functions	61
7.2.1	Stochastic sources	62
7.2.2	Frequency splitting	62
7.3	CLS lattice simulations	65
8	Autocorrelations	73
8.1	Theory and definitions	73
8.2	The Γ -method	74
8.3	The jackknife method	75
8.4	Removal of autocorrelations	77
8.5	Bootstrapping	78
9	Signal-to-noise ratio	83
9.1	The single-state fit	85
9.2	The bounding method	92
10	Finite-size effects	101
10.1	Meyer-Lellouch-Lüscher formalism	102
10.1.1	Gounaris-Sakurai parametrisation of $F_\pi(\omega)$	104
10.1.2	Computation of the Gounaris-Sakurai parameters	105
10.1.3	The limit of the elastic region	106
10.2	Hansen-Patella formalism	110
10.3	NLO ChPT	111
10.4	Results	112
11	$\hat{\Pi}$ on the lattice	117
12	Extrapolation to the physical point	119
12.1	Extrapolation of $\hat{\Pi}_{33}$ and $\hat{\Pi}_{88}$	120
12.1.1	Fit model	120
12.1.2	Total least-squares minimisation	122
12.1.3	Regularisation of the covariance matrix	124
12.1.4	Study of discretisation effects	125
12.1.5	Results	132
12.2	Extrapolation of $\hat{\Pi}_{cc}$	133
12.3	Extrapolation of $\hat{\Pi}_{08}$	134

13 $\hat{\Pi}$, $(\Delta\alpha)_{\text{had}}$ and $(\Delta\sin^2\theta_W)_{\text{had}}$ at the physical point	137
13.1 Transition between low and high momentum	137
13.2 Scale-setting uncertainty	138
13.3 Isospin-breaking effects	140
13.4 $\hat{\Pi}$, $(\Delta\alpha)_{\text{had}}$ and $(\Delta\sin^2\theta_W)_{\text{had}}$	142
13.5 Comparison with previous results	142
13.6 Padé approximants	144
14 Conclusions and Outlook	149

List of Figures

2.1	QCD Feynman diagrams in the continuum	9
2.2	Running of the strong coupling constant	10
3.1	Link variables	15
3.2	Sum of plaquettes $Q_{\mu\nu}(n)$	17
3.3	Plaquette $P_{\mu\nu}(n)$	19
3.4	Rectangle $R_{\mu\nu}(n)$	19
4.1	Full photon two-point function	34
4.2	One-particle-irreducible contributions to the vacuum polarisation	34
4.3	Standard Model global fits	37
5.1	Hadronic contribution to the $\gamma - Z$ -mixing Feynman diagram	40
5.2	$\sin^2 \theta_W$ via the renormalisation group equations and measurements	41
6.1	Integrand of the subtracted vacuum polarisation	54
7.1	Set of Coordinated Lattice Simulations ensembles used in this project	67
8.1	Subtracted vacuum polarisation vs bin size	77
8.2	Subtracted vacuum polarisation vs number of bootstrap samples	80
9.1	Effective mass plot	86
9.2	Original integrand, one exponential tail and bounding method	88
9.3	Bounding method for $\hat{\Pi}_{33}$ and $\hat{\Pi}_{88}$	93
9.4	Bounding method for $\hat{\Pi}_{08}$	94
10.1	Reconstruction of the subtracted vacuum polarisation integrand	108
10.2	Meyer-Lellouch-Lüscher upper limit of integration	109
10.3	Comparison between the various methods to obtain the finite-size effects	114
10.4	Comparison between H105 and N101	115
10.5	Comparison between H200 and N202	116
11.1	Lattice results for E250, D200 and N200 vs Q^2	117
12.1	Regularisation of the covariance matrix	126
12.2	Continuum extrapolation at $Q^2 = 0.5 \text{ GeV}^2$ (I)	128
12.3	Continuum extrapolation at $Q^2 = 0.5 \text{ GeV}^2$ (II)	129
12.4	Continuum extrapolation at $Q^2 = 5 \text{ GeV}^2$ (I)	130

12.5	Continuum extrapolation at $Q^2 = 5 \text{ GeV}^2$ (II)	131
12.6	Extrapolation of the isovector and isoscalar components	132
12.7	Extrapolation of the charm component	133
12.8	Extrapolation of the 08 component	135
13.1	Running for various lattice spacing models	138
13.2	Running for various lattice spacing models and pion mass cuts	139
13.3	Running with step function	140
13.4	Running of the QED coupling with Q^2	142
13.5	Running of the electroweak mixing angle with Q^2	144
13.6	Comparison with other determinations of $(\Delta\alpha)_{\text{had}}$	145

List of Tables

3.1	Scale setting at every β	32
6.1	Renormalisation factors and improvement coefficients	53
7.1	Values of κ for every CLS ensemble	61
7.2	Renormalised and improved vector correlator	66
7.3	Set of CLS ensembles used in this project	68
7.4	Scale, pion mass and kaon mass for every ensemble	70
8.1	Bin size and autocorrelation time	79
9.1	Single exponential fit to $\hat{\Pi}_{33}$	89
9.2	Single exponential fit to $\hat{\Pi}_{88}$	91
9.3	Single exponential fit to $\hat{\Pi}_{08}$	91
9.4	Rho meson mass, several-pions system mass	95
9.5	Systematic effect of the bounding method on $\hat{\Pi}_{33}$	96
9.6	Systematic effect of the bounding method on $\hat{\Pi}_{88}$	98
9.7	Systematic effect of the bounding method on $\hat{\Pi}_{08}$	99
9.8	Subtracted vacuum polarisation after the bounding method tail treatment .	100
10.1	Fit parameters of the Meyer-Lellouch-Lüscher formalism	107
10.2	Estimation of the finite-size effects using the Hansen-Patella formalism . .	111
10.3	Finite-size effects correction	113
11.1	Lattice results at $Q^2 = 1 \text{ GeV}^2$	118
13.1	Subtracted vacuum polarisation at the physical point with full uncertainties	143
13.2	Running QED coupling and electroweak mixing angle with full uncertainties	143

Chapter 1

General Introduction

The Standard Model (SM) of particle physics aims to be a unified description of nature at its most fundamental level; it includes all known elementary particles, as well as the strong, electromagnetic and weak interactions. However, it is not able to explain gravity. The particle content can be divided into several categories: quarks, which interact via all interactions; charged leptons, which do not feel the strong force; neutrinos, which are blind to both colour and electromagnetism; spin-1 bosons, which mediate the fundamental interactions; and the Higgs boson, which is the only fundamental scalar and is related to the mass generation of the fundamental particles. Both quarks and leptons are divided into three generations with the same quantum numbers and increasing mass. Each generation contains two different quark flavours, one charged lepton and one neutrino. Every quark and lepton has an anti-particle, and neutrinos could be their own antiparticle (Majorana) or not (Dirac). Regarding the spin-1 bosons, the massless gluons mediate the strong force, the massive W^\pm and Z^0 bosons the weak interactions, and the photon γ is the mediator of the electromagnetic interaction.

The SM was built in several steps, starting with electromagnetism in the nineteenth and early twentieth century, and continuing with the strong and weak interactions during the second half of the twentieth century. Regarding the gauge sector, after the formulation of Yang-Mills theories in 1954 [1], the strong interactions were described using a quantum field theory with a local $SU(3)$ -colour symmetry [2] known as quantum chromodynamics (QCD). During the 1960s, the electromagnetic and weak interactions were unified by the Glashow-Weinberg-Salam theory [3, 4, 5], and the predicted W^\pm [6, 7] and Z^0 [8, 9] massive bosons mediating the weak interactions were discovered by the SPS experiment at CERN in 1983. The electroweak interactions are described by a quantum field theory possessing a gauge $SU(2)_L \times U(1)_Y$ symmetry, which is broken down to a $U(1)$ -electromagnetism group using the other relevant SM building block, the Englert-Brout-Higgs mechanism of spontaneous symmetry breaking for gauge theories [10, 11, 12]. Proposed in 1964, it predicts the existence of the Higgs boson, the only scalar of the SM, which was finally discovered by ATLAS [13] and CMS [14] at CERN in 2012. With regard to its fermionic content, some noteworthy contributions were the charm quark prediction by the Glashow-Iliopoulos-Maiani (GIM)

mechanism [15] in 1970 to explain the unexpected suppression of flavour changing neutral currents, and the subsequent experimental confirmation thanks to the discovery of the J/ψ meson by SLAC [16] and BNL [17] in 1974. Almost contemporaneous, the existence of the top and bottom quarks were proposed by Kobayashi and Maskawa [18] in 1973 to introduce CP violation in the SM. Bottomonium was discovered by the E288 experiment [19] at Fermilab in 1977, although it was not until 1995 when the CDF [20] and DZero [21] experiments at Fermilab discovered the top quark due to its heavier mass.

Despite its many successes, the SM is not the final description of nature. Among other shortcomings, it can only partially explain around 5% [22] of the matter and energy content of the Universe, while dark matter and dark energy, which constitute around 25% and 70% of the remainder, respectively, are still shrouded in mystery. Even the fourth fundamental interaction, gravity, is not included in the SM since General Relativity (GR) is a perturbatively non-renormalisable theory [23, 24]. Not only that, the SM considers neutrinos as massless Weyl particles, contradicting experiments of neutrino oscillations [25, 26]. Also, the SM fails to provide enough CP violation to explain why there is a net baryon and lepton number in the Universe with almost no anti-matter.

The efforts pursuing physics beyond the Standard Model (PBSM) can be broadly divided into two categories: Those probing the precision frontier, like the measurements of the electroweak mixing angle [27] or the electromagnetic coupling [27, 28], where a very precise theoretical prediction confronts an equally precise experimental determination looking for inconsistencies; and those pushing the energy frontier, like the experiments at the Large Hadron Collider (LHC), looking to observe the creation of heavy, exotic states. It is worth noting that, besides the finding of the Higgs boson, the non-discovery of any other heavy super-symmetric particle constitutes an equally relevant result by the LHC, since it imposes very stringent tests to any SUSY or string candidate to be the theory of everything.

In this thesis, we employ a lattice regularisation of QCD [29] to study two physical processes that we are interested in.

The first one concerns the polarisation of the vacuum by a free photon [27]. Photons mediate the electromagnetic interaction between two particles. However, the effective coupling or strength of the interaction can change because, as the photon propagates, the uncertainty principle of quantum mechanics allows it to transform momentarily into other states, which can be charged themselves, polarising the vacuum. Depending on the energy of the photon (in the s-channel), or its virtuality (on the t-channel), the polarisation's magnitude varies. In particular, we restrict ourselves to the hadronic contribution to this polarisation, which is equivalent to study the situation where the photon couples to quarks but not to leptons. The contribution of the latter can be predicted reliably in perturbation theory, while that of quarks cannot. Usually, the hadronic contribution is computed from e^+e^- -cross-section data [30, 31, 32] and a dispersion integral [33]. Even though the electromagnetic coupling is very well known in the Thomson limit,

$\alpha^{-1} = 137.035999084(21)$ [34], its precision deteriorates by five orders of magnitude at the Z -pole, $\hat{\alpha}^{(5)}(M_Z^2)^{-1} = 127.952(9)$ [35, 34]. With our contribution, we give an independent, *ab initio* determination of the hadronic contribution to the running coupling, and try to improve the precision at low momenta, which is the main source of uncertainty entering the dispersion integral.

A precise knowledge of the running is not only necessary as an auxiliary quantity in many computations, but its value at the Z -pole mass enters the global electroweak fits of the SM [34], which test the consistency of its various parameters. Besides, there is a direct relation [36] between the running of the coupling and what is, perhaps, the most well-known probe for PBSM as of today, the anomalous magnetic moment of the muon [37], $(g - 2)_\mu$, which shows a four sigma discrepancy between the most recent prediction [38] and the experiments [39, 40]. Beyond this tantalising tension, there is an even more intriguing interplay between the predictions for the anomalous magnetic moment of the muon and the Higgs boson mass via the global electroweak fits [34]. Excluding the kinematic constraints, the global fits infer $M_H = 90_{-16}^{+18}$ GeV [34], which is 1.8σ below the experimentally measured value [41, 42]. However, if the prediction of the leading hadronic contributions to $(g - 2)_\mu$ increases (agreeing with experiment), the electromagnetic coupling would increase as well, lowering the Higgs mass obtained from loop effects [43].

The second process we consider is the mixing of a Z -boson and a photon, with intermediate QCD states connecting both. Later, we will see that this particular polarisation of the vacuum allows us to compute the electroweak mixing angle [27], our second quantity of interest, which relates some of the generators of the $SU(2)_L \times U(1)_Y$ group to the Z and photon fields. The electroweak mixing angle also enters the global fits of the SM, but its current precision is orders of magnitude lower than that of the electromagnetic coupling, and its running is poorly known. Explicitly, its most precise determination at low virtuality reads $\sin^2 \hat{\theta}_W = 0.2383(11)$ at $Q = 0.158$ GeV [44]. New experiments focus on measuring the electroweak mixing angle at low virtualities with increased accuracy, and detecting possible deviations between prediction and experiment. These efforts are concentrated at JLAB [45, 46] and the Institute of Nuclear Physics in Mainz University [47]. Theoretically, one usually works with a dispersion relation and e^+e^- -data [48, 49, 50] to obtain the hadronic contribution to the electroweak mixing angle in a similar fashion to the electromagnetic coupling. However, since the data couple only to the electromagnetic current, it is necessary to separate each quark-flavour component, and replace the electric charges with the weak charges. This method, known as flavour separation [48, 49, 50], requires of certain assumptions, inducing a systematic uncertainty. A lattice calculation includes flavour separation automatically, making its use to compute the electroweak mixing angle a worthwhile endeavour.

This thesis is divided into several chapters: Chapter 2 gives an introduction to QCD, presenting some basic facts in the continuum before turning to the lattice in chapter 3, where we give the vital background to understand the remainder of this work. Then, we define the electromagnetic coupling in chapter 4 and the electroweak mixing angle in chapter 5, expanding the information already given in the introduction. Afterwards, we

introduce the equations of the time-momentum representation used to compute the target quantities in chapter 6, together with the vector-correlator renormalisation and improvement. We explain how the quark-connected and quark-disconnected data for our analysis were generated in chapter 7, where we also give a summary of the various Coordinated Lattice Simulations (CLS) ensembles that we use. After introducing the main pre-requisites, we present our analysis: First, chapter 8 shows the removal of autocorrelations, then chapter 9 details the study of the signal-to-noise ratio problem, and chapter 10 presents the various methods that we have used to remove the infrared cut-off on our lattices. Chapter 11 summarizes our results on the lattice, and chapter 12 describes the extrapolation of the lattice data to the physical point. Finally, chapter 13 gathers our results for the electromagnetic coupling and the electroweak mixing angle at the physical point as a function of Q^2 , and our conclusions and outlook are gathered in chapter 14.

Several milestones of this thesis have appeared in proceedings of the annual Lattice Conference, which make possible to follow the historical development of this project,

- Teseo San José et al. “The hadronic contribution to the running of the electromagnetic coupling and electroweak mixing angle”. In: *38th International Symposium on Lattice Field Theory*. Sept. 2021. arXiv: 2109.04537 [hep-lat]
- Marco Cè et al. “The hadronic contribution to the running of the electromagnetic coupling and the electroweak mixing angle”. In: *PoS LATTICE2019* (2019), p. 010. DOI: 10.22323/1.363.0010. arXiv: 1910.09525 [hep-lat]

From the start, our work was tightly linked to the Mainz efforts on $(g - 2)_\mu$, and our contributions have appeared on the conference proceedings

- Hartmut Wittig et al. “Lattice calculation of the hadronic leading order contribution to the muon $g - 2$ ”. In: *EPJ Web Conf.* 234 (2020). Ed. by G. D’Ambrosio et al., p. 01016. DOI: 10.1051/epjconf/202023401016. arXiv: 1912.01950 [hep-lat]

and the peer-reviewed work

- T. Aoyama et al. “The anomalous magnetic moment of the muon in the Standard Model”. In: *Phys. Rept.* 887 (2020), pp. 1–166. DOI: 10.1016/j.physrep.2020.07.006. arXiv: 2006.04822 [hep-ph].

Chapter 2

QCD in the continuum

Our aim in this thesis is to study the strong interactions between quarks mediated via gluons using the mathematical framework given by QCD, which comprises our current knowledge of the strong interactions. The objective is to present the main results and definitions upon which we build the remainder of this work rather than to review QCD exhaustively. For the latter, we recommend the reader to see, e.g. , [54, 27, 29]. The layout of this chapter follows the PhD theses [55, 56, 57].

2.1 Action in the continuum

To construct the Lagrangian of QCD, we should include all terms of mass dimension four or less that are allowed by the gauge symmetries and Lorentz invariance [54]. Of the free parameters the theory might have, the criterion of naturalness [58] tells us that they should be of magnitude $\mathcal{O}(1)$. Interestingly enough, as presented in section 2.1.3, QCD seems to defy the notion of naturalness with a θ angle compatible with zero; possible solutions, not yet proven, hint to the existence of extra symmetries and new particles. In this section, we present the action of N_f quark-flavours and the eight different gluons, from whose Lagrangian the equations of motion (EOM) can be derived using the Euler-Lagrange Equations [54].

2.1.1 Fermion action

Quarks are spin one-half particles represented by fermion fields $\psi(x)$. The latter are Dirac 4-spinors evaluated at a position x , carrying a colour index $c = 1, 2, 3$, a Dirac index $\alpha = 1, 2, 3, 4$ and a flavour index $f = u, d, c, s, t, b$. Using vector notation, the action for N_f free fermions is written as [54]

$$S_{\text{M,F}}^0[\psi, \bar{\psi}] = \int d^4x \bar{\psi}(x)(i\gamma^\mu \partial_\mu - M)\psi(x), \quad (2.1)$$

where the mass matrix $M = \text{diag}(M_u, M_d, \dots)$ is obtained in the SM via the Higgs mechanism after spontaneous symmetry breaking [54]. The subscript M in $S_{\text{M,F}}^0$ indicates we use the

Minkowski metric with signature $(-, +, +, +)$ [54]. We also make use of tensor notation. Equation (2.1) is invariant under Lorentz transformations. Now, in order to introduce a theory with interactions, we make eq. (2.1) symmetric under local $SU(3)_c$ transformations [54]

$$\left\{ \Omega(x) \mid \Omega^\dagger(x) = \Omega^{-1}(x), \det \Omega(x) = 1 \right\}, \quad (2.2)$$

where $\Omega(x)$ are 3×3 matrices in colour space in the fundamental representation. Quarks transform according to [54]

$$\begin{aligned} \psi(x) &\rightarrow \psi'(x) = \Omega(x)\psi(x), \\ \bar{\psi}(x) &\rightarrow \bar{\psi}'(x) = \bar{\psi}(x)\Omega(x)^\dagger, \end{aligned} \quad (2.3)$$

and we introduce the Lie algebra gauge fields $A_\mu(x) \in \mathfrak{su}(3)_c$ [54],

$$\left\{ A_\mu(x) \mid A_\mu^\dagger(x) = A_\mu(x), \text{Tr } A_\mu(x) = 0 \right\}, \quad (2.4)$$

whose transformation properties are determined by requiring invariance of the fermion action under $SU(3)_c$ transformations [54],

$$A_\mu(x) \rightarrow A'_\mu(x) = \Omega(x)A_\mu(x)\Omega(x)^\dagger + \frac{i}{g_s}\Omega(x)\partial_\mu\Omega(x)^\dagger. \quad (2.5)$$

The fields $A_\mu(x)$ are 3×3 matrices that can be decomposed in terms of the generators of the Lie algebra, $A_\mu(x) = A_\mu^a(x)T^a$, with $a = 1, \dots, 8$ —for the colour indices we simply use the Einstein convention, and therefore repeated indices are summed, g_s is the coupling constant of the strong interactions, which we further study in section 2.4, and section 2.1.2 gives the dynamics of A_μ . The generator matrices T^a are hermitian and traceless, and obey the commutation relations and normalisation [54]

$$[T^a, T^b] = if^{abc}T^c, \quad (2.6)$$

$$\text{Tr}(T^a T^b) = \frac{1}{2}\delta^{ab}, \quad (2.7)$$

where the real numbers f^{abc} are the structure constants of $SU(3)_c$. These constants are non-zero because we work with matrices, which in general do not commute; as a consequence, $SU(3)_c$ is a non-Abelian group. Elements of the $SU(3)_c$ group and its algebra can be related using an exponential map via the generators T^a ,

$$\Omega(x) = e^{-i\alpha^a(x)T^a}, \quad (2.8)$$

with $\alpha^a(x) \in \mathbb{R}$. More in general, $SU(N)$ groups were first used to study gauge theories by Yang and Mills [59]. Then, the action for interacting fermions is given by [54]

$$S_{\text{M,F}}[\psi, \bar{\psi}, A] = \int d^4x \bar{\psi}(x) (i\gamma^\mu D_\mu - M) \psi(x), \quad (2.9)$$

where the covariant derivative $D_\mu = \partial_\mu - ig_s A_\mu$ has the transformation properties

$$D_\mu(x) \rightarrow D'_\mu(x) = \Omega(x) D_\mu(x) \Omega^\dagger(x). \quad (2.10)$$

Therefore, substituting the partial with the covariant derivative yields an interacting $SU(3)_c$ -invariant theory. Equation (2.9) includes an interaction between one fermion, one anti-fermion and a gauge field. The corresponding Feynman vertex is shown in fig. 2.1a.

2.1.2 Gluon action

The kinetic term, the so-called Yang-Mills action, describing the dynamics of the newly added A_μ fields is a Lorentz scalar, built taking the QED gauge action as a model [54],

$$S_{M,G}[A] = -\frac{1}{2} \int d^4x \operatorname{Tr} (F^{\mu\nu}(x) F_{\mu\nu}(x)), \quad (2.11)$$

where the field tensor $F_{\mu\nu}(x)$ is defined as

$$F_{\mu\nu}(x) = \frac{i}{g_s} [D_\mu(x), D_\nu(x)] = \partial_\mu A_\nu(x) - \partial_\nu A_\mu(x) - ig_s [A_\mu(x), A_\nu(x)]. \quad (2.12)$$

From the transformation properties of $D_\mu(x)$ in eq. (2.10), the field strength tensor transforms according to

$$F_{\mu\nu}(x) \rightarrow F'_{\mu\nu}(x) = \Omega(x) F_{\mu\nu}(x) \Omega^\dagger(x). \quad (2.13)$$

If one writes eq. (2.11) in terms of A_μ^a , the non-abelian nature of the theory manifests itself giving gluon self-interactions. In particular, the Feynman rules include vertices of three (proportional to g_s) and four (proportional to g_s^2) gluons, which are shown in figs. 2.1b and 2.1c.

2.1.3 θ -term

One last term remains to be added to the action [34],

$$S_{M,\theta}[A] = -\theta g_s^2 \int d^4x \operatorname{Tr} (F_{\mu\nu} \tilde{F}^{\mu\nu}), \quad (2.14)$$

where the QCD vacuum angle is allowed to take on values in the range $-\pi \leq \theta \leq \pi$, and $\tilde{F}_{\mu\nu}$ is the dual of the field strength tensor,

$$\tilde{F}_{\mu\nu} = \frac{1}{2} \epsilon_{\mu\nu\sigma\rho} F^{\sigma\rho}, \quad (2.15)$$

with $\epsilon_{\mu\nu\sigma\rho}$ the totally antisymmetric Levi-Civita symbol. Assuming naturalness [58], one would naively expect $|\theta| \sim \mathcal{O}(1)$. However, current experimental limits on the neutron dipole moment [60] constrain the QCD vacuum angle to $|\theta| \lesssim 10^{-10}$. This mismatch between expectation and experiment is known as the strong \mathcal{CP} problem [61, 62] because eq. (2.14) violates \mathcal{CP} . The most well known solution to explain the small magnitude of θ

is the Peccei-Quinn mechanism, by which one introduces a global $U(1)_{PQ}$ symmetry that breaks spontaneously, generating a pseudo-Goldstone boson known as axion [63, 64].

Since the numerical value of θ is compatible with zero, we do not consider the term of eq. (2.14) in the rest of this thesis, and we work with the QCD action

$$S_M[\psi, \bar{\psi}, A] = \int d^4x \left(\bar{\psi}(x) (i\gamma^\mu D_\mu - M) \psi(x) - \frac{1}{2} \text{Tr} (F^{\mu\nu}(x) F_{\mu\nu}(x)) \right). \quad (2.16)$$

Equation (2.16) is invariant under the discrete transformations of charge conjugation \mathcal{C} , time reversal \mathcal{T} and parity \mathcal{P} [29].

2.2 Gauge transporter

When we discuss the lattice regularisation of QCD in chapter 3, it will be important to connect the discretised version of the QCD action with the continuum expressions that we just discussed. Due to this, we define here the gauge transporter, which is a path-ordered exponential of the gauge fields, connecting two points x and y along a curve \mathcal{C}_{xy} [29],

$$G(x, y) = P \exp \left(ig_s \int_{\mathcal{C}_{xy}} A_\mu ds^\mu \right), \quad (2.17)$$

where P indicates the exponential is path-ordered. Under an $SU(3)_c$ transformation $\Omega(x)$, the gauge transporter becomes [29]

$$G(x, y) \rightarrow G'(x, y) = \Omega(x) G(x, y) \Omega(y)^\dagger. \quad (2.18)$$

Therefore, $G(x, y)$ is an element of $SU(3)_c$ and one can create $SU(3)_c$ -invariant quantities with it [29]. E.g., $\bar{\psi}(x) G(x, y) \psi(y)$.

2.3 Path integral quantisation

Instead of the canonical quantisation, we use the path integral formalism presented in [65]. The Feynman quantisation prescription writes expectation values as integrals over classical fields, with the field configurations weighted by the action of the theory. In particular, in Minkowski space, the expectation value of an operator $O[\psi, \bar{\psi}, A]$ is [54]

$$\langle O \rangle = \frac{1}{Z} \int \mathcal{D}[A] \mathcal{D}[\psi, \bar{\psi}] \exp (iS_M[\psi, \bar{\psi}, A]) O[\psi, \bar{\psi}, A], \quad (2.19)$$

where the partition function normalises the integral, such that $\langle 1 \rangle = 1$, and S_M is defined in eq. (2.16). Next, we apply a Wick rotation to eq. (2.19) [54]. We rotate the time variable to the imaginary axis and consider $x_4 = ix_0$. In this way, $iS_M \rightarrow -S$, with $S = \int d^4x \mathcal{L}$ and $d^4x = dx_1 dx_2 dx_3 dx_4$. This change of variables allows to think of the exponential of the action as a Boltzmann weight, and it will become relevant in section 3.3.2, when

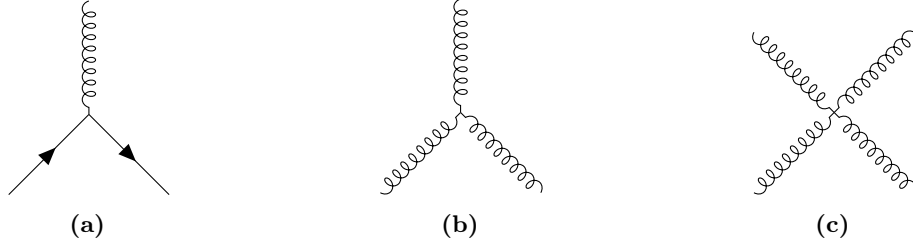


Figure 2.1: Interaction vertices of QCD. Figure 2.1a indicates the quark-gluon interaction. Figure 2.1b shows the three gluon self-interaction. Figure 2.1c shows the four gluon self-interaction.

we discuss how to perform the integral in eq. (2.19) employing importance sampling and Monte Carlo methods. The path integral becomes

$$\langle O \rangle = \frac{1}{Z} \int \mathcal{D}[A] \mathcal{D}[\psi, \bar{\psi}] \exp(-S_F[\psi, \bar{\psi}, A] - S_G[A]) O[\psi, \bar{\psi}, A]. \quad (2.20)$$

The change of variables modifies the Minkowski metric to the trivial Euclidean metric with signature $(+, +, +, +)$. From now on, therefore, we no longer need to work with covariant and contravariant tensor notation; the simple Einstein convention remains though, and repeated indices are summed over. We refer the reader to [29] for the conventions used in Euclidean space, including the definition of the γ_μ matrices. Bare in mind the two references [54, 29] use two different conventions for the Minkowski metric. While [29] uses $(+, -, -, -)$, [54] employs $(-, +, +, +)$. Also, one needs to translate the gauge fields. The fields $g_s A_\mu$ in [54] are redefined as simply A_μ [29]. The second form yields the coupling as an overall prefactor $1/g_s^2$ of the gluon action, and we will use this form when we discuss the formulation on the lattice. The fermion and gluon actions are modified to

$$S_F[\psi, \bar{\psi}, A] = \int d^4x \bar{\psi}(x) (\gamma_\mu D_\mu + M) \psi(x), \quad (2.21)$$

$$S_G[A] = \frac{1}{2} \int d^4x \text{Tr} (F_{\mu\nu}(x) F_{\mu\nu}(x)). \quad (2.22)$$

2.4 Strong running coupling α_s

Besides the quark masses, the strong coupling g_s or $\alpha_s = g_s^2/(4\pi)$ is the only other parameter of QCD. In perturbation theory, observables are expressed in terms of the renormalised coupling $\alpha_s(\mu_R^2)$, with the renormalisation energy scale μ_R [34]. The coupling fulfils the renormalisation group equations (RGE) [34]

$$\mu_R^2 \frac{\partial}{\partial \mu_R^2} \frac{\alpha_s}{4\pi} = \beta(\alpha_s) = - \left(\frac{\alpha_s}{4\pi} \right)^2 \sum_{n=0} \left(\frac{\alpha_s}{4\pi} \right)^n \beta_n, \quad (2.23)$$

where the 1-loop coefficient of the $\beta(\alpha_s)$ function is independent of the renormalisation scheme and defined as [66]

$$\beta_0 = 11 - \frac{2}{3}N_f. \quad (2.24)$$

In eq. (2.24), N_f is the number of flavours with masses $M \ll \mu_R$. The minus sign on the RHS of eq. (2.23) indicates that, at high momentum transfers, fermions and gluons behave as free particles; this is the so-called asymptotic freedom of QCD [67, 68]. However, only $SU(3)_c$ -scalar particles have been observed. This property is known as confinement [29]. Including only β_0 , it is possible to find the dependence of the strong coupling on the energy [68, 66],

$$\alpha_s(\mu_R^2) = \frac{4\pi}{\beta_0} \frac{1}{\log(\mu_R^2/\Lambda^2)}, \quad (2.25)$$

where the QCD scale parameter Λ adopts a value $\Lambda \approx 0.34 \text{ GeV}$ in the $\overline{\text{MS}}$ renormalisation scheme for $N_f = 3$ [69, 66]. All the u , d , s , c and b quarks hadronize on a timescale $\sim 1/\Lambda$ [34], becoming part of either a meson or a baryon. The t quark decays before it can hadronize [34]. Figure 2.2 shows the running of α_s with the energy. One can see how, at high energies, the coupling vanishes asymptotically, removing interactions from the theory. On the other hand, at small momentum, the coupling becomes $\mathcal{O}(1)$ and perturbation theory breaks down.

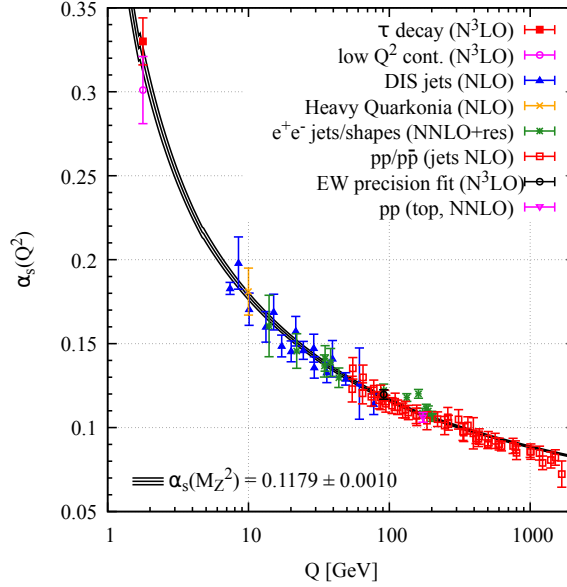


Figure 2.2: Running with the energy of the strong coupling α_s [34], indicating the measurements and the perturbation-theory order used to extract the values (NLO:next-to-leading order; NNLO: next-to-next-to-leading order; NNLO+res.: NNLO matched to a resummed calculation; N3LO: next-to-NNLO).

2.5 Global symmetries

In the case of N_f massless quark-flavours, the action in eq. (2.9) with $M = \text{diag}(0, 0, \dots, 0)$ is invariant under the group of global transformations [29]

$$\text{SU}(N_f)_V \times \text{SU}(N_f)_A \times \text{U}(1)_V \times \text{U}(1)_A. \quad (2.26)$$

The $N_f^2 - 1$ vector transformations corresponding to $\text{SU}(N_f)_V$ are defined as [29]

$$\psi' = e^{i\alpha T_i} \psi, \quad \bar{\psi}' = \bar{\psi} e^{-i\alpha T_i}, \quad (2.27)$$

where $i = 1, \dots, N_f^2 - 1$, T_i are a basis of the $\mathfrak{su}(N_f)$ algebra, and α is a continuous parameter. The $\text{SU}(N_f)_V$ symmetry holds for both massless and mass-degenerate quarks. For this thesis, we work with an exact $\text{SU}(2)_V$ symmetry, known as isospin symmetry. This means choosing mass-degenerate u and d quarks, $M_u = M_d$. In the $\overline{\text{MS}}$ scheme at a scale $\mu \approx 2 \text{ GeV}$, one finds $M_u = 2.16_{-0.26}^{+0.49} \text{ MeV}$ and $M_d = 4.67_{-0.17}^{+0.48} \text{ MeV}$ [34]. This means isospin symmetry is not exact, but a good approximation given the precision we aim at. The strange quark has a mass of $M_s = 93_{-5}^{+11} \text{ MeV}$, which is much closer to the typical QCD energy scale Λ presented in section 2.4 and, therefore, a $\text{SU}(3)_f$ symmetry would be much more inexact.

The $\text{U}(1)_V$ -symmetry transformation is [29]

$$\psi' = e^{i\alpha \mathbf{1}} \psi, \quad \bar{\psi}' = \bar{\psi} e^{-i\alpha \mathbf{1}}, \quad (2.28)$$

with $\mathbf{1}$ the $N_f \times N_f$ unit matrix. The $\text{U}(1)_V$ symmetry holds for zero and non-zero masses. In the case of arbitrary quark masses, we have one $\text{U}(1)_V$ symmetry per flavour and the conserved quantity is the baryon number.

The chiral symmetry $\text{SU}(N_f)_A$ is defined by the transformation [29]

$$\psi' = e^{i\alpha \gamma_5 T_i} \psi, \quad \bar{\psi}' = \bar{\psi} e^{-i\alpha \gamma_5 T_i}, \quad (2.29)$$

and holds only for the massless case, and therefore $M = 0$ is usually called the chiral limit. The fermion action is chirally symmetric if

$$D\gamma_5 + \gamma_5 D = 0. \quad (2.30)$$

Even though the massless quark action is invariant under the chiral rotations of eq. (2.29), the ground state of the theory is not and chiral symmetry breaks spontaneously. Since eq. (2.29) is a continuous transformation, the spontaneous breaking should generate a set of massless Goldstone bosons, the pions. Given that the u and d quarks are not exactly massless, we obtain pions with masses much smaller than the nucleon.

The axial vector $\text{U}(1)_A$ symmetry changes the fermion fields according to [29]

$$\psi' = e^{i\alpha \gamma_5 \mathbf{1}} \psi, \quad \bar{\psi}' = \bar{\psi} e^{i\alpha \gamma_5 \mathbf{1}}. \quad (2.31)$$

However, even though eq. (2.31) is a symmetry of the action, it is not observed in experiments. Using the path integral explained in section 2.3, one realises that $\text{U}(1)_A$ is anomalous upon quantisation [70, 71]; the measure of the path integral is not invariant under eq. (2.31)

Chapter 3

QCD on the lattice

Now, we introduce the lattice regularisation for QCD. The main points that differentiate it from other regularisations are [29]:

1. First, we replace the continuum space-time by a 4D lattice,

$$\Lambda = \{n = (n_1, n_2, n_3, n_4) | n_1, n_2, n_3 = 0, 1, \dots, N_L - 1, n_4 = 0, 1, \dots, N_T - 1\}, \quad (3.1)$$

where each space-time node is labelled by a 4-tuple n . The distance between the nodes is known as lattice spacing, abbreviated as a . For this thesis, the lattice spacing is taken equal for all directions. N_L and N_T are the number of lattice sites in the spatial and temporal directions, respectively.

2. The Euclidean QCD action S is discretised in such a way that removing the regulator, $a \rightarrow 0$, we recover the continuum action.
3. The Feynman path integral quantisation condition in eq. (2.20) is applied. Every operators is substituted by a functional of classical fields living on the nodes or the links—which connect adjacent nodes— of the lattice.

In the following, we discretise the fermion action of eq. (2.21) in section 3.1 and the gluon action of eq. (2.22) in section 3.2. We introduce the path integral of eq. (2.20) on the lattice in section 3.3. Methods to perform the integration are described in sections 3.3.2 and 3.4. The specific methods to include dynamical quarks are given in sections 3.4.1 and 3.4.2. We end the chapter introducing the scale setting procedure in section 3.5. Some introductory textbooks to Lattice QCD (LQCD) are [29, 72, 73]. We based the structure of this chapter on the PhD theses [55, 56, 57].

3.1 $\mathcal{O}(a)$ -improved Wilson fermion action

In this section, we discuss the discretisation of the interacting fermion action given in eq. (2.21). We consider only one flavour though, as the difference between them at this point is only the value of the quark mass. This will simplify our expressions. Later, in

section 3.3, when we start considering the computation of expectation values, we consider the computational differences between the different flavours.

3.1.1 Naive lattice fermion action

We start from the discretisation of the free fermion action in Euclidean space-time,

$$S_F^0[\psi, \bar{\psi}] = \int d^4x \bar{\psi}(x)(\gamma_\mu \partial_\mu + M)\psi(x), \quad (3.2)$$

where the superscript 0 is used to refer to the free action. We employ the symmetric discretisation of the derivative for ∂_μ [29],

$$S_F^0[\psi, \bar{\psi}] = a^4 \sum_{n \in \Lambda} \bar{\psi}(n) \left(\sum_{\mu=1}^4 \gamma_\mu \frac{\psi(n + \hat{\mu}) - \psi(n - \hat{\mu})}{2a} + M\psi(n) \right), \quad (3.3)$$

where the single-flavour fermion fields ψ and $\bar{\psi}$ are placed on the lattice sites, and have indices $a, b, \dots = 1, 2, 3$ in colour space and $\alpha, \beta, \dots = 1, 2, 3, 4$ in Dirac space. To implement Fermi statistics, the fermion fields $\psi, \bar{\psi}$ are described by Grassmann (anti-commuting) numbers —see [29] for an introduction to their most important properties. As it was previously done for the continuum action, we enforce eq. (3.3) to be $SU(3)_c$ symmetric. This time, however, it is required to introduce the group elements $U_\mu(n), U_{-\mu}(n) \in SU(3)_c$, where $U_{-\mu}(n) = U_\mu(n - \hat{\mu})^\dagger$ [29]. The variable $U_\mu(n)$ is placed on the links of the lattice, and connects the site n with $n + \hat{\mu}$. Therefore, they are referred to as link variables. As elements of the $SU(3)_c$ group, they transform as [29]

$$\begin{aligned} U_\mu(n) &\rightarrow U'_\mu(n) = \Omega(n)U_\mu(n)\Omega^\dagger(n + \hat{\mu}), \\ U_{-\mu}(n) &\rightarrow U'_{-\mu}(n) = \Omega(n)U_{-\mu}(n)\Omega^\dagger(n - \hat{\mu}). \end{aligned} \quad (3.4)$$

Incorporating the link variables, the gauge invariant action for interacting fermions is [29]

$$S_F[\psi, \bar{\psi}, U] = a^4 \sum_{n \in \Lambda} \left(\bar{\psi}(n) \sum_{\mu=1}^4 \gamma_\mu \frac{U_\mu(n)\psi(n + \hat{\mu}) - U_{-\mu}(n)\psi(n - \hat{\mu})}{2a} + M\psi(n) \right). \quad (3.5)$$

The use of the symmetric derivative in eq. (3.5) allows to recover the continuum action in eq. (2.21) with $\mathcal{O}(a^2)$ discretisation effects [74]. The link variables are no more than the discretisation of the continuum gauge transporter in eq. (2.17) [29]. In particular, a link is a transporter between n and $n + \hat{\mu}$ along a lattice link of length a

$$U_\mu(n) = \exp(iaA_\mu(n)). \quad (3.6)$$

The continuum gauge transporter is recovered for small lattice spacings with corrections of $\mathcal{O}(a)$ [29], $U_\mu(n) = G(n, n + \hat{\mu}) + \mathcal{O}(a)$. From eq. (3.5), we can define the naive discretisation of the Dirac operator [29],

$$D_{\text{naive}}(n, m)_{ab, \alpha\beta} = \sum_{\mu=1}^4 (\gamma_\mu)_{\alpha\beta} \frac{U_\mu(n)_{ab} \delta_{n+\hat{\mu}, m} - U_{-\mu}(n)_{ab} \delta_{n-\hat{\mu}, m}}{2a} + M\delta_{\alpha\beta} \delta_{ab} \delta_{n, m}. \quad (3.7)$$

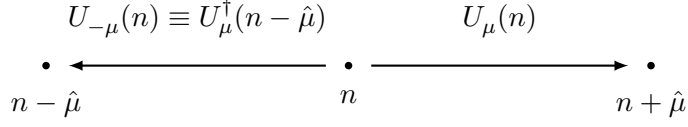


Figure 3.1: Link variables $U_\mu(n)$ and $U_{-\mu}(n)$ employed to transport the fields from position n to $n + \hat{\mu}$ and $n - \hat{\mu}$, respectively [29].

3.1.2 Wilson fermion action

If one inverts the Dirac operator defined by eq. (3.7) in the Fourier space representation, one finds the fermion propagator in momentum space. In the first Brillouin zone $p_\mu = (-\pi/a, \pi/a]$, the latter has sixteen poles instead of only one [29]. All extra fermions are called doublers and we need to remove them. To do this, we add the so-called Wilson term, which vanishes for the physical pole but increases the mass of all doublers with a term $2/a$ [29]. Taking the continuum limit, the doubler modes become infinitely heavy and decouple from the theory, effectively removing them. Adding the Wilson term to eq. (3.7), we obtain the Wilson-Dirac operator [29, 75, 76]

$$D_{\text{Wilson}}(n, m)_{ab, \alpha\beta} = \left(M + \frac{4}{a}\right) \delta_{\alpha\beta} \delta_{ab} \delta_{n, m} - \frac{1}{2a} \sum_{\mu=\pm 1}^{\pm 4} (\mathbf{1} - \gamma_\mu)_{\alpha\beta} U_\mu(n)_{ab} \delta_{n+\hat{\mu}, m}. \quad (3.8)$$

One can factor out $M + 4/a \equiv 1/(2a\kappa)$, with $1/\kappa = 2(aM + 4)$ the hopping parameter, and redefine the quark fields as $\psi \rightarrow 1/\sqrt{2a\kappa}\psi$ and $\bar{\psi} \rightarrow 1/\sqrt{2a\kappa}\bar{\psi}$. Then, eq. (3.8) can be rewritten as [29]

$$D_{\text{Wilson}}(n, m)_{ab, \alpha\beta} = \delta_{\alpha\beta} \delta_{ab} \delta_{n, m} - \kappa H(m, n)_{ab, \alpha\beta}, \quad (3.9)$$

with the hopping term

$$H(n, m)_{ab, \alpha\beta} = \sum_{\mu=\pm 1}^{\pm 4} (\mathbf{1} - \gamma_\mu)_{\alpha\beta} U_\mu(n)_{ab} \delta_{n+\hat{\mu}, m}. \quad (3.10)$$

The hopping parameter κ receives its name from the fact that the hopping term H in eq. (3.9) describes the interactions between nearest neighbours. Using either eq. (3.8) or eq. (3.9), the fermion action in eq. (3.5) is modified to

$$S_{\text{Wilson}}[\psi, \bar{\psi}, U] = a^4 \sum_{n, m \in \Lambda} \bar{\psi}(n) D_{\text{Wilson}}(n, m) \psi(m), \quad (3.11)$$

with $D_{\text{Wilson}}(n, m)$ given by eq. (3.8). Unfortunately, the Wilson-Dirac operator violates chiral symmetry, eq. (2.30), at finite lattice spacing even at zero quark mass due to the Wilson term and, therefore, it is difficult to study chiral symmetry using this fermion discretisation. In fact, the Nielsen-Ninomiya theorem [77, 78, 79] states that one cannot have a lattice theory that is simultaneously doubler-free and chirally symmetric in the sense of eq. (2.30). In section 3.1.4, we discuss briefly how extending the notion of chiral symmetry to the lattice has spurred the design of other fermion discretisations.

3.1.3 $\mathcal{O}(a)$ improvement

Equation (3.11) approaches the continuum with $\mathcal{O}(a)$ -lattice artefacts [29], rather than the naive fermion action, which approaches with $\mathcal{O}(a^2)$. In order to reduce the systematic uncertainty of the final results, it is advantageous to have a difference with the continuum as small as possible. To achieve this, we use the Symanzik improvement program [80, 81, 82, 83]. The first step is to expand the lattice action in eq. (3.11) in powers of a [29],

$$S_F = \int d^4x \left(L^{(0)}(x) + aL^{(1)}(x) + a^2L^{(2)} + \dots \right). \quad (3.12)$$

$L^{(0)}(x)$ denotes the Lagrangian in the continuum limit, and all other terms $L^{(k)}(x)$ are linear combinations of operators with the same symmetries as $L^{(0)}(x)$ and dimension a^{-4-k} . To have only $\mathcal{O}(a^2)$ artefacts, it is necessary to find all terms and pre-factors contributing to $L^{(1)}(x)$, and subtract their lattice-discretised version from the Wilson action. *A priori*, $L^{(1)}(x)$ is formed by a total of five terms. However, if we are only interested in improving on-shell quantities, some are related via the Dirac equation and others are proportional to terms already present in the fermion and gauge actions, with the quark mass acting as proportionality factor, and can be accounted for redefining the bare quark mass M and coupling β . Then, the only 5-dimensional term $L^{(1)}(x)$ we need is [29]

$$\frac{1}{2}\bar{\psi}(x)\sigma_{\mu\nu}F_{\mu\nu}(x)\psi(x), \quad (3.13)$$

where $\sigma_{\mu\nu} = \frac{1}{2i} [\gamma_\mu, \gamma_\nu]$ and $F_{\mu\nu}$ is the field strength tensor. Therefore, one needs to add to the Wilson action a discrete version of eq. (3.13) with the appropriate prefactor to remove $\mathcal{O}(a)$ lattice artefacts from the action,

$$S_{\text{clover}}[\psi, \bar{\psi}, U] = c_{\text{SW}} a^5 \sum_{n \in \Lambda} \sum_{\mu < \nu} \bar{\psi}(n) \frac{1}{2} \sigma_{\mu\nu} \hat{F}_{\mu\nu}(n) \psi(n), \quad (3.14)$$

where $c_{\text{SW}} \in \mathbb{R}$ is the Sheikholeslami-Wohlert coefficient [84] and $\hat{F}_{\mu\nu}(n)$ is a discrete version of the field strength tensor,

$$\begin{aligned} \hat{F}_{\mu\nu}(n) &= \frac{-i}{8a^2} (Q_{\mu\nu}(n) - Q_{\nu\mu}(n)), \\ Q_{\mu\nu}(n) &\equiv P_{\mu\nu}(n) + P_{\nu,-\mu}(n) + P_{-\mu,-\nu}(n) + P_{-\nu\mu}(n). \end{aligned} \quad (3.15)$$

$Q_{\mu\nu}(n)$ is displayed in fig. 3.2, and the plaquette $P_{\mu\nu}(n)$ is defined in eq. (3.19) and depicted schematically in fig. 3.3. Due to the shape of a clover leaf, eq. (3.14) is also called clover term or clover improvement. The coefficient c_{SW} was determined for each of our lattice spacings in [85].

Finally, the fermion action without doublers and $\mathcal{O}(a)$ improvement can be written as a bilinear of the quark fields,

$$S_F = S_{\text{Wilson}} + S_{\text{clover}} = \bar{\psi} D \psi. \quad (3.16)$$

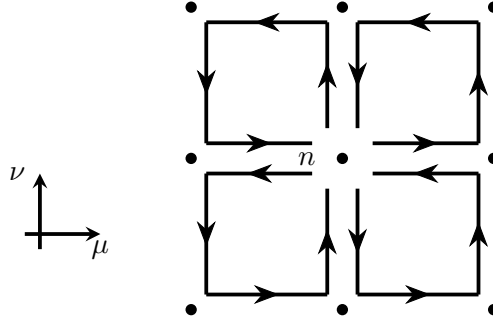


Figure 3.2: Representation of the sum of plaquettes $Q_{\mu\nu}(n)$ defined in eq. (3.15).

Despite its success, Symanzik improvement is not pursued beyond $\mathcal{O}(a)$ in fermions. At dimension six, four more fermion operators need to be included [73]. Then, the action would no longer be a bilinear of fermion fields and, therefore, we would not be able to integrate the Grassmann variables without including auxiliary fields [73]. To complete the discussion of the fermion action, we mention that $S_F[\psi, \bar{\psi}, U]$ is invariant under charge conjugation \mathcal{C} , time reversal \mathcal{T} and parity transformations \mathcal{P} [29]. In addition, the Dirac operator D is γ_5 -hermitian [29], i.e.

$$D^\dagger = \gamma_5 D \gamma_5. \quad (3.17)$$

Most Dirac operators fulfil eq. (3.17), except those including a chemical potential, a θ -term like in section 2.1.3 or a twisted mass term [29].

3.1.4 Other fermion discretisations

In section 3.1.2, we have seen that the Wilson term not only removes the fermion doublers but also breaks chiral symmetry as stated in eq. (2.30). However, it is possible to extend the notion of chiral symmetry to the lattice. In [86], the Ginsparg-Wilson equation was proposed at finite lattice spacing,

$$D\gamma_5 + \gamma_5 D = aD\gamma_5 D, \quad (3.18)$$

where a contact term, vanishing in the continuum, is added on the right-hand side (RHS) of eq. (2.30). The first solutions D for eq. (3.18) were reported in [87, 88]. The new definition in eq. (3.18) stems a lattice version of chiral rotations that reduces to eq. (2.30) in the continuum [89]. The removal of doublers and the treatment of chiral symmetry is a central aspect when building a lattice action, and here we briefly present other fermion discretisations.

Overlap fermions [90] are a solution of the Ginsparg-Wilson equation [88] and, therefore, respect chiral symmetry on the lattice. However, the action is not ultra-local, as no solutions of the Ginsparg-Wilson equation are [91]. This implies non-causal interactions that must be prevented imposing further requirements to the overlap operator to recover a local theory in the continuum [92].

Twisted-mass (tmQCD) fermions were introduced in [93, 94, 95] as a formulation with two mass-degenerate quark flavours of Wilson fermions, although it can be extended with quarks of different masses [96, 97]. An additional chirally twisted mass term is introduced to avoid zero modes of the Dirac operator and can be tuned to maximal twist to achieve $\mathcal{O}(a)$ improvement [98]. See [99, 100, 101] for some recent calculations employing tmQCD.

Domain wall (DW) fermions, defined in [102] and further developed in [103, 104, 105]. The idea is to embed 4D Dirac fermions on a 5D lattice. Since they essentially use Wilson fermions, the same methods and techniques can be used to simulate DW fermions, modulo some modifications, and only nearest-neighbour interactions appear on the Dirac operator. Like overlap fermions, they fulfil the Ginsparg-Wilson equation. See [106, 107] for an example of simulations using DW fermions.

Staggered or Kogut-Susskind fermions [108] reduce the sixteen roots of the naive fermion discretisation to only four, while keeping a remnant of chiral symmetry. The original fermion fields undergo a space-time-dependent transformation which mixes the Dirac and lattice indices and removes the γ_μ matrices. For analysis purposes [109, 110], the sites of a 4D cube are grouped together, giving four fermions with 4-spinor structure. To differentiate between these quark species, one refers to them as tastes, in analogy to the flavours of usual QCD. Unfortunately, these tastes are mixed at finite lattice spacing. To make contact with the physical world however, one needs to work with, for example, two mass-degenerate light fermions plus another heavier one, representing the u , d and s quarks. One may take the root of the fermion determinants to do so —see 3.3 to learn more about the fermion determinant—, but rooting raises some conceptual questions about staggered fermions [111, 112, 113, 114]. Despite the latter, they yield results in good agreement with experiments and other lattice discretisations [115, 116, 117, 118], they are cheaper to simulate due to the distributed Dirac structure, and they are chirally symmetric.

3.2 Tree-level Lüscher-Weisz gauge action

In section 3.1, we have introduced the field $U_\mu(n)$ to obtain interactions on the lattice. This field has its own EOM, and we built its action creating an object that is $SU(3)_c$ invariant. The plaquette $P_{\mu\nu}(n)$, depicted in fig. 3.3, is the shortest closed path one can take on a lattice and is defined as [29]

$$P_{\mu\nu}(n) = U_\mu(n)U_\nu(n + \hat{\mu})U_\mu^\dagger(n + \hat{\nu})U_\nu^\dagger(n). \quad (3.19)$$

Due to the transformation properties of the link variables in eq. (3.4), the trace of $P_{\mu\nu}(n)$ is $SU(3)_c$ invariant. The first gauge action on the lattice, proposed by Wilson [119], is a sum over all plaquettes, counting each one in a single direction,

$$S_{\text{Wilson}}[U] = \frac{\beta}{3} \sum_{n \in \Lambda} \sum_{\mu < \nu} \text{Re Tr} [\mathbf{1} - P_{\mu\nu}(n)], \quad (3.20)$$

where $\beta = 6/g_s^2$ is the inverse squared coupling for $SU(3)_c$. Equation (3.20) is often referred to as the Wilson gauge action. Using the exponential representation given in eq. (3.6) for

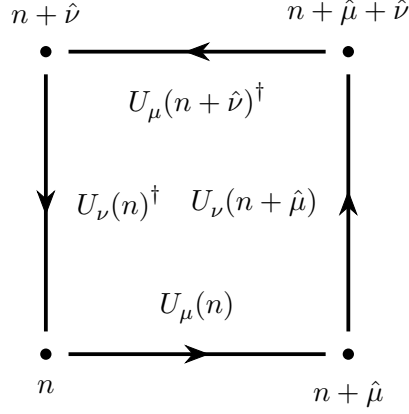


Figure 3.3: Plaquette $P_{\mu\nu}(n)$ defined in eq. (3.19) [29].

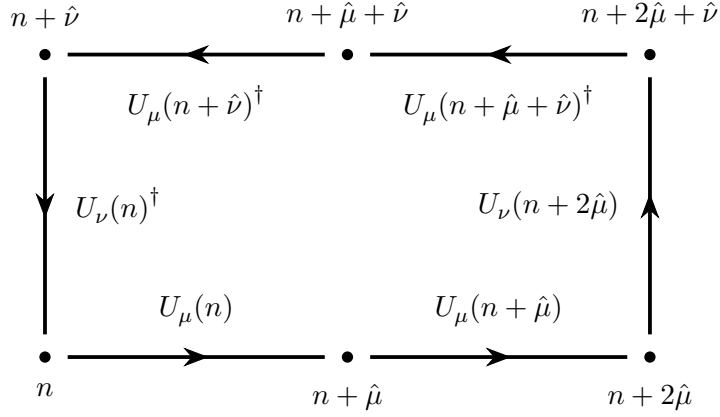


Figure 3.4: Rectangle $R_{\mu\nu}$ defined in eq. (3.23) [120].

the link variables and the Baker-Campbell-Hausdorff formula, it is possible to relate the plaquette with the continuum field strength tensor developing the former in a Taylor series for small lattice spacing [29],

$$P_{\mu\nu}(n) = \exp \left(i a^2 F_{\mu\nu} + \mathcal{O}(a^3) \right). \quad (3.21)$$

This allows one to recover the continuum gauge action with $\mathcal{O}(a^2)$ lattice artefacts [120, 82, 121, 73],

$$S_{\text{Wilson}} = \frac{1}{2g_s^2} \int d^4x \left(\text{Tr} F_{\mu\nu} F_{\mu\nu} + \frac{a^2}{12} \text{Tr} \left[F_{\mu\nu} \left(D_\mu^2 + D_\nu^2 \right) F_{\mu\nu} \right] \right) + \mathcal{O}(a^4), \quad (3.22)$$

where D_μ , D_ν are the covariant derivative and should not be confused with the Dirac operator. Since the plaquette is invariant under the transformation $U_\mu \rightarrow U_\mu^\dagger$ while $F_{\mu\nu}$ is odd, odd powers are absent of the lattice spacing in eq. (3.22) [120]. On top of this, one

may remove the $\mathcal{O}(a^2)$ term with the rectangle of link variables depicted in fig. 3.4 and defined as

$$R_{\mu\nu} = U_\mu(n)U_\mu(n + \hat{\mu})U_\nu(n + 2\hat{\mu})U_\mu(n + \hat{\mu} + \hat{\nu})^\dagger U_\mu(n + \hat{\nu})^\dagger U_\nu(n)^\dagger. \quad (3.23)$$

In particular, if one considers the plaquette and rectangle of eqs. (3.19) and (3.23) in the form

$$\tilde{P}_{\mu\nu} = \frac{1}{3} \text{Re Tr} (\mathbf{1} - P_{\mu\nu}), \quad \tilde{R}_{\mu\nu} = \frac{1}{3} \text{Re Tr} (\mathbf{1} - R_{\mu\nu}), \quad (3.24)$$

one can expand both expressions for small lattice spacing and find a combination of the two terms given in eq. (3.22) [120]. Then, an appropriate linear combination of $\tilde{P}_{\mu\nu}$ and $\tilde{R}_{\mu\nu}$ cancels the $\mathcal{O}(a^2)$ term. In this way, we obtain the improved gauge action [82]

$$S_G = \beta \sum_{n, \mu > \nu} \left(\frac{5}{3} \tilde{P}_{\mu\nu} - \frac{1}{12} (\tilde{R}_{\mu\nu} + \tilde{R}_{\nu\mu}) \right). \quad (3.25)$$

Equation (3.25) approaches the continuum limit with $\mathcal{O}(a^4)$ corrections [82]. S_G is referred to as the tree-level improved Lüscher-Weisz gauge action, because the improvement coefficients $c_0 = 5/3$ and $c_1 = -1/12$ are computed using only tree-level perturbation theory [82].

3.3 Feynman integration

After presenting the discretisation of the Euclidean action, we consider the changes that we need to apply to the path integral formulation in the continuum given in section 2.3. In particular, the expectation value of an operator $O[\psi, \bar{\psi}, U]$ on the lattice is defined as [29]

$$\langle O \rangle = \frac{1}{Z} \int \mathcal{D}[U] \mathcal{D}[\psi, \bar{\psi}] \exp(-S_F[\psi, \bar{\psi}, U] - S_G[U]) O[\psi, \bar{\psi}, U], \quad (3.26)$$

with the partition function

$$Z = \int \mathcal{D}[U] \mathcal{D}[\psi, \bar{\psi}] \exp(-S_F[\psi, \bar{\psi}, U] - S_G[U]). \quad (3.27)$$

In section 3.3.1, we study the measure of the integral, $\mathcal{D}[U]\mathcal{D}[\psi, \bar{\psi}]$; in section 3.3.2, we start working with the u , d and s quark flavours in the fermion action, which we integrate, and introduce the concept of importance sampling to integrate over the gauge fields.

3.3.1 Integration measure

So far, making $SU(3)_c$ -invariant the actions $S_F[\psi, \bar{\psi}, U]$ and $S_G[U]$ has allowed us to introduce interactions for fermions and gluons. Now, the expectation value in eq. (3.26) must also be $SU(3)_c$ invariant. This forces $\mathcal{D}[U]$ and $\mathcal{D}[\psi, \bar{\psi}]$ to be invariant. First, let us concentrate on the product measure [29]

$$\mathcal{D}[U] = \prod_{n \in \Lambda} \prod_{\mu=1}^4 dU_\mu(n), \quad (3.28)$$

The differential $dU_\mu(n)$ integrates the link variables $U_\mu(n)$ over the entire $SU(3)_c$ group manifold and it is known as a Haar measure, defined by the two properties [29]

$$dU_\mu(n) = d(U_\mu(n)V) = d(VU_\mu(n)) , \quad (3.29)$$

$$\int dU_\mu(n) = 1. \quad (3.30)$$

Equation (3.29) indicates that $dU_\mu(n)$ must be invariant under left or right multiplication by any other group element $V \in SU(3)_c$. This ensures $dU_\mu(n)$ is invariant under the gauge transformations given in eq. (3.4). Equation (3.30) fixes the normalisation. Explicit constructions of Haar measures can be found in [29, 72]. Regarding the fermion integration measure [29]

$$\mathcal{D}[\psi, \bar{\psi}] = \prod_n \psi(n) \bar{\psi}(n), \quad (3.31)$$

we simply state that it follows the rules of integration with Grassmann variables and refer the reader to [29] for a compendium of such properties.

3.3.2 Importance sampling

After defining every piece of the Feynman path integral, we study how to perform the actual integration. We start by considering a fermion action for three flavours, the u , d and s quarks. The fermion action for every quark is identical, and their only difference at this stage is their mass. Applying the Matthews-Salam equation for every flavour [29], it is possible to integrate the fermion action. This changes the partition function to

$$Z = - \int \mathcal{D}[U] \exp(-S_G[U]) \det D_u[U] \det D_d[U] \det D_s[U]. \quad (3.32)$$

Therefore, we replace the exponent of the Euclidean action by the so-called fermion determinants. Then, one may apply Wick's theorem [29] to integrate the fermionic Grassmann variables in an expectation value,

$$\begin{aligned} \langle O \rangle &= \left\langle O[\bar{\psi}, \psi, U] \right\rangle_G = \\ &= \frac{1}{Z} \int \mathcal{D}[U] \exp(-S_G[U]) \det D_u[U] \det D_d[U] \det D_s[U] O[\bar{\psi}, \psi, U]. \end{aligned} \quad (3.33)$$

In eq. (3.33), $O[\bar{\psi}, \psi, U]$ is a functional of the fermion propagator $D^{-1}[U]$. Since we use $SU(2)$ isospin symmetry for this project, we drop the u and d quarks and use instead a generic light flavour ℓ , in such a way that $\det D_u[U] \det D_d[U] = \det D_\ell^2[U]$. Therefore, whenever the fermions appear bi-linearly on the action, we can integrate them analytically, and only the integral over the link variables remains. The latter can only be computed numerically, employing importance sampling [29]. It consists on approximating the expectation value in

eq. (3.33) by a sum over a set of N_{cnfg} configurations U_τ sampled according to the weight factor $W[U]$,

$$\begin{aligned}\langle O \rangle &= \frac{1}{N_{\text{cnfg}}} \sum_{\tau=1}^{N_{\text{cnfg}}} O[D^{-1}[U_\tau], U_\tau] + \mathcal{O}\left(\frac{1}{\sqrt{N_{\text{cnfg}}}}\right), \\ W[U] &= \frac{1}{Z} \mathcal{D}[U] \det[D_\ell^2] \det[D_s] \exp(-S_G[U]).\end{aligned}\tag{3.34}$$

The configurations U_τ are obtained using a Markov process [29], which starts from an arbitrary configuration U_0 , and obtains all configurations one after another, forming a Markov chain,

$$U_0 \rightarrow U_1 \rightarrow U_2 \rightarrow \dots,\tag{3.35}$$

where the subscript, usually called the computer time τ , indicates the position in the chain of a given configuration. The first configurations will not be distributed according to $W[U]$, but if one updates the fields sufficient times the equilibrium distribution $W[U]$ will be eventually reached [72] —this process is usually called thermalization. Once equilibrium is achieved, the Markov process fulfils the balance equation

$$\sum_U T(U'|U) W(U) = \sum_{U'} T(U|U') W(U') = W(U'),\tag{3.36}$$

where $T(U'|U)$ is the probability to transition from one configuration U to another U' . Equation (3.36) indicates $W[U]$ is a fixed point of the Markov process and, therefore, once the equilibrium probability is achieved, all subsequent configurations will be chosen according to it. To enforce eq. (3.36), one usually employs the so-called detailed balance equation,

$$T(U'|U) W[U] = T(U|U') W[U'].\tag{3.37}$$

The speed at which the system approaches equilibrium depends on many different aspects: the algorithm used, the observable studied, the gauge coupling β , the size of the lattice and the action. For instance, large lattices with finer spacings require more steps to thermalize [29]. See [122] for an example of thermalizing an ensemble at the physical pion masses.

Using importance sampling to compute eq. (3.33) requires the probability density $W[U]$ to be real and non-negative. Indeed, employing γ_5 -hermiticity, it is possible to see that every determinant is real,

$$\det[D^\dagger] = \det[\gamma_5 D \gamma_5] = \det[D],\tag{3.38}$$

and having mass-degenerate u and d quarks renders their determinant non-negative,

$$0 \leq \det[D_\ell] \det[D_\ell] = \det[D_\ell] \det[D_\ell^\dagger] = \det[D_\ell D_\ell^\dagger],\tag{3.39}$$

where we used eq. (3.38), and D_ℓ is the Dirac operator for either the u or d quarks. However, in our simulations, D_s appears isolated and with a mass different from that of the light quarks. In section 3.4, we explain that while D_ℓ is positive, D_s has a small amount of

negative eigenvalues. Also, we gather techniques to compute the fermion determinants. Note that our lattices have roughly $|\Lambda| \sim \mathcal{O}(100^4)$ lattice sites, and then the Dirac operator is a matrix with dimensions $N = 12|\Lambda|$. It is clear that a brute force computation of the determinant would be unfeasible.

3.4 Hybrid Monte Carlo

To generate configurations of link variables with dynamical quarks, we apply the hybrid Monte Carlo (HMC) algorithm [123]. The basic idea of this algorithm is to generate random fields, make them evolve in Markov time τ via molecular dynamics equations of motion, and introduce a Metropolis step to accept or reject the proposed new configuration. First, it was noted in [124] that we can substitute the fermion determinants in eq. (3.33) by an integral over pseudo-fermion fields ϕ , which are bosons with the same colour, Dirac, flavour and lattice indices as normal fermions. Then, the light quark determinant changes to

$$\det \left(D[U] D^\dagger[U] \right) = \pi^{-N} \int \mathcal{D}[\phi^\dagger] \mathcal{D}[\phi] e^{-\phi^\dagger (D[U] D^\dagger[U])^{-1} \phi}. \quad (3.40)$$

Note that the left-hand side (LHS) must be positive to ensure the convergence of the Gaussian integral. The objective of eq. (3.40) is to avoid a direct computation of the determinant, which is unfeasible in most simulations [29]. Equation (3.40) modifies the Boltzmann factor of eq. (3.33), where we now have $S = S_G[U] + \phi^\dagger (D[U] D^\dagger[U])^{-1} \phi$ instead of just $S_G[U]$. In S , the link action is local and cheaper to compute, while the factor $(D[U] D^\dagger[U])^{-1}$ makes the pseudo-fermion term more expensive to compute and highly non-local, relating all lattice sites with one another [29]. Next, we introduce an auxiliary field $\pi_\mu(n, \tau) \in \mathfrak{su}(3)$ distributed according to a Gaussian distribution [29],

$$\pi_\mu(n, \tau) = \pi_\mu^i(n, \tau) T^i, \quad (3.41)$$

where T^i are the group generators. The algebra elements π_μ^i are the conjugate momenta of the gauge fields $A_\mu^i(n, \tau)$ that give the link variables

$$U_\mu(n, \tau) = \exp \left(i A_\mu^i(n, \tau) T^i \right). \quad (3.42)$$

At this stage, the partition function to evaluate an observable is modified to

$$Z = \int \mathcal{D}[U] \mathcal{D}[\pi^\dagger, \pi] \mathcal{D}[\phi^\dagger, \phi] \exp \left(-S[U] - \phi^\dagger \left(D[U] D^\dagger[U] \right)^{-1} \phi - \sum_{n, \mu} \text{tr} \pi_\mu^2 \right), \quad (3.43)$$

Introducing the auxiliary field π_μ allows to study eq. (3.43) in the microcanonical ensemble [29]. This means that the Hamiltonian is a constant of the system,

$$H[U, \pi, \phi] = S_G[U] + \phi^\dagger \left(D[U] D^\dagger[U] \right)^{-1} \phi + \sum_{n, \mu} \text{tr} \pi_\mu^2. \quad (3.44)$$

The equations of motion in Markov time for the conjugate variables π_μ^i and A_μ^i are [29]

$$\frac{d\pi_\mu^i(n, \tau)}{d\tau} = -\frac{\partial S}{\partial A_{\mu,i}(n, \tau)}, \quad \frac{dA_\mu^i(n, \tau)}{d\tau} = \pi_\mu^i(n, \tau). \quad (3.45)$$

Equation (3.45) is also known as the molecular dynamics equation because it determines the time evolution of a classical system of particles [29]. Together, eqs. (3.41), (3.42) and (3.45) allow us to compute the dynamics of $U_\mu(n, \tau)$ and $\pi_\mu(n, \tau)$ [29],

$$\frac{dU_\mu(n, \tau)}{d\tau} = i\pi_\mu(n, \tau) U_\mu(n, \tau), \quad \frac{d\pi_\mu(n, \tau)}{d\tau} = -\frac{\partial S}{\partial A_\mu^i(n, \tau)} T_i \equiv F_\mu(n, \tau), \quad (3.46)$$

where $F_\mu(n, \tau)$ is the force term. The HMC algorithm consists of several steps [29]:

1. Compute the pseudo-fermion fields via $\phi = D[U]\chi$, with χ an auxiliary vector sampled from a Gaussian distribution with probability $\propto \exp(-\chi^\dagger \chi)$.
2. Compute a conjugate field $\pi_\mu(n, \tau)$ for every link variable $U_\mu(n, \tau)$ sampling from the probability $\exp(-\sum_{n,\mu} \text{tr} \pi_\mu^2(n, \tau))$.
3. Evolve numerically U_μ and π_μ in Markov time to obtain a new candidate configuration U'_μ and π'_μ using, for example, the leapfrog algorithm [29] or the Omelyan, Mryglod, and Folk (OMF) integrator [125]. The latter was used in the simulation of the CLS ensembles [126]. In order to fulfil the detailed balance condition given in eq. (3.37), any integrator that we use should satisfy the following properties [29]:

- The area of the integration measure $\mathcal{D}[U] \mathcal{D}[\pi^\dagger, \pi]$ is preserved.
- The trajectory is reversible, which means that from U_μ and π_μ , we obtain U'_μ and π'_μ , and from U'_μ and $-\pi'_\mu$, we get U_μ and $-\pi_\mu$.

For the actual Markov time evolution, the leapfrog algorithm alternates updates of the link variables and conjugate momenta in the following steps [29]:

- First, we evolve the momenta by $\Delta\tau/2$,

$$\pi_\mu(n, \tau + \Delta\tau/2) = \pi_\mu(n, \tau) - \frac{\Delta\tau}{2} F_\mu[U_\mu(n, \tau), \phi]. \quad (3.47)$$

- Then, we perform $k = 1, \dots, m-1$ intermediate steps,

$$U_\mu(n, \tau + k\Delta\tau) = \exp(i\Delta\tau\pi_\mu(n, \tau + (k-1/2)\Delta\tau)) \times U_\mu(n, \tau + (k-1)\Delta\tau), \quad (3.48)$$

$$\pi_\mu(n, \tau + (k+1/2)\Delta\tau) = \pi_\mu(n, \tau + (k-1/2)\Delta\tau) - \Delta\tau F_\mu[U_\mu(n, \tau + k\Delta\tau), \phi]. \quad (3.49)$$

- Finally, a last step by $\Delta\tau$ for the link variable and $\Delta\tau/2$ for the momenta,

$$U_\mu(n, \tau + m\Delta\tau) = \exp(i\Delta\tau\pi_\mu(n, \tau + (m - 1/2)\Delta\tau)) \times U_\mu(n, \tau + (m - 1)\Delta\tau), \quad (3.50)$$

$$\pi_\mu(n, \tau + m\Delta\tau) = \pi_\mu(n, \tau + (m - 1/2)\Delta\tau) - \frac{\Delta\tau}{2} F_\mu[U_\mu(n, \tau + m\Delta\tau), \phi]. \quad (3.51)$$

Each iteration of the molecular dynamics equation is called a molecular dynamics unit (MDU), and a sequence of m MDU with $m\Delta\tau \approx 1$ is called a trajectory [29].

4. The fields $U'_\mu(n, \tau + m\Delta\tau)$, $\pi'_\mu(n, \tau + m\Delta\tau)$ are proposed for a new configuration. The proposal is accepted or rejected according to a Metropolis step, eliminating all discretisation effects. The changes are accepted if a random number $r \in [0, 1)$ is smaller than the acceptance probability T_A , [29],

$$r < T_A(U'_\mu, \pi'_\mu | U_\mu, \pi_\mu) = \min \left(1, \frac{\exp(-H[U', \pi', \phi])}{\exp(-H[U, \pi, \phi])} \right) \quad (3.52)$$

It is relevant to note that, if the molecular dynamics could be done exactly, all configurations would be accepted, since the hamiltonian is a constant of motion [29]. The numerical implementation introduces errors of $\mathcal{O}(\Delta\tau^2)$, which are removed by the Metropolis step [29]. On the one hand, $\Delta\tau$ needs to be large to reduce the number of evaluations of the pseudo-fermion action and, therefore, reduce computational costs. On the other hand, choosing $\Delta\tau$ too large will reduce the acceptance rate of new configurations, increasing the computational cost. Therefore, it is necessary to find a balance, and it is common to have trajectories of $\mathcal{O}(100)$ steps [29]. Since the momenta is generated with a random distribution, it is possible to reach every possible configuration and, therefore, we say HMC is ergodic [29].

3.4.1 Dynamical up and down quarks

The Wilson-Dirac operator may have eigenvalues below the quark mass. To avoid zero and small eigenvalues, CLS simulations include a version of twisted-mass re-weighting presented in [127] together with even-odd preconditioning [128] and frequency splitting [129]. Here, we briefly explain these three techniques. In this section, it is understood that all operators refer to the light-quark operators unless otherwise stated.

The first step is to rewrite the light-quark determinant using even-odd preconditioning [128]. Instead of working with the Wilson-Dirac operator D itself, we take the hermitian quantity $Q = \gamma_5 D$. This does not make any difference, since $\det D^2 = \det Q^2$, with $D^2 = D^\dagger D$. We start organizing the Dirac operator matrix Q in even and odd sites [126],

$$Q = \begin{pmatrix} Q_{ee} & Q_{eo} \\ Q_{oe} & Q_{oo} \end{pmatrix}, \quad (3.53)$$

where the diagonal blocks connect only even or odd sites —even (odd) sites have even (odd) $\sum_\alpha x_\alpha$. Then, it is possible [73] to apply a Schur decomposition to eq. (3.53), dividing the original operator into upper, lower and diagonal matrices,

$$Q = U\hat{Q}L = \begin{pmatrix} 1 & Q_{eo}Q_{oo}^{-1} \\ 0 & 1 \end{pmatrix} \begin{pmatrix} Q_{ee} - Q_{eo}Q_{oo}^{-1}Q_{oe} & 0 \\ 0 & Q_{oo} \end{pmatrix} \begin{pmatrix} 1 & 0 \\ Q_{oo}^{-1}Q_{oe} & 1 \end{pmatrix}. \quad (3.54)$$

This decomposition greatly simplifies the inversion of the Dirac operator, as we now only have to invert triangular and block diagonal matrices. Next, we can segregate even and odd sites in the original system $Qg = U\hat{Q}Lg = b$. Defining $Lg \equiv x$ and $U^{-1}h \equiv b$, we have

$$\begin{pmatrix} \hat{Q}_{ee} & 0 \\ 0 & Q_{oo} \end{pmatrix} \begin{pmatrix} x_e \\ x_o \end{pmatrix} = \begin{pmatrix} b_e \\ b_o \end{pmatrix}, \quad (3.55)$$

where $\hat{Q}_{ee} = Q_{ee} - Q_{eo}Q_{oo}^{-1}Q_{oe}$ acts only on even sites. Applying even-odd preconditioning to $\det D^2$ yields [126]

$$\det D^2 = \det Q^2 = \det Q_{oo}^2 \det \hat{Q}_{ee}^2. \quad (3.56)$$

The next step is to regularise the Schur complement \hat{Q}_{ee} of the light-quark determinant including a twisted-mass parameter $\mu_0 > 0$ to avoid zero eigenvalues [126]. Equation (3.56) is modified to

$$\det D^2 = \underbrace{\det \left[\hat{Q}_{ee}^2 \frac{\hat{Q}_{ee}^2 + 2\mu_0^2}{(\hat{Q}_{ee}^2 + \mu_0^2)^2} \right]}_{w_\ell} \times \det Q_{oo}^2 \det \frac{\hat{Q}_{ee}^2 + \mu_0^2}{\hat{Q}_{ee}^2 + 2\mu_0^2} \det [\hat{Q}_{ee}^2 + \mu_0^2], \quad (3.57)$$

where w_ℓ is a re-weighting factor that must be included in the measurements, together with the observable O we want to compute. In practice, one needs to probe different values for μ_0 to find the optimal point. On the one hand, it should be large enough to make all configuration space accessible and, on the other hand, it should be small enough to damp the re-weighting factor fluctuations, so that statistical uncertainties remain under control [130]. The light quark mass gives an order of magnitude [126].

The last technique that we have to consider is frequency splitting, employing Hasenbusch's mass factorization [129] with a twisted mass [131]. We split the last determinant on eq. (3.57) in $p+1$ terms, each one with a particular twisted-mass parameter $\mu_0 < \mu_1 < \dots < \mu_p$ [126, 132],

$$\det [\hat{Q}_{ee}^2 + \mu_0^2] = \det [\hat{Q}_{ee}^2 + \mu_p^2] \prod_{i=1}^p \det \frac{\hat{Q}_{ee}^2 + \mu_{i-1}^2}{\hat{Q}_{ee}^2 + \mu_i^2}. \quad (3.58)$$

Reference [132] lists the values of μ_i for several ensembles and how they were chosen. It is observed that the i -th factor in eq. (3.58) is dominated by the spectrum in an interval around μ_i delimited by the other twisted-masses [126], hence the name of frequency splitting. Finally, we employ eq. (3.40) to substitute every term —except the reweighting factor w_ℓ —

in eqs. (3.57) and (3.58) with an integral over pseudo-fermion fields. This introduces $p + 2$ pseudo-fermion fields, one per determinant, and the pseudo-fermion action reads [126, 132]

$$S_\ell[U, \phi_0, \dots, \phi_{p+1}] = \phi_0^\dagger \frac{\hat{Q}_{ee}^2 + 2\mu_0^2}{\hat{Q}_{ee}^2 + \mu_0^2} \phi_0 + \sum_{i=1}^p \phi_i^\dagger \frac{\hat{Q}_{ee}^2 + \mu_i^2}{\hat{Q}_{ee}^2 + \mu_{i-1}^2} \phi_i + \phi_{p+1}^\dagger \frac{1}{\hat{Q}_{ee}^2 + \mu_p^2} \phi_{p+1} - 2 \log \det Q_{oo}. \quad (3.59)$$

Therefore, instead of evaluating just one pseudo-fermion field and one conjugate momenta for the HMC, we consider $p + 2$ pseudo-fermion fields with their respective momenta and the re-weighting factor w_ℓ .

3.4.2 Dynamical strange quark

After discussing the light sector of the Feynman integral, we explain how to include the dynamical strange quark. Unless otherwise stated, all operators in this section refer to the strange-quark operators. We follow the rational hybrid Monte Carlo (RHMC) method [133, 134], which substitutes the strange determinant with an integral over pseudofermions, and approximates the Dirac propagator with a rational functional. Unlike the u - and d -quarks, which are considered to be mass-degenerate all the way down to the physical mass, the heavier-quark masses differ substantially and they cannot be grouped by pairs, which means their determinant will not have the form $\det D^\dagger D$ that guarantees semi-positivity. In general, D would be positive if both chiral symmetry and γ_5 -hermiticity were fulfilled, but the former is explicitly broken for Wilson fermions. Then, not all the configuration space of D has the same sign necessarily [135]. Potentially, this amounts to a negative probability density in the importance sampling for some configurations. In the simulation of the CLS ensembles, it has been assumed that these areas with negative determinant are negligible [135]. Following [135], we consider the following holds,

$$\det D = \det \sqrt{D^\dagger D} = \det \sqrt{Q^\dagger Q} = \det |Q|, \quad (3.60)$$

where $Q = \gamma_5 D$ is the hermitian Dirac operator. As it was done for the light sector, we apply even-odd preconditioning [132], obtaining

$$\det D = \det Q_{oo} \det \sqrt{\hat{Q}_{ee}^2}. \quad (3.61)$$

The Schur conjugate is now written in terms of a rational approximation to achieve frequency splitting [126, 132],

$$\det D = \underbrace{\det [\hat{Q}_{ee} R]}_{w_s} \det Q_{oo} \det R^{-1}, \quad R = C \prod_{i=1}^m \frac{\hat{Q}_{ee}^2 + \omega_i^2}{\hat{Q}_{ee}^2 + \nu_i^2}, \quad (3.62)$$

where R denotes Zolotarev's optimal rational approximation with parameters C , ω_i and ν_i [136]. As for the light sector, we have an extra reweighting factor w_s that needs to be

included in the simulations together with the observable O and the light reweighting factor w_ℓ . Finally, we use eq. (3.40) to represent the determinants as integrals of pseudofermions. The simplest option is to introduce m fields for the m different factors, which means to include in the action for the HMC the terms [126, 132]

$$S_s[U, \phi_0, \dots, \phi_m] = \sum_{i=0}^m \phi_i^\dagger \frac{\hat{Q}_{ee}^2 + \omega_i^2}{\hat{Q}_{ee}^2 + \nu_i^2} \phi_i - \log \det \hat{Q}_{oo}. \quad (3.63)$$

Therefore, the HMC algorithm needs to probe $p+2$ light pseudo-fermions, m strange pseudo-fermions, and the corresponding momenta. For further details on the implementation of the RHMC algorithm for the CLS effort, see [126, 132].

For Wilson quarks, the assumption of positivity of $\det D$ is usually justified, up to very unlikely configurations, thanks to the heavy mass of the strange quark, which would assure the spectra is non-negative [135]. However, there is no proof $\det D$ is positive and very rough gauge fields will lead to a negative value. In fact, it was recently reported in [130] that the assumption of positivity is not true. Due to γ_5 -hermiticity, the Dirac operator is still real, $\det D = \det \gamma_5 D \gamma_5 = \det D^\dagger$, which means its eigenvalues are either real or appear in complex conjugate pairs [130]. Now, it is clear eq. (3.60) is no longer an equality, rather a replacement of the original action $\det D$ by a new one $\det |Q|$. This can be solved introducing a new re-weighting,

$$w_- = \frac{\det D}{\det |D|} = (-1)^{n_{\text{neg}}}, \quad (3.64)$$

with n_{neg} the number of real, negative eigenvalues. The problem for strange quarks was identified for the light quarks and solved using twisted-mass reweighting [127]. An extensive study of this problem has been conducted in [130], determining that around 2% of configurations have negative eigenvalues at $\beta = 3.4$ and $\beta = 3.46$, 0.3% at $\beta = 3.55$ and only 0.05% at $\beta = 3.7$. This indicates the problem vanishes in the continuum, although the effect is relevant for our coarsest lattice ensembles. See [130] for more details about the detection of negative eigenvalues.

3.4.3 Re-weighting

We have seen in sections 3.4.1 and 3.4.2 that the action used for HMC differs from the original action. For the light sector, this is due to the use of twisted mass reweighting [132] and, for the strange sector, the inclusion of Zolotarev's rational approximation [132] together with the realization that the negative eigenvalues of the Dirac-Wilson operator are relevant [130]. Then, there are two different expectation values, each one with a different partition function,

$$Z = - \int \mathcal{D}[U] \det[D_\ell^2[U]] \det[D_s[U]] e^{-S_G}, \quad (3.65)$$

$$Z' = - \int \mathcal{D}[U] \mathcal{D}[\phi^\dagger, \phi, \tilde{\phi}^\dagger, \tilde{\phi}] \mathcal{D}[\pi^\dagger, \pi, \tilde{\pi}^\dagger, \tilde{\pi}] e^{-S_G - S_\ell - S_s - \sum \text{tr} \pi^2 - \sum \text{tr} \tilde{\pi}^2}, \quad (3.66)$$

where $S_\ell[U, \phi_0, \dots, \phi_{n+1}]$ is defined in eq. (3.59), $S_s[U, \tilde{\phi}_0, \dots, \tilde{\phi}_m]$ in eq. (3.63), and $\mathcal{D}[\phi^\dagger, \phi, \tilde{\phi}^\dagger, \tilde{\phi}] = \mathcal{D}[\phi^\dagger] \mathcal{D}[\phi] \mathcal{D}[\tilde{\phi}^\dagger] \mathcal{D}[\tilde{\phi}]$. An expectation value in the target theory $\langle O \rangle$ can be written in terms of the action used for the molecular dynamics simply including the three re-weighting factors [132, 130],

$$\langle O \rangle = \frac{\langle w_\ell w_s w_- O \rangle'}{\langle w_\ell w_s w_- \rangle'}, \quad (3.67)$$

with w_ℓ defined in eq. (3.57), w_s in eq. (3.62), and w_- eq. (3.64).

3.4.4 Boundary conditions

One vital feature of the CLS simulations is the use of open boundary conditions (OBC) in the temporal direction for most ensembles [132]. This allows to simulate at finer lattice spacings while alleviating the increase in the autocorrelation length (see chapter 8) of many observables. Perhaps, the most well known case is the topological charge [137, 138, 139], although subsequent advances, notably the introduction of the gradient flow [140, 141], have shown that other quantities suffer the same freezing or critical slow down, as it is commonly called. Two undesired consequences of OBC are, first, that translation invariance in time is lost and, second, that boundary states with the vacuum quantum numbers appear [142]. These states will fall off exponentially with the distance to the boundary and their respective energy. In particular, the lightest state will decay as $\exp(-2M_\pi n_4)$. For comparison, the finite volume effects are of order $\exp(-M_\pi L)$ [143] and, therefore, one needs large ensembles in time and space. In the simulations, the observables computed adopt their expectation value up to corrections due to this effects.

When the lattice spacing is still relatively coarse, it is still possible to use periodic boundary conditions (PBC) for bosons in all dimensions (and anti-periodic boundary conditions (APBC) in time for fermions) without having a critical slow down of the lattice observables. Since they are also more convenient, PBC are used in some ensembles produced recently. In this case, at a time-slice n_4 , each state contributes to a correlator $G(n_4)$ with two infinite towers of exponentials; one corresponds to the forward propagator, evaluated at times $n_4 + wN_T$, with $w = 0, 1, 2, 3, \dots$, the winding number of the propagator around the torus; the other corresponds to the backward propagator, evaluated at times $n_4 - wN_T$. Then, instead of the standard spectral representation with a tower of exponentials, one has an extra series, which can be summed exactly [29],

$$\begin{aligned} G(n_4; \text{forward}) &= \sum_{s=1}^{\infty} A_s \sum_{w=0}^{\infty} e^{-E_s(n_4 + wN_T)} = \\ &= \sum_{s=1}^{\infty} A_s e^{-E_s n_4} \sum_{w=0}^{\infty} \left(e^{-E_s N_T} \right)^w = \sum_{s=1}^{\infty} A_s \frac{e^{-E_s n_4}}{1 - e^{-E_s N_T}}. \end{aligned} \quad (3.68)$$

In the last step of eq. (3.68), we express the infinite series of the winding number using the Taylor expansion of $1/(1-x)$ for $x < 1$. Then, if we suppose the correlator $G(n_4)$ has a

definite time-reversal parity number, that is $G(n_4) = \pm G(-n_4)$, which will be the case for the mesonic correlators we are interested in, we have for the backward propagator [29],

$$\begin{aligned} G(n_4; \text{backward}) &= (-1)^{\mathcal{T}} \sum_{s=1}^{\infty} A_s \sum_{w=0}^{\infty} e^{E_s(n_4-(w+1)N_T+1)} = \\ &= (-1)^{\mathcal{T}} \sum_{s=1}^{\infty} A_s e^{E_s(n_4-N_T+1)} \sum_{w=0}^{\infty} \left(e^{-E_s N_T} \right)^w = (-1)^{\mathcal{T}} \sum_{s=1}^{\infty} A_s \frac{e^{E_s(n_4-N_T+1)}}{1 - e^{-E_s N_T}}, \end{aligned} \quad (3.69)$$

where $\mathcal{T} = 0, 1$ for an even/odd correlator under time reversal, N_T is the number of time-slices and the boundary conditions are imposed on the time-slices $n_4 = 0$ and $n_4 = N_T - 1$. However, $e^{-E_s N_T}$ is small, and the most relevant contributions are the forward and backward propagators with $w = 0$. Therefore, neglecting all non-zero winding numbers, we may express the correlator as

$$\begin{aligned} G(n_4) &= G(n_4; \text{forward}) + G(n_4; \text{backward}) = \sum_{s=1}^{\infty} A_s \left(e^{-E_s n_4} + (-1)^{\mathcal{T}} e^{E_s(n_4-N_T+1)} \right) = \\ &= \sum_{s=1}^{\infty} 2A_s e^{-E_s(N_T-1)/2} \left(e^{-E_s(n_4-(N_T-1)/2)} + (-1)^{\mathcal{T}} e^{E_s(n_4-(N_T-1)/2)} \right) / 2. \end{aligned} \quad (3.70)$$

The parenthesis in eq. (3.70) is either a cosh or sinh, depending on the time reflection symmetry of the correlator under consideration.

3.5 Scale setting

All quantities but pure numbers computed on the lattice are obtained in units of powers of the lattice spacing a . Therefore, we need the lattice spacing in physical units to predict a physical result. Also, depending on the details of the simulations, we have to define the physical point, which is the set of parameters where it is possible to compare with experiment, and set a strategy to reach it. For instance, the CLS ensembles only have u -, d - and s -quark content in the sea, and they lack isospin-breaking (IB) effects. Therefore, the pion and kaon masses that define the physical point should be modified accordingly. For this project, we take the lattice spacing from [142], where the former is obtained from different scales, the reference value t_0 of the flow time [141, 144, 145] and a linear combination of the decay constants of the pion f_π and kaon f_K mesons. The method followed exemplifies how to set the scale in lattice simulations, but the choice of scale is arbitrary and other quantities may be used instead, some of which are known experimentally, like the Ω^- baryon mass [146], the Υ - Υ' mass splitting [147], and some others which are not, like the scale r_0 [148] or t_0 itself. However, the choice affects the final precision of the lattice spacing. The aim in the following lines is to summarize the definition of t_0 , the strategy followed in [142] and the main results for the scale setting that we employ in our analysis.

First of all, the reference value t_0 of the flow time t is a quantity with dimensions energy^{-2} , defined implicitly through the relation [141, 144, 145]

$$t^2 \langle E(n_4, t) \rangle \Big|_{t=t_0} = 0.3, \quad E(n_4, t) = \frac{1}{4} G_{\mu\nu}^a G_{\mu\nu}^a, \quad (3.71)$$

where $G_{\mu\nu}^a$ is an expression for the gauge-field tensor at flow time t [141], and a indicates the colour component. The value of t_0 is not a physical quantity that can be measured by experiments, but can only be computed on lattice simulations, and its value depends on the number of flavours on the sea. For example, the $N_f = 2$ CLS determination [149] yields $\sqrt{8t_0} = 0.434(2)$ fm, and the $N_f = 2 + 1$ result [142] is $\sqrt{8t_0} = 0.415(4)(2)$ fm. Other determinations for $N_f = 2 + 1$ include BMW's $\sqrt{8t_0} = 0.414(7)$ fm [150], QCDSF's $\sqrt{8t_0} = 0.427(7)$ fm [151] and RBC-UKQCD's $\sqrt{8t_0} = 0.407(2)$ fm [152]. There are also determinations with $N_f = 2 + 1 + 1$ flavours by the MILC collaboration, $\sqrt{8t_0} = 0.4005_{-11}^{+22}$ fm [153], and the HPQCD collaboration, $\sqrt{8t_0} = 0.4016(22)$ fm [154]. One can see a downward trend when adding heavier dynamical quarks.

Second, to obtain $\mathcal{O}(a)$ improvement all bare parameters need to be modified with a mass-dependent term [155]. In particular, the bare coupling should be

$$\tilde{g}_0^2 = g_0^2 \left(1 + \frac{b_g}{3} a \sum_{f=1}^3 (M_{0,f} - M_{cr}) \right), \quad (3.72)$$

with the critical quark mass M_{cr} . The modified coupling constant \tilde{g}_0^2 needs to be kept fixed as we vary the sea quark masses to keep the lattice spacing unchanged. This is equivalent to keeping fixed the sum of the bare quark masses

$$a \text{tr} M_0 = a \sum_{f=1}^3 M_{0,f} = \text{const.} \quad (3.73)$$

To accomplish eq. (3.73) and set the quark masses in the simulation, one can evaluate on each ensemble the dimensionless quantities [132]

$$\phi_2 = 8t_0 M_\pi^2 \quad \text{and} \quad \phi_4 = 8t_0 \left(M_K^2 + \frac{M_\pi^2}{2} \right), \quad (3.74)$$

because to leading order of chiral perturbation theory (ChPT) ϕ_2 and ϕ_4 are proportional to the quark masses with $\phi_2 \propto M_{0,u} + M_{0,d}$ and $\phi_4 \propto M_{0,u} + M_{0,d} + M_{0,s}$ [156, 157]. Then, one generates ensembles at different points (ϕ_2, ϕ_4) along a trajectory that fulfils eq. (3.73) and spans between the physical point and $M_u = M_d = M_s$. At each point (ϕ_2, ϕ_4) , several lattice spacings are computed, so that a continuum limit can be taken.

The physical meson masses where the data is extrapolated are [158, 34],

$$\begin{aligned} M_\pi^{\text{phy}} &= M_{\pi^0} = 134.9768(5) \text{ MeV}, \\ M_K^{\text{phy}} &= \frac{1}{2} \left(M_{K^+}^2 + M_{K^0}^2 - M_{\pi^+}^2 + M_{\pi^0}^2 \right) = 495.011(15) \text{ MeV}, \end{aligned} \quad (3.75)$$

β	t_0^{sym}/a^2	a [fm]
3.4	2.860 (11) (03)	0.08636 (98) (40)
3.46	3.659 (16) (03)	0.07634 (92) (31)
3.55	5.164 (18) (03)	0.06426 (74) (17)
3.7	8.595 (29) (02)	0.04981 (56) (10)

Table 3.1: Scale setting results employed for every coupling β , taken from [142]. The first error is statistical and the second systematic.

and they include neither quantum electrodynamics (QED) effects, nor strong isospin-breaking effects.

Finally, after these considerations, [142] proposes an iterative determination of the scale t_0 . As a first step, a putative value $\sqrt{8\tilde{t}_0}$ for the gradient flow is proposed, and the corresponding value of the physical point $\tilde{\phi}_2, \tilde{\phi}_4$ is defined. Second, t_0/a^2 is computed on every ensemble, together with a linear combination of the pseudo-scalar decay constants of the pion f_π and kaon f_K ,

$$\sqrt{8\tilde{t}_0}f_{\pi K} = \frac{2}{3}\sqrt{8\tilde{t}_0}\left(f_K + \frac{f_\pi}{2}\right). \quad (3.76)$$

This quantity was chosen because its next-to-leading order expansion in SU(3) ChPT [159] predicts $f_{\pi K}$ to be constant up to small corrections. If one extrapolates $\sqrt{8\tilde{t}_0}f_{\pi K}$ to the physical point, and since $f_{\pi K}$ is known from experiment, one can compute the corresponding value of t_0 at the physical point $(\sqrt{8\tilde{t}_0}f_{\pi K})^{\text{phy}}/f_{\pi K}^{\text{exp}}$, where $(\sqrt{8\tilde{t}_0}f_{\pi K})^{\text{phy}}$ is the result extrapolated to the physical point. Of course, the ratio must be equal to the initial guess $\sqrt{8\tilde{t}_0}$. To make this happen, the initial guess is varied until $(\sqrt{8\tilde{t}_0}f_{\pi K})/f_{\pi K}^{\text{exp}} = \sqrt{8\tilde{t}_0}$. The final result is [142]

$$\sqrt{8t_0^{\text{phy}}} = 0.415(4)(2) \text{ fm}, \quad (3.77)$$

The lattice spacing is obtained from the ensembles at the SU(3)-flavour-symmetric point, where the flow time reference value is labelled as $8t_0^{\text{sym}}$. Extrapolating $\sqrt{8t_0^{\text{sym}}}f_{\pi K}$ to the continuum and physical meson masses and taking the ratio $(\sqrt{8t_0^{\text{sym}}}f_{\pi K})^{\text{phy}}/f_{\pi K}^{\text{exp}}$ one gets $\sqrt{8t_0^{\text{sym}}} = 0.413(5)(2) \text{ fm}$. Finally, the lattice spacing is obtained from the ratio

$$a = \sqrt{\frac{8t_0^{\text{sym}}}{8t_0^{\text{sym}}/a^2}}. \quad (3.78)$$

The lattice spacing and t_0 for every β is given in table 3.1. The relative precision of a is of order 1%, while that of $8t_0^{\text{sym}}$ reaches 0.04%. Therefore, rather than using the lattice spacing, it is advantageous to employ t_0 to set the scale. For more details on the scale-setting, we refer to reference [142].

Chapter 4

The electromagnetic coupling

Charged particles can interact via the exchange of one or several photons. As photons propagate, they may polarise the vacuum by transforming into pairs of fermions and anti-fermions, which annihilate to continue propagating as a photon after a time dictated by the uncertainty principle. These virtual particles may be charged and, therefore, they can interact via photon exchange. This vacuum polarisation modifies the straightforward propagation of a photon and the interaction between physical particles. For this thesis, our aim is to study the contribution to this effect from quarks and gluons. First, we want to give a parametrisation of the QED coupling in Minkowski space-time. We start from the QED Lagrangian density [28]

$$\mathcal{L} = \bar{\psi} (i\gamma^\mu [\partial_\mu - ieA_\mu] - M_\psi) \psi - \frac{1}{4e_0^2} F_{\mu\nu} F^{\mu\nu}, \quad (4.1)$$

where ψ , $\bar{\psi}$ are the fermion fields of mass M_ψ , A_μ is the massless photon field, and we use the standard definition of the field strength tensor $F_{\mu\nu}$ with the bare electric charge e_0 . For this chapter, we follow mostly [28], such that the Minkowski metric $g_{\mu\nu}$ is mostly negative $(+, -, -, -)$. The first term of the Lagrangian includes the fermion-photon vertex and the fermion mass, and the second describes the dynamics of the QED bosons. From the last term in eq. (4.1), it is possible to obtain the free photon propagator [28],

$$iD_{\mu\nu}(q) = -i\frac{e_0^2}{q^2} \left[g_{\mu\nu} - (1 - \xi) \frac{q_\mu q_\nu}{q^2} \right], \quad (4.2)$$

where q_μ is the four-momentum of the photon, $g_{\mu\nu}$ the Minkowski metric and ξ the gauge parameter. Although we leave the latter undetermined, a particularly good choice in our situation would be the Feynman gauge, $\xi = 1$. However, the free photon propagator is modified by an infinite number of Feynman diagrams, and the full photon propagator is given by the series in fig. 4.1. The shaded blob on each diagram is the vacuum polarisation tensor $i\Pi_{\mu\nu}(q)$ [28], which is the sum of all one-particle-irreducible (1PI) insertions into the photon propagator [27]. Some of the QED diagrams contributing to $i\Pi_{\mu\nu}(q)$ can be seen in fig. 4.2. They include the propagation of a pair of lepton and anti-lepton, which can exchange,

emit and reabsorb photons. However, for this thesis we will be more interested in the QCD contributions to the vacuum polarisation, which at low energies are non-perturbative. Looking again at fig. 4.2, this means that the asymptotic series of Feynman diagrams with gluons instead of photons does not converge. Using gauge and Lorentz invariance, we can

$$\text{wavy line with shaded circle} = \text{wavy line} + \text{wavy line with 1PI circle} + \text{wavy line with 1PI 1PI circles} + \dots$$

Figure 4.1: Full photon two-point function.

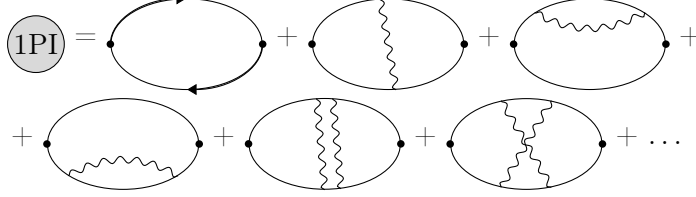


Figure 4.2: Some 1PI Feynman diagrams contributing to the vacuum polarisation. The photon propagators can transform into fermion-anti-fermion pairs, further increasing the fermion loop-order of the diagrams. We omit those diagrams for simplicity.

write more explicitly the tensor structure of the vacuum polarisation [28],

$$\Pi_{\mu\nu}(q) = \left(q_\mu q_\nu - g_{\mu\nu} q^2 \right) \Pi(q^2), \quad (4.3)$$

where the vacuum polarisation function (VPF) Π is non-negative. Following fig. 4.1, the full photon propagator is given by a geometric series where we intercalate propagator and VPF terms [28],

$$\begin{aligned} iD_{\mu\nu}^F &= iD_{\mu\nu}(q) + iD_{\mu\lambda}(q) i\Pi^{\lambda\rho} iD_{\rho\nu}(q) + iD_{\mu\lambda}(q) i\Pi^{\lambda\rho} iD_{\rho\sigma}(q) i\Pi^{\sigma\kappa} iD_{\kappa\nu}(q) + \dots \\ &= -i \frac{e_0^2}{q^2} \left(g_{\mu\nu} - \frac{q_\mu q_\nu}{q^2} \right) \left(1 + e_0^2 \Pi(q^2) + [e_0^2 \Pi(q^2)]^2 + \dots \right) - i\xi \frac{e_0^2}{q^2} \frac{q_\mu q_\nu}{q^2} \\ &= -i \frac{1}{q^2} \frac{e_0^2}{1 - e_0^2 \Pi(q^2)} \left(g_{\mu\nu} - \frac{q_\mu q_\nu}{q^2} \right) - i\xi \frac{e_0^2}{q^2} \frac{q_\mu q_\nu}{q^2}. \end{aligned} \quad (4.4)$$

To derive eq. (4.4), we make use of the conservation equations $q^\mu \Pi_{\mu\nu} = 0$, which cancel almost all terms with the gauge parameter ξ [28]. In any S-matrix calculation, at least one end of the photon propagator connects with a fermion line, and when one sums over all places where they could connect, all terms proportional to q_μ vanish [27]. In this case, the full photon propagator reduces to

$$\text{wavy line with shaded circle} = iD_{\mu\nu}^F = -i \frac{g_{\mu\nu}}{q^2} \frac{e_0^2}{1 - e_0^2 \Pi(q^2)}. \quad (4.5)$$

As long as $\Pi(q^2)$ is regular at $q^2 = 0$ (single-valued and differentiable), it is clear that $D_{\mu\nu}^F$ has a pole at $q^2 = 0$ [27]. This means that the photon propagator remains massless to all

orders of perturbation theory [27]. The residue of the pole at $q^2 = 0$ is the renormalised electric charge [28]

$$e^2 \equiv \frac{e_0^2}{1 - e_0^2 \Pi(0)}. \quad (4.6)$$

Equation (4.6) is what is actually measured by experiments [27], and substituting e_0 by e in eq. (4.5), we obtain an energy-dependent coupling [27],

$$e^2(q^2) = \frac{e^2}{1 - e^2 (\Pi(q^2) - \Pi(0))}. \quad (4.7)$$

In the following, instead of working with Π , we will use the subtracted vacuum polarisation (sVPF) instead, $\hat{\Pi}(q^2) = \Pi(q^2) - \Pi(0)$. Using the relation between the fine-structure constant and the electric charge $4\pi\alpha = e^2$ in eq. (4.7), we find one of the key equations for this project, a parametrisation for the QED running coupling

$$\alpha(q^2) = \frac{\alpha}{1 - (\Delta\alpha)_{\text{lep}}(q^2) - (\Delta\alpha)_{\text{had}}(q^2)}, \quad (4.8)$$

where

$$(\Delta\alpha)_{\text{had}}(q^2) = 4\pi\alpha\hat{\Pi}_{\gamma\gamma}(q^2). \quad (4.9)$$

In eq. (4.8), we have divided the sVPF into its two contributions at $\mathcal{O}(\alpha)$ (at higher order there is mixing between the two): $(\Delta\alpha)_{\text{lep}}$ for leptons and $(\Delta\alpha)_{\text{had}}$ for hadrons. The former can be computed in perturbation theory, while the latter requires non-perturbative techniques and focuses our attention. In eq. (4.9), we mark the sVPF of the electromagnetic current with a subscript $\gamma\gamma$ to differentiate it from the sVPF used in chapter 5 to study the electroweak mixing angle.

The most common and precise method to compute the QED running coupling employs the analyticity and unitarity of $\Pi_{\gamma\gamma}(q^2)$, together with the optical theorem $R(q^2) = 12\pi\text{Im} [\Pi_{\gamma\gamma}(q^2)]$, where $R(q^2)$ is the normalised e^+e^- -cross-section data [33]

$$R(q^2) = \frac{\sigma_{\text{total}}(e^+e^- \rightarrow \text{hadrons})}{\sigma(e^+e^- \rightarrow \mu^+\mu^-)}, \quad (4.10)$$

to evaluate the coupling via the dispersion integral [33]

$$(\Delta\alpha)_{\text{had}}(q^2) = \frac{\alpha q^2}{3\pi} \text{P} \int ds^2 \frac{R(s^2)}{s^2 (q^2 - s^2)}, \quad (4.11)$$

where P indicates the principal part of the integral. The R-ratio is computed using perturbative quantum chromodynamics (pQCD) in those regions where the latter can be trusted, generally beyond a few GeV. Updated R-ratio datasets are used in [30, 31, 32]

to compute eq. (4.11). In chapter 12, after estimating $\alpha(q^2 < 0)$ at the physical point, we compare these phenomenological determinations with our own results at a subset of points.

Let us now look at two relevant values of $\alpha(q^2)$. On one extreme, in the so-called Thomson-limit $q^2 \rightarrow 0$, the QED coupling becomes the fine-structure constant $\alpha(q^2) = \alpha$. The latter is commonly extracted from either of two methods [34]: the e^\pm anomalous magnetic moment [160], which produces $\alpha^{-1} = 137.035999150(33)$ [161], or interferometry of atomic recoil kinematics, whose average gives $\alpha^{-1} = 137.035999042(26)$ [34]. In particular, the latest and most precise result in [162] uses rubidium atoms and interferometry to obtain $\alpha^{-1} = 137.035999206(11)$. The current world average, which we use in this thesis, combines results from both approaches and yields $\alpha^{-1} = 137.035999084(21)$ [34]. It is interesting to note the 2.6σ tension between the results for the two techniques used to produce the world-average. On the other extreme, the value of the coupling at the Z -pole mass $\alpha(M_Z^2)$ is usually computed evaluating eq. (4.11) at $q^2 = M_Z^2$ [33, 31, 30, 32], and the result is approximately 7% larger than the fine-structure constant. In the modified minimal-subtraction ($\overline{\text{MS}}$) scheme, for example, the five-quark-flavour coupling $\hat{\alpha}^{(5)}(M_Z^2)^{-1} = 127.952(9)$ [35, 34]. Note the loss in precision between the Thomson limit and the Z -pole, which negatively affects the precision of experiments carried out at high energies. One important application of $\alpha(M_Z^2)$ is to constrain new physics via the so-called global fits of the SM [34]. The basic premise of the latter is as follows: If, for example, we do not know the Higgs boson mass M_H , but we have a theory quantifying its effects on an experiment through loop-suppressed interactions, we should be able to give bounds to the mass based on the experimental and theoretical results and uncertainties. In particular, the Higgs boson mass M_H can be constrained by the electroweak mixing angle $\sin^2 \theta_W$ (see chapter 5), the W boson mass M_W , the Z boson mass M_Z , the Fermi constant G_F , the QED coupling $\hat{\alpha}^{(5)}(M_Z^2)$ and the t quark mass M_t . Then, if one excludes the kinematic constraints from ATLAS [41] and CMS [42], the Higgs boson mass is constrained to be [34] $M_H = 90_{-16}^{+18}$ GeV, which is 1.8σ below the experimentally measured value. Figure 4.3, taken from [34], indicates the constraints to the Higgs boson mass from different quantities. The red blob indicates its expected value and error while the horizontal orange line shows the actual measurement at the LHC. One can see that the low value found for M_H is driven by the result for M_W . Not only the SM global fits, but also future experiments, like possible future colliders operating around the Z pole mass [32], would benefit from an improved precision of the QED coupling. In fact, using both $\alpha(M_Z^2)$ and the weak-mixing angle $\sin^2 \theta_W(M_Z^2)$, it is possible to test theories of grand unification predicting the strong coupling $\alpha_s(M_Z)$ [163, 164].

In order to perform an *ab initio* computation of $\alpha(q^2)$ without the need of e^+e^- data, we need to be able to connect the LQCD description, valid in the space-like region $q^2 < 0$, and the time-like regime $q^2 > 0$. The connection can be established using the Adler function $D(Q^2)$ [165], which is the derivative of the running coupling [33, 166, 167, 168, 169] evaluated at the momentum exchange in the space-like region $Q^2 = -q^2 > 0$,

$$D(Q^2) = \frac{3\pi}{\alpha} Q^2 \frac{d(\Delta\alpha)_{\text{had}}(Q^2)}{dQ^2}. \quad (4.12)$$

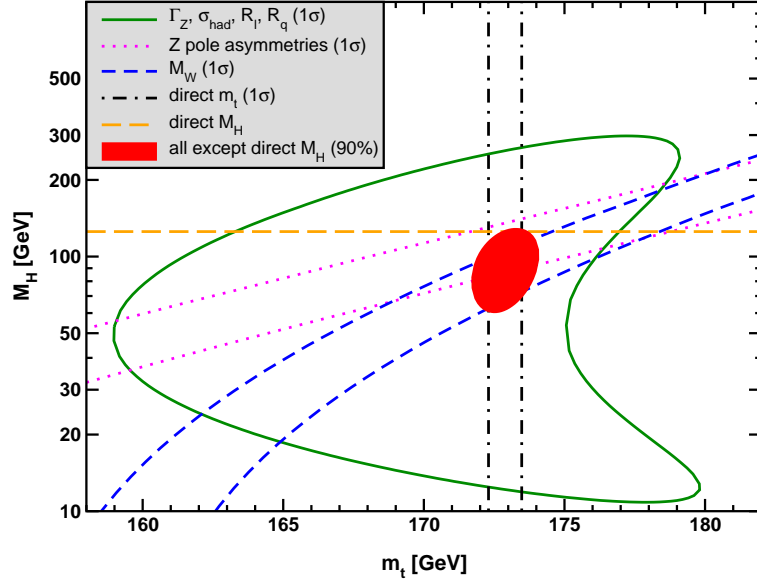


Figure 4.3: Comparison between the predicted Higgs boson mass from the SM global fits and the direct measurement at the LHC, figure taken from [34].

Upon integration of eq. (4.12), we can, for instance, obtain the coupling at the Z pole using the split technique [167]

$$\begin{aligned}
 (\Delta\alpha)_{\text{had}}^{(5)}(M_Z^2) &= (\Delta\alpha)_{\text{had}}^{(5)}(Q_0^2) \\
 &+ \left[(\Delta\alpha)_{\text{had}}^{(5)}(-M_Z^2) - (\Delta\alpha)_{\text{had}}^{(5)}(Q_0^2) \right]^{\text{pQCD}} \\
 &+ \left[(\Delta\alpha)_{\text{had}}^{(5)}(M_Z^2) - (\Delta\alpha)_{\text{had}}^{(5)}(-M_Z^2) \right]^{\text{pQCD}}, \quad (4.13)
 \end{aligned}$$

where Q_0^2 is a space-like virtuality chosen such that both LQCD and pQCD can be trusted, $(\Delta\alpha)_{\text{had}}^{(5)}(M_Z^2)$ is evaluated on the time-like region and $(\Delta\alpha)_{\text{had}}^{(5)}(-M_Z^2)$ on the space-like. For Q_0^2 , we have to select a value large enough so the perturbative expansion converges while, at the same time, lattice artefacts are kept under control on the lattice. The second term in eq. (4.13) can be computed using pQCD and the last line is equal to 0.000045(2) [167]. The specific purpose of this thesis is to compute the first term, $(\Delta\alpha)_{\text{had}}^{(5)}(Q_0^2)$. The remainder of the computation of $(\Delta\alpha)_{\text{had}}(M_Z^2)$ is being carried out by colleagues in the Mainz group. In fact, their analysis will decide what is the best option for the turning point Q_0^2 ; our efforts will focus on giving reliable results for the sVPF for Q^2 as high as possible. Regarding the flavour content, our simulations include dynamical u , d and s quarks, and the c quark appears at the quenched level. Meanwhile, our simulations do not include the b quark, but we expect its contribution to be almost negligible at our level of precision. See [170] for a study of the b quark contribution using LQCD.

On Euclidean space, the vacuum polarisation tensor can be expressed in terms of the correlation function of the electromagnetic current in the form [171, 172, 173]

$$\Pi_{\gamma\gamma,\mu\nu}(Q) = \int d^4x e^{iQx} \langle 0 | V_{\gamma,\mu}(x) V_{\gamma,\nu}(0) | 0 \rangle, \quad (4.14)$$

where the electromagnetic current is given by

$$V_{\gamma,\mu}(x) = \frac{2}{3} \bar{u}(x) \gamma_\mu u(x) - \frac{1}{3} \bar{d}(x) \gamma_\mu d(x) + \frac{2}{3} \bar{c}(x) \gamma_\mu c(x) \\ - \frac{1}{3} \bar{s}(x) \gamma_\mu s(x) + \frac{2}{3} \bar{t}(x) \gamma_\mu t(x) - \frac{1}{3} \bar{b}(x) \gamma_\mu b(x). \quad (4.15)$$

In section 6.1, we give the expectation value of eq. (4.14) in terms of improved and renormalised flavour components and, in section 6.2, we introduce the time-momentum representation to express eq. (4.14) in a form that we can evaluate on the lattice.

Before finishing this section, we want to briefly elaborate on the relation between $\alpha(Q^2)$ and the anomalous magnetic moment of the muon $a_\mu^{\text{HLO}} \equiv (g-2)_\mu/2$, which is one of the most active topics on PBSM. Both can be computed with similar techniques, either using the R-ratio data or the electromagnetic current; in fact, they are directly proportional to each other, with the relation being a relatively simple integral [174, 36]. Therefore, one sees that a variation in either of the two quantities will affect the other and, consequently, the mass of the Higgs boson obtained from the global fits will be modified [43]. Before the E989 experiment released their first results back in April 2021 [39], the theory predictions, gathered in [38], already disagreed by $3\sigma - 4\sigma$ with the results from the E821 experiment [40]. The new data from Fermilab reproduces the earlier result from Brookhaven, and the combination of both datasets increases the tension between experiment and the SM prediction, which is obtained using the R-ratio approach. If these news were not exciting enough already, the BMW collaboration published their new results [175], which favour the experimental value and whose uncertainties are at the level of the phenomenological determinations. If their value was to be used to compute the Higgs boson mass in the SM global fits, the value obtained would be even lower, increasing the tension with the direct measurements [43]. Therefore, if we bridge the gap between the theoretical prediction and the experimental result of a_μ , this would, via the relation of the latter with the QED coupling, increase tensions between the bounds for the Higgs boson mass and the direct measurement.

Chapter 5

The electroweak mixing angle

The part of the Standard Model related to electromagnetic and weak interactions, the Glashow-Weinberg-Salam (GWS) theory, is represented by a $SU(2)_L \times U(1)_Y$ gauge symmetry initially introduced by Glashow, Salam and Ward [3, 4]. The $SU(2)_L$ group, also known as weak isospin, has a coupling strength g and three spin-1 vector generators, A_μ^1 , A_μ^2 and A_μ^3 ; and the $U(1)_Y$ group, called hypercharge symmetry, has the coupling g' and the spin-1 vector boson B_μ^0 . Later, Weinberg applied in [176] the Higgs mechanism [177, 178, 179, 12, 10] to $SU(2)_L \times U(1)_Y$ including a complex, spin-0 scalar doublet, the so-called Higgs field — a more complete historical introduction can be seen in [180] and references therein. When the Higgs field assumes its ground state, it causes the spontaneous breaking of the $SU(2)_L \times U(1)_Y$ symmetry into a reduced group $U(1)_{em}$ of electromagnetic interactions. This mechanism yields a massless boson A_μ , which is identified as the photon, and three massive particles corresponding to the W^\pm and Z^0 bosons. In particular, the mass eigenstates A_μ and Z^0 are related to the original fields A_μ^3 and B_μ^0 via a linear transformation given by the electroweak mixing angle θ_W [27]

$$\begin{pmatrix} Z_\mu^0 \\ A_\mu \end{pmatrix} = \begin{pmatrix} \cos \theta_W & -\sin \theta_W \\ \sin \theta_W & \cos \theta_W \end{pmatrix} \begin{pmatrix} A_\mu^3 \\ B_\mu^0 \end{pmatrix}, \quad (5.1)$$

where the electroweak mixing angle is defined in terms of the couplings g and g' [27],

$$\cos \theta_W = \frac{g}{\sqrt{g^2 + g'^2}}, \quad \sin \theta_W = \frac{g'}{\sqrt{g^2 + g'^2}}. \quad (5.2)$$

One of the predictions of the GWS theory is the relation, valid at tree-level, between the masses of the W^\pm and Z^0 bosons and the electroweak mixing angle [27],

$$\sin^2 \theta_W = 1 - \frac{M_W^2}{M_Z^2}. \quad (5.3)$$

In 1971, Gerhard 't Hooft proved that gauge theories with spontaneous symmetry breaking are renormalisable [181]. In particular, the value of $\sin^2 \theta_W$ depends on the renormalisation



Figure 5.1: Hadronic contribution to the $\gamma - Z$ -mixing Feynman diagram.

prescription used, and several have been proposed. At first, an on-shell scheme was employed [182, 183], which promotes eq. (5.3) to an identity to all loop orders in perturbation theory. Its main disadvantage was the introduction of large corrections of $\mathcal{O}(\alpha M_t^2/M_W^2)$ to weak neutral (Z) current processes [180]. In this scheme, $\sin^2 \theta_W = 0.22337(10)$ [34]. A second option emerged at LEP, an effective $\sin^2 \theta_W^{\text{eff}}$ defined by the $Z - \mu^- - \mu^+$ -vertex coupling at the Z -pole mass [184, 185], with $\sin^2 \theta_W^{\text{eff}} = 0.23153(4)$ [34]. Finally, one can also define the electroweak mixing angle using the more theoretically motivated $\overline{\text{MS}}$ scheme [186, 187],

$$\sin^2 \hat{\theta}_W(\mu) = \frac{\hat{e}^2(\mu)}{\hat{g}^2(\mu)}, \quad (5.4)$$

where we denote quantities in the $\overline{\text{MS}}$ scheme with a caret, μ is an arbitrary energy scale and $\sin^2 \hat{\theta}_W(M_Z) = 0.23121(4)$ [34]. The various definitions of $\sin^2 \theta_W$ differ at the level of one-loop computations and beyond, which can reveal interesting new physics [27]. For a summary of the renormalisation schemes discussed here, see [180].

One may obtain a similar expression to eqs. (4.8) and (4.9) for $\sin^2 \theta_W$. For this project, we use a specific definition of the running electroweak-mixing angle, appearing in polarised Møller scattering experiments [188, 189], $e^- e^- \rightarrow e^- e^-$,

$$\sin^2 \theta_W(Q^2) = \left(\frac{1 - \Delta\alpha_2(Q^2)}{1 - \Delta\alpha(Q^2)} + \Delta\kappa_b(Q^2) - \Delta\kappa_b(0) \right) \sin^2 \theta_W(0), \quad (5.5)$$

where $\Delta\kappa_b$ represents the contribution from bosonic loops, given in [188, 189] to one-loop order, $\Delta\alpha$ is the total variation of the QED coupling in eq. (4.8), and $\Delta\alpha_2$ is the running of the coupling $4\pi\alpha_2 = g^2$, which can be defined in a similar fashion to the running of α , following the discussion in chapter 4 [48, 49, 50],

$$\alpha_2(q^2) = \frac{\alpha_2}{1 - \Delta\alpha_2(q^2)}. \quad (5.6)$$

The hadronic contribution to $\Delta\alpha_2(q^2)$ is [190, 191]

$$\Delta\alpha_{2,\text{had}}(q^2) = \frac{4\pi\alpha}{\sin^2 \theta_W(0)} \hat{\Pi}_{T_3\gamma}(q^2), \quad (5.7)$$

where $\hat{\Pi}_{T_3\gamma}$ is the subtracted vacuum polarisation function including the electromagnetic current $V_{\gamma,\mu}(x)$ and the third component of the weak isospin current [48]

$$\begin{aligned} J_{T_3,\mu}(x) = & \frac{1}{4} (\bar{u}\gamma_\mu(1 - \gamma_5)u - \bar{d}\gamma_\mu(1 - \gamma_5)d) \\ & + \frac{1}{4} (\bar{c}\gamma_\mu(1 - \gamma_5)c - \bar{s}\gamma_\mu(1 - \gamma_5)s) \\ & + \frac{1}{4} (\bar{t}\gamma_\mu(1 - \gamma_5)t - \bar{b}\gamma_\mu(1 - \gamma_5)b). \end{aligned} \quad (5.8)$$

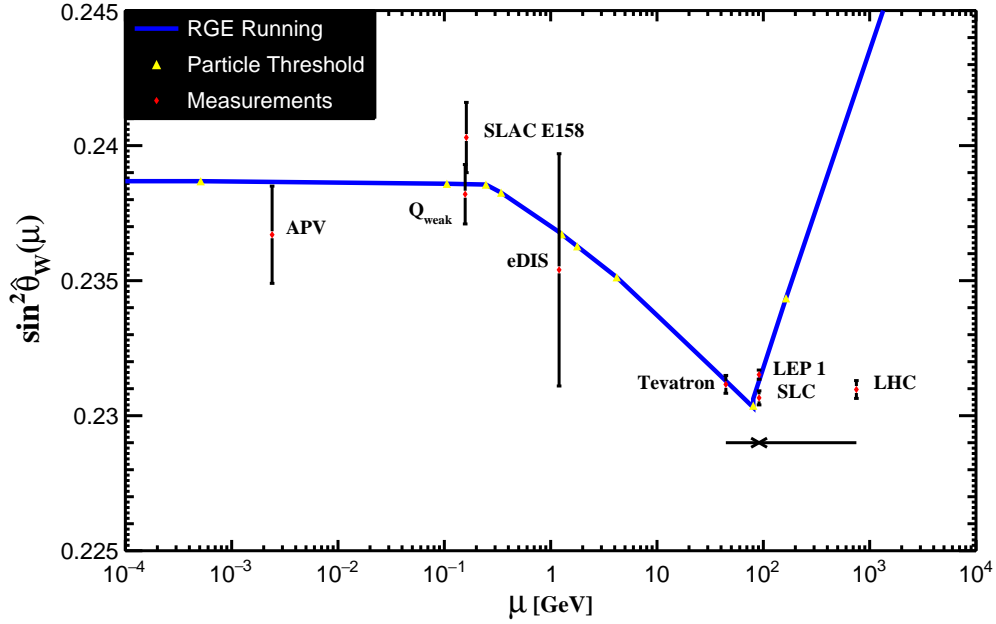


Figure 5.2: Running of the electroweak mixing angle as given by the renormalisation group equations compared with various measurements [34]. The different particle thresholds are indicated in yellow.

Equation (5.8) can be divided in two parts, an axial-vector and a vector component. The first has the γ -structure $\gamma_\mu \gamma_5$ and positive parity, while the second has negative parity and the γ -structure γ_μ . We are solely interested in two-point functions of the form $\langle J_{T_3,\mu}(x) V_{\gamma,\nu}(y) \rangle$, where we project an initial vector state into the two components of eq. (5.8) and take the expectation value in QCD. Since parity is a symmetry of QCD, it is clear that only the vector component of $J_{T_3,\mu}(x)$ will yield a non-zero expectation value. Therefore, in chapter 7, where we develop the expressions for the correlation functions that we need to consider, we only work with vector currents. To obtain the hadronic contribution to eq. (5.5), one can expand the ratio of eq. (5.5) in a Taylor series. In this way, we can write eq. (5.5) in the simpler form [171, 48]

$$\sin^2 \theta_W(q^2) = \sin^2 \theta_W(0) \left(1 + \Delta \sin^2 \theta_W(q^2) \right). \quad (5.9)$$

Then, by taking only the hadronic parts and leaving out the bosonic terms $\Delta \kappa_b$, one finds the hadronic contribution to the running of $\sin^2 \theta_W$ at leading order [171, 48],

$$(\Delta \sin^2 \theta_W)_{\text{had}}(q^2) = (\Delta \alpha)_{\text{had}}(q^2) - \Delta \alpha_{2,\text{had}}(q^2) = -\frac{4\pi\alpha}{\sin^2 \theta_W(0)} \hat{\Pi}_{Z\gamma}(q^2), \quad (5.10)$$

where $\hat{\Pi}_{Z\gamma}(q^2)$ is the sVPF mixing the electromagnetic current $V_{\gamma,\mu}(x)$ and the vector part

of the neutral weak current [48]

$$V_{Z,\mu}(x) = J_{T_3,\mu}(x)|_{\text{vector}} - \sin^2 \theta_W(0) V_{\gamma,\mu}(x). \quad (5.11)$$

There is a growing number of experiments [192, 34] probing electroweak precision observables in the region of low-momentum transfers, $q^2 \ll M_Z^2$, whose aim is detecting deviations from the expected running of the electroweak mixing angle due to PBSM. Their main focus is on parity-violating lepton scattering [193, 194, 195, 196]; atomic parity-violation [197, 192, 198, 199] with precise measurements in a small set of heavy atoms [200, 201, 202, 203, 204, 205]; and neutrino scattering off leptons [206] with several determinations of $\sin^2 \theta_W$ [207, 208, 209]. So far, the most precise experimental determination was carried out by the Q_{weak} experiment at JLAB [44], which measures the weak charge

$$Q_w = 1 - 4 \sin^2 \theta_W \quad (5.12)$$

of the proton to determine $\sin^2 \hat{\theta}_W = 0.2383(11)$ at $Q = 0.158 \text{ GeV}$. However, these results are far less precise than the corresponding values of the QED coupling shown in chapter 4. Fortunately, there are a number of projects aiming at improving this situation, concentrated at JLAB and the Institute of Nuclear Physics in Mainz University. At JLAB, we find the MOLLER [45] and SoLID [46] experiments. Members of the first project want to improve the determination of parity-violation in Møller scattering, reducing the uncertainty of the previous SLAC E158 experiment by a factor of five. From there, they could obtain the weak charge of the electron. Meanwhile, the second experiment wants to study parity violation in deep inelastic scattering (DIS) between an electron and a proton or a deuteron, obtaining $\sin^2 \theta_W$ with a precision below 1%. The same physical process was already used in SLAC's experiment E122 back in 1978 [193], whose results helped to establish the current SM of physics and determined $\sin^2 \theta_W$ with a 10% precision. In the Mainz facilities, we find the P2 experiment [47], which will use electron-proton elastic scattering to measure the weak charge of the proton and extract $\sin^2 \theta_W$ with a precision of 0.14%, similar to those measurements at the Z-pole, at a four-momentum transfer $Q^2 = 4.5 \times 10^{-3} \text{ GeV}^2$. To gather the necessary statistics, the new Mainz Energy-Recovering Superconducting Accelerator (MESA) experiment is under construction.

From the theory side, the hadronic contribution $(\Delta \sin^2 \theta_W)_{\text{had}}$ is usually obtained from a dispersion relation employing e^+e^- -data [48, 49, 50], just like $(\Delta\alpha)_{\text{had}}$. However, e^+e^- -information couples only to the QED current and, therefore, it is necessary to separate the different quark components and re-weight them with the appropriate weak charge. This process, known as flavour separation [48, 49, 50], is a source of systematic uncertainty affecting the determination of $\sin^2 \theta_W$ but not α . Our computation of $\sin^2 \theta_W$ with LQCD would allow not only to test our current knowledge of weak interactions with an *ab initio* theoretical determination, but, because one computes each quark component separately on the lattice, flavour separation is a natural by-product of our formulation. In section 6.1, we show the main equations to compute $\sin^2 \theta_W$ on the lattice. Some previous work on the determination of $\sin^2 \theta_W$ using LQCD can be found in [171, 172, 210, 211].

Chapter 6

The hadronic vacuum polarisation

After introducing the quantities that we want to study, now we give the main results that allow us to compute the vector current on the lattice, including $\mathcal{O}(a)$ improvement and renormalisation. First of all, to have a better handle of the continuum extrapolation described in chapter 12, we construct the currents using two different discretisations, which have different behaviour approaching the continuum. The simplest is the local (l) discretisation (more exactly point-like, ultra-local discretisation), the bilinear [29]

$$V_{(f,f'),\mu}^1(n) = \bar{\psi}_f(n)\gamma_\mu\psi_{f'}(n), \quad (6.1)$$

with quark flavours f and f' and support in just one lattice site. The second form is the symmetric, point-split (s) vector current [29],

$$V_{(f,f'),\mu}^s(n) = \frac{1}{2} \left(V_{(f,f'),\mu}^{\text{ps}}(n) + V_{(f,f'),\mu}^{\text{ps}}(n - a\hat{\mu}) \right), \quad (6.2)$$

where the point-split (ps) current $V_{(f,f'),\mu}^{\text{ps}}(n)$ [29]

$$V_{(f,f'),\mu}^{\text{ps}}(n) = \frac{1}{2} \left(\bar{\psi}_f(n + a\hat{\mu})(1 + \gamma_\mu)U_\mu^\dagger(n)\psi_{f'}(n) - \bar{\psi}_f(n)(1 - \gamma_\mu)U_\mu(n)\psi_{f'}(n + a\hat{\mu}) \right) \quad (6.3)$$

depends on quark fields on two different lattice sites. Equation (6.3) is a conserved current, which has a trivial renormalisation, and is constructed varying the quark fields of the expectation value and demanding the latter to remain constant [29]. In particular, if one performs the non-anomalous infinitesimal transformation of the quark fields [29]

$$\begin{aligned} \delta\psi_f &= i\epsilon(n)\psi_f, \\ \delta\bar{\psi}_f &= -i\bar{\psi}_f\epsilon(n), \end{aligned} \quad (6.4)$$

the expectation value eq. (3.26) should remain unchanged. The fermion action in eq. (3.16),

$$S_F = \sum_{n,m} \bar{\psi}_f(n)D(n,m)\psi_f(m) \quad (6.5)$$

will change, however. If eq. (6.4) is a symmetry of the theory, the variation should be zero [29],

$$\delta S_{\text{fermion}} = i \sum_{n,m} \bar{\psi}_f(n) \left(D(n,m) \epsilon(m) - \epsilon(n) D(n,m) \right) \psi_f(m) \equiv 0. \quad (6.6)$$

Factoring out the arbitrary ϵ , one arrives at the conservation equation [29]

$$\Delta V_{(f,f),\mu}^{\text{ps}}(n) = \sum_{\mu=1}^4 \frac{1}{a} \left(V_{(f,f),\mu}^{\text{ps}}(n + \hat{\mu}) - V_{(f,f),\mu}^{\text{ps}}(n) \right) = 0, \quad (6.7)$$

where Δ represents a lattice derivative. Equation (6.7) implies that the current $V_{(f,f),\mu}^{\text{ps}}(n)$ is conserved.

6.1 Renormalisation and $\mathcal{O}(a)$ improvement

The currents defined in eqs. (6.1) and (6.2) have $\mathcal{O}(a)$ -discretisation errors [29]. This means that we need to improve them, not only the action, to obtain a fully $\mathcal{O}(a)$ -improved expectation value. The $\mathcal{O}(a)$ improvement and renormalisation of an operator O has the general form [212]

$$O_{\text{I}} = O + a \sum I, \quad O_{\text{RI}}^i = Z^{ij} O_{\text{I}}^j, \quad (6.8)$$

where I represents the improvement terms, i, j run over the flavour components, O_{I} refers to the $\mathcal{O}(a)$ -improved operator and O_{RI} to the renormalised and $\mathcal{O}(a)$ -improved case. As indicated by eq. (6.8), it is possible that different flavours mix under renormalisation. In a similar way to the action, to improve the vector currents, we look for all dimension three operators with the same symmetries as the currents themselves [213]. Some of these terms are proportional to the currents, and can be absorbed into the renormalisation factor [212]. Of course, to relate quantities computed with the lattice regularisation at vanishing lattice spacing and their corresponding physical quantities we still need to renormalise the former. For the vector currents, the multiplicative renormalisation coefficients assume finite values in the continuum limit [29]. Following [212], the renormalisation and $\mathcal{O}(a)$ improvement of the vector correlator with isospin zero mix non-singlet and singlet flavour currents. Because of this, instead of directly working on the flavour components, we use a $\text{SU}(3)$ -flavour basis and study the components given by the Gell-Mann matrices λ_3 , λ_8 and the identity matrix $\mathbf{1}_{3 \times 3}$. In this basis, we have

$$\begin{aligned} V_{3,\mu}^d(n) &= \frac{1}{2} \left(V_{(u,u),\mu}^d(n) - V_{(d,d),\mu}^d(n) \right), \\ V_{8,\mu}^d(n) &= \frac{1}{2\sqrt{3}} \left(V_{(u,u),\mu}^d(n) + V_{(d,d),\mu}^d(n) - 2V_{(s,s),\mu}^d(n) \right), \\ V_{0,\mu}^d(n) &= \frac{1}{2} \left(V_{(u,u),\mu}^d(n) + V_{(d,d),\mu}^d(n) + V_{(s,s),\mu}^d(n) \right), \end{aligned} \quad (6.9)$$

plus the original charm current $V_{c,\mu}^d(n)$, where d indicates a specific discretisation, $V_{3,\mu}^d(n)$ is the isovector component, $V_{8,\mu}^d(n)$ the isoscalar and $V_{0,\mu}^d(n)$ the $\text{SU}(3)_f$ -singlet contribution.

From the definition of the isospin components in eq. (6.9) and the definition of $V_{\gamma,\mu}(n)$ and $V_{Z,\mu}(n)$ in eq. (4.15) and eq. (5.11), respectively, we may write our target currents in the $SU(3)_f$ basis,

$$V_{\gamma,\mu}^d(n) = V_{3,\mu}^d(n) + \frac{1}{\sqrt{3}}V_{8,\mu}^d(n) + \frac{4}{9}V_{c,\mu}^d(n), \quad (6.10)$$

$$V_{Z,\mu}^d(n) = \left(\frac{1}{2} - \sin^2 \theta_W(0)\right) V_{\gamma,\mu}^d(n) - \frac{1}{6}V_{0,\mu}^d(n) - \frac{1}{12}V_{c,\mu}^d(n). \quad (6.11)$$

6.1.1 $\mathcal{O}(a)$ improvement

The improved currents [214, 212] for both discretisations can be defined in a similar fashion thanks to the use of the symmetric, point-split discretisation [95],

$$V_{i,\mu,I}^S(n) = V_{i,\mu}^S(n) + ac_V^S \partial_\nu \Sigma_{i,\mu\nu}^1(n), \quad (6.12)$$

$$V_{i,\mu,I}^1(n) = V_{i,\mu}^1(n) + ac_V^1 \partial_\nu \Sigma_{i,\mu\nu}^1(n), \quad (6.13)$$

where $i = 3, 8, 0, c$ and $\Sigma_{i,\mu\nu}^1(n)$ is the local tensor current,

$$\Sigma_{(f,f'),\mu\nu}^1(n) = -\frac{1}{2}\bar{\psi}_f(n)[\gamma_\mu, \gamma_\nu]\psi_{f'}(n), \quad (6.14)$$

Its $SU(3)_f$ decomposition is the same as eq. (6.9), substituting the vector currents by the tensor ones. The numerical values for c_V^1 and c_V^S used for this thesis are obtained from [212] and gathered in table 6.1. For our analysis, we take the improvement terms c_V^1 and c_V^S exactly, without any uncertainty, because their error is not related to the knowledge of the correlator itself, but rather indicates the possibility of residual $\mathcal{O}(a)$ lattice artefacts, and we study the presence of the latter in the extrapolation to the physical point in chapter 12.

There are various possibilities for the definition of the discrete derivate ∂_μ , each one introducing different discretisation effects and affecting the continuum extrapolation in a different way. We perform the complete analysis using either the forward, symmetric or backward definitions for the improvement derivative ∂_μ . Respectively,

$$\frac{f(n + \hat{\mu}) - f(n)}{a}, \quad \frac{f(n + \hat{\mu}) - f(n - \hat{\mu})}{2a}, \quad \frac{f(n) - f(n - \hat{\mu})}{a}. \quad (6.15)$$

However, our implementation of these derivatives is not standard. Let us suppose that we locate the source of our correlators (see chapter 7) in the middle of the lattice, $n_4 = T/2$. Then, we want to avoid the source from entering the improvement term at $n_4 = T/2 \pm 1$. That is why, if we use the symmetric derivative for the entire time extension, then we use the forward derivative at $n_4 = T/2 + 1$ and the backward derivative at $n_4 = T/2 - 1$. In a similar fashion, the forward (backward) derivative is substituted by the backward (forward) derivative at $n_4 = T/2 - 1$ ($n_4 = T/2 + 1$). Also, locating the source at $n_4 = N/2$ means that the time-slices $n_4 > N/2$ and $n_4 < N/2$ of the vector meson correlator are related via

a time reversal transformation, which is centred around the source. Since the time-reversed forward derivative is minus the backward derivative, when we use the forward (backward) derivative for $n_4 > N/2$, we need to use the backward (forward) derivative for $n_4 < N/2$.

After explaining the implementation of the derivative, we select which one minimizes discretisation effects. It is true that, in principle, the symmetric derivative would be the natural choice, as it is an eigenfunction of parity like the vector current. But using the forward and backward derivatives only breaks parity to $\mathcal{O}(a^2)$ (the derivatives themselves have $\mathcal{O}(a)$ discretisation errors, and since we apply them to the improvement term the effect is only $\mathcal{O}(a^2)$), and as such it is possible to use them without affecting the $\mathcal{O}(a)$ improvement. In chapter 12, we select the symmetric derivative for the isovector and isoscalar components, and the forward derivative for the charm quark, because they shorten the extrapolation to the continuum limit.

6.1.2 Renormalisation

After applying the $\mathcal{O}(a)$ improvement to both discretisations, we detail the renormalisation procedure. The renormalised local vector currents can be computed as [214, 212]

$$V_{3,\mu,\text{RI}}^1(n) = Z_V^{(3)} V_{3,\mu,\text{I}}^1(n), \quad (6.16)$$

$$V_{8,\mu,\text{RI}}^1(n) = Z_V^{(8)} V_{8,\mu,\text{I}}^1(n) + Z_V^{(80)} V_{0,\mu,\text{I}}^1(n), \quad (6.17)$$

where the three mass-dependent renormalisation factors we need are [214, 212]

$$\begin{aligned} Z_V^{(3)} &= Z_V(g_0) \left(1 + 3\bar{b}_V^{\text{eff}} a m_{q,\text{av}} + b_V a m_{q,\text{l}} \right), \\ Z_V^{(8)} &= Z_V(g_0) \left(1 + 3\bar{b}_V^{\text{eff}} a m_{q,\text{av}} + \frac{b_V}{3} a (m_{q,\text{l}} + 2m_{q,\text{s}}) \right), \\ Z_V^{(80)} &= Z_V(g_0) \left(\frac{b_V}{3} + f_V \right) \frac{2}{\sqrt{3}} a (m_{q,\text{l}} - m_{q,\text{s}}). \end{aligned} \quad (6.18)$$

The subtracted bare quark mass $m_{q,\text{i}}$, the averaged quark mass $m_{q,\text{av}}$ and the remaining factors are defined in [212]. The factors $Z_V(g_0)$, \bar{b}_V^{eff} and b_V are computed non-perturbatively [212], enforcing the vector Ward identity derived from the transformation in eq. (6.4) for every lattice spacing and pion mass. With the appropriate implementation, this is equivalent to demand the electric charge of the pion to be unity at every lattice spacing [212]. For more details on the computation of the renormalisation and improvement factors, see [213, 212]. A perturbative determination is also possible, with results in [215, 216, 217] for the various coefficients but at the couplings we study, there is a sizeable difference between perturbative and non-perturbative determinations. The mass-dependent renormalisation factors $Z_V^{(c)}$ were obtained in [218] demanding the charm quantum number of the pseudo-scalar $c\bar{s}$ -meson to be unity on every ensemble. Table 6.1 shows the renormalisation factors of eq. (6.18). Both $Z_V^{(3)}$ and $Z_V^{(8)}$ have similar values and are approximately constant. For $Z_V^{(80)}$, we clearly see the proportionality to the quark-mass difference, which vanishes at the $\text{SU}(3)_f$ -symmetric point, and since it is proportional to the lattice spacing, its magnitude

is much smaller. The symmetric, point-split discretisation has trivial renormalisation, $V_{i,\mu,\text{RI}}^d(n) = V_{i,\mu,\text{I}}^d(n)$.

6.1.3 The vector current

From the previous definitions, the renormalisation and improvement of the vector two-point function can be derived to $\mathcal{O}(a)$. At the source, we use only the local discretisation, while at the sink we use either the local or symmetric, point-split. Therefore, from now on we usually indicate only the discretisation at the sink of the two-point functions, while the local discretisation is understood to be used at the source. The renormalised, $\mathcal{O}(a)$ -improved isovector component is

$$\begin{aligned} G_{33}^{\text{S}}(n_4) = & -\frac{1}{3} \sum_{j=1,2,3} \sum_{\vec{n}} \left\langle V_{3,j,\text{RI}}^{\text{S}}(n) V_{3,j,\text{RI}}^{\text{I}}(0) \right\rangle = \\ & -\frac{1}{3} \sum_{j=1,2,3} \sum_{\vec{n}} Z_{\text{V}}^{(3)} \left(\left\langle V_{3,j}^{\text{S}}(n) V_{3,j}^{\text{I}}(0) \right\rangle + ac_{\text{V}}^{\text{I}} \left\langle V_{3,j}^{\text{S}}(n) \partial_4 \Sigma_{3,j4}^{\text{I}}(0) \right\rangle \right. \\ & \left. + ac_{\text{V}}^{\text{S}} \left\langle \partial_4 \Sigma_{3,j4}^{\text{I}}(n) V_{3,j}^{\text{I}}(0) \right\rangle \right), \quad (6.19) \end{aligned}$$

$$\begin{aligned} G_{33}^{\text{I}}(n_4) = & -\frac{1}{3} \sum_{j=1,2,3} \sum_{\vec{n}} \left\langle V_{3,j,\text{RI}}^{\text{I}}(n) V_{3,j,\text{RI}}^{\text{I}}(0) \right\rangle = \\ & -\frac{1}{3} \sum_{j=1,2,3} \sum_{\vec{n}} \left(Z_{\text{V}}^{(3)} \right)^2 \left(\left\langle V_{3,j}^{\text{I}}(n) V_{3,j}^{\text{I}}(0) \right\rangle + ac_{\text{V}}^{\text{I}} \left\langle V_{3,j}^{\text{I}}(n) \partial_4 \Sigma_{3,j4}^{\text{I}}(0) \right\rangle \right. \\ & \left. + ac_{\text{V}}^{\text{I}} \left\langle \partial_4 \Sigma_{3,j4}^{\text{I}}(n) V_{3,j}^{\text{I}}(0) \right\rangle \right). \quad (6.20) \end{aligned}$$

To improve the signal, we average over the three spatial polarisations. Since the spatial coordinates follow PBC and we sum over the spatial coordinates, the spatial derivatives will cancel and, therefore, we only need to consider the time derivative of the improvement term, $\partial_4 \Sigma_{3,j4}^{\text{I}}(n)$. The charm component can be obtained simply substituting the isospin index and $Z_{\text{V}}^{(3)}$ by $Z_{\text{V}}^{(c)}$ in eqs. (6.19) and (6.20),

$$\begin{aligned} G_{cc}^{\text{S}}(n_4) = & -\frac{1}{3} \sum_{j=1,2,3} \sum_{\vec{n}} \left\langle V_{c,j,\text{RI}}^{\text{S}}(n) V_{c,j,\text{RI}}^{\text{I}}(0) \right\rangle = \\ & -\frac{1}{3} \sum_{j=1,2,3} \sum_{\vec{n}} Z_{\text{V}}^{(c)} \left(\left\langle V_{c,j}^{\text{S}}(n) V_{c,j}^{\text{I}}(0) \right\rangle + ac_{\text{V}}^{\text{I}} \left\langle V_{c,j}^{\text{S}}(n) \partial_4 \Sigma_{c,j4}^{\text{I}}(0) \right\rangle \right. \\ & \left. + ac_{\text{V}}^{\text{S}} \left\langle \partial_4 \Sigma_{c,j4}^{\text{I}}(n) V_{c,j}^{\text{I}}(0) \right\rangle \right), \quad (6.21) \end{aligned}$$

$$\begin{aligned}
 G_{cc}^1(n_4) = & -\frac{1}{3} \sum_{j=1,2,3} \sum_{\vec{n}} \left\langle V_{c,j,\text{RI}}^1(n) V_{c,j,\text{RI}}^1(0) \right\rangle = \\
 & -\frac{1}{3} \sum_{j=1,2,3} \sum_{\vec{n}} \left(Z_V^{(c)} \right)^2 \left(\left\langle V_{c,j}^1(n) V_{c,j}^1(0) \right\rangle + ac_V^1 \left\langle V_{c,j}^1(n) \partial_4 \Sigma_{c,j4}^1(0) \right\rangle \right. \\
 & \left. + ac_V^1 \left\langle \partial_4 \Sigma_{c,j4}^1(n) V_{c,j}^1(0) \right\rangle \right). \quad (6.22)
 \end{aligned}$$

The isoscalar component is more involved, but we can simplify it restricting ourselves to terms of $\mathcal{O}(a)$,

$$G_{88}^S(n_4) = -\frac{1}{3} \sum_{j=1,2,3} \sum_{\vec{n}} \left\langle V_{8,j,\text{RI}}^S(n) V_{8,j,\text{RI}}^1(0) \right\rangle = \quad (6.23)$$

$$\begin{aligned}
 & -\frac{1}{3} \sum_{j=1,2,3} \sum_{\vec{n}} Z_V^{(8)} \left(\left\langle V_{8,j}^S(n) V_{8,j}^1(0) \right\rangle + \right. \\
 & \left. + ac_V^1 \left\langle V_{8,j}^S(n) \partial_4 \Sigma_{8,j4}^1(0) \right\rangle + ac_V^S \left\langle \partial_4 \Sigma_{8,j4}^1(n) V_{8,j}^1(0) \right\rangle \right) + \\
 & -\frac{1}{3} \sum_{j=1,2,3} \sum_{\vec{n}} Z_V^{(80)} \left\langle V_{8,j}^S(n) V_{0,j}^1(0) \right\rangle,
 \end{aligned}$$

$$G_{88}^1(n_4) = -\frac{1}{3} \sum_{j=1,2,3} \sum_{\vec{n}} \left\langle V_{8,j,\text{RI}}^1(n) V_{8,j,\text{RI}}^1(0) \right\rangle = \quad (6.24)$$

$$\begin{aligned}
 & -\frac{1}{3} \sum_{j=1,2,3} \sum_{\vec{n}} \left(Z_V^{(8)} \right)^2 \left(\left\langle V_{8,j}^1(n) V_{8,j}^1(0) \right\rangle + \right. \\
 & \left. + ac_V^1 \left\langle V_{8,j}^1(n) \partial_4 \Sigma_{8,j4}^1(0) \right\rangle \right. \\
 & \left. + ac_V^1 \left\langle \partial_4 \Sigma_{8,j4}^1(n) V_{8,j}^1(0) \right\rangle \right) + \\
 & -\frac{1}{3} \sum_{j=1,2,3} \sum_{\vec{n}} Z_V^{(8)} Z_V^{(80)} \left(\left\langle V_{8,j}^1(n) V_{0,j}^1(0) \right\rangle + \left\langle V_{0,j}^1(n) V_{8,j}^1(0) \right\rangle \right).
 \end{aligned}$$

In eqs. (6.23) and (6.24), we do not consider the improvement of the singlet current $V_{0,\mu}^d(n)$ because $V_{0,\mu}^d(n)$ appears only in combination with $Z_V^{(80)} \propto a$ and then the improvement of the singlet current would appear as an $\mathcal{O}(a^2)$ correction, which we do not aim to take into account. The renormalised, $\mathcal{O}(a)$ -improved SU(3)_f-singlet component is

$$\begin{aligned}
 G_{08}^S(n_4) = & -\frac{1}{3} \sum_{j=1,2,3} \sum_{\vec{n}} \left\langle V_{0,j,\text{RI}}^S(n) V_{8,j,\text{RI}}^1(0) \right\rangle = \\
 & -\frac{1}{3} \sum_{j=1,2,3} \sum_{\vec{n}} Z_V^{(8)} \left(\left\langle V_{0,j}^S(n) V_{8,j}^1(0) \right\rangle + \right. \\
 & \left. + ac_V^1 \left\langle V_{0,j}^S(n) \partial_4 \Sigma_{8,j4}^1(0) \right\rangle + ac_V^S \left\langle \partial_4 \Sigma_{0,j4}^1(0) V_{8,j}^1(0) \right\rangle \right) + \\
 & -\frac{1}{3} \sum_{j=1,2,3} \sum_{\vec{n}} Z_V^{(80)} \left\langle V_{0,j}^S(n) V_{0,j}^1(0) \right\rangle. \quad (6.25)
 \end{aligned}$$

The renormalisation coefficients of $V_{0,\mu,\text{RI}}^1(n)$ are not known. Therefore, we only include eq. (6.25) in our analysis, where the symmetric, point-split discretisation is used instead. In the extrapolation to the physical point, explained in chapter 12, we will see that using a single discretisation is more than sufficient.

To compute eqs. (6.19) to (6.25), we need to swap the position of the derivative ∂_4 to the operator in the sink, which contains the time dependence, and move the tensor current to the source, because we have no data with the tensor current at the sink. However, we only have two types of terms in need of modification, with forms $\langle V_{i,\mu}^d(n) \partial_4 \Sigma_{i',\nu 4}^{d'}(m) \rangle$ and $\langle \partial_4 \Sigma_{i,\mu 4}^d(n) V_{i',\nu}^{d'}(m) \rangle$. To accomplish our objective, we use translation invariance and the properties of the vector and tensor currents under time reversal. For mesonic two-point functions with PBC, translation invariance implies

$$\langle \mathcal{O}(x) \mathcal{O}(y) \rangle = \langle \mathcal{O}(x + \Delta) \mathcal{O}(y + \Delta) \rangle. \quad (6.26)$$

Equation (6.26) is always exact for the spatial coordinates of all ensembles and for the temporal direction in those ensembles with PBC. In the case of OBC, eq. (6.26) is corrected by boundary states exponentially suppressed with the time separation to the boundary (see section 3.4.4). Therefore, placing the correlator sources on the bulk of the lattice allows to isolate this contamination and preserve eq. (6.26) there. Let us first see how to shift the lattice derivative to the sink,

$$\begin{aligned} \langle V_{i,\mu}^d(n) \partial_4 \Sigma_{i',\nu 4}^{d'}(m) \rangle &= \frac{1}{2a} \langle V_{i,\mu}^d(n) \Sigma_{i',\nu 4}^{d'}(m + a\hat{4}) - V_{i,\mu}^d(n) \Sigma_{i',\nu 4}^{d'}(m - a\hat{4}) \rangle \\ &= \frac{1}{2a} \langle V_{i,\mu}^d(n - a\hat{4}) \Sigma_{i',\nu 4}^{d'}(m) - V_{i,\mu}^d(n + a\hat{4}) \Sigma_{i',\nu 4}^{d'}(m) \rangle \\ &= - \langle \partial_4 V_{i,\mu}^d(n) \Sigma_{i',\nu 4}^{d'}(m) \rangle, \end{aligned} \quad (6.27)$$

where we have used the definition of the symmetric derivative and eq. (6.26). The other property that we have to take into account is the symmetry, under time reversal, of the vector and tensor currents. The former is symmetric and the latter is antisymmetric [29]. Then, vector-tensor and vector-vector two-point functions transform under time reversal in the following way,

$$\begin{aligned} \langle V_{i,\mu}^d(n) \Sigma_{i',\nu 4}^{d'}(m) \rangle &= - \langle \Sigma_{i',\nu 4}^{d'}(\vec{m}, n_4) V_{i,\mu}^d(\vec{n}, m_4) \rangle, \\ \langle V_{i,\mu}^d(n) V_{i',\nu}^{d'}(m) \rangle &= \langle V_{i',\nu}^{d'}(\vec{m}, n_4) V_{i,\mu}^d(\vec{n}, m_4) \rangle. \end{aligned} \quad (6.28)$$

Using eq. (6.28), we can modify terms of the form

$$\begin{aligned} \langle \partial_4 \Sigma_{i,\mu 4}^d(n) V_{i',\nu}^{d'}(m) \rangle &= \frac{1}{2a} \langle \Sigma_{i,\mu 4}^d(n + a\hat{4}) V_{i',\nu}^{d'}(m) - \Sigma_{i,\mu 4}^d(n - a\hat{4}) V_{i',\nu}^{d'}(m) \rangle \\ &= \frac{1}{2a} \langle -V_{i',\nu}^{d'}(\vec{m}, n_4 + a) \Sigma_{i,\mu 4}^d(\vec{n}, m_4) + V_{i',\nu}^{d'}(\vec{m}, n_4 - a) \Sigma_{i,\mu 4}^d(\vec{n}, m_4) \rangle \\ &= - \langle \partial_4 V_{i',\nu}^{d'}(\vec{m}, n_4) \Sigma_{i,\mu 4}^d(\vec{n}, m_4) \rangle. \end{aligned} \quad (6.29)$$

Then, the renormalised, $\mathcal{O}(a)$ -improved two-point functions we compute change to

$$G_{33}^S(n_4) = -\frac{1}{3} \sum_{j=1,2,3} \sum_{\vec{n}} Z_V^{(3)} \times \\ \times \left(\left\langle V_{3,j}^S(n) V_{3,j}^1(0) \right\rangle - ac_V^1 \partial_4 \left\langle V_{3,j}^S(n) \Sigma_{3,j4}^1(0) \right\rangle - ac_V^S \partial_4 \left\langle V_{3,j}^1(n) \Sigma_{3,j4}^1(0) \right\rangle \right), \quad (6.30)$$

$$G_{33}^1(n_4) = -\frac{1}{3} \sum_{j=1,2,3} \sum_{\vec{n}} \left(Z_V^{(3)} \right)^2 \left(\left\langle V_{3,j}^1(n) V_{3,j}^1(0) \right\rangle - 2ac_V^1 \partial_4 \left\langle V_{3,j}^1(n) \Sigma_{3,j4}^1(0) \right\rangle \right), \quad (6.31)$$

$$G_{88}^S(n_4) = -\frac{1}{3} \sum_{j=1,2,3} \sum_{\vec{n}} Z_V^{(8)} \times \\ \times \left(\left\langle V_{8,j}^S(n) V_{8,j}^1(0) \right\rangle - ac_V^1 \partial_4 \left\langle V_{8,j}^S(n) \Sigma_{8,j4}^1(0) \right\rangle - ac_V^S \partial_4 \left\langle V_{8,j}^1(n) \Sigma_{8,j4}^1(0) \right\rangle \right) \\ - \frac{1}{3} \sum_{j=1,2,3} \sum_{\vec{n}} Z_V^{(80)} \left\langle V_{8,j}^S(n) V_{0,j}^1(0) \right\rangle, \quad (6.32)$$

$$G_{88}^1(n_4) = -\frac{1}{3} \sum_{j=1,2,3} \sum_{\vec{n}} \left(Z_V^{(8)} \right)^2 \times \\ \times \left(\left\langle V_{8,j}^1(n) V_{8,j}^1(0) \right\rangle - 2ac_V^1 \partial_4 \left\langle V_{8,j}^1(n) \Sigma_{8,j4}^1(0) \right\rangle \right) \\ - \frac{2}{3} \sum_{j=1,2,3} \sum_{\vec{n}} Z_V^{(8)} Z_V^{(80)} \left(\left\langle V_{8,j}^1(n) V_{0,j}^1(0) \right\rangle \right), \quad (6.33)$$

$$G_{08}^S(n_4) = -\frac{1}{3} \sum_{j=1,2,3} \sum_{\vec{n}} Z_V^{(8)} \times \\ \times \left(\left\langle V_{0,j}^S(n) V_{8,j}^1(0) \right\rangle - ac_V^1 \partial_4 \left\langle V_{0,j}^S(n) \Sigma_{8,j4}^1(0) \right\rangle - ac_V^S \partial_4 \left\langle V_{8,j}^1(n) \Sigma_{0,j4}^1(0) \right\rangle \right) \\ - \frac{1}{3} \sum_{j=1,2,3} \sum_{\vec{n}} Z_V^{(80)} \left\langle V_{0,j}^S(n) V_{0,j}^1(0) \right\rangle. \quad (6.34)$$

Now, to compute every expectation value in terms of its flavour content, we need to Wick-contract the quark fields $\psi_f, \bar{\psi}_f$ of the same flavour [219]. There are two types of Wick contractions, quark-connected and quark-disconnected. The former can be represented by a connected Feynman diagram of quark fields, while the latter cannot. Bare in mind the quarks are submerged in a background field of gluons that may connect the different 1PI pieces of a quark-disconnected diagram. The isovector lacks any disconnected contribution, because the u - and d -quarks are mass degenerate and the relative sign between both components cancel each other. For this thesis, we do not consider charm loops because we do not expect them to be discernible at our level of precision. As an example, for the

correlator $\langle V_{8,\mu}^1(n) V_{8,\nu}^1(0) \rangle$, we substitute $V_{8,\mu}^1(n)$ and $V_{8,\nu}^1(0)$ by their flavour content using eqs. (6.1) and (6.9) and compute its Wick contractions as

$$\begin{aligned} \langle V_{8,\mu}^1(n) V_{8,\nu}^1(0) \rangle_{\text{q-con}} &= \frac{1}{12} \left(\left\langle \overline{\psi}_u(n) \gamma_\mu \psi_u(n) \overline{\eta}_u(0) \gamma_\nu \eta_u(0) \right\rangle_{\text{G}} + \right. \\ &\quad + \left\langle \overline{\psi}_d(n) \gamma_\mu \psi_d(n) \overline{\eta}_d(0) \gamma_\nu \eta_d(0) \right\rangle_{\text{G}} + \\ &\quad + 4 \left\langle \overline{\psi}_s(n) \gamma_\mu \psi_s(n) \overline{\eta}_s(0) \gamma_\nu \eta_s(0) \right\rangle_{\text{G}} \Big) = \\ &\quad \frac{1}{6} \left\langle \left(\text{Tr}_{\text{DC}} \left[D_\ell^{-1}(n, 0) \gamma_\mu D_\ell^{-1}(0, n) \gamma_\nu \right] \right. \right. \\ &\quad \left. \left. + 2 \text{Tr}_{\text{DC}} \left[D_s^{-1}(n, 0) \gamma_\mu D_s^{-1}(0, n) \gamma_\nu \right] \right) \right\rangle_{\text{G}}, \end{aligned} \quad (6.35)$$

where the traces operate on colour and Dirac space, $D_\ell^{-1}(n, 0)$ is the propagator with source in 0 and sink in n for the light quark, the subscript G refers to the gauge expectation value, eq. (3.33), and q-con indicates this is only the quark-connected contribution. The quark-disconnected contribution is computed in a similar way,

$$\begin{aligned} \langle V_{8,\mu}^1(n) V_{8,\nu}^1(0) \rangle_{\text{q-dis}} &= \frac{1}{3} \left\langle \text{Tr}_{\text{DC}} \left[\left(D_\ell^{-1}(n, n) - D_s^{-1}(n, n) \right) \gamma_\mu \right] \times \right. \\ &\quad \left. \times \text{Tr}_{\text{DC}} \left[\left(D_\ell^{-1}(0, 0) - D_s^{-1}(0, 0) \right) \gamma_\nu \right] \right\rangle_{\text{G}}. \end{aligned} \quad (6.36)$$

The combination in eq. (6.36) is known as $\ell - s$, $\ell - s$ and we refer to it in this way in the following. The other quark-disconnected piece appears in the correlator $\langle V_{0,\mu}^d(n) V_{8,\nu}^d(0) \rangle$. For the local discretisation we have

$$\begin{aligned} \langle V_{0,\mu}^1(n) V_{8,\nu}^1(0) \rangle_{\text{q-dis}} &= \left\langle \text{Tr}_{\text{DC}} \left[\left(2D_\ell^{-1}(n, n) + D_s^{-1}(n, n) \right) \gamma_\mu \right] \right. \\ &\quad \left. \times \text{Tr}_{\text{DC}} \left[\left(D_\ell^{-1}(0, 0) - D_s^{-1}(0, 0) \right) \gamma_\nu \right] \right\rangle_{\text{G}}. \end{aligned} \quad (6.37)$$

In the following, we refer to the structure in eq. (6.37) as $2\ell + s$, $\ell - s$. The Wick contractions affect the quark fields but not the γ -structure and, therefore, one finds similar expressions for the improvement terms, different isospins and discretisations. Then, it is possible to express the flavour content of $G_{33}^d(n_4)$, $G_{88}^d(n_4)$ and $G_{08}^d(n_4)$ in a succinct manner,

$$\begin{aligned} G_{33}^d(n_4) &= \frac{1}{2} C_{(\ell,\ell)}^d(n_4), \\ G_{88}^d(n_4) &= \frac{1}{6} \left(C_{(\ell,\ell)}^d(n_4) + 2C_{(s,s)}^d(n_4) + 2D_{(\ell-s,\ell-s)}^d(n_4) \right), \\ G_{08}^d(n_4) &= \frac{1}{2\sqrt{3}} \left(C_{(\ell,\ell)}^d(n_4) - C_{(s,s)}^d(n_4) + D_{(2\ell+s,\ell-s)}^d(n_4) \right). \end{aligned} \quad (6.38)$$

In eq. (6.38), a term $C_{(f,f')}^1(n_4)$ indicates a quark-connected contribution

$$\left\langle \text{Tr}_{\text{DC}} \left[D_f^{-1}(n, 0) \gamma_\mu D_{f'}^{-1}(0, n) \gamma_\nu \right] \right\rangle_{\text{G}}, \quad (6.39)$$

with renormalisation and improvement, summed over spatial coordinates and averaged over polarisations. In a similar fashion, the disconnected pieces $D_{(\ell-s, \ell-s)}^1(n_4)$ and $D_{(2\ell+s, \ell-s)}^1(n_4)$ refer to the terms in eqs. (6.36) and (6.37), respectively, without the prefactor $1/3$, but including renormalisation, improvement, summation over spatial coordinates and averaged over polarisations. Equation (6.38) contains some important information. First, as already mentioned, the isovector contribution $G_{33}^d(n_4)$ only contains quark-connected pieces of the light flavour. Second, the 08 component vanishes at the $SU(3)_f$ -symmetric point, where $M_\pi = M_K$, where the light and strange contributions cancel each other and the disconnected piece also vanishes due to the factor in the second line of eq. (6.37). For the isoscalar component, at the $SU(3)_f$ -symmetric point, the disconnected piece cancels for the same reason and $G_{33}^1(n_4) = G_{88}^1(n_4)$, $G_{33}^S(n_4) = G_{88}^S(n_4)$.

The correlators $G_{\gamma\gamma}^d(n_4)$ and $G_{Z\gamma}^d(n_4)$ can be written in terms of the isospin components of eqs. (6.30) to (6.34) plus the charm contribution as

$$\begin{aligned} G_{\gamma\gamma}^d(n_4) &= G_{33}^d(n_4) + \frac{1}{3}G_{88}^d(n_4) + \frac{4}{9}C_{(c,c)}^d(n_4), \\ G_{Z\gamma}^d(n_4) &= \left(\frac{1}{2} - \sin^2 \theta_W\right) G_{\gamma\gamma}^d(n_4) - \frac{1}{6\sqrt{3}}G_{08}^d(n_4) - \frac{1}{18}C_{(c,c)}^d(n_4). \end{aligned} \quad (6.40)$$

6.2 The time-momentum representation

Before explaining the implementation of the various vector-meson correlators in eq. (6.40) that we need to compute $\hat{\Pi}_{\gamma\gamma}$ and $\hat{\Pi}_{Z\gamma}$, we establish the connection between $\hat{\Pi}_{\gamma\gamma}(Q^2)$ in eq. (4.9), $\hat{\Pi}_{Z\gamma}(Q^2)$ in eq. (5.10), and these vector correlation functions. As we have seen in eq. (4.14), the vacuum polarisation and the vector correlator are related via Fourier transformation. The LHS of eq. (4.9) can be replaced using the explicit tensor structure of $\Pi_{\mu\nu}$, given in eq. (4.3) for the Minkowski metric $(+, -, -, -)$. In particular for zero 3-momentum $q_1 = q_2 = q_3 = 0$ and arbitrary energy q_0 , we can use eq. (4.3) to know that $\Pi_{00} = 0$, $\Pi_{\mu\nu} = 0$ for $\mu \neq \nu$, and only $\Pi_{11} = \Pi_{22} = \Pi_{33} \neq 0$. In fact, since there is no preferred polarisation, it is possible to average over the three of them to improve the statistical precision. Then, one can relate the VPF and the vector correlators defined in section 6.1, which are integrated over the spatial components and averaged over the $\mu = 1, 2, 3$ polarisations. Using the Minkowski metric $(+, -, -, -)$ [220], their relation is

$$\Pi(q^2) = \frac{1}{q^2} \int_{-\infty}^{\infty} dx_0 e^{-iq_0 x_0} G(x_0). \quad (6.41)$$

Since we work with the sVPF, we have to find Π at small energies and subtract it from eq. (6.41). In particular, $\exp(-iq_0 x_0)$ is expanded in a Taylor series for $q_0 \rightarrow 0$ [220]

$$\Pi(q^2) \approx \frac{1}{q^2} \int_{-\infty}^{\infty} dx_0 G(x_0) - \frac{1}{2} \int_{-\infty}^{\infty} dx_0 x_0^2 G(x_0) + \dots \quad (6.42)$$

CLS	$Z_V^{(3)}$	$Z_V^{(8)}$	$Z_V^{(80)}$	$Z_V^{(c)}$	c_V^S	c_V^I
H101	0.71540(17)	0.71540(17)	0.00000(0)	1.20324(27)	0.418(11)	-0.031(15)
H102	0.71211(17)	0.71869(18)	-0.00380(3)	1.19743(21)	0.418(11)	-0.031(15)
H105	0.70883(17)	0.72197(20)	-0.00758(6)	1.18964(17)	0.418(11)	-0.031(15)
N101	0.70883(18)	0.72197(20)	-0.00758(6)	1.18964(17)	0.418(11)	-0.031(15)
C101	0.70696(17)	0.72384(20)	-0.00974(8)	1.18500(11)	0.418(11)	-0.031(15)
B450	0.72645(7)	0.72645(7)	0.00000(0)	1.12972(16)	0.419(11)	-0.030(14)
S400	0.72355(8)	0.72935(8)	-0.00335(3)	1.11159(22)	0.419(11)	-0.030(14)
N451	0.72116(8)	0.73174(9)	-0.00611(5)	1.11412(20)	0.419(11)	-0.030(14)
D450	0.71918(9)	0.73372(10)	-0.00840(7)	1.10790(21)	0.419(11)	-0.030(14)
H200	0.74030(6)	0.74030(6)	0.00000(0)	1.04843(20)	0.421(11)	-0.029(14)
N202	0.74030(6)	0.74030(6)	0.00000(0)	1.04843(54)	0.421(11)	-0.029(14)
N203	0.73787(6)	0.74272(7)	-0.00280(2)	1.04534(20)	0.421(11)	-0.029(14)
N200	0.73605(6)	0.74454(7)	-0.00490(3)	1.04012(13)	0.421(11)	-0.029(14)
D200	0.73424(6)	0.74636(8)	-0.00700(4)	1.03587(12)	0.421(11)	-0.029(14)
E250	0.73324(7)	0.74735(9)	-0.00815(5)	1.03310(10)	0.421(11)	-0.029(14)
N300	0.75912(6)	0.75912(6)	0.00000(0)	0.97722(12)	0.425(11)	-0.028(13)
N302	0.75722(6)	0.76102(6)	-0.00220(2)	0.97241(11)	0.425(11)	-0.028(13)
J303	0.75547(6)	0.76277(7)	-0.00422(3)	0.96037(22)	0.425(11)	-0.028(13)
E300	0.75428(7)	0.76396(7)	-0.00559(4)	0.96639(2)	0.425(11)	-0.028(13)

Table 6.1: Mass-dependent renormalisation factors and improvement coefficients. $Z_V^{(3)}$, $Z_V^{(8)}$ and $Z_V^{(80)}$ are obtained from the Padé fits in [212], and $Z_V^{(c)}$ are published in [218]. The improvement coefficients c_V^I and c_V^S are defined in eq. (6.12) and taken from [212].

Subtracting eq. (6.42) from eq. (6.41) we obtain the sVPF [220],

$$\hat{\Pi}(q^2) = \int_{-\infty}^{\infty} dx_0 G(x_0) \left(\frac{e^{-iq_0 x_0} - 1}{q^2} + \frac{x_0^2}{2} \right). \quad (6.43)$$

Equation (6.43) can be simplified because the mesonic correlator $G(x_0)$ is even under time reversal. Using the relation $\exp(-iq_0 x_0) = \cos q_0 x_0 - i \sin q_0 x_0$, and knowing $\sin q_0 x_0$ is odd under time reflection, the imaginary part of the integral vanishes and we are left with [220]

$$\begin{aligned} \hat{\Pi}(q^2) &= 2 \int_0^{\infty} dx_0 G(x_0) \left(\frac{x_0^2}{2} - \frac{1 - \cos q_0 x_0}{q^2} \right) \\ &= \frac{1}{q^2} \int_0^{\infty} dx_0 G(x_0) \left(q^2 x_0^2 - 4 \sin^2 \frac{q_0 x_0}{2} \right). \end{aligned} \quad (6.44)$$

Equation (6.44) is the so-called time-momentum representation (TMR) in the continuum. Finally, adapting eq. (6.44) to a discrete lattice in Euclidean space with $Q_\mu = (0, 0, 0, Q_4)$,

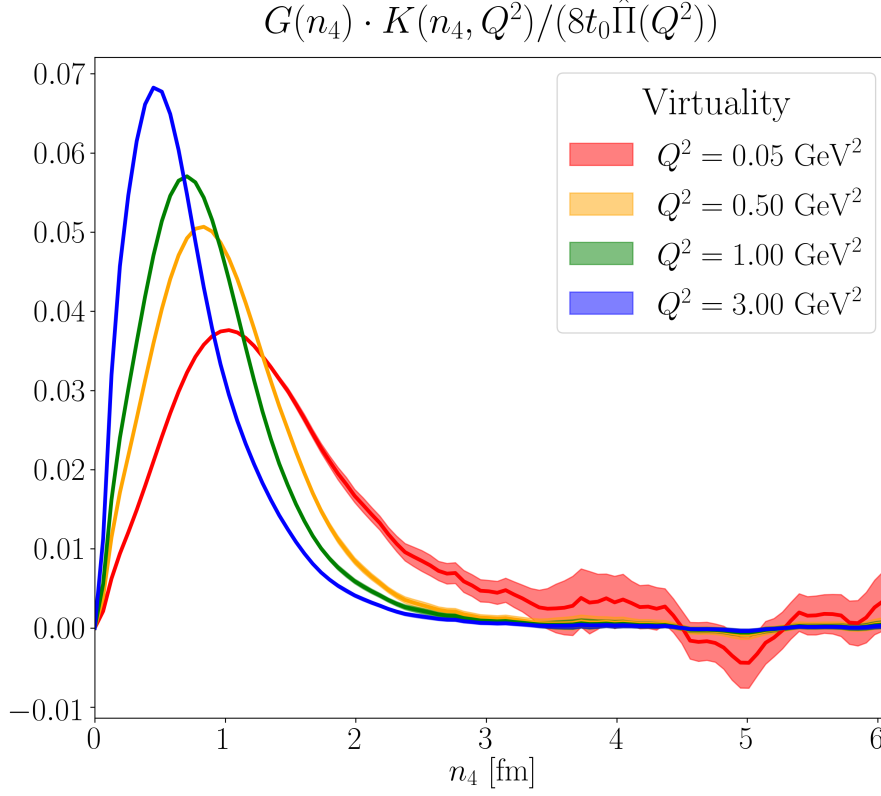


Figure 6.1: Integrand of the sVPF in eq. (6.45) normalised by the result of the integral at various virtualities Q^2 .

we obtain the relation we were looking for [220, 221],

$$\begin{aligned}\hat{\Pi}(Q^2) &= a \sum_{n_4=0}^{N_T} G(n_4) K(n_4, Q^2), \\ K(n_4, Q^2) &= \frac{1}{Q^2} \left(Q^2 n_4^2 - 4 \sin^2 \left(\frac{Q_4 n_4}{2} \right) \right),\end{aligned}\tag{6.45}$$

Both, eqs. (6.44) and (6.45), are valid for $\hat{\Pi}_{\gamma\gamma}$ and $\hat{\Pi}_{Z\gamma}$. Before moving on, let us remark that in eq. (6.45) any Q^2 may be input to the kernel, but our ensemble's size and lattice spacing limit the range of virtualities that we can reliably compute. Looking to fig. 6.1, where we plot the normalised integrand of eq. (6.45) for ensemble E250, the kernel weights the correlator depending on the energy input. On the one hand, $Q^2 \sim (\pi/a)^2 \gg 1 \text{ GeV}^2$ emphasizes the correlator at short distances, which are affected by strong cut-off effects. On the other hand, $Q^2 \ll 1 \text{ GeV}^2$ highlights long distances, where the signal-to-noise ratio problem dominates the lattice data. These two features, the signal-to-noise ratio and the ultraviolet cut-off effects, will be discussed in length in chapter 9 and chapter 12, respectively.

Chapter 7

Implementation of the mesonic two-point functions

In this chapter, we explain how the flavour components of the vector correlators $G_{\gamma\gamma}$ and $G_{Z\gamma}$ were computed. Section 7.1 details the computation of the quark-connected contributions $C_{(f,f')}^d(n_4)$ to eq. (6.38), while section 7.2 contains the methods for the quark-disconnected pieces $D_{(f,f')}^d(n_4)$. Afterwards, section 7.3 presents some basic information about the specific set of CLS ensembles that we used in our analysis. The implementation of the methods described in this chapter was not carried out by the author of this thesis but by other members of the Mainz group in the context of the computation of the anomalous magnetic moment of the muon [218], which also requires the vector-meson correlator.

7.1 Quark-connected two-point functions

We are interested in computing two-point functions with the general form [29]

$$\langle O_2(n)O_1(m) \rangle, \quad (7.1)$$

where, e.g., $O_1(m)$ creates states with specific quantum numbers from the vacuum and $O_2(n)$ annihilates them. In particular, we have to compute vector-vector and vector-tensor correlation functions, which require the operators

$$V_{f,\mu}(n) = \bar{\psi}_f(n)\gamma_\mu\psi_f(n), \quad \Sigma_{f,\mu\nu}(n) = \bar{\psi}_f(n)\sigma_{\mu\nu}\psi_f(n). \quad (7.2)$$

First, we project eq. (7.1) to a state with a well-defined 3-momentum. To do this, we employ the Fourier transformation and its inverse [29]

$$\begin{aligned} \tilde{O}(\bar{p}, n_4) &= \frac{1}{\sqrt{|\Lambda_{123}|}} \sum_{\bar{n} \in \Lambda_3} O(\bar{n}, n_4) e^{-ia\bar{n}\bar{p}}, \\ O(\bar{n}, n_4) &= \frac{1}{\sqrt{|\Lambda_{123}|}} \sum_{\bar{p} \in \Lambda_3} \tilde{O}(\bar{p}, n_4) e^{+ia\bar{n}\bar{p}}, \end{aligned} \quad (7.3)$$

where $|\Lambda_{123}| = N_1 N_2 N_3$ is the number of spatial lattice sites, and the sum only runs over the spatial directions [29]

$$\Lambda_{123} = \{\bar{n} = (n_1, n_2, n_3) | n_i = 0, 1, \dots, N_L - 1\}, \quad (7.4)$$

where N_L is the number of lattice sites on any spatial direction. The components of the spatial momentum are

$$p_i = \frac{2\pi k_i}{aN_L}, \quad k_i = -\frac{N_L}{2} + 1, \dots, \frac{N_L}{2}. \quad (7.5)$$

We do not need to consider the phases in eq. (7.3) though, because we have seen in section 6.2 that we only require the two-point function projected to $\bar{p} = 0$. Then, the generic two-point function eq. (7.1) at zero three-momentum is [57, 29]

$$\begin{aligned} \langle \tilde{O}_2(\vec{p} = 0, n_4) \tilde{O}_1(\vec{q} = 0, m_4) \rangle &= \frac{1}{|\Lambda_{123}|} \sum_{\bar{n}, \bar{m}} \langle O_2(\bar{n}, n_4) O_1(\bar{m}, m_4) \rangle \\ &= \sum_{\bar{n} - \bar{m}} \langle O_2(\bar{n} - \bar{m}, n_4) O_1(\bar{0}, m_4) \rangle \\ &= \sum_{\bar{r}} \langle O_2(\bar{r}, n_4) O_1(\bar{0}, m_4) \rangle. \end{aligned} \quad (7.6)$$

In the first equality, we have used the property of translation invariance in the spatial directions, eq. (6.26), adding $-\bar{m}$ to both positions. The sum over the origin yields a factor $|\Lambda_{123}|$. In the second equality, we rename $\bar{n} - \bar{m}$ as simply \bar{r} . An important consequence of eq. (7.6) is that we only need to compute the correlation function between the origin and any other location on the lattice, rather than computing the propagator for any two given points. The former is known as the one-to-all correlation function, while the latter is called the all-to-all propagator.

7.1.1 Point sources

From Wick's theorem, given in eq. (3.33), we know that the main object we require to compute eq. (7.1) is the fermion propagator between two points, $D^{-1}(n, m)$, which details the relation between the lattice sites m and n . The Dirac operator $D(n, m)$, for instance the Wilson-Dirac operator in eq. (3.8), is a matrix of dimensions $12|\Lambda| \times 12|\Lambda|$, approximately $\mathcal{O}(10^9) \times \mathcal{O}(10^9)$ in our ensembles. However, even if $D(n, m)$ is sparse, its inverse will not be. Therefore, an exact calculation of the propagator is unfeasible. Nonetheless, we see from eq. (7.6) that we only need to compute one column of $D^{-1}(n, m)$, connecting the origin to every other point. To do this, the so-called point source in Euclidean, Dirac and colour space is introduced [29]

$$\eta^{(m_0, \alpha_0, a_0)}(m)_a = \delta(m - m_0) \delta_{\alpha\alpha_0} \delta_{aa_0}. \quad (7.7)$$

where m , α , and a are given. Using eq. (7.7), the solution Ψ of the inhomogeneous Dirac equation for a generic point source is defined as [29]

$$D(n, m) \Psi^{(m_0, \alpha_0, a_0)}(m) = \eta^{(m_0, \alpha_0, a_0)}(n). \quad (7.8)$$

The inversion of the Dirac operator is performed using the DFL + SAP + GCR solver [222, 223, 224] from the openQCD package [126]. Once the Dirac propagator between m_0 and n is already computed, it is possible to use γ_5 -hermiticity to obtain the propagator from n to m_0 , which is required for the mesonic two-point functions [29],

$$(\gamma_5)_{\alpha\alpha'} D^{-1}(m_0, n)_{\alpha'\beta'}^\dagger (\gamma_5)_{\beta'\beta} = D^{-1}(n, m_0)_{\beta\alpha} \quad (7.9)$$

Then, let us suppose that we want to compute the vector-vector two-point function projected to zero 3-momentum, eq. (7.6). Then, one needs to Wick contract the fermion fields for the polarisations $j, k = 1, 2, 3$,

$$\begin{aligned} \langle V_j(n) V_k^\dagger(m) \rangle &= \langle \bar{\psi}(n) \gamma_j \psi(n) \bar{\psi}(m) \gamma_k \psi(m) \rangle = \left\langle \overline{\bar{\psi} \gamma_j \psi \bar{\psi} \gamma_k \psi} \right\rangle_G \\ &= - \left\langle \text{tr}_{\text{CD}} \left(D^{-1}(m, n) \gamma_j D^{-1}(n, m) \gamma_k \right) \right\rangle_G, \end{aligned} \quad (7.10)$$

where $V_j^\dagger(m)$ creates the vector-meson state, and $\bar{\psi} = \psi^\dagger \gamma_4$. Next, one should apply γ_5 -hermiticity, eq. (7.9), to have only the propagator from the lattice point m to n ,

$$\langle V_j(n) V_k^\dagger(m) \rangle = - \left\langle \text{tr}_{\text{CD}} \left(\gamma_5 D^{-1}(n, m)^\dagger \gamma_5 \gamma_j D^{-1}(n, m) \gamma_k \right) \right\rangle_G. \quad (7.11)$$

Finally, point sources are introduced at the origin, such that it is possible to compute the point-to-all propagator for zero 3-momentum eq. (7.6),

$$\langle \tilde{V}_j(n_4) \tilde{V}_k^\dagger(0) \rangle = - \sum_{\vec{n}} \left\langle \text{tr}_{\text{CD}} \left(\gamma_5 \Psi^{(0, \alpha_0, a_0)}(n)^\dagger \gamma_5 \gamma_j \Psi^{(0, \alpha_0, a_0)}(n) \gamma_k \right) \right\rangle_G. \quad (7.12)$$

To compute eq. (7.12) for a specific flavour, twelve point sources are needed, one per combination of colour and Dirac index. This means that the inhomogeneous Dirac equation has to be solved twelve times to obtain the associated fermion propagator. For a given configuration, and assuming time-translation invariance, it is possible to locate sources at various time locations to enhance the signal. Time-translation invariance is exact only for periodic boundary conditions, while for open boundary conditions it is valid in the bulk of the lattice up to exponentially suppressed effects from the boundaries. For different configurations, it is possible to choose different time-slices to decorrelate them. For the CLS ensembles included in this analysis, all quark-connected contributions use point sources randomly distributed in space, and located in the center of the lattice in the time direction, $N_T/2$ [218]. The exception is E250, which uses stochastic sources.

7.1.2 Stochastic sources

A different option to compute expectation values is to introduce a set of N_S stochastic sources with the basic properties [225]

$$\begin{aligned} \left\langle \eta(n)_a^\alpha \right\rangle_S &\equiv \lim_{N_S \rightarrow \infty} \frac{1}{N_S} \sum_{i=1}^{N_S} \eta_i(n)_a^\alpha = 0, \quad \forall(n, \alpha, a), \\ \left\langle \eta(n)_a^\alpha \eta(m)_b^\dagger \right\rangle_S &= \delta_{nm} \delta_{\alpha\beta} \delta_{ab}. \end{aligned} \quad (7.13)$$

Each noise component $\eta_i(n)_a^\alpha$ can be drawn from a set of different distributions \mathcal{D} that fulfil eq. (7.13). One possibility is to use the cyclic group \mathbb{Z}_2 [226],

$$\eta_i(n)_a^\alpha \in \mathcal{D} = \{\pm 1\}. \quad (7.14)$$

or the combination $\mathbb{Z}_2 \otimes i\mathbb{Z}_2$ [227],

$$\eta_i(n)_a^\alpha \in \mathcal{D} = \left\{ \frac{1}{2} (\pm 1 \pm i) \right\}. \quad (7.15)$$

However, in the case of ensemble E250, we employ the unit circle $U(1)$,

$$\eta_i(n)_a^\alpha \in \mathcal{D} = e^{i\phi}, \quad \phi \in [0, 2\pi), \quad (7.16)$$

such that every noise component is a random phase. Both \mathbb{Z}_2 and $U(1)$ noise are seen to minimize the uncertainty introduced by the noise vectors [226].

After selecting the source type, one needs to solve the inhomogeneous Dirac equation

$$\sum_n D(m, n)_{\beta\alpha} \Psi_i(n)_a^\alpha = \eta_i(m)_\beta. \quad (7.17)$$

The fermion propagator can be written in the following way. Multiplying eq. (7.17) by $\eta_i(r)_\gamma^\dagger$ from the right and taking the average over the stochastic sources yields [55]

$$\sum_n \left\langle D(m, n)_{\beta\alpha} \Psi(n)_a^\alpha \eta(r)_\gamma^\dagger \right\rangle_S = \left\langle \eta(m)_\beta \eta(r)_\gamma^\dagger \right\rangle_S = \delta_{m,r} \delta_{\beta\gamma} \delta_{bc}. \quad (7.18)$$

Then, eq. (7.18) indicates that the inverse of the Dirac operator can be computed as

$$D^{-1}(n, m)_{\alpha\beta} = \left\langle \Psi(n)_a^\alpha \eta(m)_b^\dagger \right\rangle_S. \quad (7.19)$$

The simplest use of stochastic sources consists on substituting every propagator via eq. (7.19). For a two-point function with a generic Γ -structure [225],

$$\begin{aligned} \langle O_1(n) O_2(m) \rangle &= - \left\langle \text{tr}_{\text{CD}} \left(D^{-1}(n, m) \Gamma_1 D^{-1}(m, n) \Gamma_2 \right) \right\rangle_G \\ &= - \left\langle \text{tr}_{\text{CD}} \left(\left\langle \Psi(n) \eta(m)^\dagger \right\rangle_S \Gamma_1 \left\langle \Psi(m)' (\eta(n)')^\dagger \right\rangle_{S'} \Gamma_2 \right) \right\rangle_G \end{aligned} \quad (7.20)$$

A different set of sources is used for every propagator. The drawback of eq. (7.20) is that it adds a large stochastic noise, due to the limited statistics of the sources, on top of the initial gauge noise, which comes from the number of gauge configurations [228].

There is a better alternative when the correlator is diagonal in Dirac space, e.g., for a pseudo-scalar $\Gamma = \gamma_5$ or a scalar current $\Gamma = \mathbf{1}$. It is possible to compute stochastically the two-point function using only one single random source distributed over all colour and Dirac components within one time-slice [225]. In particular, for the pseudo-scalar two-point function at zero 3-momentum,

$$\begin{aligned} \langle \tilde{P}(n_4) \tilde{P}^\dagger(0) \rangle &= - \sum_{\vec{n}} \left\langle \text{tr}_{\text{CD}} \left\{ D^{-1}(n, 0) \gamma_5 D^{-1}(0, n) \gamma_5 \right\} \right\rangle_G \\ &= - \sum_{\vec{n}} \left\langle \left\langle \text{tr}_{\text{CD}} \left\{ D^{-1}(n, 0) \eta(0) \eta(0)^\dagger D^{-1}(n, 0)^\dagger \right\} \right\rangle_S \right\rangle_G \quad (7.21) \\ &= - \sum_{\vec{n}} \left\langle \left\langle \text{tr}_{\text{CD}} \left\{ \Psi(n)^\dagger \Psi(n) \right\} \right\rangle_S \right\rangle_G. \end{aligned}$$

In the second line of eq. (7.21), a pair of stochastic sources is introduced using the second property in eq. (7.13), and γ_5 -hermiticity is applied. In the third line, the definition of the solution vectors is used together with the cyclic property of the trace. Comparing with point sources, the number of inversions and thus the numerical effort are reduced by a factor twelve per source. Then, using $N_S = 12$ has the same number of inversions that one point source, but it yields smaller statistical error. This particular use of stochastic sources is known as the one-end trick (OET), introduced in [227, 229].

Unfortunately, the OET can not be applied on the basic object of this study, the vector and tensor currents. Nonetheless, one can generalize the OET using stochastic sources diagonal in Dirac space [225],

$$\eta_i(n)_a^\alpha = \xi_i(n)_a \delta_{\alpha\tau}, \quad \xi_i(n)_a \in \mathcal{D}, \quad (7.22)$$

where τ is given and ξ fulfils

$$\left\langle \xi(n)_a \xi(m)_b^\dagger \right\rangle_\xi = \delta_{nm} \delta_{ab}. \quad (7.23)$$

Since $\eta(n)$ is a stochastic source, it still follows eq. (7.13), but it has only support on a particular spin component τ . The solution vector for every noise component is

$$\Psi_i(n)_a^\alpha = \sum_m D^{-1}(n, m)_{\alpha\beta} \xi(m)_b \delta_{\beta\tau}. \quad (7.24)$$

In this way, it is still possible to introduce one pair of stochastic sources and move one of them using the cyclic property of the trace. For a two-point function with a generic Γ structure and zero 3-momentum,

$$\langle \tilde{O}_1(n_4) \tilde{O}_2(0) \rangle = - \sum_{\vec{n}} \left\langle \left\langle \text{tr}_{\text{CD}} \left\{ \Gamma_1 \gamma_5 \Psi(n)^\dagger \gamma_5 \Gamma_2 \Psi(n) \right\} \right\rangle_S \right\rangle_G. \quad (7.25)$$

This method is known as the generalized one-end trick (gOET) or the linked source method [230]. Again, comparing with point sources the numerical effort is reduced by a factor three, as one needs different sources for every spinor component. For the particular case of pseudo-scalar mesons, where using linked sources is not necessary, the latter were not found to be inferior compared with standard stochastic sources [231, 225].

It is possible to further reduce the noise associated with standard noise vectors. With this aim, it is common to restrict the support of the source vector to individual time-slices, Dirac or colour components. This is the so-called dilution method [232], whose most common variant is time dilution. It consists on locating the source at a particular time-slice m_4 , such that [232]

$$\eta_i(n)_\alpha = \eta_i(\vec{n})_\alpha \delta_{n_4 m_4}. \quad (7.26)$$

The vector correlator in ensemble E250 uses stochastic sources with noise dilution in spin, colour and time [218].

7.1.3 Tuning the charm-quark mass

The lattice action uses a quenched charm-quark. This means that the fermion determinant is set to unity, $\det D_c = 1$, in such a way that the quark sea cannot generate charm quarks. Regarding the two-point functions, the quark-connected charm component is included, while any quark-disconnected effects are neglected. The reasoning behind this is that much more energy is required to generate a pair of charm-anti-charm quarks than a pair of strange-anti-strange quarks, for example. Then, to compute a two-point function of the c -quark, it is necessary to fix the bare quark-mass or, equivalently, the κ_c parameter of the Wilson-Dirac operator in eq. (3.9). The condition that it is imposed on every ensemble [218] is that the mass of the $c\bar{s}$ -meson ground state matches the experimental mass of the D_s meson, $M_{D_s} = 1968.35(7)$ MeV [34]. To achieve this, the ground state mass of the $c\bar{s}$ meson is computed for several values of κ_c using stochastic sources with colour, spin and time dilution [218]. Finally, κ_c can be interpolated linearly to the value corresponding to M_{D_s} . The set of $c\bar{s}$ meson masses used to determine κ_c can be seen in table IX of [218].

After tuning the κ_c parameter, it is necessary to compute $\hat{\Pi}_{cc}$. An extra set of measurements at the correct κ_c is not produced, but rather the closest values $\kappa_{c,1}$, $\kappa_{c,2}$ are taken, and a linear interpolation to κ_c is performed using a Taylor expansion to first order around $\kappa_{c,1}$ [218]. This procedure has been seen to be enough comparing with the result yielded by extra measurements in particular cases [218]. In this way, the sVPF at the correct κ_c is

$$\hat{\Pi}_{cc} = \hat{\Pi}_{cc,1} + \frac{\partial \hat{\Pi}_{cc}}{\partial \kappa_c} (\kappa_c - \kappa_{c,1}), \quad \frac{\partial \hat{\Pi}_{cc}}{\partial \kappa_c} = \frac{\hat{\Pi}_{cc,2} - \hat{\Pi}_{cc,1}}{\kappa_{c,2} - \kappa_{c,1}}. \quad (7.27)$$

The set of values that we use for κ_c , $\kappa_{c,1}$ and $\kappa_{c,2}$ can be found in table 7.1. Besides obtaining the correct sVPF, it is necessary to propagate the uncertainty in the determination of κ_c to the uncertainty of $\hat{\Pi}_{cc}$. The error of the former stems from the precision with which the $c\bar{s}$ meson mass was obtained. Using simple error propagation, the systematic

Ensemble	κ_ℓ	κ_s	κ_i	κ_c	$\kappa_{c,1}$	$\kappa_{c,2}$
H101	0.136760	0.136760	0.133009	0.122897 (18)	0.122908	0.122938
H102	0.136865	0.136549	0.132902	0.123041 (26)	0.123050	0.123080
H105	0.136970	0.136341	0.132812	0.123244 (19)	0.123251	0.123281
N101	0.136970	0.136341	0.132812	0.123244 (19)	0.123251	0.123281
C101	0.137030	0.136222	0.132762	0.123361 (12)	0.123367	0.123397
B450	0.136890	0.136890	0.133738	0.125095 (22)	0.125089	0.125129
S400	0.136984	0.136702	0.133648	0.125252 (20)	0.125267	0.125317
N451	0.137062	0.136548	0.133590	0.125439 (15)	0.125447	0.125477
D450	0.137126	0.136420	0.133540	0.125585 (7)	0.125585	0.125635
H200	0.137000	0.137000	0.134517	0.127579 (16)	0.127626	0.127666
N202	0.137000	0.137000	0.134517	0.127579 (16)	0.127626	0.127666
N203	0.137080	0.136840	0.134439	0.127714 (11)	0.127713	0.127733
N200	0.137140	0.136721	0.134392	0.127858 (7)	0.127859	0.127879
D200	0.137200	0.136602	0.134341	0.127986 (6)	0.127986	0.127956
E250	0.137233	0.136537	0.134312	0.128052 (5)	0.128054	0.128064
N300	0.137000	0.137000	0.135207	0.130099 (18)	0.130099	0.130149
N302	0.137064	0.136872	0.135153	0.130247 (9)	0.130243	0.130263
J303	0.137123	0.136755	0.135098	0.130362 (9)	0.130362	0.130382
E300	0.137163	0.136675	0.135059	0.130432 (10)	0.130421	0.130400

Table 7.1: κ values used on each ensemble, obtained from [218] or from the Mainz group.

error for $\hat{\Pi}_{cc}$ from the determination of κ_c is

$$\sigma_{\hat{\Pi}} = \left| \frac{\partial \hat{\Pi}_{cc}}{\partial \kappa_c} \right| \sigma_{\kappa}. \quad (7.28)$$

In table 7.2, the column $\hat{\Pi}_{cc}$ shows the charm contribution after applying the shift on eq. (7.27) and the corresponding statistical error. The last column details the shift corresponding to the second term on the RHS of $\hat{\Pi}_{cc}$ in eq. (7.27). Finally, the parentheses in the last column show the systematic error eq. (7.28). This uncertainty can be added in quadrature with the statistical error to obtain the total uncertainty. We see that, in some cases, the size of this systematic uncertainty can be similar to the statistical error. However, for some other ensembles, $\kappa_c = \kappa_{c,1}$ and no interpolation is necessary.

7.2 Quark-disconnected two-point functions

The type of quark-disconnected contributions that we need to study can be decomposed in two single-propagator components,

$$t(n) = -\text{tr}_{\text{CD}} \left(\Gamma D^{-1}(n, n) \right). \quad (7.29)$$

The zero three-momentum projection is, using eq. (7.3),

$$\tilde{t}(n_4) = -\frac{1}{\sqrt{|\Lambda_{123}|}} \sum_{\bar{n} \in \Lambda_{123}} \text{tr}_{\text{CD}} \left(\Gamma D^{-1}(n, n) \right). \quad (7.30)$$

In particular, it is necessary to evaluate eq. (7.30) for flavours $f = \ell, s$ and compute the combinations $\ell - s$ and $2\ell + s$, which appear on eqs. (6.36) and (6.37). First, on section 7.2.1, the simplest implementation using stochastic sources is introduced, which it was already discussed in section 7.1.2 for the connected contribution. However, these estimates show a statistical uncertainty proportional to $1/\sqrt{N_s}$ [233], which is insufficient for many observables (like the vector currents considered) when the computational cost is taken into account. Second, on section 7.2.2, a frequency splitting method is introduced where the different flavours of the simulation are computed differently according to their mass. This later algorithm was employed by the Mainz group for all the disconnected data.

7.2.1 Stochastic sources

The stochastic sources introduced in section 7.1.2 allow to compute the all-to-all propagator and, in principal, can be used to compute the quark-disconnected contributions on eq. (7.29). Using the second property on eq. (7.13), it is possible to introduce a set of N_s stochastic sources on eq. (7.30) [29],

$$\tilde{t}(n_4) = -\lim_{N_s \rightarrow \infty} \frac{1}{N_s \sqrt{|\Lambda_{123}|}} \sum_{i=1}^{N_s} \sum_{\bar{n} \in \Lambda_{123}} \text{tr}_{\text{DC}} \left(\eta_i^\dagger \Gamma \Psi_i(n) \right). \quad (7.31)$$

The variance of expectation values using stochastic sources can be divided into two parts [233]: A contribution stems from the finite statistics (gauge noise), while another from the use of stochastic sources themselves (stochastic noise). In the optimal scenario, the noise of the stochastic sources is subdominant, and the uncertainty of the correlation function is determined solely from statistics. Unfortunately, this is not the case, and the noise from random sources can be orders of magnitude larger than the gauge noise [233]. Besides, the standard deviation from the stochastic sources behaves like $\sim 1/\sqrt{N_s}$ [233], which represents a very slow convergence for vector correlators given the computational cost (e.g., see [233]). To see an explicit expression of the variance using stochastic sources and a slightly improved estimate see [233].

7.2.2 Frequency splitting

Let us say that we have a set of fermion propagators $D_1^{-1}, D_2^{-1}, \dots, D_N^{-1}$ with distinct masses $M_1 \leq M_2 \leq \dots \leq M_N$. Then, if we want to compute the trace of a particular flavour, one can add and subtract the propagator of all heavier flavours [233],

$$D_f^{-1} = D_N^{-1} + \left(D_{N-1}^{-1} - D_N^{-1} \right) + \dots + \left(D_f^{-1} - D_{f+1}^{-1} \right). \quad (7.32)$$

The difficult task of computing the single-propagator for a flavour f has been subdivided into the computation of several propagator differences and the single-propagator for the heaviest flavour. To compute eq. (7.29), a variant of the method proposed in [233] is used [234], which combines the OET [229, 225] (usually used with twisted-mass fermions [225, 235, 230], see section 3.1.4), the generalized hopping parameter expansion (gHPE) [236], and hierarchical probing (HProb) [237]. In our particular case, the number of quark flavours is $N = 4$: light, strange, an auxiliary flavour (i) with intermediate mass, and charm [234]. The bare quark mass of the extra flavour is fixed using [234]

$$\frac{1}{\kappa_i} = \frac{1-X}{\kappa_s} + \frac{X}{\kappa_c}, \quad \text{with} \quad X = \frac{1}{4}. \quad (7.33)$$

which has been found to work well for the CLS ensembles.

Generalized hopping parameter expansion

The quark propagator D_N^{-1} for the heaviest flavour is implemented following [233] using a combination of the even-odd decomposition introduced in eq. (3.53) and the hopping parameter expansion (HPE) [29], which expands the Dirac operator in a series of powers of the hopping parameter κ introduced in eq. (3.9). To obtain the inverse of the $\mathcal{O}(a)$ -improved Dirac operator D , one starts from the even-odd block decomposition [233]

$$D = \begin{pmatrix} D_{ee} & D_{eo} \\ D_{oe} & D_{oo} \end{pmatrix}. \quad (7.34)$$

Then, it is possible to invert this expression using a Schur decomposition [73]. Using the fact that D_{ee} and D_{oo} are invertible,

$$D^{-1} = \begin{pmatrix} (D_{ee} - D_{eo}D_{oo}^{-1}D_{oe})^{-1} & 0 \\ 0 & (D_{oo} - D_{oe}D_{ee}^{-1}D_{eo})^{-1} \end{pmatrix} \times \begin{pmatrix} \mathbf{1} & -D_{eo}D_{oo}^{-1} \\ -D_{oe}D_{ee}^{-1} & \mathbf{1} \end{pmatrix}. \quad (7.35)$$

Next, one may simply divide the first matrix into two parts,

$$D^{-1} = \begin{pmatrix} D_{ee}^{-1} & 0 \\ 0 & D_{oo}^{-1} \end{pmatrix} \times \begin{pmatrix} (1 - D_{eo}D_{oo}^{-1}D_{oe}D_{ee}^{-1})^{-1} & 0 \\ 0 & (1 - D_{oe}D_{ee}^{-1}D_{eo}D_{oo}^{-1})^{-1} \end{pmatrix} \times \begin{pmatrix} 1 & -D_{eo}D_{oo}^{-1} \\ -D_{oe}D_{ee}^{-1} & 1 \end{pmatrix}. \quad (7.36)$$

The last two matrices are equivalent to the inverse of a simpler matrix,

$$D^{-1} = \begin{pmatrix} D_{ee} & 0 \\ 0 & D_{oo} \end{pmatrix}^{-1} \begin{pmatrix} 1 & D_{eo}D_{oo}^{-1} \\ D_{oe}D_{ee}^{-1} & 1 \end{pmatrix}^{-1}. \quad (7.37)$$

At this stage, the inverse Dirac operator can be naturally rewritten as

$$D^{-1} = A(1 - H)^{-1}, \quad (7.38)$$

where

$$A = \begin{pmatrix} D_{ee} & 0 \\ 0 & D_{oo} \end{pmatrix}^{-1}, \quad H = \begin{pmatrix} 0 & -D_{eo}D_{oo}^{-1} \\ -D_{oe}D_{ee}^{-1} & 0 \end{pmatrix}. \quad (7.39)$$

Now, the expression of the geometric series may be applied [236],

$$(1 - H)^{-1} (1 - H^{2m}) = \sum_{i=0}^{2m-1} H^i. \quad (7.40)$$

Equations (7.38) and (7.40) together allow to obtain the inverse of D_N [233],

$$D_N^{-1} = M_{2m} + D_N^{-1} H^{2m}, \quad M_{2m} = A \sum_{i=0}^{2m-1} H^i. \quad (7.41)$$

Equation (7.41) is usually referred to as the generalized hopping parameter expansion of D_N because the $\mathcal{O}(a)$ -improvement on the Dirac operator is included [236], while the hopping parameter expansion alone commonly refers to the unimproved case. The expansion in eq. (7.41) has been shown to reduce stochastic noise especially well for heavier masses [238, 239, 240]. The specific number of terms in the hopping expansion, m , and the number of quarks N employed in eq. (7.41) depend, among other factors [233], on the particular Γ structure of the bilinear and the target observable and, in our particular case, $m = 2$ and $N = 4$ [234]. The zero three-momentum single propagator trace for the heaviest flavour can then be decomposed into two parts. The term [233]

$$\tilde{t}_{M,\Gamma} \equiv -\frac{1}{\sqrt{\Lambda_{123}}} \sum_{\bar{n}} \text{tr}_{\text{CD}} [\Gamma M_{2m}(n, n)] \quad (7.42)$$

collects the first $2n$ contributions of the gHPE, and [233]

$$\tilde{t}_{R,\Gamma} \equiv -\frac{1}{\sqrt{\Lambda_{123}}} \sum_{\bar{n}} \text{tr}_{\text{CD}} \left[\Gamma \left\{ D_N^{-1} H^{2m} \right\} (n, n) \right], \quad (7.43)$$

the remainder. D_N^{-1} can be reused for the other term on eq. (7.32) where it appears [234]. In [233], it is shown that $\tilde{t}_{M,\Gamma}$ contributes more to the stochastic noise than $\tilde{t}_{R,\Gamma}$. In that same work, a probing scheme is introduced to evaluate the former in an exact way for the local, point-like operators. Since we also need the symmetric, point-split discretisation of

the vector current, HProb [237, 56] is used on spin and colour diluted stochastic sources with $N_h = 512$ Hadamard vectors to reach the gauge noise [234]. The term $D_N^{-1} H^{2m}$ is evaluated using the stochastic estimator [233]

$$\tilde{t}_{R,\Gamma} = -\frac{1}{N_s \sqrt{|\Lambda_{123}|}} \sum_{\bar{n}} \sum_{i=1}^{N_s} \text{tr}_{\text{CD}} \left\{ \left[\eta_i^\dagger H^m \right] (n) \Gamma \left[D^{-1} H^m \eta_i \right] (n) \right\}, \quad (7.44)$$

for both the local and symmetric, point-split discretisations. A set of 512 stochastic sources were used for the light quark, and 1024 for each of the heavier flavours [234]. One can see that the remainder only constitutes a small fraction of the original uncertainty [233].

Split-even estimator

The single-propagator traces of the form $D_f^{-1} - D_{f'}^{-1}$ in eq. (7.32) can be expressed via [233]

$$\text{tr}_{\text{CD}} \left[\Gamma \left(D_f^{-1}(n, n) - D_{f'}^{-1}(n, n) \right) \right] = (M_{f'} - M_f) \text{tr}_{\text{CD}} \left[\Gamma D_f^{-1}(n, n) D_{f'}^{-1}(n, n) \right], \quad (7.45)$$

where two different quark flavours f and f' are used with $M_f \neq M_{f'}$ and a given Dirac structure Γ . It has been observed [233] that there is a difference of up to two orders of magnitude for the vector current in the uncertainty of eq. (7.45) depending on where one introduces the stochastic sources. The standard estimator places them to the right of both propagators. However, the so-called split-even estimator, with the stochastic sources located between the two propagators, is much more efficient [233],

$$-\frac{M_{f'} - M_f}{N_s \sqrt{|\Lambda_{123}|}} \sum_{\bar{n}} \sum_{i=1}^{N_s} \text{tr}_{\text{CD}} \left\{ \left[\eta_i^\dagger D_{f'}^{-1} \right] (n) \Gamma \left[D_f^{-1} \eta_i \right] (n) \right\}. \quad (7.46)$$

The estimator in eq. (7.46) allows to reach the gauge noise using at most $\mathcal{O}(100)$ stochastic sources with neither colour, nor spin dilution [234]. For a more detailed study of the uncertainty associated with eq. (7.46), see [233]. Note that at the $\text{SU}(3)_f$ -symmetric point $M_f = M_{f'}$ and, therefore, all disconnected pieces vanish.

7.3 CLS lattice simulations

At this point, we have already given a succinct presentation of QCD on the lattice in chapter 3, focusing on the particular regularisation and methods used by the Coordinated Lattice Simulations (CLS) set of ensembles [132], and we have presented the method followed by the Mainz group to implement the quark-connected and quark-disconnected contributions in sections 7.1 and 7.2. In this section, we gather some relevant information about the simulations before starting with the actual analysis.

First of all, the set of ensembles employ $N_f = 2 + 1$ flavours of non-perturbatively improved Wilson fermions with a Lüscher-Weisz gauge action [132]. This means that they respect strong isospin symmetry, i.e. the u and d quarks are mass degenerate. In a

7 Implementation of the mesonic two-point functions

Ensemble	$\hat{\Pi}_{33}$	$\hat{\Pi}_{88c}$	$\hat{\Pi}_{88d}$	$\hat{\Pi}_{88}$	$\hat{\Pi}_{08c}$	$\hat{\Pi}_{08d}$	$\hat{\Pi}_{08}$	$\hat{\Pi}_{cc}$	κ_c shift
H101 s.l.	2838 (6)	2838 (6)						337.5 (1.3)	-0.5 (0.8)
l.l.	2750 (6)	2750 (6)						647.5 (2.5)	-0.9 (1.5)
H102 s.l.	2959 (10)	2738 (6)	-1 (5)	2737 (7)	195 (4)	-5 (37)	190 (36)	342.1 (1.4)	-0.4 (1.2)
l.l.	2872 (10)	2652 (7)	-2 (5)	2650 (7)				652.5 (2.6)	-0.7 (2.1)
H105 s.l.	3091 (20)	2646 (10)	-13 (30)	2633 (32)	393 (11)	20 (106)	413 (104)	349.5 (1.5)	-0.3 (0.9)
l.l.	3004 (20)	2560 (11)	-21 (30)	2539 (32)				661.4 (2.7)	-0.6 (1.6)
N101 s.l.	3162 (10)	2678 (5)	-42 (23)	2636 (23)	427 (7)	-223 (96)	204 (96)	349.8 (1.6)	-0.3 (0.9)
l.l.	3076 (10)	2592 (5)	-45 (24)	2547 (24)				661.2 (2.8)	-0.6 (1.6)
C101 s.l.	3323 (16)	2672 (7)	-54 (23)	2618 (24)	574 (9)	-155 (70)	419 (71)	353.3 (1.5)	-0.2 (0.5)
l.l.	3239 (16)	2587 (7)	-56 (23)	2531 (24)				665.2 (2.7)	-0.4 (0.8)
B450 s.l.	2725 (7)	2725 (7)						343.5 (1.5)	0.3 (1.1)
l.l.	2658 (7)	2658 (7)						594.3 (2.6)	0.5 (1.8)
S400 s.l.	2858 (12)	2641 (8)	-3 (13)	2639 (15)	191 (5)	41 (63)	232 (62)	347.7 (1.5)	-0.8 (1.1)
l.l.	2792 (12)	2575 (8)	-4 (13)	2571 (15)				590.6 (2.5)	-1.3 (1.7)
N451 s.l.	3084 (8)	2623 (3)	-21 (9)	2602 (10)	404 (4)	-41 (37)	363 (37)	357.9 (1.5)	-0.4 (0.8)
l.l.	3018 (8)	2557 (3)	-23 (9)	2534 (10)				608.3 (2.5)	-0.7 (1.2)
D450 s.l.	3265 (11)	2600 (4)	-115 (29)	2485 (29)	583 (7)	-279 (84)	304 (85)	364.1 (1.5)	0.0 (0.4)
l.l.	3200 (11)	2534 (4)	-119 (29)	2414 (29)				614.5 (2.5)	0.0 (0.6)
H200 s.l.	2618 (14)	2618 (14)						353.0 (1.4)	-3.0 (1.0)
l.l.	2572 (14)	2572 (14)						536.7 (2.0)	-4.3 (1.5)
N202 s.l.	2728 (12)	2728 (12)						353.2 (1.4)	-3.0 (1.0)
l.l.	2682 (13)	2682 (13)						536.8 (2.1)	-4.3 (1.5)
N203 s.l.	2863 (9)	2615 (7)	-14 (5)	2601 (9)	216 (5)	-51 (34)	165 (35)	359.2 (1.4)	0.1 (0.7)
l.l.	2815 (10)	2568 (7)	-15 (5)	2554 (9)				544.2 (2.0)	0.1 (1.0)
N200 s.l.	2985 (11)	2536 (5)	3 (15)	2538 (15)	393 (7)	3 (58)	396 (58)	367.3 (1.5)	-0.1 (0.5)
l.l.	2939 (11)	2489 (5)	-0 (15)	2489 (15)				552.9 (2.2)	-0.1 (0.7)
D200 s.l.	3212 (13)	2523 (5)	-58 (29)	2465 (30)	601 (8)	-97 (91)	504 (92)	375.7 (1.5)	0.0 (0.4)
l.l.	3165 (13)	2476 (5)	-65 (30)	2412 (30)				562.2 (2.2)	0.0 (0.6)
E250 s.l.	3506 (37)	2578 (13)	53 (121)	2631 (123)	809 (22)	-20 (295)	789 (296)	378.7 (1.2)	-0.2 (0.4)
l.l.	3462 (37)	2532 (13)	43 (123)	2575 (125)				564.7 (1.9)	-0.2 (0.6)
N300 s.l.	2559 (13)	2559 (13)						357.6 (1.3)	0.0 (1.5)
l.l.	2531 (13)	2531 (13)						474.0 (1.7)	0.0 (1.9)
N302 s.l.	2686 (13)	2451 (8)	-3 (7)	2448 (10)	204 (6)	-38 (35)	166 (35)	369.9 (1.4)	0.3 (0.8)
l.l.	2659 (13)	2424 (8)	-3 (7)	2420 (10)				487.1 (1.8)	0.4 (1.0)
J303 s.l.	2988 (17)	2441 (7)	-13 (31)	2428 (33)	476 (9)	-161 (110)	315 (112)	376.0 (1.6)	0.0 (0.7)
l.l.	2962 (17)	2414 (7)	-14 (31)	2400 (33)				488.2 (2.0)	0.0 (0.8)
E300 s.l.	3224 (30)	2443 (10)	-121 (56)	2322 (58)	679 (18)	-292 (204)	387 (202)	382.7 (1.2)	-0.0 (0.0)
l.l.	3197 (30)	2416 (10)	-138 (57)	2278 (58)				499.9 (1.6)	-0.0 (0.0)

Table 7.2: sVPF $\times 10^5$ at $Q^2 = 1 \text{ GeV}^2$ after $\mathcal{O}(a)$ improvement and renormalisation. We indicate the values for the various components: isovector $\hat{\Pi}_{33}$, connected isoscalar $\hat{\Pi}_{88c}$, disconnected isoscalar $\hat{\Pi}_{88d}$, connected plus disconnected (full) isoscalar $\hat{\Pi}_{88}$, connected 08 $\hat{\Pi}_{08c}$, disconnected 08 $\hat{\Pi}_{08d}$, full 08 $\hat{\Pi}_{08}$ and charm $\hat{\Pi}_{cc}$. The last column shows the shift to the central value of $\hat{\Pi}_{cc}$ necessary to tune κ_c , as well as the systematic uncertainty in such a shift.

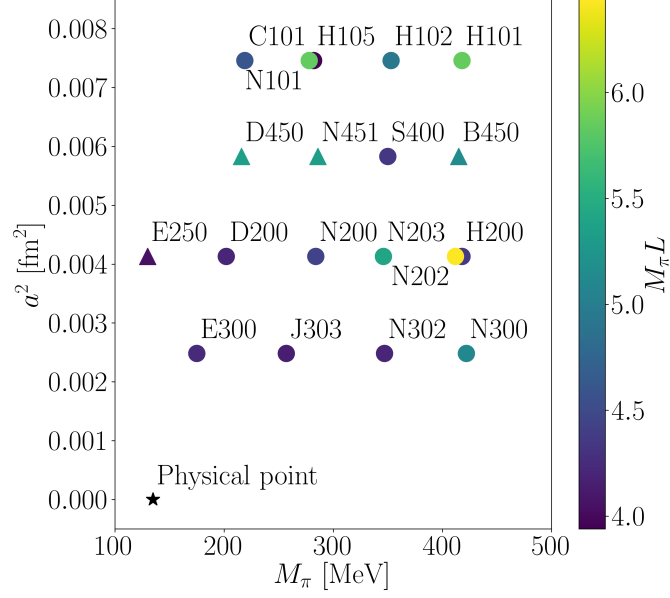


Figure 7.1: Set of CLS ensembles used in this project as a function of the lattice spacing a and pion mass M_π . Triangles indicate PBC and circles OBC in time. The product $M_\pi L$, which roughly gives the magnitude of the finite-size effects (FSE), is given with a colour code. Note in particular the different colours for the pairs (H105, N101) and (H200, N202), which are ensembles with the same parameters but the physical volume.

similar way, they omit any QED effects. Nonetheless, in section 13.3, a first estimate of the inclusion of electric charges and different masses for the light quarks is given, based on the ongoing analysis presented in [57]. The c quark is not present in the sea, as it is argued [241] that the precision which can be achieved with these ensembles at the physical point will not be able to differentiate these effects, while introducing larger lattice artefacts and making more difficult tuning the quark masses. In table 7.3, we give the basic details of the CLS ensembles that we have used for this project. For each entry and from left to right, we give the CLS label, the extension of the lattice in the temporal and spatial directions, the gradient flow at the flavour symmetric point for the different β values in lattice units, the lattice spacing and spatial extension in physical units. Besides, we gather the approximate values of the pion and kaon masses, as well as the product of the pion mass and the spatial extent. Finally, we give the number of configurations that were processed for this analysis, differentiating between quark-connected and quark-disconnected contributions for the light and strange quarks, and the charm quark-connected component.

Let us explain in a bit more detail table 7.3. The CLS label categorizes the ensemble. The initial letter refers to the geometry of the lattice: a B means $32^3 \times 64$ lattice sites, an H means $32^3 \times 96$, and so on. The first digit relates to the β or lattice spacing at the physical quark mass used, although these are disordered. The last two digits encode further information of the ensemble to differentiate it from the rest, like the κ values. OBC for the temporal direction have been adopted for most of the current iteration of ensembles, as

7 Implementation of the mesonic two-point functions

	T/a	L/a	t_0^{sym}/a^2	a [fm]	L [fm]	M_π, M_K [MeV]	$M_\pi L$	# cnfg (con., dis., charm)		
H101	96	32	2.86	0.08636	2.8	418	5.9	2000	-	1000
H102	96	32			2.8	353 438	4.9	1900	1900	975
H105*	96	32			2.8	281 463	3.9	1000	1000	500
N101	128	48			4.1	279 461	5.9	1155	1155	345
C101	96	48			4.1	219 470	4.6	2000	2000	400
B450	64	32	3.659	0.07634	2.4	414	5.1	1600	-	800
S400	128	32			2.4	351 441	4.3	1720	1720	800
N451	128	48			3.7	286 460	5.3	1000	1000	200
D450	128	64			4.9	216 475	5.3	500	500	300
H200*	96	32	5.164	0.06426	2.1	418	4.4	1980	-	480
N202	128	48			3.1	411	6.4	875	-	420
N203	128	48			3.1	345 442	5.4	1500	1500	700
N200	128	48			3.1	283 462	4.4	1695	1695	390
D200	128	64			4.1	201 480	4.2	2000	1000	500
E250	192	96			6.2	129 489	4.1	485	485	65
N300	128	48	8.595	0.04981	2.4	422	5.1	1680	-	480
N302	128	48			2.4	346 451	4.2	2190	1080	480
J303	192	64			3.2	257 474	4.2	1040	1040	100
E300	192	96			4.8	175 491	4.2	600	300	100

Table 7.3: Set of CLS ensembles used in this project. From left to right, we indicate the CLS label of the ensemble, the number of lattice sites in the temporal and spatial directions, the gradient flow at the symmetric point, the lattice spacing in physical units [142], the total physical size in the spatial direction, the approximate value of the pion and kaon mass, the product of the pion mass and the physical size, and the statistics at our disposal for every ensemble, distinguishing between quark-connected, quark-disconnected and charm components. Ensembles B450, N451, D450 and E250 use PBC in all directions, while the rest use OBC.

we already explained in section 3.4.4, with the aim of reducing the lattice spacing while keeping autocorrelation lengths low [132]. For ensembles B450, N451, D450 and E250 PBC for bosons and APBC for fermions are used in the temporal direction. All ensembles use PBC for the spatial components. One needs large L/a to reduce the finite-size effects, which scale as $\exp(-M_\pi L)$ [143], and even larger T/a to make the bulk of the simulation time-translation invariant. For that to happen, the boundary states have to decay. Since they have scalar quantum numbers, one expects them to behave like $\exp(-2M_\pi x_0)$ at long distances [126]. We rely on the $N_f = 2 + 1$ determination of the gradient flow at the physical point in [142] to connect our lattice analysis with the physical world,

$$\sqrt{8t_0^{\text{phy}}} = 0.415 \text{ (4) (2) fm.} \quad (7.47)$$

As we already pointed out in section 3.5, the precise value of $8t_0^{\text{phy}}$ depends on the sea-quark content of the lattice. However, a new set of measurements of t_0/a^2 was computed for every ensemble to take into account the correlations between the scale setting and $\bar{\Pi}$ in the extrapolation to the physical point (see chapter 12). These new measurements appear on

table 7.4. The lattice spacing a does not enter directly into our analysis, but only in relation with the gradient flow because the different lattice spacings are correlated and carry a higher uncertainty than either of the combinations t_0/a^2 or t_0^{sym}/a^2 [142]. Nonetheless, we give both, the lattice spacing and the spatial extent in physical units for informative purposes. Regarding the pion and kaon masses, these CLS simulations span from approximately 420 MeV, which corresponds to the $\text{SU}(3)_f$ -symmetric point, to the physical pion and kaon masses. Most masses given in table 7.3 are taken from [218], and the rest, which correspond to the most recent ensembles, from private communications with the Mainz group. The simulations lie on the trajectory $M_\pi^2/2 + M_K^2 = \text{const.}$ However, small corrections to this behaviour exist (due to mistuning of the bare parameters) and are relevant to the extrapolation to the physical point (see chapter 12). One can notice that there are groups of ensembles with similar meson masses at different lattice spacings. For example, N101, N451, N200 and, to a certain extent, J303, all have $M_\pi \sim 280$ MeV and $M_K \sim 460$ MeV. This layout allows to take the continuum limit, which is studied in detailed in chapter 12. At any rate, the values presented in table 7.3 are only approximate.

The meson masses used for our analysis are gathered in table 7.4. These values were obtained by the Mainz group using the procedure detailed on the PhD thesis [57] and its code implementation. Both the values of the lattice spacing and the meson masses are chosen to reduce both statistical and systematic effects, finding a balance between the two. Simulations with heavier pion masses are computationally cheaper, and with smaller quark-disconnected contributions [218] when the trajectory $\text{tr } M = \text{const}$ is used. In much the same way, at fixed physical volume, coarser lattices have fewer lattice sites, reducing the computational cost and showing smaller autocorrelation lengths. Therefore, for ensembles like H101, S400 or N101, it is possible to measure observables more precisely at a given computational cost and volume compared to ensembles with smaller lattice spacings. However, for larger lattice spacings, the Symanzik expansion starts to break down, see section 3.1.3, and ensembles with coarser lattices and heavier pion masses carry a systematic uncertainty when extrapolating to the physical point that is difficult to assess. To take the continuum limit reliably, several lattice spacings are needed, with lattice spacings as fine as possible. In a similar fashion, one requires ensembles at the physical pion and kaon masses to reduce the impact of the chiral extrapolation and obtain systematic uncertainties around $\sim 1\%$ or lower [242]. As a result, in order to quantify and reduce systematic errors, it is necessary to generate ensembles where every configuration is more expensive, and where higher statistics are more difficult to gather.

The product $M_\pi L$ is the exponent controlling the FSE in the spatial direction [143], and it serves as a simple, *a priori* measure of them. The rule of thumb tells that $M_\pi L > 4$ [243] is required for modern computations aiming at $\sim 1\%$ FSE that can be corrected using some of the methods detailed in chapter 10, for example. In principle, we should also consider finite T and $\sqrt{T^2 + L^2}$ effects [143]. However, both show an exponential suppression, similar to the effects in the spatial components [143]. Since T/a is two or three times larger than L/a on the CLS ensembles, these are sub-leading effects, which we do not take into account.

In table 7.3, we mark two ensembles with an asterisk, H105 and H200, which have the

Ensemble	$8t_0/a^2$	aM_π	aM_K
H101	22.79 (4)	0.1830 (5)	0.1830 (5)
H102	23.06 (5)	0.1546 (5)	0.1919 (4)
H105	23.12 (6)	0.1234 (13)	0.2028 (7)
N101	23.15 (3)	0.1222 (5)	0.2019 (3)
C101	23.32 (3)	0.0960 (6)	0.2057 (3)
B450	29.30 (6)	0.1605 (4)	0.1605 (4)
S400	29.55 (6)	0.1358 (4)	0.1707 (3)
N451	29.46 (2)	0.1108 (3)	0.1783 (2)
D450	29.57 (2)	0.0836 (4)	0.1840 (1)
H200	41.20 (12)	0.1363 (5)	0.1363 (5)
N202	41.35 (10)	0.1342 (3)	0.1342 (3)
N203	41.16 (5)	0.1124 (2)	0.1442 (2)
N200	41.32 (5)	0.0922 (3)	0.1506 (2)
D200	41.43 (2)	0.0655 (3)	0.1566 (1)
E250	41.62 (1)	0.0422 (2)	0.1594 (1)
N300	68.36 (33)	0.1067 (3)	0.1067 (3)
N302	68.23 (14)	0.0875 (3)	0.1140 (3)
J303	68.99 (12)	0.0649 (2)	0.1197 (2)
E300	69.31 (8)	0.0442 (1)	0.1240 (1)

Table 7.4: Gradient flow, pion and kaon masses in lattice units, as measured for every ensemble. The computation of t_0/a^2 follows the lines in [142] and takes advantage of the updated statistics. The pion and kaon masses have been obtained following the procedure in [57].

same parameters as N101 and N202, respectively, but have smaller volumes. They allow us to check whether the FSE corrections that we compute in chapter 10 fully explain the difference between the different volumes. We further cross-check our estimation of FSE using two different procedures, which we refer to by the name of their main contributors, Hansen-Patella (HP) [143, 244] and Meyer-Lellouch-Lüscher (MLL) [221, 245, 246]. Also, see that N101 and N202 have two of the highest $M_\pi L$, so we expect their FSE corrections to be rather small. Note that H105 and H200 are only used for this check, and we do not use them for the extrapolation to the physical point, relying on N101 and N202 instead.

Figure 7.1 presents the information of table 7.3 in a visual, hopefully more appealing way. The plot shows the different CLS ensembles used in this project, with their lattice spacing on the y-axis and their pion mass on the x-axis. The target physical point is marked with a star. Triangles indicate PBC in time and circles OBC. To give a sense of the finite-size effects, we give $M_\pi L$ using a colour scheme explained on the right-hand side of the plot.

In the following chapters, we gather the main contribution of this thesis, which is the analysis of the measurements of the vector correlator on the set of CLS ensembles given in table 7.3. We start by quantifying the autocorrelations among measurements in chapter 8.

Then, we continue treating the signal-to-noise ratio problem in chapter 9. We correct for FSE in chapter 10. The results for each ensemble on the lattice are gathered in chapter 11. The combined extrapolation to the continuum limit and interpolation to the physical meson masses is taken in chapter 12. Then, in chapter 13, we give analytic formulas which describe the behaviour of the hadronic contribution to the electromagnetic coupling and electroweak mixing angle as a function of the virtuality, and compare with some other lattice and phenomenological determinations. Each chapter has its own discussion, and conclusions are given for each step and method. In chapter 14, we gather the main conclusions of every step of the analysis, together with an outlook.

Chapter 8

Autocorrelations

We have seen in section 3.4 that each gauge configuration is generated from a predecessor, meaning that the result of a measurement in one configuration is affected by previous ones, and it affects measurements on the following configurations. From a statistical perspective, we can think of a set of experiments, our gauge configurations, which are not independent of one another. This is in stark contrast with the more naive expectation that different experiments produce independent results. The correlation between configurations at different Markov times τ is referred to autocorrelation, and stems from the process of simulating QCD using Markov chains. It should be distinguished from the more common correlation between lattice coordinates, which is related to physics. The presence of autocorrelations prevents the application of the usual definition of statistical uncertainty [247], which we discuss in section 8.5. Therefore, we need either a method to estimate the effects of autocorrelations on the observables, or a procedure to obtain a set of uncorrelated measurements from the original dataset. In this chapter, we summarize the basic facts about autocorrelations, and discuss two different methods which allow to produce reliable statistical errors: jackknife binning and Ulli Wolff's Γ -method, both explained in [247].

8.1 Theory and definitions

We consider a set of primary observables \mathcal{O}_α with true expectation values A_α . The index α runs over the set of primary observables, and there are $r = 1, \dots, R$ independent replicas, each one with a Markov chain of $i = 1, \dots, N_r$ configurations ϕ_i^r distributed according to the probability $P(\phi)$, totalling $N = \sum_{r=1}^R N_r$ configurations. The update algorithm has a transition probability $T(\phi \rightarrow \phi'; d)$, with d indicating the number of steps between configurations ϕ and ϕ' . The estimate of \mathcal{O}_α on a configuration is $a_\alpha^{i,r} \equiv \mathcal{O}_\alpha(\phi_i^r)$. It is possible to define an autocorrelation function $\Gamma_{\alpha\beta}$ [248, 249]

$$\begin{aligned} \Gamma_{\alpha\beta}(d)\delta_{rs} &\equiv \left\langle \left(a_\alpha^{i,r} - A_\alpha \right) \left(a_\beta^{i+d,s} - A_\beta \right) \right\rangle \\ &= \sum_{\phi_i^r} \sum_{\phi_j^s} P(\phi_i^r) T(\phi_i^r \rightarrow \phi_j^s; d) (\mathcal{O}_\alpha(\phi_i^r) - A_\alpha) (\mathcal{O}_\beta(\phi_j^s) - A_\beta), \end{aligned} \quad (8.1)$$

which correlates the fluctuation of the estimates for A_α and A_β separated by $d \geq 0$ updates. In general, $\Gamma_{\alpha\beta}(-d) = \Gamma_{\beta\alpha}(d)$ [247], but if the detailed balance condition eq. (3.37) is fulfilled, we have $\Gamma_{\alpha\beta}(d) = \Gamma_{\beta\alpha}(d)$ [247]. For the particular case $d = 0$, we recover the definition of the covariance matrix with the variance in the diagonal entries. The unbiased estimators for \mathcal{O}_α are, per replica and for all replicas combined [247],

$$\bar{a}_\alpha^r = \frac{1}{N_r} \sum_{i=1}^{N_r} a_\alpha^{i,r} \quad \text{and} \quad \bar{\bar{a}}_\alpha = \frac{1}{N} \sum_{r=1}^R N_r \bar{a}_\alpha^r. \quad (8.2)$$

However, we are usually interested in derived quantities F , which are functions of primary observables $f(\mathcal{O}_\alpha)$. We usually consider two estimators for F [247],

$$\bar{F} = f(\bar{a}_\alpha) \quad \text{and} \quad \bar{\bar{F}} = \frac{1}{N} \sum_{r=1}^R N_r f(\bar{a}_\alpha^r). \quad (8.3)$$

Taking into account autocorrelations, the true variance of a derived observable F can be related to the naive variance [247],

$$(\Delta F)^2 = 2\tau_{F,\text{int}} (\Delta_0 F)^2, \quad (8.4)$$

where the naive variance, for the case of no autocorrelations, is given by [247]

$$(\Delta_0 F)^2 = \frac{1}{N} \sum_{\alpha,\beta} f_\alpha f_\beta \Gamma_{\alpha\beta}(0), \quad (8.5)$$

and the integrated autocorrelation time for F is defined as [247]

$$\tau_{F,\text{int}} = \frac{1}{2N (\Delta_0 F)^2} \sum_{d=-\infty}^{\infty} \sum_{\alpha,\beta} f_\alpha f_\beta \Gamma_{\alpha\beta}(d). \quad (8.6)$$

f_α and f_β are the derivatives with respect to primary observables [247],

$$f_\alpha = \left. \frac{\partial f}{\partial \mathcal{O}_\alpha} \right|_{\mathcal{O}_\alpha = A_\alpha}. \quad (8.7)$$

Equation (8.4) tells us that the ratio between the true and naive uncertainty is a constant, which in the case of no autocorrelations reduces to unity, with $\tau_{F,\text{int}} = 1/2$. To use eqs. (8.4) to (8.6), we need estimators for every quantity.

8.2 The Γ -method

After giving the main expressions for the study of autocorrelations, we describe Ulli Wolff's Γ -method [247] and the jackknife binning procedure [247] to estimate the integrated autocorrelation time of a derived quantity F . Their two main differences are, besides

complexity, the different systematic errors and the fact that the former estimates $\tau_{F,\text{int}}$ explicitly and the latter implicitly. The Γ -method estimators for the autocorrelation function and the integrated autocorrelation time are [247]

$$\bar{\bar{\Gamma}}_{\alpha\beta}(d) = \frac{1}{N - Rd} \sum_{r=1}^R \sum_{i=1}^{N_r-d} \left(a_{\alpha}^{i,r} - \bar{a}_{\alpha} \right) \left(a_{\beta}^{i+d,r} - \bar{a}_{\beta} \right), \quad (8.8)$$

$$\bar{\tau}_{F,\text{int}}(w) = \frac{1}{2N \left(\Delta_0 \bar{\bar{F}} \right)^2} \sum_{d=-w}^w \sum_{\alpha,\beta} \bar{f}_{\alpha} \bar{f}_{\beta} \bar{\bar{\Gamma}}_{\alpha\beta}(d), \quad (8.9)$$

$$\left(\Delta_0 \bar{\bar{F}} \right)^2 = \sum_{\alpha,\beta} \bar{f}_{\alpha} \bar{f}_{\beta} \bar{\bar{\Gamma}}_{\alpha\beta}(0), \quad (8.10)$$

$$\left(\Delta \bar{\bar{F}} \right)^2 = 2 \bar{\tau}_{F,\text{int}} \left(\Delta_0 \bar{\bar{F}} \right)^2, \quad (8.11)$$

where the derivatives are evaluated at \bar{a} . We see that to estimate eq. (8.9), we truncate the infinite sum of autocorrelations and take only a finite window w in Markov time, large enough to include all relevant autocorrelations, but short enough so that uncorrelated data is not included. To optimize w , the uncertainty of $\bar{\tau}_{F,\text{int}}$ is minimized [247]. On the one hand, the systematic contribution to the error, stemming from the choice of w , can be modelled supposing that autocorrelations fall off exponentially with the Markov time at long distances, such that the systematic error is $\propto \exp(-w/\tau_{F,D})$, with $\tau_{F,D}$ a typical decay constant of autocorrelations [247]. On the other hand, the remaining statistics contribute to the error with a term of the form $\sqrt{w/N}$ [247], yielding a relative error [247]

$$\frac{\Delta_{\text{total}} \left(\Delta \bar{\bar{F}} \right)}{\Delta \bar{\bar{F}}} \approx \frac{1}{2} \min_w \left(e^{-w/\tau_{F,D}} + 2 \sqrt{\frac{w}{N}} \right). \quad (8.12)$$

To obtain the minimum of eq. (8.12), it is possible to apply the method described in [247]. An important advantage of the Γ -method is the relation between the systematic and statistical uncertainties. This can be easily seen approximating the solution of the transcendental eq. (8.12) using $w = \tau_{F,D} \log(N/\tau_{F,D})/2$ [247]. Then, the ratio of the systematic to the statistical uncertainties of the error reads

$$\frac{\Delta_{\text{sys}} \left(\Delta \bar{\bar{F}} \right)}{\Delta_{\text{sta}} \left(\Delta \bar{\bar{F}} \right)} \approx \frac{1}{\log(N/\tau_{F,D})}. \quad (8.13)$$

Essentially, eq. (8.13) tells us that the systematic error becomes irrelevant for sufficiently high statistics. Implementations of the Γ -method can be found in [247] for *MATLAB*, and in [250] for *Python*. For the purpose of this thesis, we have employed the latter, [250].

8.3 The jackknife method

Now, to explain the jackknife procedure [247], consider that we join the N configurations of the R replicas together and divide them into N_B bins, also called blocks, with bin size B ,

so that $N = BN_B$. Then, we form the blocked measurements of primary observables [247]

$$b_\alpha^k = \frac{1}{B} \sum_{i=1}^B a_\alpha^{(k-1)B+i}, \quad k = 1, \dots, N_B, \quad (8.14)$$

$$c_\alpha^k = \frac{1}{N-B} \left(\sum_{i=1}^N a_\alpha^i - B b_\alpha^k \right). \quad (8.15)$$

Equation (8.14) is simply the average of B consecutive measurements of the primary observable A_α . Equation (8.15) takes the average over the entire dataset except for the k -th bin, which is subtracted. Equation (8.15) means that every block contains almost all statistics, except for one bin. This is an improvement from the simple binning method [247], where each average contains only one bin, potentially increasing fluctuations. The expected value of F is \bar{F} from eq. (8.3) [247], and its uncertainty is [247]

$$(\Delta_{\text{jack}} \bar{F})^2 = \frac{N_B - 1}{N_B} \sum_{k=1}^{N_B} \left(f(c_\alpha^k) - \bar{F} \right)^2. \quad (8.16)$$

It is possible to compare the jackknife and Γ -methods computing the error of their respective error estimates, $\Delta \bar{F}^2$ and $\Delta_{\text{jack}} \bar{F}^2$. For jackknife binning, the statistical error of the error comes from the finite number of bins $\sqrt{2B/N}$, while systematics are $\propto \tau_{F,D}/B$ [247]. The total error of the error can be minimized as a function of the bin size. In particular [247],

$$\frac{\Delta_{\text{total}} (\Delta_{\text{jack}} \bar{F})}{\Delta_{\text{jack}} \bar{F}} \approx \frac{1}{2} \min_B \left(\frac{\tau_{F,D}}{B} + \sqrt{\frac{2B}{N}} \right) = \frac{3}{2} \left(\frac{2N}{\tau_{F,D}} \right)^{-1/3}. \quad (8.17)$$

The minimum occurs for $B = \tau_{F,D}(2N/\tau_{F,D})^{1/3}$ [247]. For this value of the bin size, the ratio of the systematic to statistical error is constant [247],

$$\frac{\Delta_{\text{sys}} (\Delta_{\text{jack}} \bar{F})}{\Delta_{\text{sta}} (\Delta_{\text{jack}} \bar{F})} = \frac{1}{2}. \quad (8.18)$$

Comparing eqs. (8.13) and (8.18), we see the main difference between the Γ -method and jackknife binning. While for the former the systematic error becomes negligible in comparison with the statistical uncertainty at high statistics, for the latter both sources of uncertainty keep a constant relation. This sets the Γ -method in a clear theoretical advantage, but the jackknife procedure is still widely used due to its simpler implementation. In practice, the simplest way to compute the optimal bin size B is plotting the variance in eq. (8.16) as a function of the bin size, and normalising by the variance without binning —see fig. 8.1 for an example. In such a plot, a plateau indicates that we reached the optimal bin size. Although larger B will certainly produce uncorrelated data, taking a too coarse binning will leave too few samples, making the estimation of the observable uncertainty unreliable.

8.4 Removal of autocorrelations

To reduce autocorrelations, a first step is taken during the generation of the gauge configurations [132]. A trajectory length of 2 MDU was chosen (see section 3.4 for the definitions), and only one every two configurations was selected for later measurements —modulo some exceptions with one or four trajectories per configuration. One expects growing autocorrelations as the lattice spacing is decreased. That is why many of the CLS ensembles that we use employ OBC, which alleviate the problem (see section 3.4.4). In particular, if one generates runs with the same total trajectory length, the integrated autocorrelation time of the sVPF should have a Langevin scaling, $\bar{\tau}_{\hat{\Pi},\text{int}} \propto a^{-2}$ [132]. However, this is only a functional dependence for an optimal scenario. In practice, the prefactor will depend on the observable, and different runs will have different statistics as the simulations become more expensive towards the physical point. Therefore, we take the decision to estimate the autocorrelations for the observables we are interested in on every ensemble, and we employ both the Γ - and jackknife methods to check our results.

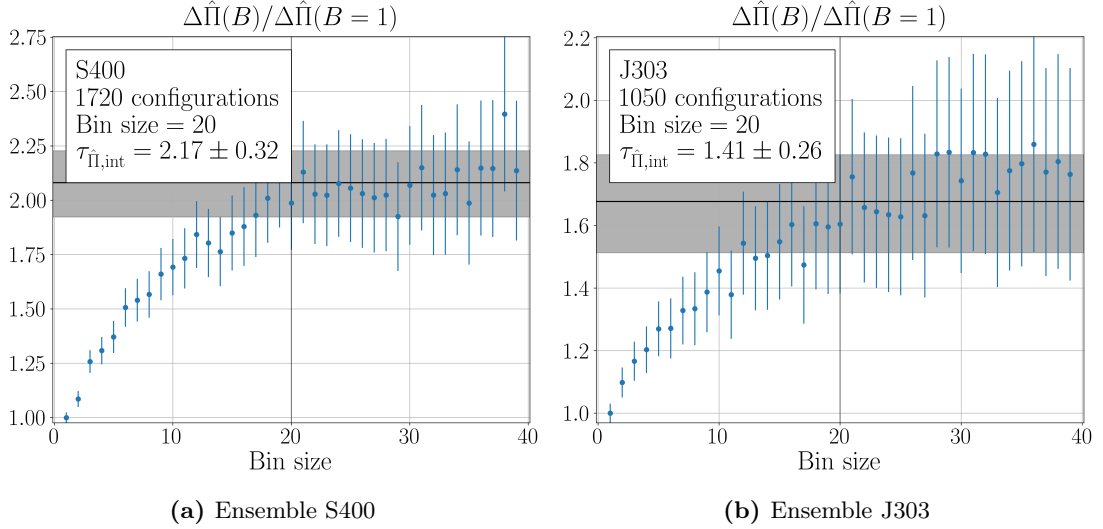


Figure 8.1: Uncertainty of $\hat{\Pi}$ normalised by the naive error vs the bin size. The vertical line shows the estimated optimal bin size $B = 2 \times w$, and the horizontal band shows $\sqrt{2\bar{\tau}_{\hat{\Pi},\text{int}}}$, which is the uncertainty increase expected when taking into account autocorrelations. The ensemble S400, with $M_\pi = 351$ MeV, is depicted on fig. 8.1a, and J303, with $M_\pi = 257$ MeV, on fig. 8.1b.

To remove autocorrelations and create statistically independent data, we find a suitable bin size B . To compute it, we apply the Γ -method [247, 250], which yields $\bar{\tau}_{\hat{\Pi},\text{int}}$ and the optimal window w . One can see from the discussion in sections 8.2 and 8.3 that the bin size plays a similar role to $2 \times w$ — a connection already pointed out in [247]—, and therefore we take $B = 2 \times w$ as our estimate for the bin size. The quantity F we apply the Γ -method to is the sVPF for the light and strange quark-flavours, including the re-weighting factors. Since each flavour might show different autocorrelations, we select the maximum $\bar{\tau}_{\hat{\Pi},\text{int}}$ of

the two. And since the long distance part of the correlator (in the time direction n_4) is dominated by noise, which might hide autocorrelations, we cut the correlator at different times, discarding everything beyond that point, and check for stability of $\tau_{\hat{\Pi},\text{int}}$ and w . Luckily, we found that the results are largely independent of this cut.

We compare both the Γ - and jackknife methods using eq. (8.11). The results are plotted in fig. 8.1. There, we plot the sVPF uncertainty for ensembles S400 and J303 as a function of the bin size, and normalise by the naive error estimate without binning. The error bars are an estimate of the error of the error, $\sqrt{B/N_{\text{cnfg}}} \Delta_{\text{jack}} \tilde{\Pi}$ [251]. On the one hand, when the blue points form a plateau, becoming independent of the bin size, this gives the jackknife-binning estimate for both, the increase of the uncertainty and the bin size. On the other hand, the Γ -method estimate for these two quantities is $\sqrt{2\bar{\tau}_{\hat{\Pi},\text{int}}}$ and $B = 2 \times w$, respectively, and are represented by a horizontal grey band and a vertical line. Indeed, we observe that the estimates of both methods agree very well. In fact, the Γ -method supplies an automatic procedure to obtain the correct bin size, while the jackknife procedure allows to check the result visually. Similar plots are found for all ensembles.

Table 8.1 shows the bin size and $\tau_{\hat{\Pi},\text{int}}$ for every ensemble. We see that there is the tendency to increase the bin size towards the continuum limit, although the expected Langevin scaling is by no means clear. For every lattice spacing, lighter pion masses tend to show smaller autocorrelations. One should bare in mind that the autocorrelations for ensembles like D450 and E250 are potentially larger (we apply a minimum binning of five configurations even when $\bar{\tau}_{\hat{\Pi},\text{int}} = 0.5$) but they are difficult to estimate because their statistics are also relatively poor in comparison with other lattices. Instead of taking a bin size arbitrarily large, which would leave us with very small statistics, and hence a badly estimated error, we treat every ensemble with the same procedure, and when more statistics are available the analysis may be updated. It is clear that the procedure described in this section is neither the Γ -method, nor the Jackknife. The reasons to work in this manner were twofold. On the one hand, to include the entire analysis within the framework of the Γ -method and its implementation in [250] is technically difficult, a problem Jackknife does not have. On the other hand, Jackknife only estimates $\tau_{\hat{\Pi},\text{int}}$ implicitly, and B is selected manually, making a bias almost unavoidable. Since we have an automated implementation of the Γ -method at our disposal, a bias is not a problem for the latter. Therefore, we use the Γ -method to avoid the bias, but we only use it to estimate a bin size.

8.5 Bootstrapping

Once we have dealt with autocorrelations, we have $N_B = N/B$ uncorrelated binned samples, with N the original number of configurations and B the bin size. With these data, our objective is to obtain expectation values and standard errors for quantities like $\hat{\Pi}_{\gamma\gamma}$ and $\hat{\Pi}_{Z\gamma}$. To do this, we apply the bootstrap method [252, 253, 254, 255, 256]. Let us say we want to evaluate a given derived quantity $\theta(x)$, finding its expectation value and standard error, where x is a primary observable. In particular, we have n data-points $x = \{x_1, x_2, \dots, x_n\}$ that follow a distribution D , which is not necessarily known. Then, we create s bootstrap

CLS	aM_π	Bin size	$\bar{\bar{\tau}}_{\Pi,\text{int}}$
H101	0.1830 (5)	25	1.70 (26)
H102	0.1546 (5)	25	1.73 (27)
H105	0.1234 (13)	20	1.32 (27)
N101	0.1222 (5)	15	0.79 (11)
C101	0.0960 (6)	20	0.79 (10)
B450	0.1605 (4)	25	1.45 (24)
S400	0.1358 (4)	20	2.17 (32)
N451	0.1108 (3)	10	0.73 (10)
D450	0.0836 (4)	5	0.55 (7)
H200	0.1363 (5)	30	1.20 (19)
N202	0.1342 (3)	35	1.86 (45)
N203	0.1124 (2)	20	1.15 (17)
N200	0.0922 (3)	15	0.77 (10)
D200	0.0655 (3)	10	0.58 (6)
E250	0.0422 (2)	5	0.47 (4)
N300	0.1067 (3)	40	3.36 (67)
N302	0.0875 (3)	30	2.07 (33)
J303	0.0649 (2)	20	1.41 (26)
E300	0.0442 (1)	20	1.07 (22)

Table 8.1: Pion mass, bin size and integrated autocorrelation time for each of the ensembles included in our study. Pion masses were obtained by the Mainz group using an implementation of the PhD thesis [57]. B and $\bar{\bar{\tau}}_{\Pi,\text{int}}$ are computed using the *Python* code [250].

samples, each one $\bar{x}_j \equiv 1/n \sum_{k=1}^n \bar{x}_{jk}$ with $j = 1, 2, \dots, s$. The elements \bar{x}_{jk} are drawn from x with equal probability $1/n$ and replacement. After that, we evaluate $\theta(\bar{x}_j)$ for every bootstrap sample \bar{x}_j , and estimate the expectation value and uncertainty of θ with the usual definitions for uncorrelated data,

$$\text{Exp } \theta \equiv \frac{1}{s} \sum_{j=1}^s \theta(\bar{x}_j), \quad (8.19)$$

$$\Delta\theta \equiv \left(\frac{1}{s-1} \sum_{j=1}^s (\theta(\bar{x}_j) - \text{Exp } \theta)^2 \right)^{1/2}. \quad (8.20)$$

It is also possible to use the original set x to compute the expectation value,

$$\text{Exp } \theta = \theta \left(\sum_{k=1}^n x_k \right), \quad (8.21)$$

and we check that the difference between using eq. (8.19) or eq. (8.21) amounts to only a rounding error in the last digit shown. Let us now apply this general theory to our study.

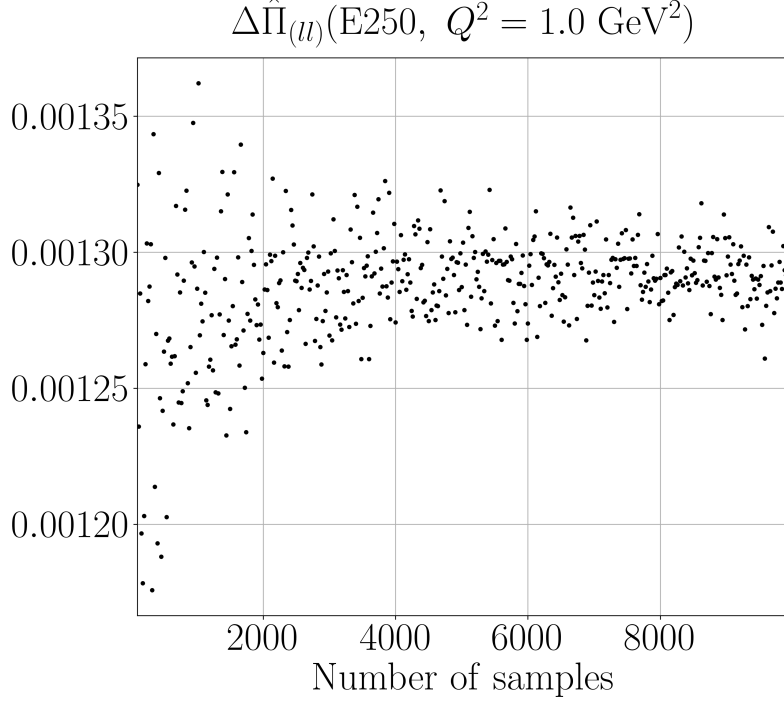


Figure 8.2: Statistical error of the sVPF function versus the number of bootstrap samples. The plot shows the light-quark component of E250, our ensemble at the physical mass.

In our particular case, we have one quantity θ of interest, the sVPF $\hat{\Pi}$, and $N_T/2$ different random variables x , the time-slices of the vector correlator $G(n_4)$. Each time-slice/random variable has $n = N_B$ measurements. To evaluate the sVPF with either the original or bootstrapped ($\bar{G}(n_4)$) datasets, we take the average of the measurements for each time-slice.

The bootstrap algorithm has a couple of advantages over analytic error propagation that makes it ideal. First, its error estimation does not rely on a particular relation between the primary observables x and the derived quantity θ , so it also works when the relation is extremely complicated or even non-analytic. Second, since one can create an arbitrary number of samples s from n observations, it is possible to combine different datasets x with various statistics n . These two aspects are key to our computation because we want to start from correlation functions on different lattices and give an expectation value with an uncertainty at the physical point, and because our ensembles (see section 7.3) do not have the same number of configurations, neither before nor after removing autocorrelations.

One important point of this method is choosing the appropriate number of bootstrap samples s . A number too small will not give a reliable estimate of the error. Even though [252] suggests using 200 samples, we decided to make the test shown in fig. 8.2, where the uncertainty of the light component of the sVPF, $\hat{\Pi}_{\ell}$, is plotted versus the number of

bootstrap samples. It is easy to recognize a bell shape pattern that indicates the error of the estimated uncertainty. It is clear that anything below 1000 samples suffers from large fluctuations, but the cost of our analysis increases linearly with the number of samples. In the end, we take the decision to use 2000 bootstrap samples as a compromise.

For some of the quantities used in our analysis, like the scale t_0 described in section 3.5 or the physical pion and kaon masses [34], we only have the expected value and uncertainty. To include them in our calculations, even if we can not include the correlations, we generate a normal distribution centred at the expected value with the uncertainty as width. In this way, each bootstrap sample has a corresponding number for the scale and physical masses.

Chapter 9

Signal-to-noise ratio

In this section, we present the analysis of the signal-to-noise ratio problem in our data. First, we quantify how, in general, the uncertainty dominates the signal at long distances, and briefly mention some possible ways to ameliorate the problem. Then, we present the single-exponential and bounding methods in sections 9.1 and 9.2, respectively, which allow us to take advantage of our theoretical knowledge of the two-point functions for reconstructing their long time behaviour and reducing their uncertainty. For each method, we present its definition and the results we obtain for the isovector, isoscalar and 08 components. We do not apply any modification to the charm correlator because its contribution to $\hat{\Pi}$ has already a statistical precision of around 0.4%.

To start, let us present the so-called signal-to-noise ratio problem on its simplest form. We consider a two-point function with a mesonic creation operator at the origin and the corresponding destruction operator at the sink time n_4 . We can compute both its expectation value $\langle F \rangle = \langle O_2(n_4) O_1(0) \rangle$ and its standard deviation $\sigma_F = (\langle F^2 \rangle - \langle F \rangle^2)^{1/2}$. We need the spectral decomposition of both quantities. In the case of F [73],

$$\langle F \rangle = \langle 0 | O_2(n_4) O_1(0) | 0 \rangle = \sum_n \langle 0 | O_2(n_4) | n \rangle \langle n | O_1(0) | 0 \rangle e^{-E_n n_4}. \quad (9.1)$$

And for F^2 , the tower of exponential reads [73]

$$\langle F^2 \rangle = \langle 0 | |O_2(n_4)|^2 |O_1(0)|^2 | 0 \rangle = \sum_r \langle 0 | |O_2(n_4)|^2 | r \rangle \langle r | |O_1(0)|^2 | 0 \rangle e^{-E_r n_4}. \quad (9.2)$$

The quantum numbers of the states created in eq. (9.1) and eq. (9.2) will differ, in general, and the energies E_n and E_r will also be different. Therefore, the signal-to-noise ratio is [73]

$$\begin{aligned} \frac{\langle F \rangle}{\sigma_F} &= \left(\sum_n \langle 0 | O_2 | n \rangle \langle n | O_1 | 0 \rangle e^{-E_n n_4} \right) \\ &\times \left(\sum_r \langle 0 | |O_2|^2 | r \rangle \langle r | |O_1|^2 | 0 \rangle e^{-E_r n_4} - \left(\sum_m \langle 0 | O_2 | m \rangle \langle m | O_1 | 0 \rangle e^{-E_m n_4} \right)^2 \right)^{-1/2}. \end{aligned} \quad (9.3)$$

Taking the limit $n_4 \rightarrow \infty$ reduces the numerator and denominator to just the ground state. Then, we see that the time dependence of the signal-to-noise ratio becomes [73]

$$\frac{\langle F \rangle}{\sigma_F} \propto e^{-(E_1 - E_{1'}/2) n_4}, \quad (9.4)$$

where E_1 and $E_{1'}$ are the ground state of $\langle F \rangle$ and $\langle F^2 \rangle$, respectively. Then, if $E_1 > E_{1'}/2$, the signal is lost exponentially fast with time. There are exceptional cases, however, for which $E_{1'} = 2E_1$ and the signal-to-noise ratio keeps constant. The latter happens, for example, when we consider the single pion state for E_1 and the corresponding two pions for $E_{1'}$.

For our particular case, we need to improve the signal of the renormalised and improved vector correlator $G(n_4)$ defined in chapter 6. Since the spectral representation of the forward-propagating correlator is, for $n_4 > 0$, a sum of exponentials [29]

$$G(n_4) = A_1 e^{-E_1 n_4} + A_2 e^{-E_2 n_4} + \dots, \quad (9.5)$$

the formal problem that we have to solve is to find the parameters A_i , E_i with sufficient precision and substitute the long time distance of the correlator. The simplest approach is the so-called single-state fit, which we study in section 9.1. It takes advantage of the fact that, in heavy pion-mass ensembles for $n_4 \gg 1$, the correlator $G(n_4)$ can be represented by the ground state alone and, therefore, it suffices fitting a single exponential to the correlator. However, for lighter pion-mass ensembles, several states contribute substantially to the correlator at all times. Unfortunately, a direct fit of several exponentials can lead to unreliable results, and several methods have been proposed for this scenario. The procedure that we use is known as the bounding method, see section 9.2, which as its name suggests sets lower and upper bounds for the correlator at every time-slice and, whenever the bounds coincide, they can be used to substitute the original data of the correlator, increasing its precision. Another methods exist, although we do not use them [29]. One option is to carry out a Bayesian analysis, where instead of minimising a χ^2 function, one minimises a modified version $\chi^2 + \lambda \phi$, where λ is a real parameter and ϕ is a stabilizing function [257] containing a certain prejudice of what the actual parameters should be (for instance, one may start with a fit to a single exponential and use the results as *Ansätze* for a two exponential fit and so on [258]). Of course, one tries to find areas where the result is independent of λ . Another option is the so-called maximum entropy method employed in [259, 260], where one writes the correlator as a Laplace transform of a given spectral density $\rho(E)$. Given the data, one tries to reconstruct $\rho(E)$ via the Bayesian approach, with a particular stabilizer function ϕ . A third option is to consider a matrix of interpolators with the target quantum numbers and solve its corresponding generalized eigenvalue problem (GEVP) [261]. The more interpolators are considered, the more excited states can be reliably disentangled. We employ the single-exponential fit and the bounding method, rather than either of these other approaches, because the former are simpler and require less information about the spectrum in our ensembles.

9.1 The single-state fit

For heavy-pion mass ensembles with $n_4 \gg 1$, the ground state will dominate the correlator, albeit where precisely will depend on the amplitudes A_i and the spectrum E_i . Therefore, if we know the parameters A_1 and E_1 , we can substitute the original noisy tail of the two-point function with the ground state. The expression to fit the correlator depends on the boundary conditions (see section 3.4.4),

$$G(n_4) = \begin{cases} Ae^{-En_4}, & \text{with OBC,} \\ 2Ae^{-ET/2} \cosh(-E(T/2 - n_4)), & \text{with PBC,} \end{cases} \quad (9.6)$$

where T is the number of time-slices of the correlator and E and A the fit parameters. Note that we differentiate between the real ground state parameters of the correlator, A_1 and E_1 , and the fit parameters A and E , because at any given time there will always be some remnant of excited states and, therefore, the fit parameters are contaminated by them. Also, the cosh expression in eq. (9.6) is only valid for even correlation functions under time-reversal and periodic boundary conditions. Instead, we could have a nucleon state $\langle N^\dagger N \rangle$, which is not an eigenfunction of time reversal and is described by exponentials, or a vector-tensor state $\langle VT \rangle$ like those used for the improvement in chapter 6, which is odd under time-reversal and requires a sinh instead. Equation (9.6) allows us to create a new estimate of the correlator with reduced uncertainty,

$$G(n_4) = \begin{cases} \text{data,} & n_4 < n_{4,\text{cut}}, \\ Ae^{-En_4}, & n_4 \geq n_{4,\text{cut}}. \end{cases} \quad (9.7)$$

To obtain the parameters A and E of eqs. (9.6) and (9.7), we perform a correlated fit of eq. (9.6) to a time interval of the original two-point function minimizing the χ^2 function

$$\chi^2 = (G_{\text{data}} - G_{\text{model}}) \text{Cov}^{-1} (G_{\text{data}} - G_{\text{model}}), \quad (9.8)$$

where Cov is the sample covariance matrix, G_{data} is the original data and G_{model} is eq. (9.6). For such a fit, we have to detail an algorithm to find the appropriate fit interval. On top of this, we need to set $n_{4,\text{cut}}$.

Let us start with the fit interval. By default, the length of the time interval is set to 0.4 fm, although this value is rounded to the closest number of lattice sites for each lattice spacing, so we only need an algorithm to find the left limit. We choose the latter based on two criteria: a proxy fit quality, which tells us where the single-exponential approximation is (more) valid, and the uncertainty of the correlator in the interval. The proxy fit quality is obtained as follows. First, one computes the effective mass of the correlator $G(n_4)$ for all time-slices [29],

$$aM_{ef} = \log \frac{G(n_4)}{G(n_4 + 1)}. \quad (9.9)$$

Looking to eq. (9.5), eq. (9.9) behaves like a decaying exponential until it reaches $M_{ef} \sim E_1$, where it shows a plateau. Therefore, the effective mass is a proxy that tells us where

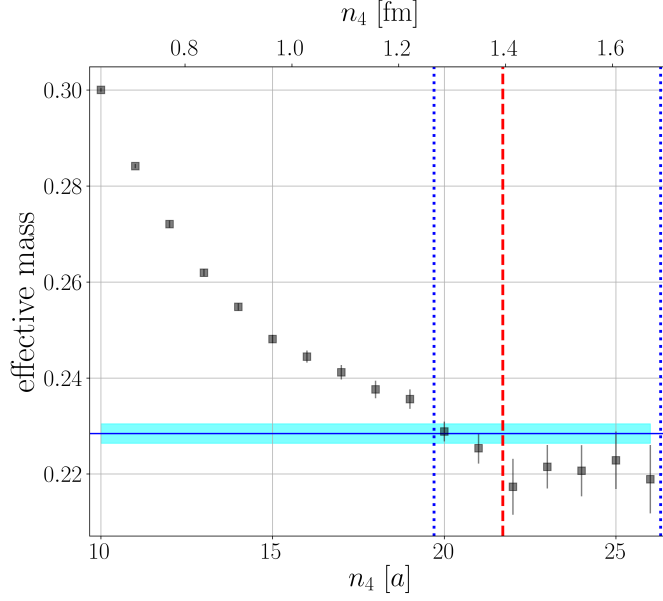


Figure 9.1: Effective mass plot of the isovector channel evaluated on ensemble E250. The black squares with errorbars represent the effective mass computed from the original correlator using eq. (9.9). The cyan band represents the single exponential fit parameter E in lattice units as given in eq. (9.6). The blue, dotted, vertical lines indicate the single exponential fit interval, and the dashed, vertical, red line shows where the original correlator is to be substituted by the result of the fit.

the single-exponential model starts to be valid. To choose the best range, we perform an uncorrelated fit of a constant to the effective mass in all possible time intervals. This constant plays the role of the average effective mass in the interval under consideration. For each fit interval we obtain a χ^2

$$\chi_{ef}^2 = \sum_{n_4 \in \text{interval}} \frac{(M_{ef}(n_4) - E[M_{ef}])^2}{\sigma_{M_{ef}}^2(n_4)}, \quad (9.10)$$

where $\sigma_{M_{ef}}(n_4)$ is the standard deviation of the effective mass on each time-slice and $E[M_{ef}]$ is the fit parameter. However, choosing the lowest χ_{ef}^2 to select the fit interval is not enough because there is one clear pathological case. Towards $n_4 \gg 1$ the uncertainty of the correlator increases, so that the χ_{ef}^2 will be minimum there. However, fitting noise will not produce a more precise estimate of the two-point function. Therefore, we need to balance the χ_{ef}^2 with a second criterion. We check that the time-slices of the interval are more precise than a certain threshold, which we set depending on the ensemble and its statistics. Then, we select the interval that fulfils the second criterion and has the smallest χ_{ef}^2 to perform the single exponential fit of eq. (9.8). Obviously, this algorithm allows for an educated initial guess of the fit interval, and we perform the fit in eq. (9.8) until p-value > 0.05 , moving both interval limits by one time-slice, first probing larger n_4 , then

smaller.

After the fit has been carried out, the next step is to select the time-slice $n_{4,\text{cut}}$. To find it automatically, we inspect the data and set an algorithm. Using the fit parameters A and E , we compute the deviation between the model and the data for both, the expectation value and the statistical error. Then, we compute the expression

$$\left(\frac{\Delta G_{\text{data}}(n_4) - \Delta G_{\text{model}}(n_4)}{\Delta G_{\text{data}}(n_4)} \right)^2 + \left(\frac{G_{\text{data}}(n_4) - G_{\text{model}}(n_4)}{G_{\text{data}}(n_4)} \right)^2, \quad (9.11)$$

where G_{model} is given by eq. (9.6), G_{data} is the original correlator, and ΔG_{model} and ΔG_{data} are their corresponding uncertainties. $n_{4,\text{cut}}$ is chosen to minimise eq. (9.11). The logic behind eq. (9.11) is that we look for time-slices where the model is close to the data and, at the same time, the uncertainty of the model is close to that of the original correlator.

Note that there are two main reasons why $n_{4,\text{cut}}$ and the fit interval should be found automatically. First, we should avoid a bias if possible and, second, we need to perform fits for all ensembles, isospins, improvement derivatives (see chapters 6 and 12) and both discretisations, resulting in several hundreds of fits. As a side remark, it is possible that, after fitting the original correlator, we have to extend eq. (9.7) beyond the original $T/2$ if the original correlator is not compatible with zero there. This can happen if the physical size of the box is very small and, in practice, we only had to extend the ensemble B450.

An example of the single-exponential method is shown in fig. 9.2, which depicts the integrand of the isoscalar sVPF evaluated on ensemble E250 at $Q^2 = 1 \text{ GeV}^2$. The original correlator appears in black, the single-state fit in orange, and the bounding method in red (see section 9.2). The upper subplot shows the integrand of the sVPF, and the lower indicates the noise-to-signal ratio. The solid vertical line marks $n_{4,\text{cut}}$, and the dashed-dotted lines indicate the fit interval. In fig. 9.2 we can see that, indeed, eq. (9.11) allows a smooth transition between the original data and the single-exponential fit; neither the integrand nor the uncertainty present noticeable steps. Also, the noise-to-signal ratio shows a very clear exponential increase (linear behaviour) between 1 fm and 2 fm, as we anticipated in eq. (9.4). Finally, we see that the uncertainty of the single-exponential method (and of the bounding method as well) is negligible in comparison with the original correlator.

After performing the fit, it is possible to do a sanity check. Figure 9.1 shows a comparison, for ensemble E250, between the effective mass as computed in eq. (9.9) (black squares) and the mass obtained from the single exponential fit to the correlator (cyan band). We see that the results tend to be similar, as both methods are based on the ground state approximation. However, they do not need to agree exactly, because the single exponential fit includes the correlations between the data points. Even if we perform a fit in both cases, lattice artefacts might make the results slightly disagree. The figure also shows the fit interval (blue, dotted lines) and $n_{4,\text{cut}}$ (red, dashed line). The main objective of this plot is to show that the fit interval roughly coincides with a plateau region in the effective mass, and that the model substitutes only the most noisy tail of the correlator. Just note, the effective mass and the other lines in the plot come from different methods, and they are only shown together as a comparison.

Finally, we discuss the results of the single exponential fit for every isospin, shown in

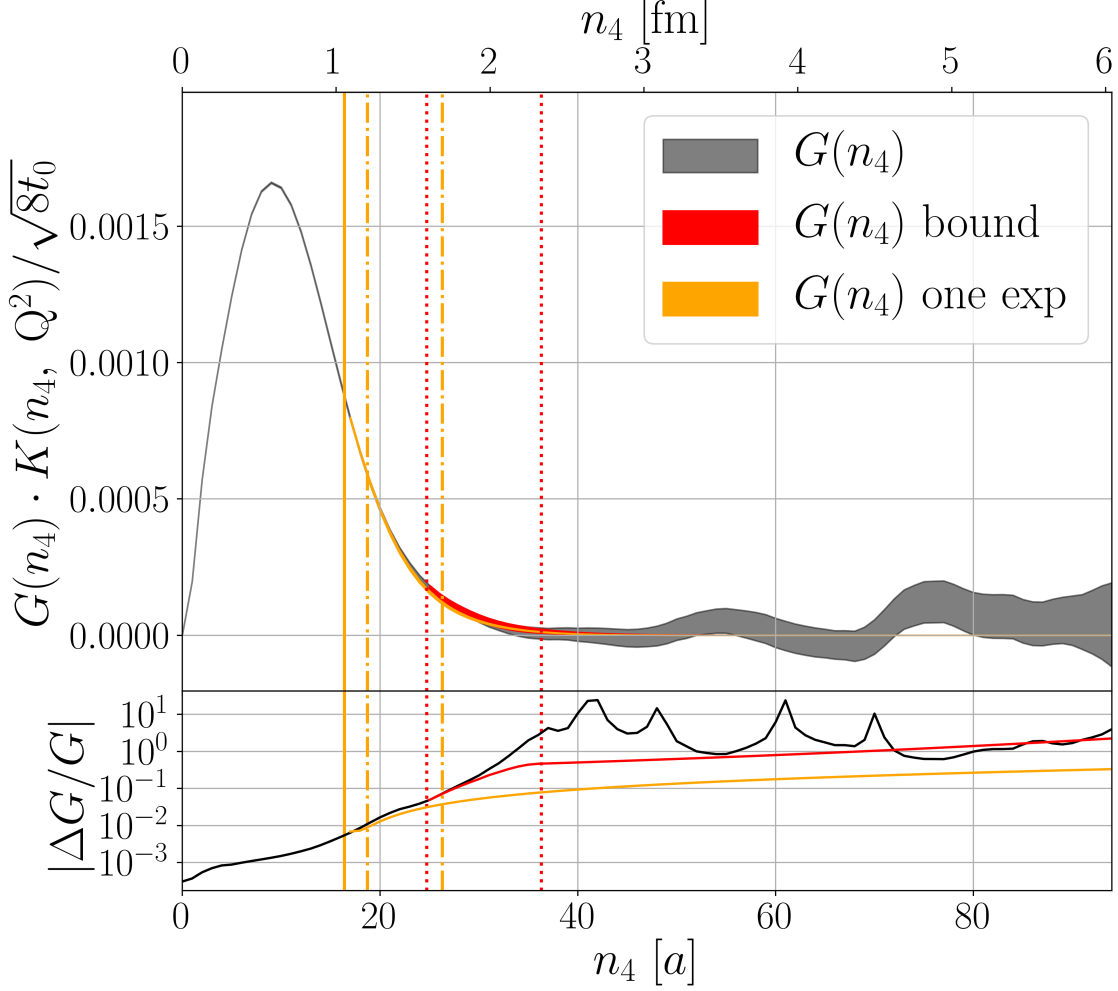


Figure 9.2: E250 isoscalar VPF integrand at 1 GeV^2 . At long distances, we compare the single exponential fit and the bounding method. The upper plot shows the integrand of the original data (black band), while the lower subplot depicts the relative error of the correlator. The solid vertical line indicates the point where we start substituting the original data by the single exponential. The fit is performed between the two dotted-dashed vertical lines. The red vertical lines show the interval averaged in the bounding method. In the lower subplot, one can clearly see the expected exponential rise of the noise-to-signal ratio between 1 fm and 2 fm before the noise completely dominates the correlator. The spikes in the lower subplot indicate a change of sign of the correlator.

Ensemble	$\Delta_{33}n_4$ [fm]	$a^3 A_{33}$	aE_{33}	$\Delta\hat{\Pi}_{33}$	$\Delta\sigma_{33}$
H101	1.55 - 2.07	91 (4)	0.3724 (27)	-0 (0)	-0 (0)
H102	1.55 - 2.07	89 (6)	0.3625 (37)	-2 (0)	-0 (4)
H105	1.73 - 2.25	86 (22)	0.3501 (126)	1 (0)	-1 (6)
N101	1.38 - 1.90	70 (5)	0.3371 (43)	-1 (0)	1 (4)
C101	1.30 - 1.81	68 (3)	0.3261 (32)	-4 (0)	-2 (10)
B450	1.22 - 1.68	72 (1)	0.3395 (15)	2 (0)	0 (1)
S400	1.37 - 1.83	58 (3)	0.3193 (34)	-5 (0)	-0 (2)
N451	1.53 - 1.98	48 (3)	0.3006 (35)	-1 (0)	-1 (7)
D450	1.37 - 1.83	45 (2)	0.2878 (23)	-1 (0)	-3 (23)
H200	1.22 - 1.67	43 (2)	0.2899 (30)	-5 (0)	-0 (1)
N202	1.22 - 1.67	41 (1)	0.2820 (19)	-3 (0)	-1 (8)
N203	1.29 - 1.74	38 (2)	0.2733 (22)	-3 (0)	-0 (0)
N200	1.35 - 1.80	32 (2)	0.2598 (27)	-2 (0)	-0 (2)
D200	1.35 - 1.80	29 (2)	0.2468 (29)	-13 (0)	-2 (13)
E250	1.29 - 1.86	22 (1)	0.2272 (22)	-81 (2)	-23 (61)
N300	1.25 - 1.69	21 (1)	0.2275 (23)	-6 (0)	-1 (7)
N302	1.20 - 1.64	20 (1)	0.2198 (20)	-7 (0)	1 (6)
J303	1.25 - 1.74	14 (1)	0.1977 (18)	-20 (1)	0 (2)
E300	1.20 - 1.69	13 (1)	0.1871 (18)	-18 (1)	-16 (50)

Table 9.1: Result of the single-state fit to $\hat{\Pi}_{33}$ at 1 GeV^2 . We indicate the CLS ensemble, the fit interval in fm and the fit parameters of eq. (9.6). The column $\Delta\hat{\Pi}_{33}$ shows the variation of the central value of $\hat{\Pi}_{33}$ multiplied by 10^5 when applying eq. (9.6). The first number is the absolute shift, and then the percentage this shift represents with respect to the original value of $\hat{\Pi}$. The same information is given for the uncertainty in the column $\Delta\sigma_{33}$.

tables 9.1 to 9.3. In table 9.1, we show the result for the isovector on each ensemble, including the fit interval in fm, the fit parameters $a^3 A \times 10^5$ and aE in lattice units, the variation of the central value of the sVPF $\times 10^5$ with respect to table 7.2 (the absolute value first, and the corresponding percentage in parenthesis); and the reduction of the uncertainty, first in absolute value and then in percentage. It is noteworthy that the central value varies only marginally — in E250, for example, just 2%, while the change in all other ensembles does not reach 1%. The reduction of the uncertainty greatly depends on the ensemble, although the lightest-pion-mass ensembles benefit the most. E250’s error diminishes by 60%, E300 by 50% and D450 by 20%. Given the fact that these ensembles have, potentially, several close lying states with similar exponential behaviour —something that can not be overcome with only one exponential—, it is questionable whether the systematic uncertainty associated with this method is negligible. In this situation, fitting to a single exponential gives us an effective amplitude and energy, which do not coincide

with neither the amplitudes nor the energies in eq. (9.5). The energy parameter will tend to be overestimated, suppressing the correlator faster than other, more exact, methods. The results for the quark-connected isoscalar channel, shown in table 9.2, are very similar to the isovector case, as the long time behaviour of both correlators is given by the light propagator, as one can see from eq. (6.38), dropping the quark-disconnected part.

The quark-disconnected piece, summarized in the same table, is obtained by simply subtracting the modelled quark-connected isoscalar contribution from the modelled full isoscalar channel. This method is not only simpler, but also yields a smaller uncertainty than performing a dedicated study of the quark-disconnected piece. Most of the original integral to the quark-disconnected part comes from large, albeit spurious contributions at long distances; therefore, substituting the tail varies wildly the central value and uncertainty of the quark-disconnected contribution. The results would be similar if, instead of using this method, we cut out the correlator where the noise dominates the signal. In table 9.2, we give the corresponding results for the full isoscalar. We see variations of 8% in the central value of E250, while other ensembles have much milder changes. The most relevant effect of the tail treatment is the reduction in uncertainty, above 90% on E250, and above 50% for many others. The full 08 component, its quark-connected part 08c, and its quark-disconnected part 08d, are shown in table 9.3. $\hat{\Pi}_{08}$ is the most affected by the tail treatment, and presents a similar behaviour to $\hat{\Pi}_{88}$ because both consist of a quark-connected and quark-disconnected pieces.

From the use of the single exponential fit, we conclude that it is sufficient to greatly reduce the noise of the quark-disconnected data but, for the quark-connected component, it can only improve those ensembles with the smallest statistics. Besides, this method has an unknown systematic error. This can be seen from the quark-connected contributions in tables 9.1 to 9.3, where we observe that all expected values of $\hat{\Pi}$ tend to decrease after applying the single exponential. This trend increases towards the chiral limit, where there are more states of similar energy and the single exponential approximation starts to break down even at long time separations. This effect was to be expected and there is a systematic uncertainty associated with it that we do not try to estimate directly. Instead, we use the bounding method given in section 9.2 to improve the signal of the correlator.

After this section, the reader might be thinking that it is inconsistent to give results for the lighter pion-mass ensembles using the single exponential fit. The reasons to do so are various. The method does not require prior knowledge of the spectrum of the correlator and it has been historically widely used, as older simulations tend to have heavier pion masses. Also, after implementing this method, it is simple to apply it for every ensemble and, then, to see the expected systematic effect towards the chiral limit. After realising that this method is not enough for the most valuable ensembles, and putting some effort to find the bounds of the bounding method, we can replace the single-exponential fit by the superior bounding method. As a side remark, we could not find noticeable differences between the fits to the local and symmetric, point-split discretisations, and we only show the results for the latter. Finally, although the tables and plots are only given at one momentum, the behaviour of the correlator seems to be consistent in the range from 0 GeV^2 to 10 GeV^2 , and only for very small virtuality does the tail treatment become more relevant.

Ensemble	$\Delta_{88} n_4$ [fm]	$a^3 A_{88}$	$a E_{88}$	$\Delta \hat{\Pi}_{88}$	$\Delta \sigma_{88}$	$\Delta_{08} n_4$ [fm]	$a^3 A_{88c}$	$a E_{88c}$	$\Delta \hat{\Pi}_{88c}$	$\Delta \sigma_{88c}$	$\Delta \hat{\Pi}_{88d}$	$\Delta \sigma_{88d}$
H101	1.47 - 1.99	97 (3)	0.3803 (22)	-3 (0)	-0 (3)	1.55 - 2.07	91 (4)	0.3724 (27)	-0 (0)	-0 (0)	-1 (117)	-4 (84)
H102	1.47 - 1.99	76 (11)	0.3705 (81)	12 (0)	-20 (59)	1.47 - 1.99	95 (3)	0.3791 (19)	-1 (0)	-0 (1)	12 (91)	-24 (81)
H105	1.55 - 2.16	85 (4)	0.3764 (32)	18 (1)	-16 (66)	1.47 - 1.99	80 (4)	0.3706 (30)	-3 (0)	0 (1)	20 (48)	-21 (91)
N101	1.38 - 1.90	95 (8)	0.3830 (52)	1 (0)	-16 (64)	1.73 - 2.25	55 (6)	0.3485 (52)	-0 (0)	-1 (5)	2 (3)	-19 (81)
C101	1.47 - 1.99	95 (8)	0.3830 (52)	1 (0)	-16 (64)	1.73 - 2.25	55 (6)	0.3485 (52)	-0 (0)	-1 (5)	2 (3)	-19 (81)
B450	1.37 - 1.83	65 (2)	0.3366 (24)	1 (0)	-5 (32)	1.22 - 1.68	72 (1)	0.3395 (15)	2 (0)	0 (1)	4 (155)	-12 (93)
S400	1.37 - 1.83	56 (4)	0.3321 (35)	1 (0)	-5 (40)	1.37 - 1.83	65 (2)	0.3369 (22)	-4 (0)	-0 (0)	3 (13)	-7 (76)
N451	1.53 - 1.98	55 (3)	0.3315 (36)	67 (3)	-22 (74)	1.83 - 2.37	45 (5)	0.3212 (43)	-0 (0)	-0 (2)	70 (60)	-25 (87)
D450	1.37 - 1.83	55 (3)	0.3315 (36)	67 (3)	-22 (74)	1.68 - 2.14	49 (4)	0.3214 (38)	-3 (0)	-1 (7)		
H200	1.48 - 1.93	39 (2)	0.2859 (20)	9 (0)	-2 (15)	1.22 - 1.67	43 (2)	0.2899 (30)	-5 (0)	-0 (1)		
N202	1.48 - 1.93	36 (2)	0.2848 (32)	-17 (1)	-9 (56)	1.22 - 1.67	41 (1)	0.2820 (19)	-3 (0)	-1 (8)		
N203	1.48 - 1.93	31 (4)	0.2797 (66)	6 (0)	-22 (72)	1.48 - 1.93	35 (2)	0.2853 (18)	-0 (0)	-0 (1)	9 (64)	-4 (81)
D200	1.48 - 2.18	43 (2)	0.2956 (33)	-201 (8)	-113 (92)	1.48 - 1.93	27 (2)	0.2826 (22)	-1 (0)	-0 (0)	-16 (656)	-12 (84)
E250	1.16 - 1.61	43 (2)	0.2956 (33)	-201 (8)	-113 (92)	1.41 - 1.86	20 (1)	0.2703 (28)	-5 (0)	-0 (5)	11 (20)	-24 (81)
N300	1.25 - 1.69	21 (1)	0.2307 (15)	3 (0)	-2 (15)	1.25 - 1.69	21 (1)	0.2275 (23)	-6 (0)	-1 (7)	-171 (321)	-113 (94)
N302	1.34 - 1.79	16 (1)	0.2224 (23)	-22 (1)	-25 (73)	1.25 - 1.69	21 (1)	0.2308 (14)	-3 (0)	0 (3)	6 (186)	-5 (69)
J303	1.15 - 1.59	17 (1)	0.2239 (23)	52 (2)	-48 (83)	1.39 - 1.84	15 (1)	0.2164 (15)	-7 (0)	-0 (2)	-17 (129)	-28 (88)
E300	1.15 - 1.59	17 (1)	0.2239 (23)	52 (2)	-48 (83)	1.34 - 1.79	13 (1)	0.2109 (22)	-11 (0)	-4 (39)	63 (52)	-49 (87)

Table 9.2: Single-state fit to the isoscalar channel $\hat{\Pi}_{88}$, its quark-connected part $\hat{\Pi}_{88c}$, and its quark-disconnected part $\hat{\Pi}_{88d}$, at 1 GeV². $\hat{\Pi}_{88d} = \hat{\Pi}_{88} - \hat{\Pi}_{88c}$. The same format as in table 9.1 is used.

Ensemble	$\Delta_{08} n_4$ [fm]	$a^3 A_{08}$	$a E_{08}$	$\Delta \hat{\Pi}_{08}$	$\Delta \sigma_{08}$	$\Delta_{08} n_4$ [fm]	$a^3 A_{08c}$	$a E_{08c}$	$\Delta \hat{\Pi}_{08c}$	$\Delta \sigma_{08c}$	$\Delta \hat{\Pi}_{08d}$	$\Delta \sigma_{08d}$
H101	1.30 - 1.81	5 (2)	0.3012 (202)	-14 (8)	-28 (79)	1.64 - 2.16	7 (2)	0.3156 (108)	0 (0)	-0 (7)	-19 (371)	-31 (85)
H102	1.21 - 1.73	8 (3)	0.2900 (225)	-33 (8)	-86 (82)	1.47 - 2.16	11 (2)	0.3027 (96)	3 (1)	-1 (6)	-46 (231)	-86 (82)
H105	1.30 - 1.81	8 (3)	0.2900 (213)	167 (81)	-82 (86)	1.38 - 1.90	8 (1)	0.2805 (68)	7 (2)	1 (13)	166 (74)	-80 (84)
N101	1.47 - 1.99	39 (56)	0.3662 (448)	29 (7)	-56 (78)	1.55 - 2.07	13 (2)	0.2867 (71)	4 (1)	-1 (10)	111 (71)	-54 (78)
C101	1.47 - 1.99	39 (56)	0.3662 (448)	29 (7)	-56 (78)	1.55 - 2.07	13 (2)	0.2867 (71)	4 (1)	-1 (10)	111 (71)	-54 (78)
B450	1.15 - 1.60	2 (0)	0.2311 (117)	-39 (17)	-54 (86)	1.30 - 1.76	2 (0)	0.2429 (68)	5 (2)	0 (7)	-46 (111)	-54 (86)
S400	1.07 - 1.53	3 (0)	0.2260 (67)	20 (6)	-27 (72)	1.53 - 1.98	6 (1)	0.2568 (52)	3 (1)	-0 (1)	-1 (3)	-27 (73)
N451	1.30 - 1.76	7 (4)	0.2555 (249)	185 (61)	-59 (70)	1.53 - 2.21	10 (1)	0.2571 (44)	-2 (0)	-2 (27)	198 (71)	-64 (76)
D450	1.30 - 1.76	7 (4)	0.2555 (249)	185 (61)	-59 (70)	1.53 - 2.21	10 (1)	0.2571 (44)	-2 (0)	-2 (27)	198 (71)	-64 (76)
H200	1.22 - 1.67	2 (1)	0.2256 (139)	29 (18)	-26 (75)	1.41 - 1.86	2 (0)	0.2182 (64)	3 (1)	0 (3)	26 (51)	-28 (81)
N202	1.16 - 1.61	2 (1)	0.2034 (118)	-30 (8)	-43 (75)	1.22 - 1.67	3 (0)	0.2091 (34)	7 (2)	-0 (0)	-39 (1237)	-46 (80)
N200	1.16 - 1.61	4 (1)	0.2084 (111)	9 (2)	-70 (76)	1.35 - 1.80	5 (0)	0.2089 (39)	5 (1)	-0 (6)	4 (4)	-71 (78)
D200	1.16 - 1.61	4 (2)	0.2037 (178)	-190 (24)	-260 (88)	1.29 - 1.74	4 (0)	0.1867 (27)	-13 (2)	-12 (55)	-176 (893)	-265 (90)
E250	1.16 - 1.61	4 (2)	0.2037 (178)	-190 (24)	-260 (88)	1.29 - 1.74	4 (0)	0.1867 (27)	-13 (2)	-12 (55)	-176 (893)	-265 (90)
N300	1.00 - 1.44	1 (0)	0.1495 (90)	63 (38)	-19 (55)	1.34 - 1.79	1 (0)	0.1791 (70)	0 (0)	0 (3)	66 (175)	-22 (64)
N302	1.05 - 1.49	2 (0)	0.1660 (66)	96 (30)	-96 (86)	1.44 - 1.89	2 (0)	0.1617 (33)	3 (1)	0 (4)	89 (56)	-97 (88)
J303	1.00 - 1.44	1 (0)	0.1276 (88)	300 (77)	-148 (73)	1.15 - 1.59	2 (0)	0.1494 (24)	28 (4)	-7 (37)	272 (93)	-151 (74)
E300	1.00 - 1.44	1 (0)	0.1276 (88)	300 (77)	-148 (73)	1.15 - 1.59	2 (0)	0.1494 (24)	28 (4)	-7 (37)	272 (93)	-151 (74)

Table 9.3: Single-state fit to the full 08 component $\hat{\Pi}_{08}$, its quark-connected part $\hat{\Pi}_{08c}$, and its quark-disconnected part $\hat{\Pi}_{08d}$, at 1 GeV². $\hat{\Pi}_{08d} = \hat{\Pi}_{08} - \hat{\Pi}_{08c}$. The same format as in table 9.1 is used.

9.2 The bounding method

The bounding method, described in [173, 107], substitutes the correlator $G(n_4)$ at times beyond $n_{4,\text{cut}}$ with $G(n_{4,\text{cut}})$ multiplied by a decaying exponential with time, where $n_{4,\text{cut}}$ does not need to be the same as for the single-exponential fit of section 9.1. By giving the appropriate exponents, we obtain either a lower or an upper bound of $G(n_4)$ [173, 107],

$$0 \leq G(n_{4,\text{cut}})e^{-M_{ef}(n_4-n_{4,\text{cut}})} \leq G(n_4) \leq G(n_{4,\text{cut}})e^{-E_N(n_4-n_{4,\text{cut}})}. \quad (9.12)$$

The effective mass M_{ef} is given in eq. (9.9) and, in its simplest form, $E_N = E_1$ —the ground state of the channel—. Once both bounds are obtained, we can compute the sVPF for many $n_{4,\text{cut}}$. We obtain an improved estimate of the tail of the correlator by averaging both bounds where they coincide within uncertainties in a series of $n_{4,\text{cut}}$. Figure 9.4 shows an example of this procedure for the isovector and isoscalar components. The orange points use the upper bound of eq. (9.12) beyond $n_{4,\text{cut}}$ to compute the sVPF, and the blue points use the effective mass. Depending on the channel, both bounds coincide beyond a certain point. The vertical lines indicate the interval of $n_{4,\text{cut}}$ that we average to produce the improved estimate, which is shown by the cyan band. Interestingly enough, if we were wrong in E_N and underestimate the spectrum by a certain amount, the consequence will be that the plateau where both bounds coincide will appear at longer distances, therefore making a less aggressive cut of the data, and introducing a smaller systematic error. At this point, we do not have a dedicated and up-to-date spectroscopy analysis of the ensembles included, so we decide to estimate the lightest E_1 possible for every channel.

For the isovector channel, E_1 is the minimum of either the ρ meson mass M_ρ or the two-pion state $E_{\pi\pi}$ with angular momentum $J = 1$. To estimate them, we use our finite size effects analysis, described in chapter 10. In some cases, there are results for M_ρ from the spectroscopy study [218, 262], and we center the bootstrap distribution of M_ρ around the central value $M_\pi \times M_\rho/M_\pi$, where the ratio was obtained from [218, 262], and M_π alone was computed with the current statistics using [57]. We do not use the masses obtained from the single exponential fit because the upper and lower bounds would plateau at the same time, given the fact that both bounds rely on the approximation that the ground state dominates the correlator. The ensembles where $E_{\pi\pi}$ is the ground state are C101, D450, D200, E250 and E300, as can be seen in table 9.4. We cross-check that the two-pion state used is lighter than its non-interacting version $2(M_\pi^2 + (2\pi/L)^2)^{1/2}$, and therefore it is a more conservative choice. The isoscalar and 08 quark-connected contributions have the same ground state as the isovector component because their long distance behaviour is dominated by the light correlators. For the full isoscalar contribution, we should compare the ω meson mass with the interacting three-pion mass. Obtaining both quantities would require a detailed spectroscopy analysis that we lack at the moment. Instead, we compare between M_ρ and the lightest non-interacting three-pion state with vector isoscalar quantum numbers, given in [263] as

$$E_{\pi\pi\pi} = 2\sqrt{M_\pi^2 + \left(\frac{2\pi}{L}\right)^2} + \sqrt{M_\pi^2 + 2\left(\frac{2\pi}{L}\right)^2}. \quad (9.13)$$

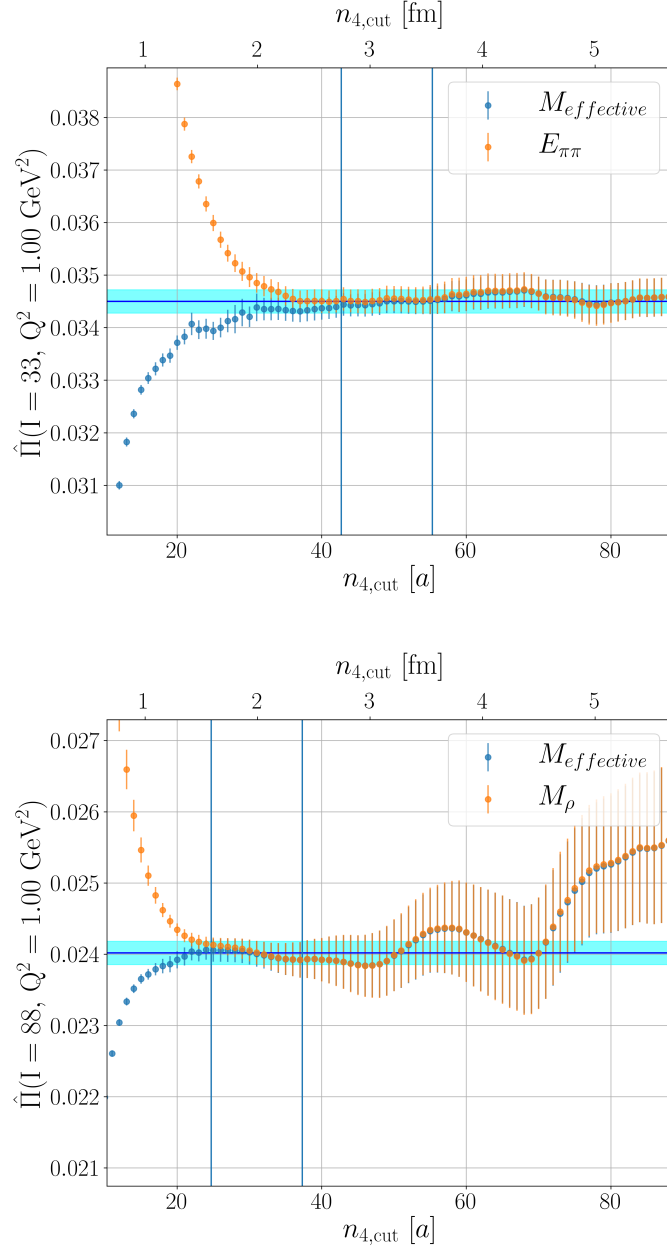


Figure 9.3: Upper plot, bounding method for ensemble E250, isovector component. The upper bound is computed with the ground state obtained from the finite-size effects analysis presented in chapter 10. The lower bound is computed using the effective mass at every time-slice. The vertical lines show the time-slices where the lower and upper bounds are averaged. The horizontal line and the band show the expected result and uncertainty of the averaged correlator. Lower plot, bounding method for ensemble E250, isoscalar component. The upper bound is computed with the ρ meson mass. The effective mass at the particular time-slice is used for the lower bound.

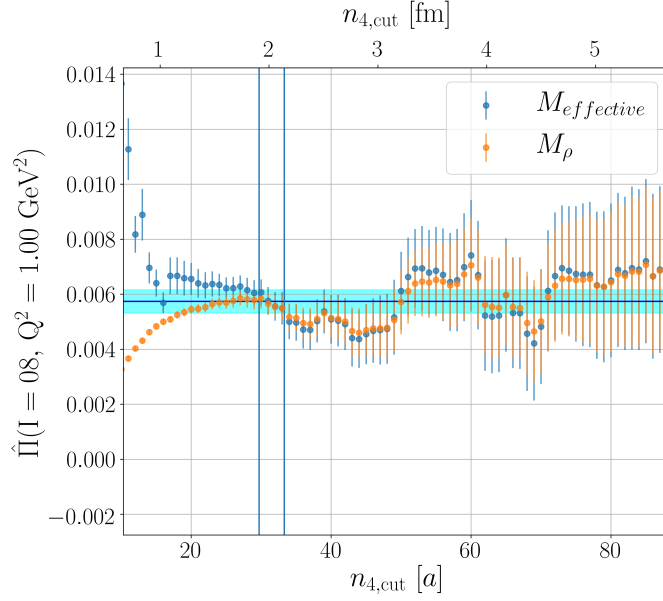


Figure 9.4: Bounding method applied to $\hat{\Pi}_{08}$ in ensemble E250. As explained in the text, $M_{\text{effective}}$ marks an upper bound and M_ρ gives the lower bound, the opposite of eq. (9.12).

Despite not belonging to the isoscalar channel, we decided to use M_ρ instead of the ω meson mass M_ω for several reasons: First, remember that we look for a conservative estimate of the spectrum and, since $M_\rho \lesssim M_\omega$ at physical pion mass, the ρ meson mass gives an educated guess of the ω meson mass and bounds it from below; second, the isoscalar correlator is noisier than the isovector channel, which makes more uncertain the masses computed from, for example, a fit; third, we can not apply our finite volume analysis to roughly estimate the isoscalar spectrum. Then, using M_ρ as a proxy for M_ω is reasonable, but one should bear in mind that our effort here is giving a lower bound to what E_1 in eq. (9.12) might be, and not telling what the true spectrum of the correlator is. For our ensembles, we find that M_ρ is always lighter than the three-pion state due to the extra momentum needed to get the correct quantum numbers in the latter. Therefore, we use M_ρ for the upper bound in eq. (9.12). Subtracting the quark-connected 88 component from the full isoscalar contribution, we find an improved estimate for the $\ell - s, \ell - s$ quark-disconnected piece. For the 08 component, the situation is a bit different, $G_{08}(n_4) \sim A_1 \exp(-E_1 n_4) + A_2 \exp(-E_2 n_4)$, with $A_1 > 0$, $A_2 < 0$, $E_2 > E_1$, and E_1 is the same ground state that we used for the isoscalar component [234]. In this situation, $G_{08}(n_4)$ approaches the ground state $A_1 \exp(-E_1 n_4)$ from below, so that $G_{08}(n_{4,\text{cut}}) \exp(-E_1(n_4 - n_{4,\text{cut}}))$ is a lower bound. In a similar way, M_{ef} is lighter than E_1 , such that $G_{08} \exp(-M_{\text{ef}}(n_{4,\text{cut}})(n_4 - n_{4,\text{cut}}))$ is an upper bound. Taking the difference between the 08 full and quark-connected parts, we find an improved estimate for the $2\ell + s, \ell - s$ quark-disconnected contribution. The spectrum studied for each ensemble appears in table 9.4. From left to right, we show the pion mass, the ρ meson mass, the two interacting pions state and the three non-interacting pions energy. All in lattice units and

Ensemble	aM_π	aM_ρ	$aE_{\pi\pi}$	$aE_{\pi\pi\pi}$
H101	0.1830 (5)	0.3749 (15)	0.5427 (6)	0.8695 (9)
H102	0.1546 (5)	0.3683 (19)	0.5076 (6)	0.8177 (9)
H105	0.1234 (13)	0.3373 (94)	0.4799 (52)	0.7677 (19)
N101	0.1222 (5)	0.3339 (38)	0.3713 (20)	0.5799 (10)
C101	0.0960 (6)	0.3260 (35)	0.3090 (16)	0.5332 (10)
B450	0.1605 (4)	0.3360 (15)	0.5135 (5)	0.8280 (7)
S400	0.1358 (4)	0.3235 (25)	0.4863 (6)	0.7866 (7)
N451	0.1108 (3)	0.3011 (27)	0.3517 (4)	0.5588 (5)
D450	0.0836 (4)	0.2962 (19)	0.2536 (5)	0.4199 (7)
H200	0.1363 (5)	0.2933 (27)	0.4909 (18)	0.7874 (7)
N202	0.1342 (3)	0.2830 (14)	0.3785 (4)	0.6035 (6)
N203	0.1124 (2)	0.2678 (30)	0.3506 (3)	0.5617 (4)
N200	0.0922 (3)	0.2521 (34)	0.3280 (3)	0.5271 (4)
D200	0.0655 (3)	0.2516 (20)	0.2277 (8)	0.3896 (4)
E250	0.0422 (2)	0.2515 (40)	0.1546 (3)	0.2575 (4)
N300	0.1067 (3)	0.2238 (20)	0.3420 (5)	0.5513 (6)
N302	0.0875 (3)	0.2150 (29)	0.3207 (4)	0.5197 (5)
J303	0.0649 (2)	0.2005 (43)	0.2423 (10)	0.3886 (3)
E300	0.0442 (1)	0.1971 (24)	0.1555 (5)	0.2606 (2)

Table 9.4: CLS name, pion mass, rho meson mass, energy of the two and three pions state.

including the statistical uncertainty. We can see that the $E_{\pi\pi\pi}$ is only close to M_ρ for E250.

Regarding the lower bound of eq. (9.12), sometimes the logarithm of the effective mass is undefined because the correlator turns negative due to the signal-to-noise problem. This issue is especially acute for the isoscalar contribution as a result of the quark-disconnected piece. In these cases, we use the last accurate value of M_{ef} , which is in fact heavier and therefore a conservative choice.

Once the most suitable values for the bounds are selected, we need to identify a region where they coincide. The interval of averaged $n_{4,\text{cut}}$ is determined automatically. By default, its length is 0.8 fm, but it might be reduced. To choose the interval's left hand side limit, we employ the effective mass as given in eq. (9.9). In some cases, M_{ef} will change sign. This may happen due to noisy data at long distances, or at short times due to lattice artefacts. To avoid these regions, we select the longest time interval I where it does not change sign. For the next step, we look at fig. 9.4, where we show the sVPF for both bounds in a range of $n_{4,\text{cut}}$. We search the earliest time-slice n_4 in I where the difference between the upper and lower bound is smaller than half the uncertainty of the least precise bound,

$$\hat{\Pi}_{\text{upper}}(n_{4,\text{cut}}) - \hat{\Pi}_{\text{lower}}(n_{4,\text{cut}}) < \frac{1}{2} \max \{ \sigma_{\text{upper}}(n_{4,\text{cut}}), \sigma_{\text{lower}}(n_{4,\text{cut}}) \}. \quad (9.14)$$

In eq. (9.14), $\sigma_{\text{upper}}(n_{4,\text{cut}})$ is the statistical uncertainty of $\hat{\Pi}_{\text{upper}}(n_{4,\text{cut}})$, and $\sigma_{\text{lower}}(n_{4,\text{cut}})$

				Ensemble	$\Delta_{33}n_4$ [fm]	$\Delta\hat{\Pi}_{33}$	$\Delta\sigma_{33}$
Ensemble	$\Delta_{33}n_4$ [fm]	$\Delta\hat{\Pi}_{33}$	$\Delta\sigma_{33}$				
H101 s.l.	1.38 - 2.16	-0 (0.0)	-0 (0.0)	H200 s.l.	1.09 - 1.86	-3 (0.1)	0 (1.1)
l.l.		-0 (0.0)	-0 (0.2)	l.l.		-3 (0.1)	0 (1.3)
H102 s.l.	1.12 - 1.90	-4 (0.1)	-1 (6.9)	N202 s.l.	1.16 - 1.93	-4 (0.1)	-1 (4.3)
l.l.		-4 (0.1)	-1 (6.5)	l.l.		-4 (0.1)	-1 (4.0)
H105 s.l.	1.38 - 2.16	6 (0.2)	-1 (3.1)	N203 s.l.	1.41 - 2.18	0 (0.0)	-0 (1.9)
l.l.		5 (0.2)	-1 (4.5)	l.l.		-0 (0.0)	-0 (1.7)
N101 s.l.	1.55 - 2.33	-3 (0.1)	-0 (2.8)	N200 s.l.	1.80 - 2.57	3 (0.1)	0 (0.2)
l.l.		-2 (0.0)	-0 (2.2)	l.l.		1 (0.0)	-0 (1.8)
C101 s.l.	1.81 - 2.59	1 (0.0)	-1 (5.0)	D200 s.l.	1.74 - 2.51	1 (0.0)	-1 (10.0)
l.l.		0 (0.0)	-2 (11.6)	l.l.		1 (0.0)	-1 (10.3)
				E250 s.l.	2.76 - 3.53	-9 (0.2)	-15 (40.5)
				l.l.		-12 (0.3)	-15 (40.2)
B450 s.l.	1.37 - 2.14	5 (0.2)	0 (2.6)	N300 s.l.	1.25 - 2.04	0 (0.0)	-0 (3.2)
l.l.		5 (0.2)	0 (2.7)	l.l.		0 (0.0)	-0 (3.1)
S400 s.l.	1.15 - 1.91	-7 (0.2)	-0 (3.1)	N302 s.l.	1.44 - 2.24	-3 (0.1)	0 (2.3)
l.l.		-7 (0.3)	-0 (2.9)	l.l.		-2 (0.1)	0 (2.1)
N451 s.l.	1.45 - 2.21	-2 (0.1)	-1 (8.7)	J303 s.l.	2.09 - 2.89	-5 (0.2)	1 (3.0)
l.l.		-2 (0.1)	-1 (9.2)	l.l.		-5 (0.2)	1 (3.4)
				E300 s.l.	2.14 - 2.94	5 (0.2)	-4 (13.4)
				l.l.		6 (0.2)	-4 (13.9)

Table 9.5: CLS label, bounding interval, shift of the central value $\times 10^5$ (in absolute value and in percentage between parenthesis) and variation of the uncertainty $\times 10^5$ for $\hat{\Pi}_{33}$.

the corresponding error for $\hat{\Pi}_{\text{lower}}(n_{4,\text{cut}})$. After computing eq. (9.14), we check that the correlator in the interval to be averaged is positive everywhere. If it is not, we shorten the interval. Comparing with the single-state fit of section 9.1, the default length of the interval doubles for the bounding method. The main reason is empirical. The covariance matrix in a fit with too many time-slices and large statistical errors might have a large uncertainty itself, yielding results that may no longer represent the data; the interval of the single-state fit had to be shorter to accommodate all ensembles. However, we do not see a noticeable effect stemming from this decision. Another reason why automating the single exponential fit and the bounding method is important is reproducibility. Most of these computations have been cross-checked by colleagues, and an automatic method allows to compare intermediate results.

In tables 9.5 to 9.7, we show the impact of the bounding method on our results for the isovector, isoscalar and 08 components, respectively. For the isovector component in table 9.5, for example, we show the averaged interval in fm, the shift of the central value (together with its value in percentage between parenthesis), and the uncertainty reduction. The correlators are bounded between 1 fm and 2 fm. We see that the change of the central value due to this method is minimal, at most 0.3% for E250. The error reduction is more important, as we dampen the noise by 40% on that same ensemble. The bounding procedure

affects mostly the isoscalar and 08 components, as it reduces greatly the noise coming from the quark-disconnected piece. The improved estimate of the latter is obtained simply subtracting the quark-connected part from the full contribution.

In table 9.8, we give the sVPF at 1 GeV^2 for every component after applying the bounding method. These numbers constitute our best estimate for the tail-treated sVPF, although they will be further modified in chapter 10 to take into account finite-size effects before extrapolating to the physical point in chapter 12.

If a dedicated spectroscopy analysis becomes available, it is possible to subtract the $N - 1$ first lightest states of the correlator [218],

$$\tilde{G}(n_4) = G(n_4) - \sum_{n=1}^{N-1} A_n e^{-E_n n_4} \quad (9.15)$$

and substitute $G(n_4)$ in eq. (9.12) by eq. (9.15). The bounded correlator plus the subtracted states would form an improved estimate. Employing eq. (9.15) would allow us to bound the correlator at earlier times, further reducing the statistical uncertainty. However, due to the exponential behaviour of the correlator, the number of levels required increases quickly at shorter distances.

Ensemble	$\Delta_{88}n_4$ [fm]	$\Delta\tilde{\Pi}_{88}$	$\Delta\sigma_{88}$	$\Delta_{88c}n_4$ [fm]	$\Delta\tilde{\Pi}_{88c}$	$\Delta\sigma_{88c}$	$\Delta\tilde{\Pi}_{88d}$	$\Delta\sigma_{88d}$
H101 s.l.				1.38 - 2.16	-0 (0.0)	-0 (0.0)		
l.l.					-0 (0.0)	-0 (0.2)		
H102 s.l.	1.81 - 2.59	-2 (0.1)	-1 (9.3)	1.73 - 2.50	0 (0.0)	-0 (1.6)	-2 (164.5)	-4 (74.4)
l.l.		-2 (0.1)	-0 (6.5)		0 (0.0)	-0 (1.6)	-2 (101.6)	-4 (72.0)
H105 s.l.	1.81 - 2.59	22 (0.8)	-20 (62.1)	1.90 - 2.68	2 (0.1)	-0 (0.8)	20 (148.0)	-22 (74.8)
l.l.		27 (1.1)	-20 (61.6)		1 (0.0)	-0 (1.0)	26 (124.8)	-22 (75.0)
N101 s.l.	2.25 - 2.68	15 (0.6)	-17 (74.2)	2.07 - 2.85	-0 (0.0)	0 (3.3)	16 (37.1)	-20 (84.3)
l.l.		17 (0.6)	-18 (74.2)		0 (0.0)	0 (3.3)	16 (36.3)	-21 (84.9)
C101 s.l.	2.07 - 2.85	4 (0.2)	-15 (62.7)	2.07 - 2.85	0 (0.0)	-0 (5.4)	4 (7.8)	-17 (71.7)
l.l.		2 (0.1)	-14 (57.7)		0 (0.0)	-0 (5.0)	2 (3.9)	-15 (66.5)
B450 s.l.				1.37 - 2.14	5 (0.2)	0 (2.6)		
l.l.					5 (0.2)	0 (2.7)		
S400 s.l.	1.68 - 2.44	5 (0.2)	-7 (44.8)	1.68 - 2.44	0 (0.0)	-0 (0.2)	5 (187.8)	-11 (86.3)
l.l.		6 (0.2)	-6 (43.6)		0 (0.0)	-0 (0.3)	6 (148.4)	-11 (86.3)
N451 s.l.	1.98 - 2.75	4 (0.1)	-6 (58.1)	2.14 - 2.90	-0 (0.0)	-0 (4.9)	4 (17.8)	-6 (64.7)
l.l.		4 (0.2)	-5 (56.8)		-0 (0.0)	-0 (5.2)	4 (19.1)	-6 (63.5)
D450 s.l.	1.68 - 2.44	86 (3.5)	-21 (73.7)	2.44 - 3.21	1 (0.0)	-1 (13.6)	86 (74.3)	-22 (74.2)
l.l.		86 (3.6)	-22 (75.1)		1 (0.0)	-1 (13.9)	85 (71.2)	-22 (75.7)
H200 s.l.				1.09 - 1.86	-3 (0.1)	0 (1.1)		
l.l.					-3 (0.1)	0 (1.3)		
N202 s.l.				1.16 - 1.93	-4 (0.1)	-1 (4.3)		
l.l.					-4 (0.1)	-1 (4.0)		
N203 s.l.	1.86 - 2.63	10 (0.4)	-2 (19.4)	1.93 - 2.70	0 (0.0)	-0 (0.5)	9 (65.3)	-3 (70.5)
l.l.		10 (0.4)	-2 (19.3)		0 (0.0)	-0 (0.4)	9 (65.2)	-3 (70.2)
N200 s.l.	2.12 - 2.89	-12 (0.5)	-9 (59.5)	2.12 - 2.89	1 (0.0)	-0 (0.5)	-13 (510.5)	-10 (69.0)
l.l.		-12 (0.5)	-9 (59.4)		1 (0.0)	-0 (0.6)	-12 (26121.9)	-10 (68.9)
D200 s.l.	1.67 - 2.44	15 (0.6)	-21 (68.6)	2.31 - 3.08	-0 (0.0)	-0 (3.9)	15 (26.1)	-21 (70.9)
l.l.		20 (0.8)	-21 (69.5)		-0 (0.0)	-0 (3.8)	20 (31.2)	-21 (71.9)
E250 s.l.	1.61 - 2.38	-181 (6.9)	-106 (86.8)	2.96 - 3.73	-3 (0.1)	-5 (36.6)	-177 (332.6)	-104 (86.3)
l.l.		-173 (6.7)	-109 (86.9)		-4 (0.1)	-5 (35.6)	-169 (393.1)	-106 (86.2)
N300 s.l.				1.25 - 2.04	0 (0.0)	-0 (3.2)		
l.l.					0 (0.0)	-0 (3.1)		
N302 s.l.	1.59 - 2.39	9 (0.4)	-1 (13.4)	1.69 - 2.49	0 (0.0)	0 (1.4)	9 (263.2)	-3 (48.0)
l.l.		9 (0.4)	-1 (14.1)		0 (0.0)	0 (1.4)	9 (263.7)	-3 (50.3)
J303 s.l.	1.69 - 2.49	-10 (0.4)	-23 (69.9)	1.74 - 2.54	-1 (0.1)	-0 (1.0)	-8 (64.7)	-26 (83.1)
l.l.		-10 (0.4)	-23 (69.5)		-1 (0.1)	-0 (0.4)	-8 (58.1)	-26 (82.6)
E300 s.l.	1.74 - 2.54	68 (2.9)	-39 (67.7)	2.34 - 3.14	2 (0.1)	-1 (12.8)	66 (54.9)	-39 (68.9)
l.l.		84 (3.7)	-40 (67.6)		2 (0.1)	-1 (12.4)	82 (59.9)	-39 (68.7)

Table 9.6: Like table 9.5 for the full isoscalar, with its quark-connected and quark-disconnected pieces.

Ensemble	$\Delta_{08} n_4$ [fm]	$\Delta \hat{\Pi}_{08}$	$\Delta \sigma_{08}$	$\Delta_{08c} n_4$ [fm]	$\Delta \hat{\Pi}_{08c}$	$\Delta \sigma_{08c}$	$\Delta \hat{\Pi}_{08d}$	$\Delta \sigma_{08d}$
H101 s.l. l.l.								
H102 s.l. l.l.	1.81 - 2.59	-18 (9.5)	-27 (75.4)	1.99 - 2.76	-0 (0.2)	-0 (2.8)	-18 (341.7)	-29 (79.3)
H105 s.l. l.l.	1.73 - 2.50	-36 (8.6)	-82 (79.2)	1.73 - 2.50	2 (0.6)	-0 (1.9)	-38 (191.7)	-85 (80.5)
N101 s.l. l.l.	1.47 - 2.25	160 (78.7)	-86 (89.3)	1.99 - 2.76	-2 (0.5)	-0 (7.5)	163 (72.9)	-88 (91.3)
C101 s.l. l.l.	1.47 - 2.25	38 (9.0)	-58 (81.3)	1.90 - 2.68	-1 (0.2)	-1 (8.8)	39 (25.1)	-58 (83.1)
B450 s.l. l.l.								
S400 s.l. l.l.	1.91 - 2.60	-45 (19.5)	-50 (81.4)	2.14 - 2.90	-0 (0.2)	-0 (1.8)	-45 (108.9)	-52 (83.3)
N451 s.l. l.l.	1.83 - 2.60	-5 (1.5)	-27 (72.5)	1.91 - 2.67	-1 (0.3)	-0 (5.7)	-4 (10.0)	-27 (73.3)
D450 s.l. l.l.	2.21 - 2.67	234 (76.8)	-54 (64.3)	2.14 - 2.90	2 (0.3)	-1 (18.2)	232 (83.0)	-54 (63.8)
H200 s.l. l.l.								
N202 s.l. l.l.								
N203 s.l. l.l.	1.86 - 2.51	35 (21.3)	-24 (69.3)	1.93 - 2.70	-1 (0.4)	-0 (2.9)	36 (70.4)	-25 (74.0)
N200 s.l. l.l.	1.86 - 2.63	-45 (11.4)	-41 (71.2)	1.67 - 2.44	-0 (0.1)	-0 (1.5)	-45 (1412.4)	-43 (73.9)
D200 s.l. l.l.	1.93 - 2.31	-18 (3.6)	-63 (68.9)	1.99 - 2.76	-1 (0.1)	-0 (5.2)	-17 (17.9)	-63 (69.4)
E250 s.l. l.l.	1.93 - 2.12	-216 (27.3)	-253 (85.6)	2.51 - 3.28	-6 (0.7)	-9 (41.2)	-210 (1071.4)	-249 (84.5)
N300 s.l. l.l.								
N302 s.l. l.l.	1.79 - 2.19	63 (37.7)	-17 (50.0)	1.94 - 2.74	-0 (0.1)	-0 (0.3)	63 (166.4)	-18 (51.4)
J303 s.l. l.l.	1.94 - 2.64	95 (30.1)	-87 (77.7)	2.09 - 2.89	-3 (0.5)	0 (5.1)	97 (60.5)	-88 (80.3)
E300 s.l. l.l.	1.59 - 2.24	143 (36.9)	-149 (73.8)	2.14 - 2.94	2 (0.3)	-2 (14.0)	141 (48.2)	-155 (76.0)

Table 9.7: Systematic effect of the bounding method on $\hat{\Pi}_{08}$, its quark-connected part and its quark-disconnected part as in table 9.5.

Ensemble	$\hat{\Pi}_{33}$	$\hat{\Pi}_{88}$	$\hat{\Pi}_{88c}$	$\hat{\Pi}_{88d}$	$\hat{\Pi}_{08}$	$\hat{\Pi}_{08c}$	$\hat{\Pi}_{08d}$
H101 s.l.	2837 (6)		2837 (6)				
l.l.	2750 (6)		2750 (6)				
H102 s.l.	2954 (9)	2736 (6)	2738 (6)	-3 (1)	172 (9)	194 (4)	-23 (8)
l.l.	2868 (10)	2649 (7)	2652 (7)	-3 (1)			
H105 s.l.	3097 (19)	2654 (12)	2648 (10)	6 (8)	377 (22)	395 (10)	-18 (21)
l.l.	3009 (19)	2566 (12)	2560 (11)	5 (7)			
N101 s.l.	3158 (10)	2651 (6)	2678 (5)	-27 (4)	364 (10)	424 (6)	-60 (8)
l.l.	3075 (10)	2563 (6)	2592 (6)	-29 (4)			
C101 s.l.	3324 (15)	2623 (9)	2672 (6)	-49 (7)	457 (13)	573 (8)	-116 (12)
l.l.	3239 (14)	2533 (10)	2587 (7)	-54 (8)			
B450 s.l.	2731 (7)		2731 (7)				
l.l.	2662 (7)		2662 (7)				
S400 s.l.	2851 (12)	2644 (8)	2641 (8)	2 (2)	187 (12)	190 (5)	-4 (10)
l.l.	2785 (12)	2577 (8)	2575 (8)	2 (2)			
N451 s.l.	3082 (7)	2606 (4)	2623 (3)	-17 (3)	358 (10)	403 (4)	-46 (10)
l.l.	3016 (7)	2538 (4)	2556 (3)	-19 (3)			
D450 s.l.	3268 (9)	2571 (8)	2600 (3)	-30 (8)	538 (30)	585 (5)	-47 (31)
l.l.	3203 (9)	2500 (7)	2534 (3)	-34 (7)			
H200 s.l.	2615 (14)		2615 (14)				
l.l.	2568 (14)		2568 (14)				
N202 s.l.	2724 (12)		2724 (12)				
l.l.	2678 (12)		2678 (12)				
N203 s.l.	2863 (9)	2611 (7)	2616 (6)	-5 (1)	200 (11)	215 (5)	-15 (9)
l.l.	2815 (9)	2563 (7)	2568 (7)	-5 (1)			
N200 s.l.	2988 (11)	2526 (6)	2536 (5)	-10 (5)	351 (17)	392 (7)	-41 (15)
l.l.	2940 (11)	2478 (6)	2490 (5)	-13 (5)			
D200 s.l.	3213 (12)	2480 (9)	2523 (5)	-43 (9)	486 (29)	600 (7)	-114 (28)
l.l.	3166 (12)	2431 (9)	2476 (5)	-44 (8)			
E250 s.l.	3498 (22)	2451 (16)	2575 (8)	-124 (17)	574 (42)	803 (13)	-230 (46)
l.l.	3450 (22)	2402 (16)	2528 (8)	-126 (17)			
N300 s.l.	2559 (12)		2559 (12)				
l.l.	2531 (12)		2531 (12)				
N302 s.l.	2683 (13)	2457 (9)	2452 (8)	6 (4)	229 (17)	204 (6)	25 (17)
l.l.	2656 (13)	2430 (9)	2424 (8)	6 (3)			
J303 s.l.	2983 (17)	2418 (10)	2440 (7)	-22 (5)	410 (25)	473 (10)	-63 (22)
l.l.	2957 (17)	2390 (10)	2413 (7)	-23 (5)			
E300 s.l.	3229 (26)	2390 (19)	2444 (9)	-54 (17)	530 (53)	681 (15)	-151 (49)
l.l.	3203 (26)	2362 (19)	2418 (9)	-55 (18)			

Table 9.8: Improved estimate of the sVPF at 1 GeV^2 after applying the bounding procedure. In this table, s.l. indicates the correlators with the l discretisation at the source and the s discretisation at the sink, while l.l. uses the l discretisation for both the source and the sink.

Chapter 10

Finite-size effects

To obtain results comparable with experiment, it is necessary to remove the infrared cut-off of our simulations, the box size. The two-point function $G(n_4)$ receives exponentially suppressed finite-size effects (FSE) in the spatial and temporal directions. These effects can be estimated to all orders from a relativistic field theory of interacting pions [143]. The leading order has the general form

$$\Delta G(n_4; T, L) = \mathcal{O}(e^{-M_\pi L}) + \mathcal{O}(e^{-M_\pi T}) + \mathcal{O}(e^{-M_\pi \sqrt{L^2 + T^2}}), \quad (10.1)$$

where the first term is the leading effect for the spatial components, the second corresponds to the temporal direction and the last indicates space and time cross-terms. In our ensembles, we have $T = 2L$ or $T = 3L$. Therefore, we neglect all but the spatial finite-size effects, which we discuss in detail in this chapter.

One important property of the correlators we work with is the behaviour of their spectral decomposition at longer time separations. The states with higher energies will decay exponentially faster than the lighter states. This means that, while at the very early times we have to deal with an infinite tower of states, which contribute substantially to the correlator, at longer times we only have to care for a reduced number of states closer to the ground energy. We concentrate on the pion states, which constitute the most relevant contribution due to its low energy, and disregard other excitations. To study these states, two regimes can be differentiated. One when we need to take into account an infinite tower of pion states wrapping around the lattice, and another one when only a few pion states are to be considered. To establish a clear boundary between both regimes, the time-slice $n_{4,i}$ is defined [264, 265],

$$n_{4,i} \equiv \frac{1}{aM_\pi} \left(\frac{M_\pi L}{4} \right)^2. \quad (10.2)$$

Equation (10.2) is a dimensionless time-slice, given by the size of the box in the sense of $M_\pi L$, which is a pure number, and the pion mass in said ensemble. It takes into account that the lighter the pion the more states will propagate further in time, delaying the moment when we can switch to a description based on just a few states. Also, larger ensembles will allow the particles to propagate further. Taking $M_\pi L = 4$ as reference [243],

$n_{4,i}$ moves to the right in those ensembles with $M_\pi L > 4$. For any $n_4 \geq n_{4,i}$, we use the MLL formalism introduced in section 10.1, modelling the vector form factor of the pion via the Gounaris-Sakurai (GS) parametrisation, which is treated in section 10.1.1. For times $n_4 < n_{4,i}$, we employ the Hansen-Patella (HP) method explained in section 10.2. In section 10.3, we describe an alternative method for this region employing NLO ChPT and derive eq. (10.2). An important note, in sections 10.1 and 10.3 all quantities are made dimensionless using the pion mass unless otherwise stated (e.g., the energy ω , the 3-momentum $k(\omega)$, the correlators, the ρ meson mass and the ρ meson width). To recover the correct dimensions, one only needs to include the appropriate number of M_π factors.

10.1 Meyer-Lellouch-Lüscher formalism

The principle of this method, proposed by Meyer *et al.* in [264, 245], is to model the isovector contribution of the vector-vector correlation function $G_{33}(n_4)$ at low energies in finite and infinite volume and take the difference as the estimator of FSE,

$$\Delta G_{33}(n_4) = G_{33}(n_4; \infty, N) - G_{33}(n_4; L, \mu), \quad (10.3)$$

where $G_{33}(n_4; \infty, \mu)$ is the correlator in infinite volume and $G_{33}(n_4; L, N)$ the one in finite volume. The vector correlator in finite volume is given by the spectral representation

$$G_{33}(n_4; L, N) = \sum_{s=1}^N |A_s|^2 e^{-\omega_s t}, \quad (10.4)$$

where N is, at this moment, finite but undetermined. *A priori*, its choice is not trivial and will be discussed in section 10.1.3. Its infinite-volume counterpart is obtained via the dispersion relation [220, 264]

$$G_{33}(n_4; \infty, \mu) = \int_2^\mu d\omega \, \omega^2 \rho(\omega) e^{-\omega n_4}, \quad (10.5)$$

Here, we remind the reader again that we normalise all the energy quantities by the pion mass to simplify the expressions, and that to recover the missing dimensions one only needs to write these pion mass factors explicitly. In particular, the integration domain starts at the energy threshold of $2M_\pi$, and it extends up to a number of μ pions, μM_π . We approximate the spectral density at long distances to be dominated by the $\pi\pi$ channel [266]

$$\rho(\omega) = \frac{1}{48\pi^2} \left(1 - \frac{4}{\omega^2}\right)^{3/2} |F_\pi(\omega)|^2. \quad (10.6)$$

The time-like pion form factor can be written as a complex number $F_\pi = |F_\pi| e^{i\delta_{11}}$ for $\omega > 2$, with $F_\pi(0) = 1$ as given by the pion charge. The upper integration limit μ will be studied in section 10.1.3. At this stage, we need to estimate the finite-volume amplitudes $|A_s|^2$ and energies ω_s , as well as the pion form factor $F_\pi(\omega)$.

In [267, 268], it was found a relation between the finite-volume spectrum ω_s of eq. (10.4) and the p-wave (vector) scattering phase shift δ_{11} of two pions in infinite volume,

$$\begin{aligned} \delta_{11}(k_s) + \phi(q_s) &= s\pi, \quad q_s = \frac{k_s L}{2\pi}, \quad s = 1, 2, 3, \dots, N \\ \phi(q) &= \arctan\left(-\frac{\pi^{3/2} q}{Z_{00}(1; q^2)}\right) + s\pi. \end{aligned} \quad (10.7)$$

Equation (10.7) is valid in the elastic region $2 < \omega < 4$ because beyond $4M_\pi$ states with four pions, which are not taken into account in the formalism, start to appear. The discrete set of 3-momenta k_s is still related to the energies ω_s via the usual relativistic dispersion relation $\omega = 2(1 + k_s^2)^{1/2}$ for non-interacting pions. The function $\phi(q)$ depends on $Z_{00}(1; q^2)$, which is the analytic continuation of the Generalized Riemann Zeta function with poles on $q^2 = \vec{n}^2$ for $\vec{n} \in \mathbb{Z}^3$. For the numerical implementation, we use the representation [269]

$$\begin{aligned} Z_{00}(1; q^2) &= -\pi + \frac{1}{\sqrt{4\pi}} \sum_{m=0}^{\infty} \nu_m \frac{e^{-(m-q^2)}}{m-q^2} \\ &+ \frac{\pi}{2} \int_0^1 \frac{dt}{t^{3/2}} (e^{tq^2} - 1) + \frac{\pi}{2} \sum_{m=1}^{\infty} \nu_m \int_0^1 \frac{dt}{t^{3/2}} e^{tq^2 - \frac{\pi^2 m}{t}}. \end{aligned} \quad (10.8)$$

We also need the expression for the derivative,

$$\begin{aligned} \frac{\partial Z_{00}}{\partial q} &= \frac{2q}{\pi} \sum_{m=0}^{\infty} \nu_m \frac{m - q^2 + 1}{(m - q^2)^2} e^{-(m-q^2)} \\ &+ \pi q \int_0^1 \frac{dt}{\sqrt{t}} e^{tq^2} + \pi q \sum_{m=1}^{\infty} \nu_m \int_0^1 \frac{dt}{\sqrt{t}} e^{tq^2 - \frac{\pi^2 m}{t}}. \end{aligned} \quad (10.9)$$

$\nu_m = 0, 1, 2, \dots$ is the multiplicity of vectors $\vec{n} \in \mathbb{Z}^3$ with $m = |\vec{n}|^2$. See that the variable $q^2 \in \mathbb{R}$ in $Z_{00}(1; q^2)$, while the relation (10.7) is only valid for the discrete set of momenta k_s . Equation (10.7) allows to compute the spectrum ω_s , and in section 10.1.2 we give a explicit strategy to obtain it. However, the reader should note that we still need a parametrisation for the phase shift δ_{11} . The latter is given in section 10.1.1.

The second piece of the MLL formalism are the amplitudes $|A_s|^2$. In [245], a way is found to compute the pion form factor in the time-like region $2 < \omega < 4$. In particular [245],

$$|F_\pi(\omega_s)|^2 = \mathbb{L}(\omega_s) \frac{3\pi\omega_s^2}{2k_s^5} |A_s|^2, \quad (10.10)$$

where the Lellouch-Lüscher factor \mathbb{L} is [245]

$$\mathbb{L}(\omega_s) = q_s \frac{\partial \phi(q_s)}{\partial q} + k_s \frac{\partial \delta_{11}(k_s)}{\partial k}. \quad (10.11)$$

Equation (10.10) is obtained in a similar fashion as the result by Lellouch and Lüscher in [246] on the matrix element determining the $K \rightarrow \pi\pi$ decay rate.

Summarizing, MLL relies on three key results. First, a relation between the finite-volume spectrum of the correlator and the infinite-volume scattering phase-shifts of $\pi\pi$ interactions in the elastic region $2 < \omega < 4$ [267, 268]. Second, the ability to compute the pion form factor in the time-like region $2 < \omega < 4$ in terms of the amplitudes of the correlator in finite volume [245]. The third and final ingredient is a description for the pion form factor F_π , which we study in section 10.1.1.

10.1.1 Gounaris-Sakurai parametrisation of $F_\pi(\omega)$

The original objective of the Gounaris-Sakurai (GS) parametrisation was to improve the predictions for the process $\rho \rightarrow e^+e^-$ given by vector-meson dominance [270]. The latter considered the ρ meson as a stable particle, and [271] introduced corrections due to the ρ meson's finite width. Therefore, neither the GS parametrisation was envisioned for computing FSE, nor it is necessary for the MLL formalism. It is possible to either use other parametrisations of the pion form factor [272] or to perform an *ab initio* calculation on the lattice [273]. The reasons to use the GS parametrisation are its simplicity, as it only depends on two parameters, and the fact that we only use it to study the FSE corrections, which are of $\mathcal{O}(1\%)$. Therefore, any systematics due to the use of the GS model are sub-leading with respect to other sources of uncertainty, like the scale setting error, the isospin-breaking effects or the statistical uncertainty.

The amplitudes A_s in eq. (10.11) and the density $\rho(\omega)$ in eq. (10.5) are written in terms of the vector pion form factor F_π , given by the Gounaris-Sakurai model [271, 264],

$$F_\pi(\omega) = \frac{\omega f}{k^3 (\cot(\delta_{11}) - i)}, \quad (10.12)$$

where f is defined by

$$f = -\frac{1}{\pi} - k_\rho^2 h(M_\rho) - b \frac{M_\rho^2}{4}. \quad (10.13)$$

δ_{11} is the phase shift and k_ρ is given below eq. (10.15). There are only two free parameters, the ρ meson mass M_ρ and the ρ decay width Γ_ρ . The p-wave pion-pion scattering phase shift is assumed to satisfy a generalized effective-range formula of the Chew-Mandelstam type [271, 274] below 1 GeV^2

$$\begin{aligned} \cot \delta_{11}(k) &= \frac{\omega}{k^3} \left(k^2 h(\omega) - k_\rho^2 h(M_\rho) + b \left(k^2 - k_\rho^2 \right) \right), \\ b &= -\frac{4k_\rho^3}{M_\rho^2 \Gamma_\rho} - h(M_\rho) - \frac{2k_\rho^2 h'(M_\rho)}{M_\rho}, \\ \frac{\partial \delta_{11}}{\partial k} &= \frac{4}{k^2} \frac{1}{1 + \tan^2 \delta_{11}} \left(\left(\frac{3k}{4} - \frac{k^3}{\omega^2} \right) \tan \delta_{11} - \frac{\omega(h+b)/2 + k^2 h'}{\cot^2 \delta_{11}} \right), \end{aligned} \quad (10.14)$$

where we indicate a derivative with a prime. The momentum and the energy are related via the relativistic dispersion relation [271, 264]

$$k(\omega) = \begin{cases} \sqrt{\left(\frac{\omega}{2}\right)^2 - 1}, & \omega \geq 2, \\ i\sqrt{1 - \left(\frac{\omega}{2}\right)^2}, & 0 < \omega < 2, \end{cases} \quad (10.15)$$

and $k_\rho = k(M_\rho)$. The other auxiliary function is [271, 264]

$$h(\omega) = \begin{cases} \frac{2}{\pi} \frac{k}{\omega} \log\left(\frac{\omega + 2k}{2}\right), & \omega \geq 2, \\ \frac{2i}{\pi} \frac{k}{\omega} \operatorname{arccot} \sqrt{\frac{\omega^2}{4 - \omega^2}}, & 0 < \omega < 2. \end{cases} \quad (10.16)$$

and its derivative reads

$$h'(\omega) = \begin{cases} \frac{2}{\pi} \left(\left(\frac{k'}{\omega} - \frac{k}{\omega^2} \right) \log\left(\frac{\omega + 2k}{2}\right) + \frac{k}{\omega} \frac{2k' + 1}{\omega + 2k} \right), & \omega \geq 2, \\ \frac{2i}{\pi} \left(\left(\frac{k'}{\omega} - \frac{k}{\omega^2} \right) \operatorname{arccot} \left(\sqrt{\frac{\omega^2}{4 - \omega^2}} \right) - \frac{k}{\omega} \frac{1}{\sqrt{4 - \omega^2}} \right), & 0 < \omega < 2. \end{cases} \quad (10.17)$$

The range $0 < \omega < 2$ extends below the two-pion threshold, and we use it to check that $F_\pi(0) = 1$ [271, 264]. Finally, the arc-cotangent is mainly defined in two different ways in the literature. We are interested in using the definition [275], which renders the function continuous in the real line,

$$\operatorname{arccot}(z) = \begin{cases} \arctan(1/z), & z > 0, \\ \arctan(1/z) + \pi, & z < 0, \\ \pi/2, & z = 0, \end{cases} \quad (10.18)$$

$$\arctan(z) = \frac{1}{2i} \log\left(\frac{1 + iz}{1 - iz}\right). \quad (10.19)$$

Summarizing, thanks to the GS parametrisation, we can express $|F_\pi|$ and δ_{11} in terms of two new unknowns, the ρ meson mass M_ρ and the ρ meson width Γ_ρ . In section 10.1.2, we discuss how we compute these two parameters in our ensembles.

10.1.2 Computation of the Gounaris-Sakurai parameters

The variables of the GS parametrisation of the pion form factor, M_ρ and Γ_ρ , are *a priori* unknown in our ensembles, or only studies with less statistics exist [262]. To estimate them, we fit a set of time-slices of the isovector correlator to the tower of exponentials in eq. (10.4),

where the energies fulfil eq. (10.7) and the amplitudes eq. (10.10). The fitted time interval is selected around the long-distance region of the correlator where most excited states can be neglected, and it is determined based on χ^2 . We include between three and six states in the fit model for all ensembles and check that our results do not change upon increasing the number of states in the fit. Note that since all amplitudes and energies follow eqs. (10.7) and (10.10) and we use the GS parametrisation, we only have two parameters to fit despite using a tower of many exponentials. After obtaining M_ρ and Γ_ρ , we can obtain the energy levels ω_s and amplitudes $|A_s|^2$ of the finite volume correlator in eq. (10.4) and the energy density $\rho(\omega)$ of the infinite volume correlator of eq. (10.5). The fit interval, together with the ρ meson mass M_ρ and the ρ meson width Γ_ρ are given in table 10.1. For the width, we use a form that shows little pion mass dependence [218]

$$g_{\rho\pi\pi} = \sqrt{\frac{6\pi M_\rho^2 \Gamma_\rho}{k_\rho^3}}. \quad (10.20)$$

Figure 10.1 shows the fit for ensemble D200 at $\beta = 3.55$. We represent the integrand of $\hat{\Pi}_{33}$ at $Q^2 = 1 \text{ GeV}^2$. The points $G(n_4, L)$, $l \leq s$ show the cumulative sum of states in eq. (10.4), with amplitudes and energies obtained following the MLL method. The black triangles $G_{33}(n_4, L)$ are the original data without FSE corrections and $G(n_4, \infty)$ is the correlator in infinite volume. The green lines indicate the fit interval, a red line shows $n_{4,i}$, and the textbox gives the result of the fit.

10.1.3 The limit of the elastic region

After section 10.1.2, we have obtained the spectral density $\rho(\omega)$, the amplitudes A_s , and the energy levels ω_s . Then, one can sum the various states to obtain eq. (10.4) and integrate $\rho(\omega)$ to compute eq. (10.5). However, the Lüscher formalism is only valid for elastic two-pion interactions. Therefore, we should be careful with what upper limit for the sum/integral we choose in principle. That is, either most of the contributions to the sum/integral comes from the elastic regime or we have to cut the sum/integral around the transition to the inelastic interactions.

Strictly speaking, the upper integration limit should be $4M_\pi$ [266, 220]. However, we consider the limit $M_\rho + 1$ instead, where inelastic interactions start to dominate [220]. For our ensembles with heavier pion masses the latter limit is more stringent than the former, because $3 < M_\rho + 1 < 4$ in many cases. On the other hand, $M_\rho + 1$ relaxes somewhat the four pion rule for our lightest ensembles because $M_\rho + 1 > 4$.

First, we study how relevant are the energies beyond the elastic region. For the correlator in infinite volume in eq. (10.5), a possibility is to integrate up to several energies μ , and normalise by the integration up to infinity, looking for the upper integration limit μ that makes $G_{33}(n_4; \infty; \mu)/G_{33}(n_4; \infty, \infty) \sim 1$. We plot this test for several ensembles at $\beta = 3.55$ in fig. 10.2, where the contour lines represent the value of μ for which $G_{33}(n_4; \infty, \mu)/G_{33}(n_4; \infty, \infty) = 0.6, 0.9, 0.99, 0.999$ for every time-slice n_4 . The horizontal black line indicates the inelastic threshold $M_\rho + 1$. On the RHS of every figure, we indicate

Ensemble	Fit interval	χ^2/dof	M_π	M_ρ	$g_{\rho\pi\pi}$
H101	[14, 19]	1.25	0.1830 (5)	2.048 (8)	4.835 (16)
H102	[14, 25]	0.80	0.1546 (5)	2.329 (13)	4.876 (20)
H105	[18, 22]	1.97	0.1234 (13)	2.725 (69)	5.168 (141)
N101	[15, 21]	1.42	0.1222 (5)	2.809 (29)	4.953 (38)
C101	[14, 19]	0.63	0.0960 (6)	3.461 (40)	4.954 (37)
B450	[15, 19]	0.21	0.1605 (4)	2.093 (8)	4.857 (10)
S400	[17, 24]	1.39	0.1358 (4)	2.307 (17)	5.011 (31)
N451	[19, 26]	0.97	0.1108 (3)	2.722 (25)	5.060 (41)
D450	[17, 25]	0.36	0.0836 (4)	3.543 (30)	5.031 (27)
H200	[17, 25]	0.94	0.1363 (5)	2.152 (18)	4.863 (26)
N202	[19, 29]	1.04	0.1342 (3)	2.109 (11)	4.820 (25)
N203	[23, 29]	1.46	0.1124 (2)	2.401 (27)	4.927 (65)
N200	[22, 29]	0.84	0.0922 (3)	2.767 (38)	5.103 (60)
D200	[18, 29]	1.36	0.0655 (3)	3.892 (31)	4.995 (23)
E250	[22, 31]	0.76	0.0422 (2)	5.629 (100)	5.276 (76)
N300	[25, 40]	1.94	0.1067 (3)	2.098 (21)	4.944 (42)
N302	[27, 34]	1.81	0.0875 (3)	2.457 (33)	5.007 (67)
J303	[28, 34]	1.62	0.0649 (2)	2.922 (65)	5.338 (91)
E300	[23, 32]	1.54	0.0442 (1)	4.456 (54)	5.004 (29)

Table 10.1: Fit parameters of the MLL formalism. We indicate the ensemble name, the fit interval, the quality of the fit to the correlator data, the pion mass, the ρ meson mass and the ρ decay width in the form of eq. (10.20). The fit interval is given in lattice units, M_ρ appears in M_π units and $g_{\rho\pi\pi}$ is dimensionless.

the discrete spectrum of eq. (10.4). We order the ensembles in fig. 10.2 with decreasing pion mass from left to right and top to bottom. As we increase the pion mass, the integral saturates at lower μ , but because the rho meson also becomes closer to $2M_\pi$ the threshold energy $M_\rho + 1$ also diminishes. Looking, for example, at ensemble D200 in fig. 10.2c, one sees that the integral saturates to its value at $\mu \rightarrow \infty$ well before the inelastic threshold for most time-slices. However, the two upper states of the discrete spectrum go over the inelastic threshold.

Therefore, the question we ask ourselves now is whether cutting the sum/integral at $M_\rho + 1$ makes a difference or only excludes irrelevant contributions. To cut the sum/integral, we multiply the correlators in eqs. (10.4) and (10.5) with a smooth step function whose parameters are chosen such that all elastic states fully contribute to the correlator, while

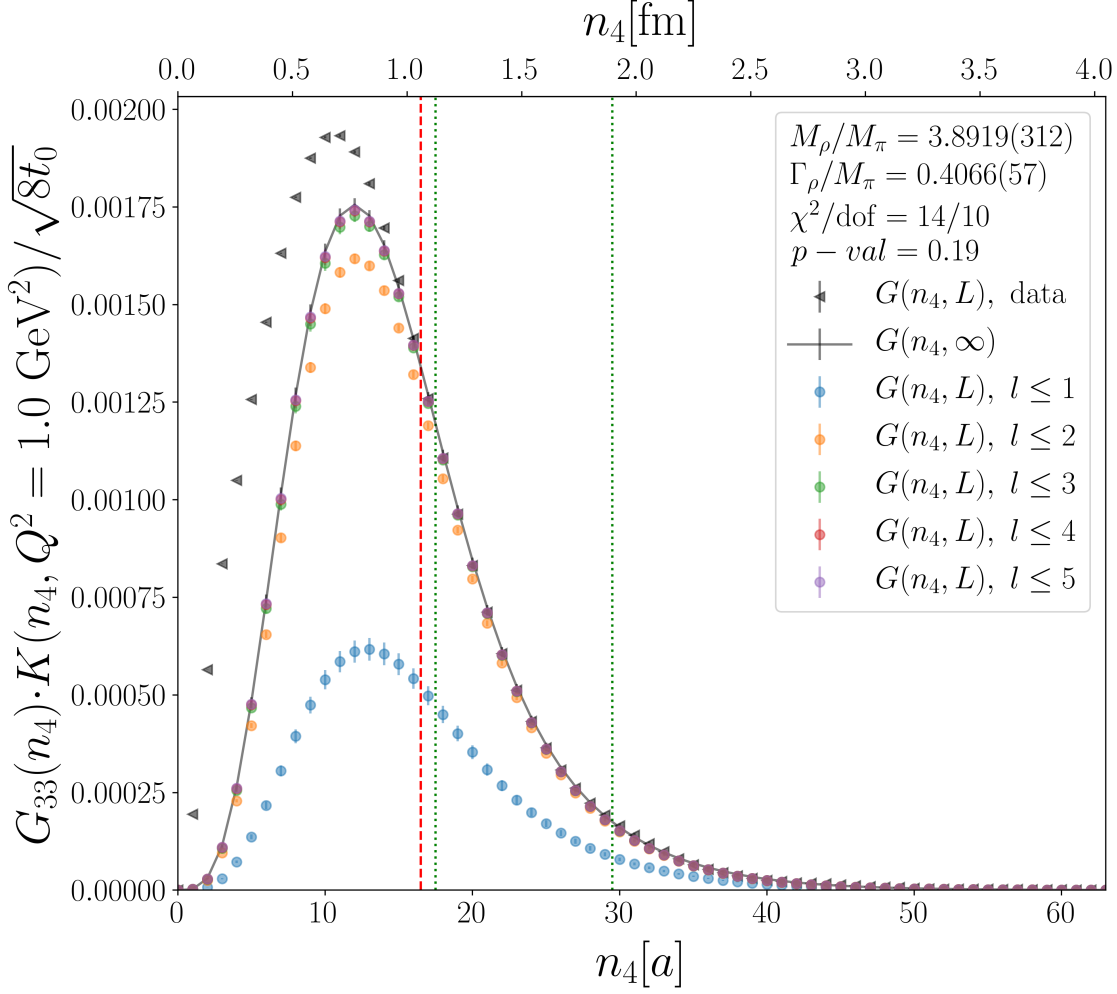


Figure 10.1: Reconstruction of the sVPF integrand at 1 GeV^2 for ensemble D200. $G(n_4, L)$ is the isovector correlator before FSE correction, $G(n_4, \infty)$ is given by eq. (10.5), and the other points represent the cumulative sum of levels given in eq. (10.4). The red vertical line indicates $n_{4,i}$, the green vertical lines show the fit interval, and we include the result of the fit in a textbox.

the non-elastic ones are quickly cut off.

$$\begin{aligned}
 G_{33}(n_4; L \rightarrow \infty, \mu = M_\rho + 1) &= \int_2^\infty d\omega \, \omega^2 \rho(\omega) e^{-\omega n_4} \Theta(\omega, M_\rho + 1), \\
 G_{33}(n_4; L, \mu = M_\rho + 1) &= \sum_{n=1}^\infty |A_n|^2 e^{-\omega_n x_0} \Theta(\omega, M_\rho + 1), \\
 \Theta(x, y) &= \frac{1 - \tanh(5 \cdot (x - y + 0.5))}{2}.
 \end{aligned} \tag{10.21}$$

In the fifth and sixth columns of table 10.3, one can see that the difference between applying

or not the cut Θ is similar in size to the statistical uncertainty of the FSE correction. Therefore, cutting or not the sum in eq. (10.4) and the integral in eq. (10.5) is irrelevant, and we opt to employ the original expressions eqs. (10.4) and (10.5) to compute the FSE correction in eq. (10.3), using $N = 5$ in eq. (10.4) and $\mu = \infty$ in eq. (10.5).

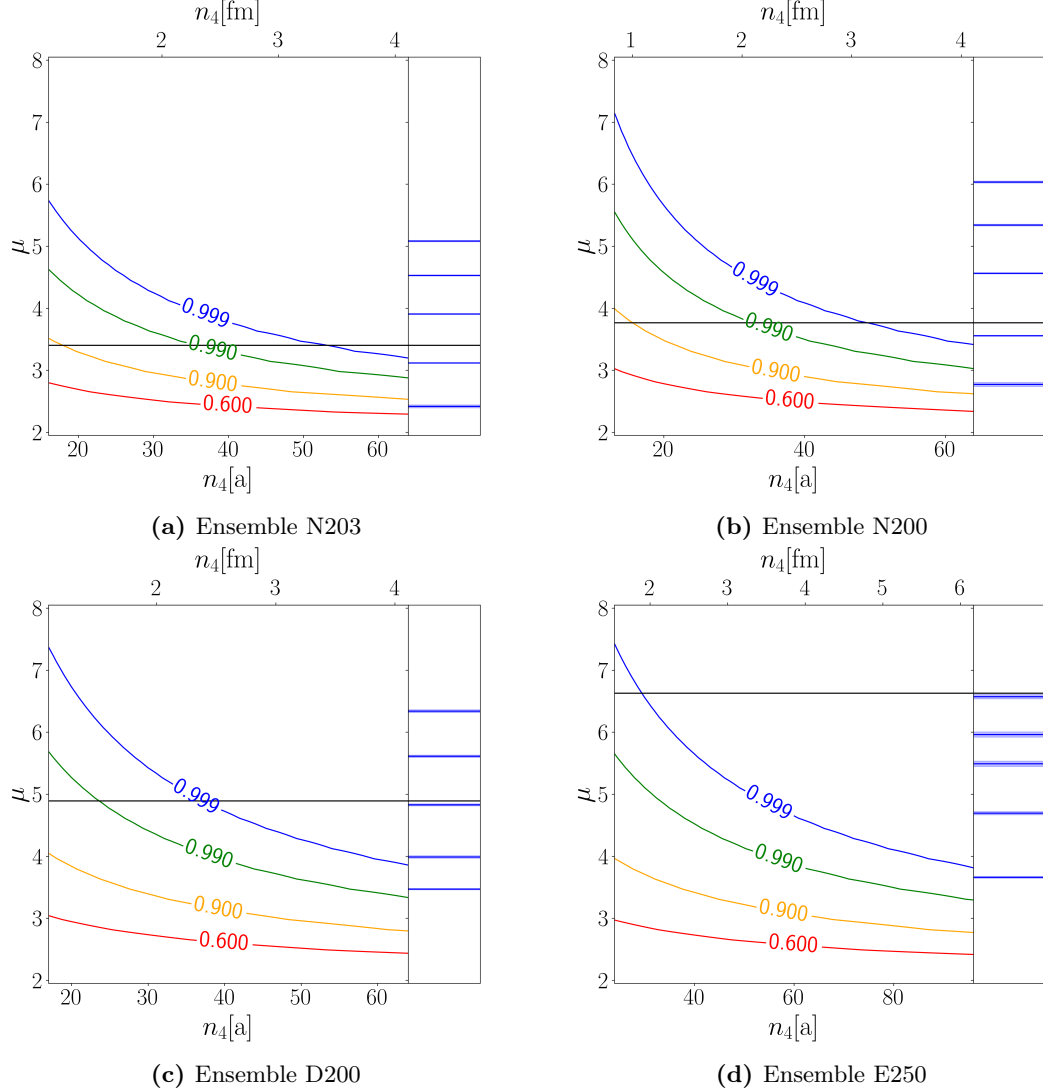


Figure 10.2: The contours on the LHS of each plot give, for each time-slice of eq. (10.5), the upper integration limit μ where 60%, 90%, 99% and 99.9% of the integral up to infinity is reached. The time-slices plotted correspond to $n_4 \geq n_{4,i,4}$, with $n_{4,i}$ defined in eq. (10.2). The RHS shows the spectrum in finite volume ω_s .

10.2 Hansen-Patella formalism

A new method was recently presented in [143, 244]. The FSE are computed non-perturbatively considering a relativistic, effective theory of pions with local interactions in the isospin-symmetric limit. The correction is proportional to the forward Compton scattering of the pion, and is computed as a series of terms proportional to $\exp(-|\vec{m}|M_\pi L)$, where $m_{j=1,2,3}$ indicates the wrapping number of a pion loop around the j -th spatial direction. Contributions proportional to $\exp(-M_\pi L)$, $\exp(-\sqrt{2}M_\pi L)$ and $\exp(-\sqrt{3}M_\pi L)$ —corresponding to $|\vec{m}|^2 = 1, 2, 3$, respectively— are fully taken into account, while the first contribution neglected is proportional to $\exp(-\sqrt{2 + \sqrt{3}}M_\pi L) \approx \exp(-1.93M_\pi L)$. The spatial FSE are dominated by the single-pion exchange in the Compton scattering amplitude, which is completely described by the pion electromagnetic form factor in the space-like region. For the latter, a simpler parametrisation than the GS model is used, the monopole model [276]:

$$F_\pi(-Q^2) = \frac{1}{1 + \frac{Q^2}{M(M_\pi)^2}}, \quad (10.22)$$

$$M(M_\pi)^2 = 0.517(23) \text{ GeV}^2 + 0.647(30)M_\pi^2. \quad (10.23)$$

For the monopole Ansatz, the finite size correction can be written as [143]

$$\begin{aligned} \Delta G(n_4; L) = \sum_{\vec{m} \neq 0} \frac{1}{6\pi|\vec{m}|L} & \left(\text{Im} \int_{\mathbb{R}+i\mu} \frac{dk_3}{2\pi} \frac{e^{ik_3|n_4|} (4M_\pi^2 + k_3^2) M^2}{(M^2 + k_3^2)^2} \frac{e^{-|\vec{m}|L\sqrt{M_\pi^2 + k_3^2}/4}}{4k_3} \right. \\ & \left. + \int \frac{dp_3}{2\pi} e^{-|\vec{m}|L\sqrt{M_\pi^2 + p_3^2}} \frac{d}{dz} \left[\frac{e^{-z|n_4|} (z^2 - 4M_\pi^2) M^2}{(z + M)^2 (z^2 + 4p_3^2)} \right]_{z=M} \right). \end{aligned} \quad (10.24)$$

As explained in [143], the convergence of the series in eq. (10.24) is better for small and intermediate time separations n_4 ; therefore, we decide to use it solely for the regime $n_4 < n_{4,i}$. Nonetheless, in tables 10.2 and 10.3, where we compare the integrand of the sVPF given by the various methods, one can see that the HP and MLL formalisms give very similar results at long distances. This tempts us to use the HP method for the whole time range. Even though it is possible to compute eq. (10.24) for every $|\vec{m}|$, the term $|\vec{m}|^2 = 2 + \sqrt{3}$ is already neglected, and contributions $|\vec{m}|^2 > 2$ would be sub-leading. Therefore, only the terms $|\vec{m}|^2 = 1, 2, 3$ are computed for this analysis. A natural estimate for this method's systematic uncertainty could be the level $|\vec{m}|^2 = 3$, the last one to be taken consistently into account. Another option, suggested in [143], would be to sum all contributions $|\vec{m}|^2 \geq 2$.

The results of the HP formalism are gathered in Table 10.2. There, we show the sVPF $\times 10^5$ for every ensemble, with the integration over the entire time direction, and not just $n_4 < n_{4,i}$. The ensemble name appears on the first column; the result for the individual levels $\vec{m}^2 = 1, 2, 3$ on the second, third and fourth columns with a purely statistical uncertainty; the sum of the three appear on the last column.

Ensemble	$\vec{m}^2 = 1$	$\vec{m}^2 = 2$	$\vec{m}^2 = 3$	HP
H101	7.8 (0.5)	1.6 (0.1)	0.2 (0.0)	9.5 (0.5)
H102	15.8 (0.9)	4.7 (0.2)	0.7 (0.0)	21.3 (1.2)
H105	30.7 (2.0)	15.0 (0.8)	3.2 (0.2)	48.9 (2.9)
N101	5.9 (0.3)	1.3 (0.0)	0.2 (0.0)	7.3 (0.3)
C101	14.4 (0.6)	5.7 (0.2)	1.0 (0.0)	21.1 (0.8)
B450	15.3 (0.9)	4.0 (0.2)	0.6 (0.0)	19.9 (1.1)
S400	28.0 (1.8)	10.7 (0.5)	2.0 (0.1)	40.6 (2.5)
N451	9.7 (0.5)	2.6 (0.1)	0.4 (0.0)	12.8 (0.6)
D450	8.0 (0.3)	2.3 (0.1)	0.3 (0.0)	10.6 (0.4)
H200	34.1 (2.3)	12.2 (0.7)	2.2 (0.1)	48.6 (3.0)
N202	4.7 (0.2)	0.7 (0.0)	0.1 (0.0)	5.5 (0.3)
N203	10.8 (0.6)	2.7 (0.1)	0.4 (0.0)	13.8 (0.7)
N200	21.7 (1.2)	8.5 (0.3)	1.6 (0.1)	31.7 (1.5)
D200	19.6 (0.8)	9.4 (0.3)	1.9 (0.0)	30.9 (1.1)
E250	16.8 (0.5)	9.8 (0.3)	2.2 (0.1)	28.7 (0.8)
N300	17.6 (1.1)	4.7 (0.2)	0.7 (0.0)	22.9 (1.3)
N302	33.7 (2.1)	13.5 (0.6)	2.6 (0.1)	49.9 (2.8)
J303	26.0 (1.3)	11.8 (0.4)	2.4 (0.1)	40.1 (1.8)
E300	17.8 (0.6)	8.7 (0.2)	1.8 (0.0)	28.3 (0.8)

Table 10.2: Estimation of the finite-size effects using the Hansen-Patella formalism. We indicate the sVPF $\times 10^5$ for each level and for the total. The uncertainty is purely statistical. Numbers kindly shared by the Mainz group.

10.3 NLO ChPT

A simpler option than the HP method of section 10.2 would be to consider a theory of free, point-like pions, i.e. $F_\pi(Q^2) = 1$. The isovector current can be written as $\epsilon^{abc} \pi^b \partial_\mu \pi^c$ [264], with ϵ^{abc} the Levi-Civita symbol for three dimensions. Then, the FSE correction can be written in terms of a non-oscillating integrand [265],

$$\begin{aligned}
\Delta G(n_4) &= -\frac{1}{3} \left[\frac{1}{L^3} \sum_{\vec{k}} - \int \frac{d^3 k}{(2\pi)^3} \right] \frac{\vec{k}^2}{\vec{k}^2 + 1} e^{-2n_4 \sqrt{\vec{k}^2 + 1}} \\
&= -\frac{n_4}{3\pi^2} \sum_{\vec{n} \neq 0} \left(\frac{K_2 \left(\sqrt{L^2 \vec{n}^2 + 4n_4^2} \right)}{L^2 \vec{n}^2 + 4n_4^2} \right. \\
&\quad \left. - \frac{1}{L|\vec{n}|} \int_1^\infty dy K_0 \left(y \sqrt{L^2 \vec{n}^2 + 4n_4^2} \right) \sinh(L|\vec{n}|(y-1)) \right),
\end{aligned} \tag{10.25}$$

where $K_s(x)$ is the second solution to the modified Bessel function [277] and $\vec{n} \in \mathbb{Z}^3$. The integrand in the last line of eq. (10.25) contains increasing and decreasing exponentials. To stabilize the numerical integration for $y > 25$, we do the replacement [277],

$$\lim_{y \rightarrow \infty} K_0 \left(y \sqrt{L^2 \vec{n}^2 + 4n_4^2} \right) \sinh(L|\vec{n}|(y-1)) = \left(\frac{\pi}{8y \sqrt{L^2 \vec{n}^2 + 4n_4^2}} \right)^{1/2} e^{-y \sqrt{L^2 \vec{n}^2 + 4n_4^2} + L|\vec{n}|(y-1)}. \quad (10.26)$$

Since we only work with the modulus $|\vec{n}|$, we can speed up the computation of each term in the series of eq. (10.25) by summing over $|\vec{n}|$ instead of \vec{n} and multiplying each term by its multiplicity. The FSE correction estimated using this method appears in table 10.3 for every ensemble. One clearly sees that the estimate using NLO ChPT is smaller than those obtained employing either HP or MLL. In fig. 10.3, we compare NLO ChPT with the other methods discussed in sections 10.1 and 10.2 for ensemble D200. One can see that NLO ChPT roughly corresponds to the first level of the HP method.

The expression in eq. (10.2) for $n_{4,i}$ is derived from a saddle point approximation for the integral in eq. (10.25). Then, the FSE correction is [264]

$$\Delta G(n_4; L) \propto \sum_{\vec{n} \neq 0} \exp \left(-\frac{M_\pi L^2 \vec{n}^2}{4n_4} \right). \quad (10.27)$$

If the exponent of the exponential is large, the series will converge quickly. This means that n_4 should be smaller than $M_\pi L^2$. By requiring the exponent to be at least four, one finds what is the maximum time-slice where the series in eq. (10.27) converges quickly enough, which is precisely eq. (10.2). After appearing in [244, 143], the HP method superseded our previous determination using NLO ChPT at $n_4 < n_{4,i}$, although we keep the division at $n_{4,i}$ between early and late times. We give the results for both methods, but only use the HP estimate to continue the analysis towards the chiral and continuum extrapolations.

10.4 Results

Table 10.3 shows the main results of this chapter. Columns three through seven indicate the FSE correction in the form of the sVPF $\times 10^5$. The first column indicates the ensemble name, the second the value of $n_{4,i}$ defined in eq. (10.2), the third gathers the results using NLO ChPT, the fourth indicates the result for HP if we only integrate times $n_4 < n_{4,i}$; the fifth and sixth columns show the FSE correction using MLL for times $n_4 \geq n_{4,i}$, with the fifth column computed via eq. (10.21) and the sixth with eqs. (10.4) and (10.5). Finally, the last column shows our estimate for the FSE correction for every ensemble. The central value is obtained integrating the correction

$$\Delta G_{33}(n_4) = \begin{cases} \Delta G_{33}^{\text{HP}}(n_4), & n_4 < n_{4,i}, \\ \Delta G_{33}^{\text{MLL}}(n_4), & n_4 \geq n_{4,i}. \end{cases} \quad (10.28)$$

This is not equal to $\hat{\Pi}_{33}^{\text{HP}}(n_4 < n_{4,i}) + \hat{\Pi}_{33}^{\text{MLL}}(n_4 \geq n_{4,i})$ because the time-slice $n_{4,i}$ might differ between both methods. To estimate the systematic error that we incur when using the last column of table 10.3, we use HP as an alternative. We apply each method to our data and, after extrapolating to the physical point in chapter 12, we take the difference between the results obtained at every virtuality using HP or MLL. This uncertainty is given in tables 13.1 and 13.2 for a representative set of energies.

Ensemble	$n_{4,i}$	whole range NLO ChPT	$n_4 < n_{4,i}$ HP	$n_4 \geq n_{4,i}$ MLL, cut	$n_4 \geq n_{4,i}$ MLL	whole range HP + MLL
H101	12	3.5 (0.1)	4.09 (0.09)	5.9 (0.1)	5.8 (0.1)	10.0 (0.2)
H102	10	8.2 (0.1)	5.38 (0.09)	17.4 (0.3)	17.4 (0.3)	23.0 (0.4)
H105	8	22.4 (0.3)	5.74 (0.13)	53.7 (2.3)	55.0 (2.2)	61.0 (2.2)
N101	18	4.4 (0.1)	4.66 (0.12)	3.0 (0.1)	3.0 (0.1)	7.7 (0.1)
C101	14	13.9 (0.4)	8.01 (0.18)	15.3 (0.5)	15.5 (0.5)	23.6 (0.5)
B450	10	6.2 (0.1)	4.09 (0.05)	16.8 (0.3)	16.9 (0.3)	21.1 (0.3)
S400	9	13.4 (0.2)	5.41 (0.06)	39.1 (0.9)	39.5 (0.8)	45.1 (0.9)
N451	16	6.8 (0.1)	5.85 (0.12)	7.6 (0.2)	7.6 (0.1)	13.5 (0.2)
D450	21	7.4 (0.2)	5.91 (0.15)	5.2 (0.1)	5.3 (0.1)	11.3 (0.2)
H200	9	12.2 (0.1)	4.20 (0.04)	46.2 (1.0)	46.0 (0.9)	50.4 (0.9)
N202	19	2.1 (0.0)	3.07 (0.08)	2.3 (0.0)	2.3 (0.0)	5.3 (0.1)
N203	16	5.8 (0.1)	5.10 (0.09)	8.9 (0.2)	8.7 (0.2)	13.9 (0.2)
N200	13	14.4 (0.2)	6.23 (0.07)	28.1 (0.5)	27.5 (0.6)	33.8 (0.6)
D200	17	20.2 (0.3)	9.08 (0.13)	23.8 (0.4)	24.3 (0.4)	33.5 (0.4)
E250	24	25.2 (0.5)	10.20 (0.20)	23.3 (0.5)	25.2 (0.5)	35.8 (0.6)
N300	15	6.2 (0.1)	4.33 (0.07)	16.9 (0.4)	16.9 (0.4)	21.3 (0.4)
N302	13	15.1 (0.2)	5.42 (0.04)	41.3 (1.2)	41.8 (1.1)	47.3 (1.1)
J303	17	19.0 (0.2)	7.70 (0.08)	36.0 (0.8)	35.6 (1.1)	43.3 (1.2)
E300	26	20.2 (0.2)	10.14 (0.15)	19.1 (0.2)	20.2 (0.2)	30.4 (0.3)

Table 10.3: FSE correction in the form $\text{sVPF} \times 10^5$. We indicate the ensemble name, the value of $n_{4,i}$ where we switch between the short and long distance models, the HP estimate if we only integrate times $n_4 < n_{4,i}$, the estimate using MLL for times $n_4 \geq n_{4,i}$ with eq. (10.21), MLL for times $n_4 \geq n_{4,i}$ with eqs. (10.4) and (10.5), and our estimate for the FSE correction for every ensemble.

In fig. 10.3, we compare the methods we have studied in this chapter. The y-axis shows the integrand of the sVPF at $Q^2 = 1 \text{ GeV}^2$ for the isovector correlator, and the x-axis the time in lattice spacings and fm. The grey area indicates the statistical error after we apply the tail treatment in chapter 9. The black line corresponds to NLO ChPT, the blue line to MLL, and the others represent the cumulative sum of the $\vec{m}^2 = 1, 2, 3$ levels of HP. We observe that the FSE are larger than the statistical error. Also, the HP and MLL estimates tend to agree for long distances, but the former is systematically below the latter.

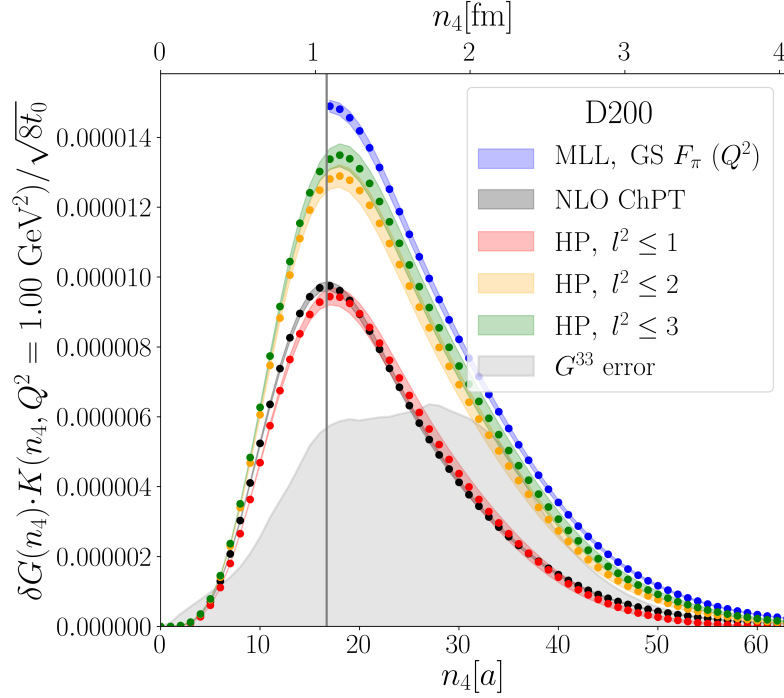


Figure 10.3: Integrand of the FSE contributing to the sVPF on ensemble D200. For the HP formalism, we plot the cumulative sum of the levels printed in table 10.2. For comparison, we also plot the size of the statistical error at each time-slice after we apply the bounding method in chapter 9. We only plot MLL in its range of validity $n_4 \geq n_{4,i}$.

Now is the moment when we can make use of ensembles H105, H200, N101 and N202. As stated in table 7.3, ensembles H105 and N101 share the same parameters except the volume, and the same happens for H200 and N202. Therefore, we can check if, after applying the FSE corrections, H105 coincides with N101, and H200 does the same with N202. Figure 10.4 compares H105 with N101 for a set of intermediate time-slices, and fig. 10.5 does the same with H200 and N202. Looking at fig. 10.4, we represent the dimensionless integrand of the isovector sVPF as a function of time for $Q^2 = 1 \text{ GeV}^2$. The red dots indicate the smaller volume before FSE correction, while the triangles show both volumes after being shifted (we show neither N101, nor N202 before the correction because the shift is very small). We can see that before adding the FSE, H105 and N101 differ substantially at every time-slice. However, after the correction, the agreement is good within uncertainties. In fig. 10.5, it is possible to appreciate that the difference between both volumes is even more extreme than for H105 and N101, perhaps due to the very small physical volume of H200. Despite this, the estimate of FSE accounts for the difference to a big extent, although it does not fill the gap completely. In fact, looking at the physical size L in table 7.3, one sees H200 is the smallest ensemble. Since we only use it to perform the comparison in fig. 10.5 and exclude it from the extrapolation to the physical point, we are confident any remaining FSE in other ensembles will be sub-leading.

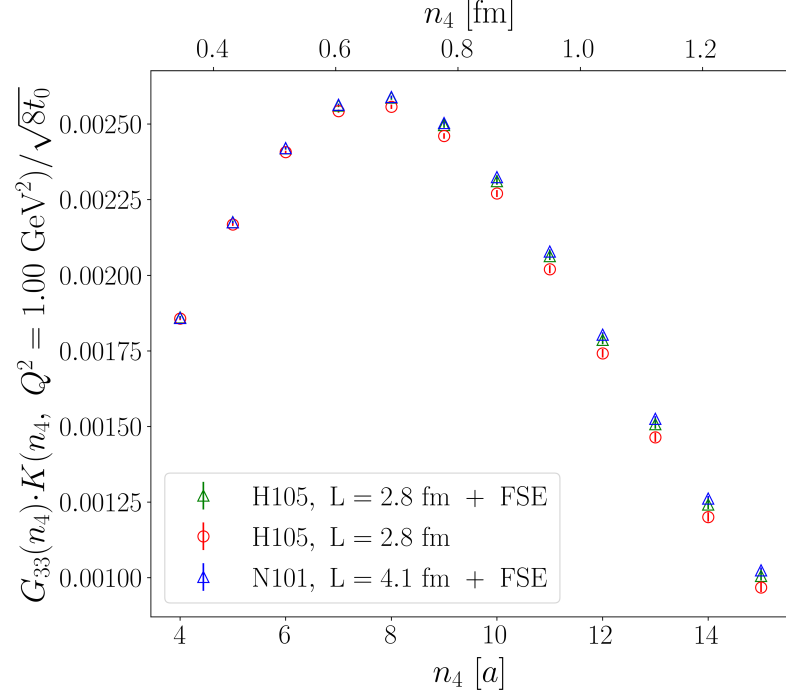


Figure 10.4: Comparison between ensembles H105 and N101, which have the same parameters except the volume. The y-axis indicates the dimensionless integrand of the sVPF, and the x-axis the time-slices. The three different sets of points represent the integrand of the two ensembles before (circles) and after (triangles) the FSE correction is applied. For N101, the FSE are very small and we only show the corrected data to improve visibility.

The FSE showed in table 10.3 are applied to both discretisations of the isovector component $G_{33}(n_4)$. However, at the $SU(3)_f$ -symmetric point, the two light and the strange quark propagators are mass degenerate, and they all contribute equally to the FSE. Since we have supposed that the two light quarks are the main source of FSE, we need to multiply our results by a factor $3/2$. It is true that the kaons will contribute to the FSE of all ensembles, but this factor approaches 1 exponentially fast with the kaon mass, $1.0 + 0.5 \times \exp(-[M_K - M_{K,SU(3)_f}]L)$. Then, since they are a sub-leading correction to an $\mathcal{O}(1\%)$ effect, we decide to use the pre-factor $3/2$ only at the $SU(3)_f$ -symmetric point.

After extensively discussing the corrections to the isovector channel, we turn briefly our attention to the other components. First, for ensembles at the $SU(3)_f$ -symmetric point, $\hat{\Pi}_{33} = \hat{\Pi}_{88}$, and we apply the same FSE to $\hat{\Pi}_{33}$ and $\hat{\Pi}_{88}$ with the same enhancement factor 1.5. Besides the $SU(3)_f$ point, however, we do not apply any FSE correction to $\hat{\Pi}_{88}$, and we correct neither $\hat{\Pi}_{08}$, nor $\hat{\Pi}_{cc}$. Nonetheless, the quark-connected and quark-disconnected components of $\hat{\Pi}_{88}$ and $\hat{\Pi}_{08}$ suffer from FSE because the light correlators dominate at long distances. This can be seen taking the ratio between the quark-connected piece and the

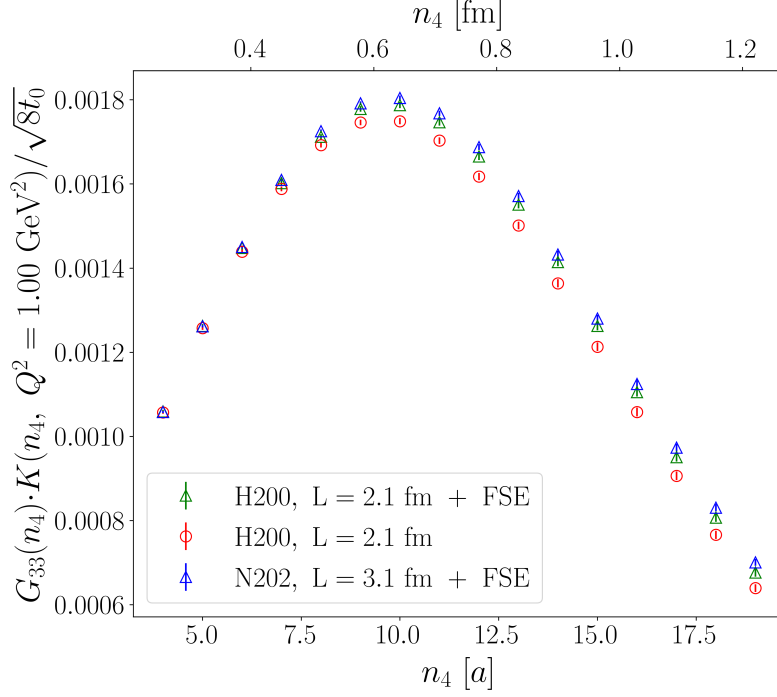


Figure 10.5: Comparison between ensembles H200 and N202, with the same format as fig. 10.4.

isovector correlator, both given in eq. (6.38). Taking the limit $n_4 \rightarrow \infty$, we have [265]

$$\lim_{n_4 \rightarrow \infty} \frac{G_{88}^{\text{con}}(n_4)}{G_{33}(n_4)} = \frac{1}{3}, \quad \lim_{n_4 \rightarrow \infty} \frac{G_{08}^{\text{con}}(n_4)}{G_{33}(n_4)} = \frac{1}{\sqrt{3}}. \quad (10.29)$$

Then, the FSE for non-SU(3)_f-symmetric ensembles are $1/3 \times \Delta G_{33}(n_4)$ for $G_{88}^{\text{con}}(n_4)$, and $1/\sqrt{3} \times \Delta G_{33}(n_4)$ for $G_{08}^{\text{con}}(n_4)$. In eq. (10.29), we have used the fact that the strange contribution $C_{(s,s)}(n_4)$ decays exponentially faster than the light component. For the quark-disconnected pieces, one can do the same, and take the ratios $G_{08}^{\text{dis}}(n_4)/G_{33}(n_4)$ and $G_{88}^{\text{dis}}(n_4)/G_{33}(n_4)$. The ratios at long distances yield the prefactors in eq. (10.29), but with opposite sign. Then, the correction to the quark-disconnected piece cancels that of the quark-connected as expected. Therefore, we use $-1/3$ for $G_{88}^{\text{dis}}(n_4)$ and $-1/\sqrt{3}$ for $G_{08}^{\text{dis}}(n_4)$. No more factors need to be considered because $\hat{\Pi}_{08}$, $\hat{\Pi}_{08}^{\text{con}}$, $\hat{\Pi}_{08}^{\text{dis}}$ and $\hat{\Pi}_{88}^{\text{dis}}$ are all zero at the SU(3)_f point, which is easy to understand looking at eqs. (6.36) to (6.38) and remembering that the light and strange propagators have the same mass, cancelling each other. Table 11.1 shows the sVPF $\times 10^5$ at $Q^2 = 1 \text{ GeV}^2$ after including the finite-size effects with the appropriate enhancement prefactor.

Chapter 11

$\hat{\Pi}$ on the lattice

Here, we gather the results for the various components of the sVPF after applying the tail treatment in chapter 9 and the finite-size effects in chapter 10. In table 11.1, we show $\hat{\Pi} \times 10^5$

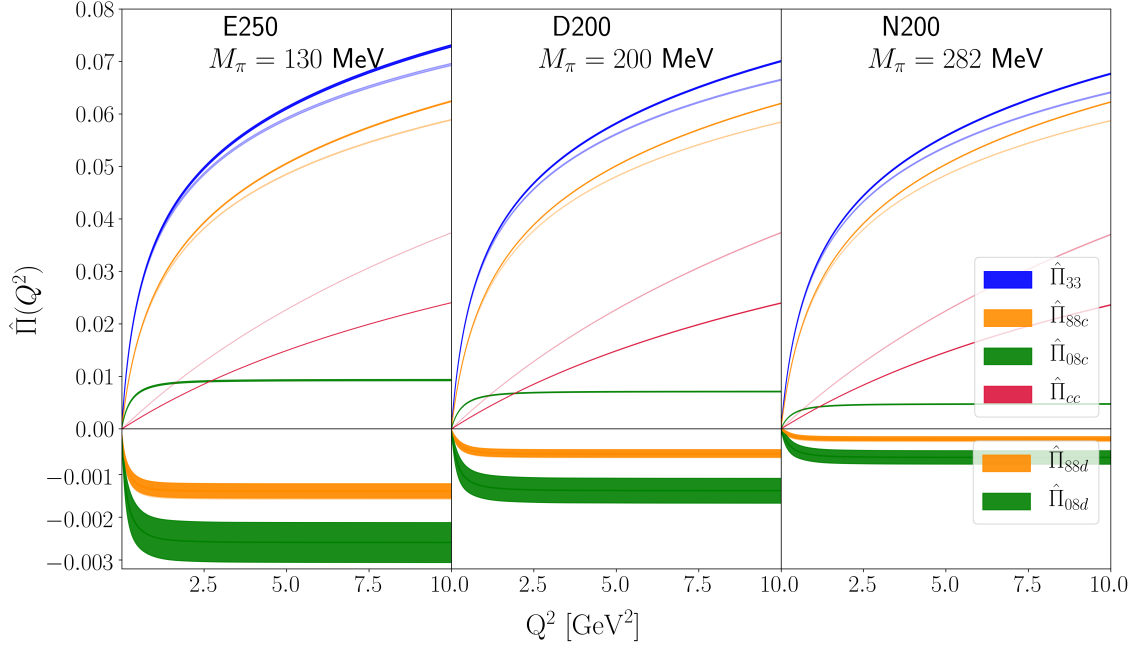


Figure 11.1: The sVPF for ensembles E250, D200 and N200. Note the different scale for positive and negative values. We show the l (fainter colour) and s discretisations. For the disconnected piece, both discretisations lie on top of each other.

at $Q^2 = 1 \text{ GeV}^2$ for all the components that we need to compute $(\Delta\alpha)_{\text{had}}$ and $(\Delta \sin^2 \theta_W)_{\text{had}}$. The quark-connected and quark-disconnected pieces are given separately. Note $\hat{\Pi}_{33} = \hat{\Pi}_{88}^{\text{con}}$ at the $\text{SU}(3)_f$ -symmetry point, and that we only show the non-zero components. We only have data for the symmetric, point-split discretisation for the 08 component. The second parenthesis for $\hat{\Pi}_{cc}$ corresponds to the κ -tuning uncertainty, discussed in section 7.1.3.

Ensemble	$\hat{\Pi}_{33}$	$\hat{\Pi}_{88}^{\text{con}}$	$\hat{\Pi}_{88}^{\text{dis}}$	$\hat{\Pi}_{88}$	$\hat{\Pi}_{08}^{\text{con}}$	$\hat{\Pi}_{08}^{\text{dis}}$	$\hat{\Pi}_{08}$	$\hat{\Pi}_{cc}$
H101 c.l.	2852 (6)	2852 (6)					338.8 (0.8) (0.8)	
l.l.	2765 (6)	2765 (6)					650.1 (1.4) (1.5)	
H102 c.l.	2977 (9)	2746 (6)	-11 (1)	2736 (6)	208 (4)	-36 (8)	172 (9)	339.7 (0.8) (1.2)
l.l.	2891 (10)	2660 (7)	-11 (1)	2649 (7)				647.9 (1.5) (2.1)
H105 c.l.	3158 (20)	2668 (10)	-14 (8)	2654 (12)	431 (11)	-53 (21)	377 (22)	346.1 (1.1) (0.9)
l.l.	3070 (20)	2581 (11)	-15 (8)	2566 (12)				655.1 (2.0) (1.6)
N101 c.l.	3166 (10)	2680 (5)	-29 (4)	2651 (6)	429 (6)	-65 (8)	364 (10)	346.0 (0.9) (0.9)
l.l.	3083 (10)	2594 (6)	-31 (4)	2563 (6)				654.0 (1.5) (1.6)
C101 c.l.	3348 (15)	2680 (6)	-57 (7)	2623 (9)	586 (8)	-130 (12)	457 (13)	347.1 (0.8) (0.5)
l.l.	3262 (14)	2595 (7)	-62 (8)	2533 (10)				653.5 (1.2) (0.8)
B450 c.l.	2762 (7)	2762 (7)						343.1 (0.8) (1.1)
l.l.	2694 (8)	2694 (8)						593.7 (1.4) (1.8)
S400 c.l.	2896 (12)	2656 (8)	-13 (2)	2644 (8)	216 (5)	-30 (10)	187 (12)	344.6 (0.9) (1.1)
l.l.	2830 (12)	2590 (8)	-13 (2)	2577 (8)				585.3 (1.4) (1.7)
N451 c.l.	3096 (7)	2627 (3)	-22 (3)	2606 (4)	411 (4)	-53 (10)	358 (10)	355.8 (0.2) (0.8)
l.l.	3030 (8)	2561 (3)	-23 (3)	2538 (4)				604.8 (0.5) (1.2)
D450 c.l.	3279 (9)	2604 (3)	-33 (8)	2571 (8)	592 (5)	-54 (31)	538 (30)	360.7 (0.2) (0.4)
l.l.	3214 (9)	2538 (3)	-38 (7)	2500 (7)				608.7 (0.4) (0.6)
H200 c.l.	2690 (15)	2690 (15)						353.9 (1.2) (1.0)
l.l.	2644 (15)	2644 (15)						538.1 (1.7) (1.5)
N202 c.l.	2732 (12)	2732 (12)						352.9 (1.1) (1.0)
l.l.	2686 (12)	2686 (12)						536.4 (1.7) (1.5)
N203 c.l.	2877 (9)	2620 (6)	-10 (1)	2611 (7)	223 (5)	-23 (9)	200 (11)	360.4 (0.7) (0.7)
l.l.	2829 (10)	2573 (7)	-10 (1)	2563 (7)				546.0 (1.0) (1.0)
N200 c.l.	3022 (11)	2548 (5)	-22 (4)	2526 (6)	412 (7)	-61 (15)	351 (17)	367.2 (1.0) (0.5)
l.l.	2974 (11)	2502 (5)	-24 (5)	2478 (6)				552.8 (1.3) (0.7)
D200 c.l.	3247 (12)	2534 (5)	-54 (9)	2480 (9)	619 (7)	-133 (28)	486 (29)	374.7 (0.8) (0.4)
l.l.	3199 (12)	2487 (5)	-56 (8)	2431 (9)				560.6 (1.0) (0.6)
E250 c.l.	3533 (22)	2587 (8)	-136 (17)	2451 (16)	824 (13)	-251 (46)	574 (42)	376.1 (0.1) (0.4)
l.l.	3486 (22)	2540 (8)	-138 (17)	2402 (16)				560.8 (0.2) (0.6)
N300 c.l.	2591 (13)	2591 (13)						359.6 (1.8) (1.5)
l.l.	2563 (13)	2563 (13)						476.6 (2.3) (1.9)
N302 c.l.	2731 (14)	2467 (8)	-10 (4)	2457 (9)	231 (6)	-2 (17)	229 (17)	372.6 (1.0) (0.8)
l.l.	2703 (14)	2440 (8)	-10 (3)	2430 (9)				490.7 (1.3) (1.0)
J303 c.l.	3027 (18)	2454 (7)	-36 (5)	2418 (10)	498 (10)	-88 (22)	410 (25)	374.8 (1.2) (0.7)
l.l.	3000 (18)	2427 (7)	-37 (5)	2390 (10)				486.7 (1.5) (0.8)
E300 c.l.	3259 (26)	2455 (9)	-65 (17)	2390 (19)	699 (15)	-169 (49)	530 (53)	379.9 (0.4) (0.0)
l.l.	3233 (26)	2428 (9)	-65 (18)	2362 (19)				496.2 (0.5) (0.0)

Table 11.1: $\text{sVPF} \times 10^5$ to be extrapolated at $Q^2 = 1 \text{ GeV}^2$ for every ensemble, discretisation and component. The first uncertainty is statistical, and for the charm contribution we also indicate the error due to the κ_{charm} mistuning, explained in section 7.1.3.

Chapter 12

Extrapolation to the physical point

So far, we have computed $\hat{\Pi}_{33}(Q^2)$, $\hat{\Pi}_{88}(Q^2)$, $\hat{\Pi}_{cc}(Q^2)$ and $\hat{\Pi}_{08}(Q^2)$ at several physical and unphysical meson masses with a non-zero lattice spacing. After treating the signal-to-noise ratio problem in chapter 9, and estimating the results in infinite volume in chapter 10, whose results at $Q^2 = 1 \text{ GeV}^2$ are presented in table 11.1, it is still necessary to extrapolate to the physical point, which allows us to make a testable prediction of the quantities subject of this project. The strategy we employ was firstly devised for the isovector $\hat{\Pi}_{33}$ and isoscalar $\hat{\Pi}_{88}$ components, which constitute the bulk of our computation. Therefore, we explain first their extrapolation in section 12.1, where we give all the details about the fit procedure. Later, in sections 12.2 and 12.3, we use the same method to extrapolate $\hat{\Pi}_{cc}$ and $\hat{\Pi}_{08}$, respectively. We decided to fit the full $\hat{\Pi}_{88}$ and $\hat{\Pi}_{08}$, instead of their quark-connected and quark-disconnected pieces alone, because they show better fit quality and they are closer to what can be compared with phenomenology.

First of all, we define the physical point of isospin-symmetric QCD (QCD_{iso}) by the pion and kaon meson masses [158, 34]

$$\begin{aligned} M_{\pi}^{\text{phy}} &= M_{\pi^0}^{\text{exp}} = 134.9768(5) \text{ MeV}, \\ M_K^{\text{phy}} &= \frac{1}{2} \left(\left(M_{K^+}^{\text{exp}} \right)^2 + \left(M_{K^0}^{\text{exp}} \right)^2 - \left(M_{\pi^+}^{\text{exp}} \right)^2 + \left(M_{\pi^0}^{\text{exp}} \right)^2 \right) = \\ &= 495.011(15) \text{ MeV}. \end{aligned} \quad (12.1)$$

where the pion and kaon masses do not include neither QED effects, nor strong IB effects. We denote the sVPPF extrapolated to the physical point as $\hat{\Pi}^{\text{phy}}$. Throughout this section, the independent variables used for the extrapolation are

$$\frac{a^2}{8t_0^{\text{sym}}}, \quad \phi_2 = 8t_0 M_{\pi}^2, \quad \phi_4 = 8t_0 (M_{\pi}^2/2 + M_k^2), \quad (12.2)$$

where $8t_0^{\text{sym}}/a^2$ is the scale at the $\text{SU}(3)_f$ -symmetric point shown in table 3.1 for every lattice spacing, and $8t_0$, M_{π} and M_K are given in table 7.4. For the purpose of the extrapolation to the continuum limit, using $8t_0^{\text{sym}}/a^2$ means that all ensembles at the same β share the same scale. The quantities ϕ_2 and ϕ_4 , on the other hand, are evaluated on each

ensemble. The physical point can also be defined in terms of the dimensionless quantities ϕ_2 and ϕ_4 employing eq. (12.1) and $(8t_0^{\text{phy}})^{1/2} = 0.415(4)(2)$ fm [142],

$$\begin{aligned}\phi_2^{\text{phy}} &= 8t_0^{\text{phy}} \left(M_\pi^{\text{phy}}\right)^2 = 0.0805(17), \\ \phi_4^{\text{phy}} &= 8t_0^{\text{phy}} \left(\left(M_\pi^{\text{phy}}\right)^2 / 2 + \left(M_K^{\text{phy}}\right)^2 \right) = 1.124(24).\end{aligned}\tag{12.3}$$

12.1 Extrapolation of $\hat{\Pi}_{33}$ and $\hat{\Pi}_{88}$

The biggest contribution to our target quantity $\hat{\Pi}$ comes from the isovector and isoscalar components. We perform the extrapolation of both together, in such a way that we take into account the correlations between the two, which are the most relevant in our problem. This is the most complicated fit that we have to carry out, and we use this section to explain our fit strategy, applying it directly to the isovector and isoscalar components to make it more concrete. We start in section 12.1.1 presenting the fit model that we employ. Then, we explain the method of total least-squares in section 12.1.2, and we discuss the regularisation of the covariance matrix in section 12.1.3. In section 12.1.4, we further study the continuum extrapolation. Finally, we present the results in section 12.1.5.

12.1.1 Fit model

We start our discussion stating that, from the fits we have performed, the fit model can be divided into two parts, one which encapsulates the dependence with the lattice spacing, $\hat{\Pi}_{\text{lat}}$, and another which only varies with the mass variables ϕ_2 and ϕ_4 . Mixing terms depending on both the lattice spacing and the meson masses have been found to be irrelevant. Then, our most general model can be written as

$$\hat{\Pi}(a, \phi_2, \phi_4; d, i) = \hat{\Pi}_{\text{lat}}(a; d) + \hat{\Pi}_{\text{mass}}(\phi_2, \phi_4; i).\tag{12.4}$$

The arguments $d = \text{s}, \text{l}$ and $i = 33, 88$ indicate that we use different fit parameters depending on the discretisation or the isospin. $\hat{\Pi}_{\text{lat}}(0; d) = 0$ for both discretisations, in such a way that $\hat{\Pi}_{\text{mass}}(\phi_2, \phi_4; i)$ indicates the dependence in the continuum. In particular, $\hat{\Pi}_{\text{mass}}(\phi_2^{\text{phy}}, \phi_4^{\text{phy}}; i) = \hat{\Pi}^{\text{phy}}(i)$ is the sVPF at the physical point for each isospin. In the following lines, we present the specific expressions for $\hat{\Pi}_{\text{lat}}(a; d)$ and $\hat{\Pi}_{\text{mass}}(\phi_2, \phi_4; i)$ that we have used for $i = 33, 88$. Note that the models for the charm and the 08 components also accept the simple decomposition in eq. (12.4), and we will give their explicit formulas in sections 12.2 and 12.3.

For the lattice dependence, our correlators are $\mathcal{O}(a)$ improved, and therefore we expect a leading behaviour $\propto a^2$ with the lattice spacing. At higher virtualities Q^2 , we also find a sizeable contribution from an a^3 term. Also, following [278], we investigated the possibility of terms $\sim a^2 \log a^2$, but they were compatible with zero and we do not include them. Then,

the models we have used for $\hat{\Pi}_{\text{lat}}(a; d)$ are

$$\hat{\Pi}_{\text{lat}}(a; d) = \begin{cases} \alpha_{2,d} \frac{a^2}{8t_0^{\text{sym}}}, & (12.5) \\ \alpha_{2,d} \frac{a^2}{8t_0^{\text{sym}}} + \alpha_{3,d} \left(\frac{a^2}{8t_0^{\text{sym}}} \right)^{3/2}, & (12.6) \end{cases}$$

where the fit parameters are $\alpha_{2,d}$ and $\alpha_{3,d}$ and we have checked that the lattice artefacts of $i = 33$ and $i = 88$ are compatible.

Regarding the mass dependence, the kaon mass on our ensembles oscillates between -3.5% and $+5.5\%$ of the target physical value ϕ_4^{phy} . This motivates the use of a simple linear dependence on ϕ_4 to model small deviations from the expected behaviour $M_K^2 + M_\pi^2/2 = \text{const.}$ With respect to the pion mass dependence, the data shows a linear behaviour in ϕ_2 at high pion masses (see fig. 12.6), while it develops a curvature towards the chiral limit $M_\pi \rightarrow 0$. To model the latter, we note that the isovector contribution is singular towards this limit [242], and use a logarithmic term,

$$\begin{aligned} \hat{\Pi}_{\text{mass}}(\phi_2, \phi_4; i = 33) = & \hat{\Pi}^{\text{sym}} + \beta_{1,33} (\phi_2 - \phi_2^{\text{sym}}) \\ & + \delta (\phi_4 - \phi_4^{\text{sym}}) + \beta_{2,33} \log(\phi_2/\phi_2^{\text{sym}}). \end{aligned} \quad (12.7)$$

The isoscalar contribution is finite at the chiral limit [242], so we use a quadratic term in ϕ_2 ,

$$\begin{aligned} \hat{\Pi}_{\text{mass}}(\phi_2, \phi_4; i = 88) = & \hat{\Pi}^{\text{sym}} + \beta_{1,88} (\phi_2 - \phi_2^{\text{sym}}) \\ & + \delta \left(\phi_4 - \frac{3}{2} \phi_2^{\text{sym}} \right) + \beta_{2,88} (\phi_2 - \phi_2^{\text{sym}})^2. \end{aligned} \quad (12.8)$$

Note that $\phi_4^{\text{sym}} = 3/2 \phi_2^{\text{sym}}$ and, therefore, it is not a free parameter. In total, our fit model has 9 parameters, which are $\hat{\Pi}^{\text{sym}}$, ϕ_2^{sym} , $\alpha_{2,1}$, $\alpha_{2,8}$, $\beta_{1,33}$, $\beta_{1,88}$, $\beta_{2,33}$, $\beta_{2,88}$, and δ . We center eqs. (12.7) and (12.8) around the $\text{SU}(3)_f$ -symmetric point $(\phi_2^{\text{sym}}, \phi_4^{\text{sym}})$, where the model yields $\hat{\Pi}^{\text{sym}}$, such that the fit does not depend on the specific definition of the physical point. The latter is not trivial in our case, as we lack IB effects in our simulations, and we have used several different definitions during the course of time. Then, even if the physical point is redefined, we can still use the same fit results to obtain the corresponding $\hat{\Pi}^{\text{phy}}$.

Besides eqs. (12.7) and (12.8), we tried other two possibilities for β_2 , which model the data towards the chiral limit in a slightly different way. For the isovector,

$$\beta_{2,i} (1/\phi_2^{\text{sym}} - 1/\phi_2), \quad (12.9)$$

which still shows a singularity at the chiral limit. And for the isoscalar,

$$\beta_{2,i} (\phi_2 \log \phi_2 - \phi_2^{\text{sym}} \log \phi_2^{\text{sym}}). \quad (12.10)$$

We choose eqs. (12.7) and (12.8) for the isovector and isoscalar channels, respectively, because they reproduce the value of our physical mass ensemble E250 and yield the best fit quality —see fig. 12.6.

The way we use eqs. (12.5) to (12.8) is simple. We have two fit models for every isospin. For example, we fit the isovector to $\hat{\Pi}(a, \phi_2, \phi_4; d, i = 33)$ in eq. (12.4) with either eq. (12.5) or eq. (12.6) for the continuum extrapolation $\hat{\Pi}_{\text{lat}}(a; d)$, and eq. (12.7) for the interpolation to the physical point $\hat{\Pi}_{\text{mass}}(\phi_2, \phi_4; i)$. Then, we obtain two values for $\hat{\Pi}(a, \phi_2, \phi_4; d, i = 33)$ at every Q^2 , which might differ if $\alpha_{3,d} \neq 0$. Later, in section 12.1.4, we explain eqs. (12.5) and (12.6) further and, in section 13.1, we describe how we obtain a single value for $\hat{\Pi}_{33}(a, \phi_2, \phi_4; d, i = 33)$ at every Q^2 .

12.1.2 Total least-squares minimisation

The method that we use to find the fit parameters is called total least squares [279, 280], which means that we include the errors of both the x and y axes in the minimisation of a χ^2 . For the minimisation itself, we use the routine *least_squares* of the SciPy package [281], which implements the Levenberg-Marquardt algorithm [282]. In our case, we include the uncertainties of the sVPF, ϕ_2 and ϕ_4 , which include the uncertainty of $8t_0/a^2$ measured on each ensemble. The data belonging to one ensemble is fully correlated, while different ensembles are completely independent — if we were to use $8t_0^{\text{sym}}$ instead of $8t_0/a^2$ to compute ϕ_2 , ϕ_4 and $\hat{\Pi}$, this would induce correlations among all ensembles with the same β . The χ^2 that we need to minimize is

$$\chi^2 = \sum_e \chi_e^2 \equiv \sum_e \begin{cases} \chi_{e,-}^2, & \text{if } M_{\pi,e} \neq M_{K,e}, \\ 1/2 (\chi_{e,33}^2 + \chi_{e,88}^2), & \text{if } M_{\pi,e} = M_{K,e}. \end{cases} \quad (12.11)$$

The index e runs over the ensembles, and depending on whether a given box lies at the $\text{SU}(3)_f$ -symmetric point or not, we use the second or the first line on eq. (12.11) to define χ_e^2 . $\chi_{e,-}^2$, $\chi_{e,33}^2$ and $\chi_{e,88}^2$ can be written with the same generic structure $r^T \text{Cov}^{-1} r$, where $r = \text{model} - \text{data}$ is the vector of residues, and Cov is the covariance matrix. However, the explicit expression of the latter elements, r and Cov , depend on whether $M_{\pi,e} = M_{K,e}$ or not on a particular ensemble,

The residue vector r for non- $\text{SU}(3)_f$ -symmetric ensembles is defined as

$$r_{e,-} = \begin{pmatrix} \phi_2 \\ \phi_4 \\ \hat{\Pi}(a, \phi_2, \phi_4; d = 1, i = 33) \\ \hat{\Pi}(a, \phi_2, \phi_4; d = s, i = 33) \\ \hat{\Pi}(a, \phi_2, \phi_4; d = 1, i = 88) \\ \hat{\Pi}(a, \phi_2, \phi_4; d = s, i = 88) \end{pmatrix} - \begin{pmatrix} \phi_2 \\ \phi_4 \\ \hat{\Pi}_{33}^1 \\ \hat{\Pi}_{33}^s \\ \hat{\Pi}_{88}^1 \\ \hat{\Pi}_{88}^s \end{pmatrix}_e, \quad (12.12)$$

where the subscript e on the RHS column indicates that it uses the data for the given ensemble. The LHS column includes the model of eq. (12.4). On the LHS column, we leave

ϕ_2 and ϕ_4 as free parameters, giving $\phi_2 = \phi_{2,e}$ and $\phi_4 = \phi_{4,e}$ as a first guess. Then, ϕ_2 and ϕ_4 are allowed to change by an amount close to their uncertainty and, after the χ^2 has been minimized, their final result might slightly differ from their initial value. This accounts for the fact that ϕ_2 and ϕ_4 carry an uncertainty. Of course, a large deviation will increment the χ_e^2 , so changes bigger than $\phi_{2,e}$'s and $\phi_{4,e}$'s uncertainty are penalized. On top of this, the inclusion of ϕ_2 and ϕ_4 does not modify the number of degrees of freedom.

For $SU(3)_f$ -symmetric ensembles, $\chi_{e,33}^2$ and $\chi_{e,88}^2$ are defined differently. The residue is given by

$$r_{e,i} = \left(\frac{\phi_2}{\hat{\Pi}(a, \phi_2, 3\phi_2/2; d=1, i)} \right) - \left(\frac{\phi_2}{\hat{\Pi}_i^1} \right)_e. \quad (12.13)$$

By construction, $\chi_{e,33}^2$ and $\chi_{e,88}^2$ are not equal, because $\chi_{e,33}^2$ uses the model for the isovector, and $\chi_{e,88}^2$ for the isoscalar. Of course, the rightmost column, which contains the data, is the same for both isospin components. Equation (12.11) is what enforces $\chi_{e,33}^2 = \chi_{e,88}^2$, although the coincidence does not have to be exact.

Turning now our attention to the symmetric covariance matrix Cov, we start with the non- $SU(3)_f$ -symmetric ensembles. The index structure is

$$\text{Cov}_{e,-} = \begin{pmatrix} \phi_2, \phi_2 & \phi_2, \phi_4 & \phi_2, \hat{\Pi}_{33}^1 & \phi_2, \hat{\Pi}_{33}^S & \phi_2, \hat{\Pi}_{88}^1 & \phi_2, \hat{\Pi}_{88}^S \\ \vdots & \phi_4, \phi_4 & \phi_4, \hat{\Pi}_{33}^1 & \phi_4, \hat{\Pi}_{33}^S & \phi_4, \hat{\Pi}_{88}^1 & \phi_4, \hat{\Pi}_{88}^S \\ \vdots & \vdots & \hat{\Pi}_{33}^1, \hat{\Pi}_{33}^1 & \hat{\Pi}_{33}^1, \hat{\Pi}_{33}^S & \hat{\Pi}_{33}^1, \hat{\Pi}_{88}^1 & \hat{\Pi}_{33}^1, \hat{\Pi}_{88}^S \\ \vdots & \vdots & \vdots & \hat{\Pi}_{33}^S, \hat{\Pi}_{33}^S & \hat{\Pi}_{33}^S, \hat{\Pi}_{88}^1 & \hat{\Pi}_{33}^S, \hat{\Pi}_{88}^S \\ \vdots & \vdots & \vdots & \vdots & \hat{\Pi}_{88}^1, \hat{\Pi}_{88}^1 & \hat{\Pi}_{88}^1, \hat{\Pi}_{88}^S \\ \dots & \dots & \dots & \dots & \dots & \hat{\Pi}_{88}^S, \hat{\Pi}_{88}^S \end{pmatrix}_e \quad (12.14)$$

It is straightforward to adapt eq. (12.14) to obtain the corresponding covariance matrix for $SU(3)_f$ -symmetric ensembles,

$$\text{Cov}_{e,i} = \begin{pmatrix} \phi_2, \phi_2 & \phi_2, \hat{\Pi}_i^1 & \phi_2, \hat{\Pi}_i^S \\ \vdots & \hat{\Pi}_i^1, \hat{\Pi}_i^1 & \hat{\Pi}_i^1, \hat{\Pi}_i^S \\ \dots & \dots & \hat{\Pi}_i^S, \hat{\Pi}_i^S \end{pmatrix}_e \quad (12.15)$$

The entry x, y of any of the covariance matrices on eqs. (12.14) and (12.15) can be computed from the bootstrap distribution [252],

$$\text{Cov}_{e.,[x,y]} = \frac{1}{N_b - 1} \sum_{s=1}^{N_b} (x_s - E[x]) (y_s - E[y]), \quad (12.16)$$

where $.$ refers to either of $-$ or i , with N_b the number of bootstrap samples, and $E[x]$ is the expectation value of x . For the latter, as explained in section 8.5, we can use the

estimate given by the original set of configurations after applying the bounding method and correcting for FSE. The inverse is obtained performing a Cholesky decomposition, $\text{Cov} = LL^T$, and inverting the lower triangular matrix L . The reason why we require a different structure for $\text{SU}(3)_f$ and non- $\text{SU}(3)_f$ symmetric ensembles is simple. At the $\text{SU}(3)_f$ point, $\phi_4 = 3/2\phi_2$ and $\hat{\Pi}_{88} = \hat{\Pi}_{33}$ sample by sample. Therefore, eq. (12.14) would be a singular matrix which cannot be inverted. As a consequence, we can not include the isovector and isoscalar components together in the covariance matrix.

At this point, our model comprises of several parameters plus one or two free masses per ensemble. This renders the minimisation process very difficult. However, we found that giving the derivative of the χ^2 function with respect to the fit parameters in the form of a Jacobian matrix speeds up the convergence. To compute the Jacobian for every ensemble, we define a vector y of length $m \times 1$ containing all the fit parameters,

$$y \equiv (\hat{\Pi}^{\text{sym}}, \alpha_{2,\text{S}}, \alpha_{3,\text{S}}, \beta_{1,33}, \text{ etc.}). \quad (12.17)$$

The vector y includes ϕ_2 for the $\text{SU}(3)_f$ -symmetric ensembles, and ϕ_2 and ϕ_4 for the rest —note ϕ_2 is a variable, while $\phi_{2,e}$ is a data-point. Then, we apply the Cholesky decomposition on either of $\chi_{e,-}^2$, $\chi_{e,33}^2$ or χ_{88}^2 ,

$$\chi_{e,.} = L_{e,.}^{-1} r_{e,.}, \quad (12.18)$$

such that $\chi_{e,.}$ is a $n \times 1$ vector, with n the number of independent ($\hat{\Pi}$) plus dependent (ϕ_2, ϕ_4) variables for a given ensemble. Then, we need to compute the $m \times n$ matrix of derivatives

$$\frac{\partial \chi_{e,.}}{\partial y} = \frac{\partial r_{e,.}}{\partial y} (L_{e,.}^{-1})^T, \quad (12.19)$$

or alternatively

$$\left(\frac{\partial \chi_{e,.}}{\partial y} \right)^T = L_{e,.}^{-1} \left(\frac{\partial r_{e,.}}{\partial y} \right)^T, \quad (12.20)$$

which is simpler to compute, as it is the solution of a system of the type $Ax = b$. The vector of residues $r_{e,.}$ corresponds with eq. (12.12) for non- $\text{SU}(3)_f$ -symmetric ensembles, and with eq. (12.13) for $\text{SU}(3)_f$ -symmetric ensembles. Correspondingly, one uses the Cholesky decomposition of eq. (12.14) and eq. (12.15). For $\text{SU}(3)_f$ -symmetric ensembles, $m = 10$ and $n = 3$, while $m = 11$ and $n = 6$ for the rest. Then, the Jacobian for every ensemble is the derivative of eq. (12.11) — see [283] for the set of matrix derivative rules —, with

$$\frac{\partial \chi_e}{\partial y} \chi_e = \begin{cases} \frac{\partial \chi_{e,-}}{\partial y} \chi_{e,-}, & \text{if } M_{\pi,e} \neq M_{K,e} \\ \frac{1}{2} \left(\frac{\partial \chi_{e,33}}{\partial y} \chi_{e,33} + \frac{\partial \chi_{e,88}}{\partial y} \chi_{e,88} \right), & \text{if } M_{\pi,e} = M_{K,e}. \end{cases} \quad (12.21)$$

12.1.3 Regularisation of the covariance matrix

Although the covariance matrix plays a central role in the minimisation problem, we only have a stochastic estimate of the former with unknown uncertainty. In fact, fitting together both l and s discretisations might provoke a nearly singular covariance matrix, because they

are very correlated. However, we believe the gain in precision when doubling the amount of data-points fitted together outweighs the drawbacks, if we can maintain the singularity of the covariance matrix under control. Therefore, we need to study the correlations and the impact they have in the final result and assess the corresponding uncertainty. To this end, we modify the covariance matrix, and use a so-called Ledoit-Wolf shrinkage estimator [284, 285],

$$\text{Cov} = \lambda \text{Cov} + (1 - \lambda) \text{diag}(\text{Cov}), \quad (12.22)$$

where $\lambda \in [0, 1]$. The combination of Cov and $\text{diag}(\text{Cov})$ in eq. (12.22) simply scales the off-diagonal elements in the covariance matrix. See [286] for a more complete implementation of shrinkage estimators in *Python*. Figure 12.1 shows how the fit quality and the extrapolated value look like as a function of λ for the isovector and isoscalar components. The x-axis shows the various values of λ , the right y-axis indicates the extrapolated value of the sVPF for the isovector and the isoscalar components with its corresponding uncertainty, and the left y-axis shows the variation of the fit quality, given as χ^2/dof . The best fit quality is indicated by a star. $\lambda = 1$ corresponds to a fit where the covariance matrix is taken as it is computed in eq. (12.14), while a value $\lambda = 0$ corresponds to an uncorrelated fit. Two aspects are relevant in the plot. First, the central values are largely independent of the correlations included in the fit. Second, the fit quality is far from constant. With a maximum at $\lambda = 1$, a small variation of approximately 5 to 10% drives the fit quality to a region where its value barely changes, finding a minimum at $\lambda \approx 0.6$. For the results of this project, we decide to select $\lambda = 0.95$, keeping the correlations of the covariance matrix as intact as possible. Any further reduction of λ barely changes neither the fit quality, nor the results.

12.1.4 Study of discretisation effects

Higher momentum Q^2 give more weight to the early time-slices in the integrand $\hat{\Pi}$, as can be seen in fig. 6.1. In this region, the integrand rises to the apex, around $an_4 = 1$ fm or earlier, in few time steps. Together with the small statistical errors in this region, it is clear the lattice spacing has an impact on the sVPF that becomes more relevant with increasing virtuality. Before modelling these effects, there are two ways to ameliorate them and ease the continuum extrapolation. First, one may compare the impact of different definitions for the derivative of the $\mathcal{O}(a)$ -improvement term in eq. (6.12). Each alternative, either the forward, symmetric or backward derivative, introduces different $\mathcal{O}(a^2)$ effects that might benefit the continuum extrapolation. In particular, it might reduce lattice artefacts, decreasing the difference between the sVPF on each particular β and the continuum. One simply needs to plot fig. 12.6 for the various options and compare. For the components $\hat{\Pi}_{33}$, $\hat{\Pi}_{88}$ and $\hat{\Pi}_{08}$, we choose the symmetric derivative, while we select the forward derivative for $\hat{\Pi}_{cc}$. Second, one can employ different integration schemes for $\hat{\Pi}$. We decide to use the simple right Riemann sum, which only introduces $\mathcal{O}(a^2)$ discretisation errors. Since the integrand is not a monotonic function, the real error introduced by this choice might be smaller, as the sVPF is overestimated at early times and underestimated afterwards.

The different choices for the derivative and the integration method should yield the

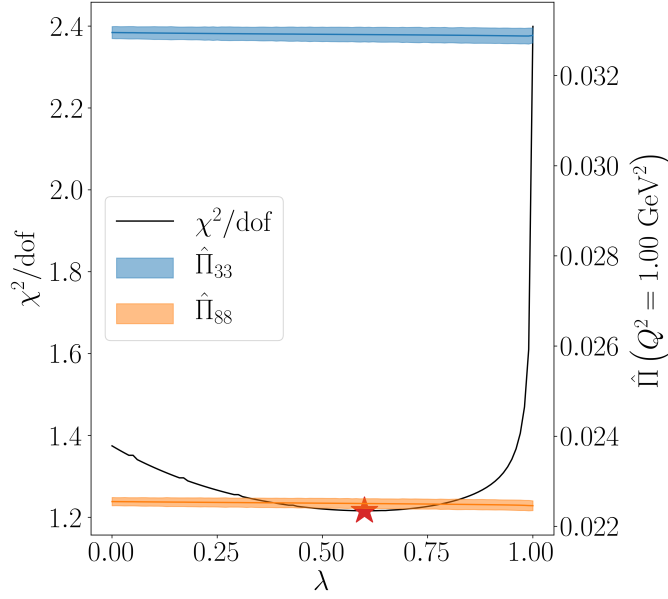


Figure 12.1: Dependence of the fit quality and the result on the size of the off-diagonal elements of the covariance matrix. The left-hand y-axis indicates the fit quality, while the right-hand y-axis the change of the isovector's (upper band) and isoscalar's (lower band) central value and error. The x-axis indicates the off-diagonal multiplicative factor. The star indicates the best fit quality.

same results, but they might require models of various complexities for the continuum extrapolation. Since the data are not determined with infinite precision and we have a limited set of ensembles, one may not be able to fit arbitrarily difficult models; therefore, we consider only the extrapolation with smaller lattice artefacts and discard the other derivatives as suboptimal. We simply check that all options give the same results within uncertainties.

To study the continuum extrapolation, we work with several possibilities: First, we want to rule out the option of residual $\mathcal{O}(a)$ lattice artefacts; second, we fit an $\mathcal{O}(a^2)$ term, which is our naive expectation after full $\mathcal{O}(a)$ improvement; third, we study the possibility of a dependence of the form $\alpha_2 a^2 + \alpha_3 a^3$, where a^2 is the dominant effect and a^3 only a correction; finally, we consider the option where we have the combination $\alpha a + \alpha_2 a^2$. To do this, we follow a procedure suggested by the authors of [218]. The lattice artefacts are gathered, mainly, on the first time-slices of the correlator. Then, we get rid of the tail of the correlator multiplying by a smooth step-function [107],

$$\begin{aligned} \hat{\Pi}^{\text{short}}(Q^2; n_{4,0}, \delta) &= \frac{1}{a} \sum_{n_4=0}^T G(n_4) K(n_4, Q^2) (1 - \Theta(an_4, an_{4,0}, \delta)), \\ \Theta(an_4, an_{4,0}, \delta) &= \frac{1}{2} (1 + \tanh((an_4 - an_{4,0})/\delta)), \end{aligned} \quad (12.23)$$

where $an_{4,0} = 1$ fm and $\delta = 0.15$ fm. Next, we fit $\hat{\Pi}_{33}^{\text{short}}$ using eq. (12.5) without the ϕ_4

term. Our objective is to perform a very simple fit which allows us to interpolate groups of ensembles at the same M_π , M_K . We gather the following sets of ensembles at the same mass: H101, B450, N202 and N300 at $M_\pi = M_K = 420$ MeV; H102, S400, N203 and N302 at $M_\pi = 350$ MeV and $M_K = 440$ MeV; N101, N451, N200 and J303 at $M_\pi = 280$ MeV and $M_K = 470$ MeV; and finally, C101, D450, D200 and E300 at $M_\pi = 220$ MeV and $M_K = 480$ MeV. Each ensemble is fully correlated with the other members of its group after we interpolate to the same mass.

Then, we extrapolate each of these groups to the continuum using the models

$$\hat{\Pi}_{33}^{\text{short}}(a, d) = \hat{\Pi} + \alpha_d \frac{a}{\sqrt{8t_0^{\text{sym}}}}, \quad (12.24)$$

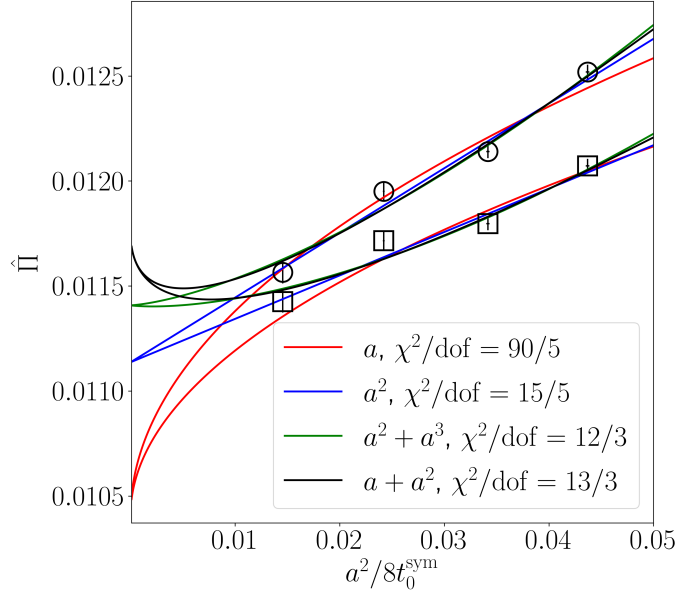
$$\hat{\Pi}_{33}^{\text{short}}(a, d) = \hat{\Pi} + \alpha_{2,d} \frac{a^2}{8t_0^{\text{sym}}}, \quad (12.25)$$

$$\hat{\Pi}_{33}^{\text{short}}(a, d) = \hat{\Pi} + \alpha_{2,d} \frac{a^2}{8t_0^{\text{sym}}} + \alpha_{3,d} \left(\frac{a^2}{8t_0^{\text{sym}}} \right)^{3/2}, \quad (12.26)$$

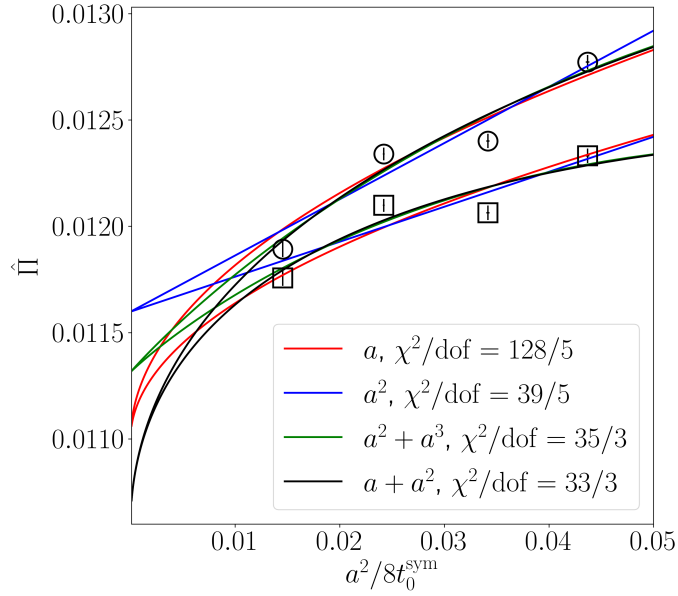
$$\hat{\Pi}_{33}^{\text{short}}(a, d) = \hat{\Pi} + \alpha_d \frac{a}{\sqrt{8t_0^{\text{sym}}}} + \alpha_{3,d} \left(\frac{a^2}{8t_0^{\text{sym}}} \right)^{3/2}, \quad (12.27)$$

where $\hat{\Pi}$ is the result in the continuum limit and both correlator discretisations are fitted together. All parameters, $\hat{\Pi}$, α_d , $\alpha_{2,d}$ and $\alpha_{3,d}$, depend implicitly on M_π , M_K and Q^2 . Note as well, these do not have the same value as in eqs. (12.5) and (12.6), but are fitted to the clusters of ensembles aforementioned. Figures 12.2 and 12.3 show the results of the extrapolation at $Q^2 = 0.5 \text{ GeV}^2$, and figs. 12.4 and 12.5 depict the extrapolation at $Q^2 = 5 \text{ GeV}^2$. Each subplot shows the extrapolation of one particular set of ensembles: H101, B450, N202 and N300 in figs. 12.2a and 12.4a; H102, S400, N203 and N302 in figs. 12.2b and 12.4b; N101, N451, N200 and J303 in figs. 12.3a and 12.5a; and C101, D450, D200 and E300 in figs. 12.3b and 12.5b. The most important feature of these plots is the comparison of the fit quality χ^2/dof for each model, given in the legend. We see that the model linear on a on eq. (12.24) can be ruled out in all cases. At small momentum, the models of eqs. (12.26) and (12.27) tend to over-fit the data, leaving the model linear on a^2 , eq. (12.25), as the best option. For higher momentum, one single parameter is insufficient because all plots in figs. 12.4 and 12.5 show curvature. Between the models in eqs. (12.26) and (12.27), the one with an a^2 term outperforms the model with residual $\mathcal{O}(a)$ effects.

Concluding this section, the study of discretisation effects presented here suggests that we should use a model with a^2 dependence, eq. (12.25), at small momentum, while we should add an extra a^3 term, eq. (12.26), to describe the onset of stronger lattice artefacts at higher Q^2 . However, as one can see from the fit quality in figs. 12.2 to 12.5, we find very difficult to fit the data given by eq. (12.23), which is much more precise than the full correlator. This prevents us from stating that, without a doubt, eqs. (12.5) and (12.6) are the true or best models to extrapolate to the continuum. A more dedicated study of correlators at short distances has recently appeared in [278], which suggests a logarithmically-enhanced term $\propto a^2/8t_0^{\text{sym}} \log(8t_0^{\text{sym}}/a^2)$ for the components $\hat{\Pi}_{33}$ and $\hat{\Pi}_{88}$. Either because we use

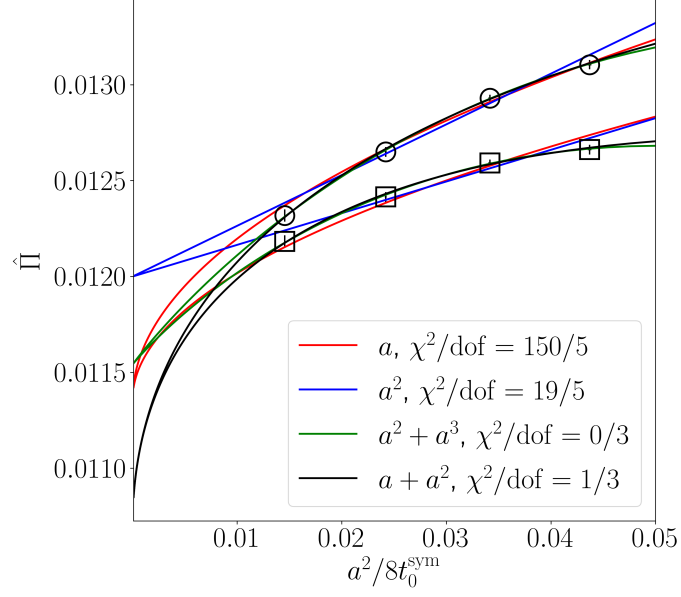


(a) Extrapolation of ensembles H101, B450, N202 and N300 at $M_\pi = M_K = 420$ MeV.

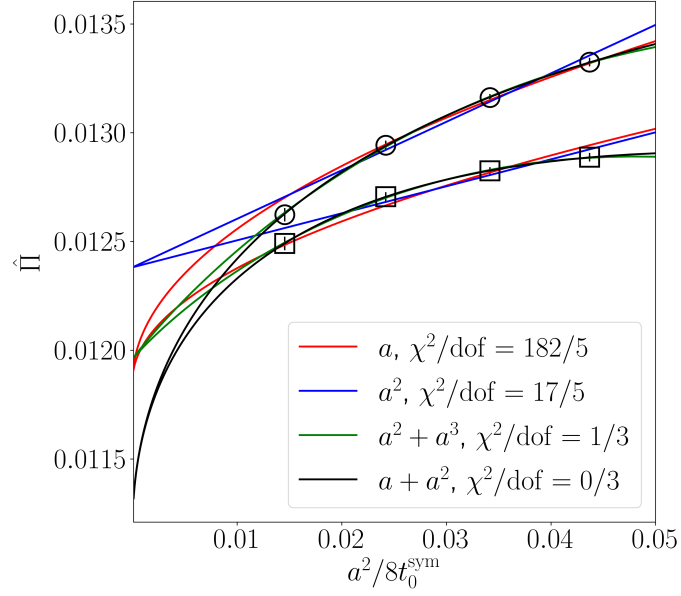


(b) Extrapolation of ensembles H102, S400, N203 and N302 at $M_\pi = 350$ MeV, $M_K = 440$ MeV.

Figure 12.2: Extrapolation to the continuum limit of $\hat{\Pi}_{33}$ at $Q^2 = 0.5 \text{ GeV}^2$ using both discretisations. The circles correspond to the l-discretisation and the squares with the s-discretisation. The legend of each plot indicates the χ^2/dof for each fit.

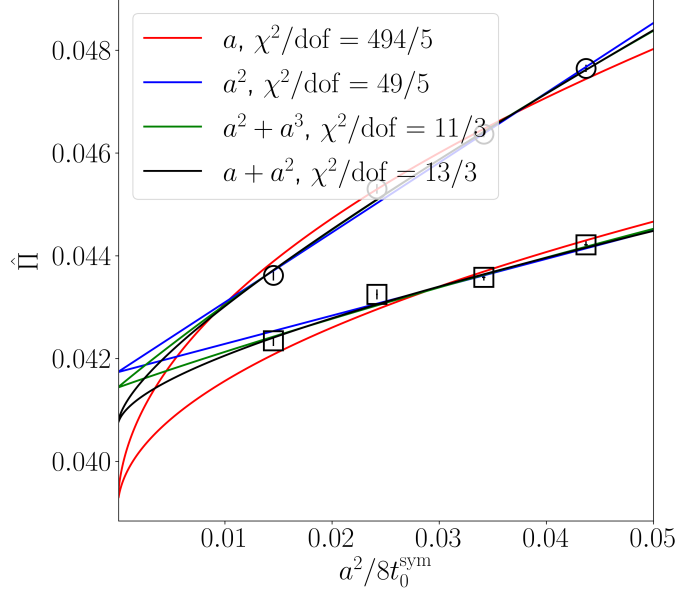


(a) Extrapolation of ensembles N101, N451, N200 and J303 at $M_\pi = 280$ MeV, $M_K = 470$ MeV.

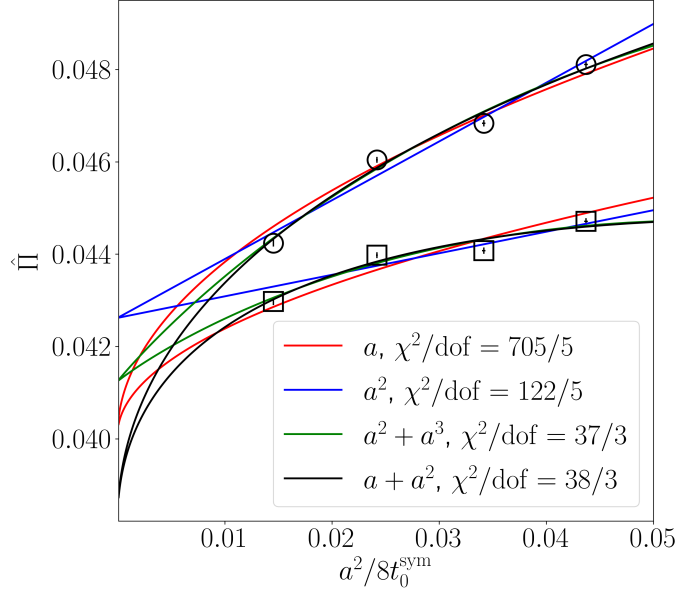


(b) Extrapolation of ensembles C101, D450, D200 and E300 at $M_\pi = 220$ MeV, $M_K = 480$ MeV.

Figure 12.3: Extrapolation to the continuum limit of $\hat{\Pi}_{33}$ at $Q^2 = 0.5 \text{ GeV}^2$ using both discretisations. The circles correspond to the l-discretisation and the squares with the s-discretisation. The legend of each plot indicates the χ^2/dof for each fit.

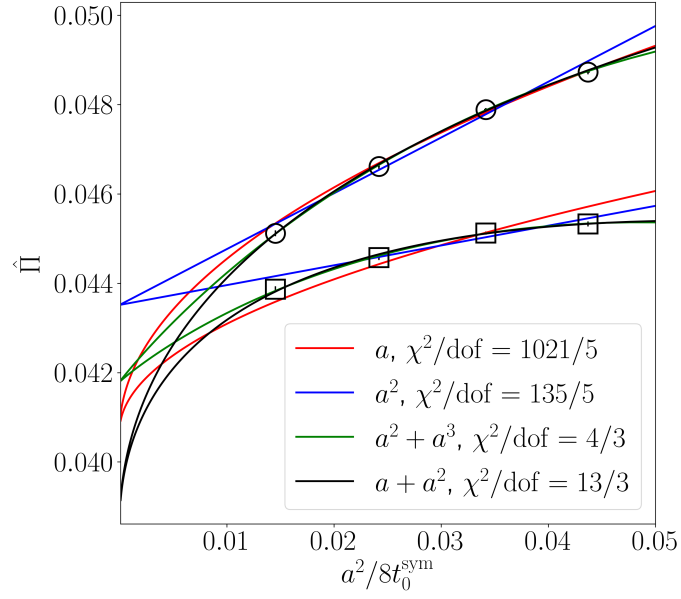


(a) Extrapolation of ensembles H101, B450, N202 and N300 at $M_\pi = M_K = 420$ MeV.

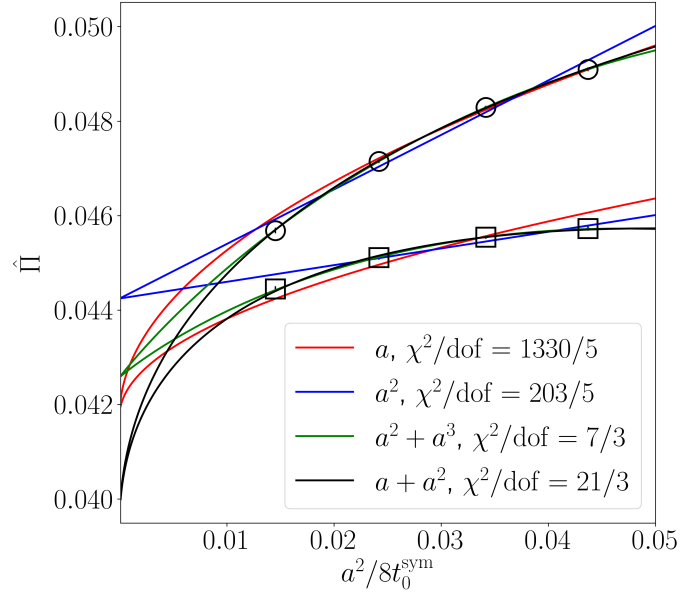


(b) Extrapolation of ensembles H102, S400, N203 and N302 at $M_\pi = 350$ MeV, $M_K = 440$ MeV.

Figure 12.4: As fig. 12.2, but at $Q^2 = 5 \text{ GeV}^2$.



(a) Extrapolation of ensembles N101, N451, N200 and J303 at $M_\pi = 280$ MeV, $M_K = 470$ MeV.



(b) Extrapolation of ensembles C101, D450, D200 and E300 at $M_\pi = 220$ MeV, $M_K = 480$ MeV.

Figure 12.5: As fig. 12.3, but at $Q^2 = 5 \text{ GeV}^2$.

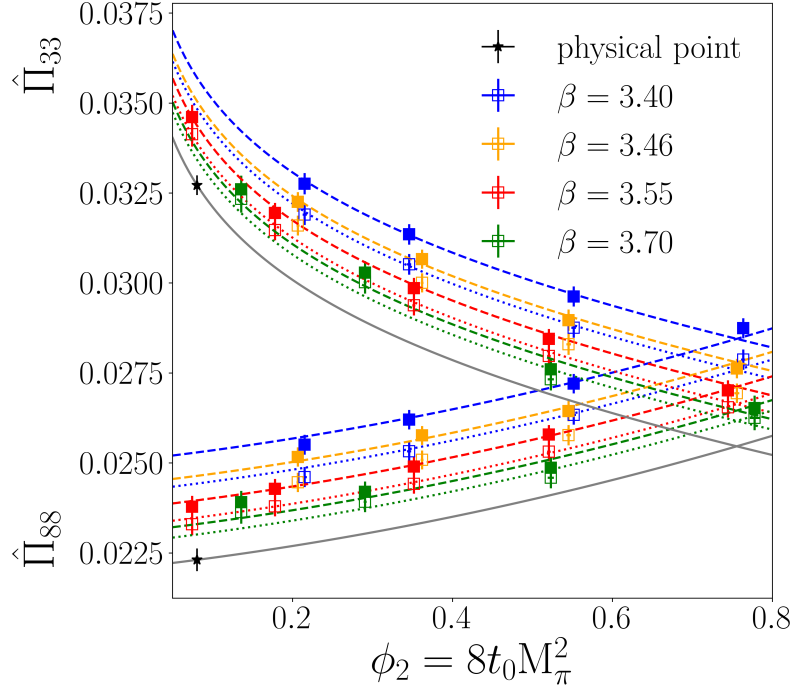


Figure 12.6: Extrapolation of $\hat{\Pi}_{33}$ and $\hat{\Pi}_{88}$ to the physical point at 1 GeV^2 . The different lattice spacings are depicted with several colours, with the symmetric, point-split discretisation in solid squares and dashed lines, and the local discretisation in open squares and dotted lines. The result in the continuum limit is shown with a grey line, and the physical point is given by a black dot.

lattice spacings that are too coarse for the diverging behaviour of the logarithm to stand out, or because our statistics are too low, we do not seem to observe this term. As better techniques, more ensembles and statistics become available, we will be able (and forced) to further refine our extrapolation model.

12.1.5 Results

In fig. 12.6, we show the extrapolation of the isovector and isoscalar components at $Q^2 = 1 \text{ GeV}^2$, whose values $\times 10^5$ are given in table 11.1. We depict the different lattice spacings in different colours; the dashed and dotted lines indicate the fit model for the sl and ll correlator discretisations, respectively, while the data-points are either full or empty squares. The upper part of the plot includes the isovector component, while the lower half shows the isoscalar contribution. Both coincide at the $\text{SU}(3)_f$ point, $\hat{\Pi}_{33} = \hat{\Pi}_{88}$. The continuum extrapolations of the two components, depicted with a grey line, cross each other at the point $(\phi_2^{\text{sym}}, \hat{\Pi}^{\text{sym}})$. $\hat{\Pi}^{\text{phy}}(i = 33)$ and $\hat{\Pi}^{\text{phy}}(i = 88)$ are depicted by the black stars with their corresponding statistical uncertainty. One important feature this plot shows is the fact that the model, shown by the different lines, describes well the data-points at the physical pion mass (ensemble E250). The inclusion of, at least, one ensemble at the

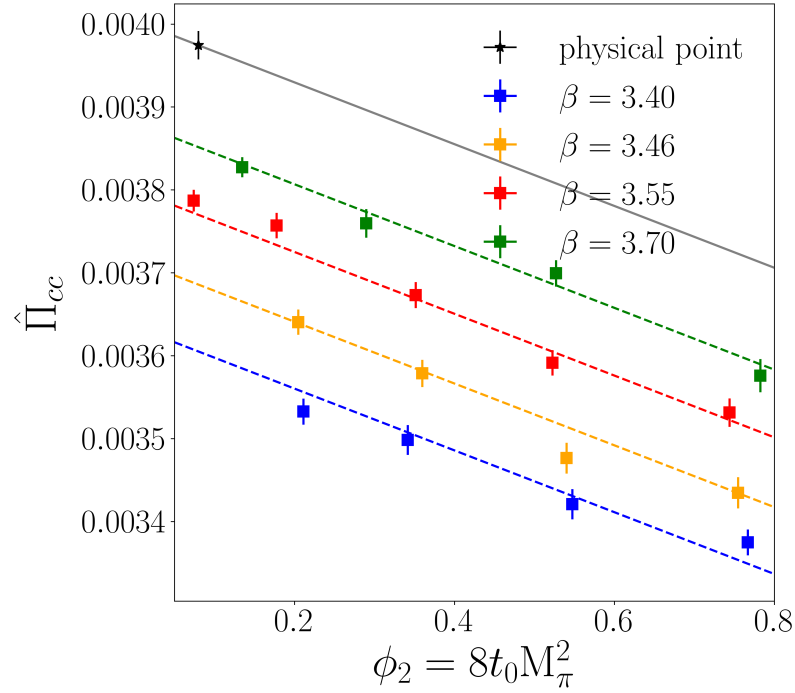


Figure 12.7: Extrapolation of $\hat{\Pi}_{cc}$ at $Q^2 = 1 \text{ GeV}^2$, using the same notation as fig. 12.6.

physical meson masses has been shown [242] to be necessary to control the extrapolation in the mass variables at the level of precision we aim at. To explore the systematic uncertainty of the fit, we remove those ensembles with $\phi_2 > 0.6$ in the extrapolation, corresponding to the $\text{SU}(3)_f$ point. Note that we do not show plots fitting this reduced set, as the difference with fitting all ensembles, like in fig. 12.6, is hardly visible. We take half the difference between the fits with and without cut as an estimate of the extrapolation uncertainty at the physical point. Table 13.1 shows fit results at several energies, with the breakdown of the various sources of statistical and systematic error, which are discussed in section 13.1. The fit quality of the entire CLS set is given in the lower panel of fig. 13.1, and the fit quality for the set with $\phi_2 < 0.6$ appears in fig. 13.2. The rapid deterioration of the χ^2/dof for the model using only an a^2 term to take the continuum limit prompts the discussion in section 13.1.

12.2 Extrapolation of $\hat{\Pi}_{cc}$

In comparison with the isovector and isoscalar components, the charm contribution shows characteristics of its own, and we choose to extrapolate it alone. To begin with, one may compare the two correlator discretisations to be extrapolated in table 11.1. On the one hand, the conserved-local case shows less than 10% difference between points at similar pion masses and different lattice spacings. On the other hand, the lattice artefacts of the

local-local discretisation reach 30%. Indeed, we could expect the lattice artefacts for the charm component to be large, because the integrand of the sVPF peaks almost at the origin, concentrating the entire integral around a handful of time-slices. The different improvement term might cause one discretisation to suffer from larger lattice artefacts than the other. Therefore, we choose to extrapolate only the symmetric, point-split data to avoid an increase of the systematic uncertainty. Second, the uncertainty due to the mistuning of κ_{charm} is sometimes as sizeable, or even larger, than the statistical uncertainty (see table 7.2 and section 7.1.3). Third, the $\text{SU}(3)_f$ -symmetric point has no special relevance in this case, and we extrapolate directly to the physical point. Fourth, the statistics of the charm component are smaller than for the other components and the small correlations between them could not be included reliably in the covariance matrices on eqs. (12.14) and (12.15). Finally, the meson mass dependence is very mild and we are not sensitive to any curvature. Then, we can describe the charm data-points with a simple linear term in ϕ_2 ,

$$\hat{\Pi}_{\text{charm}}(a, \phi_2) = \hat{\Pi}^{\text{phy}} + \alpha_{2,\text{S}} \frac{a^2}{8t_0^{\text{sym}}} + \beta_{1,c} \left(\phi_2 - \phi_2^{\text{phy}} \right). \quad (12.28)$$

To study the systematics of this extrapolation, we perform two cuts in the pion masses. One excludes all ensembles with $\phi_2 > 0.6$ in fig. 12.7, the second excludes all ensembles with $\phi_2 > 0.4$. Results between the various cuts are fully compatible. There is one last modification that we need to take into account. The gradient flow $8t_0$ has its own dependence with the meson masses. In the case of the isovector and isoscalar extrapolation, this dependence was absorbed by the fit model in eqs. (12.7) and (12.8). However, our fit function is much simpler now, and using $8t_0$ to compute $\phi_{2,e}$, $\phi_{4,e}$ and $\hat{\Pi}_c^{\text{S}}(Q^2)$ yields data-points which cannot be fitted with eq. (12.28). Therefore, we replace $8t_0$ by $8t_0^{\text{sym}}$, which has the same value irrespective of the meson mass, and fig. 12.7 has been produced using this modified version of the data-points. Note that this introduces correlations between all ensembles at the same lattice spacing, increasing the size of the covariance matrix, making more difficult the extrapolation. As for the isovector and isoscalar components, we give the fit quality of the charm extrapolation in figs. 13.1 and 13.2. The fit quality becomes acceptable for the cut $\phi_2 < 0.4$, while the $\chi^2/\text{dof} \gtrsim 2$ for the entire set of ensembles and for the cut $\phi_2 < 0.6$. However, since the results of the various cuts fully agree, we do not consider this as a problem. The origin of the bad fit quality might come from the larger size of the covariance matrix.

12.3 Extrapolation of $\hat{\Pi}_{08}$

As we saw in chapter 6, the 08 component should be zero at the $\text{SU}(3)_f$ point (c.f. eqs. (6.37) and (6.38)). Then, our model should only depend on terms of the form $\phi_4 - 3\phi_2/2 \propto M_K^2 - M_\pi^2$, but not on ϕ_2 or ϕ_4 individually. On top of this, a term proportional to a^2 was found to be compatible with zero. Therefore, the model we employ is simply

$$\hat{\Pi}_{08}(\phi_2, \phi_4) = \hat{\Pi} \cdot \left(\phi_4 - \frac{3}{2}\phi_2 \right) = 8t_0 \hat{\Pi} \cdot \left(M_K^2 - M_\pi^2 \right). \quad (12.29)$$

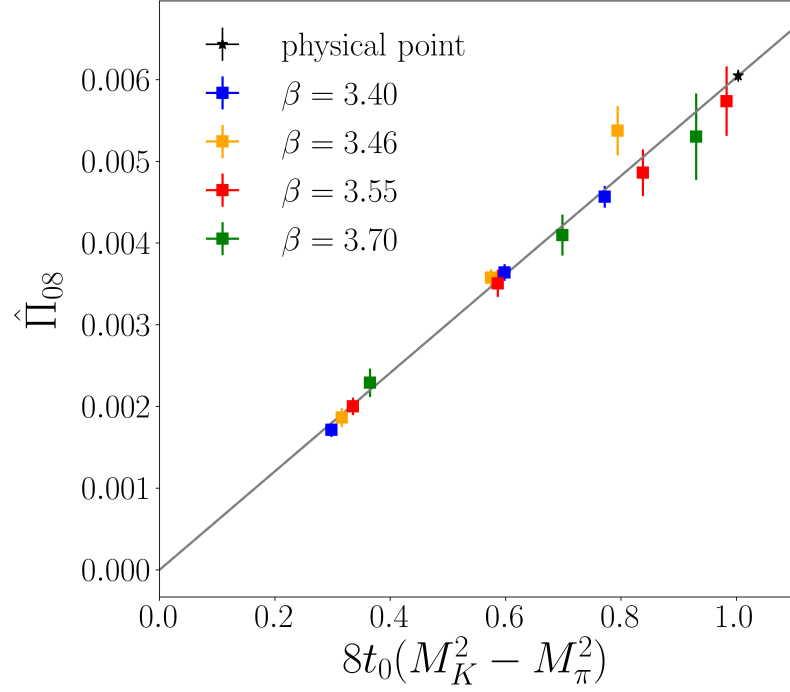


Figure 12.8: Extrapolation of $\hat{\Pi}_{08}$ at $Q^2 = 1 \text{ GeV}^2$, using the same notation as fig. 12.6.

Figure 12.8 shows the extrapolation of the 08 component using eq. (12.29). The data show neither a lattice spacing dependence, nor curvature. To estimate the systematics of the extrapolation, we cut all ensembles with masses $\phi_4 - 3\phi_2/2 < 0.4$. Although we only have at our disposal data for the symmetric, point-split discretisation, the small contribution of the 08 component to $\hat{\Pi}_{Z\gamma}$ and the simple fit model required to fit the data suggest that one discretisation is enough at our level of precision. Again, figs. 13.1 and 13.2 contain the extrapolation fit quality for the 08 component, finding always an excellent $\chi^2/\text{dof} < 1$.

Chapter 13

$\hat{\Pi}$, $(\Delta\alpha)_{\text{had}}$ and $(\Delta \sin^2 \theta_W)_{\text{had}}$ at the physical point

13.1 Transition between low and high momentum

To study the energy dependence of the sVPF, we extrapolate at $\mathcal{O}(100)$ different points from 0 to 10 GeV^2 . In figs. 13.1 and 13.2, we plot these results in the form of bands, indicating the running with the momentum of the various sVPF components. Each plot includes an upper and lower panel. While the upper panel indicates the dependence of the sVPF on Q^2 , the lower panel shows the corresponding fit quality. Both isovector and isoscalar components have two different runnings depending on whether we use a model with only an a^2 term, eq. (12.5), or also an a^3 component, eq. (12.6), for the continuum extrapolation. In the upper plot, we observe that the results for both models agree well within uncertainties up to, approximately, 3 GeV^2 , but eq. (12.6) has larger uncertainties than eq. (12.5). For $Q^2 < 3 \text{ GeV}^2$, the parameters $\alpha_{3,d}$ in eq. (12.6) are compatible with zero, and the fit itself has the same quality as the model in eq. (12.5) but with larger errors. This clearly indicates that eq. (12.6) over-fits the data at small momenta and eq. (12.5), with only an a^2 term, is sufficient. However, at larger momenta, eq. (12.5) is no longer enough to describe the lattice dependence, and the fit quality deteriorates sharply. There, one needs to use eq. (12.6), whose fit quality remains largely independent of the energy, and the parameters $\alpha_{3,d}$ are different from zero.

Therefore, while at small momenta the a^2 model in eq. (12.5) describes the data well and the extra a^3 term in eq. (12.6) over-fits, we require the latter instead for larger energies, where the pure a^2 model is insufficient. To give a unique description of the sVPF at each energy, we transition from one model to the other with a smooth step function,

$$\begin{aligned} \hat{\Pi}(0, \phi_2^{\text{phy}}, \phi_4^{\text{phy}}; i, Q^2) = & \hat{\Pi}_{a^2}(0, \phi_2^{\text{phy}}, \phi_4^{\text{phy}}; i) \left(1 - \Theta(Q^2)\right) \\ & + \hat{\Pi}_{a^3}(0, \phi_2^{\text{phy}}, \phi_4^{\text{phy}}; i) \Theta(Q^2), \end{aligned} \quad (13.1)$$

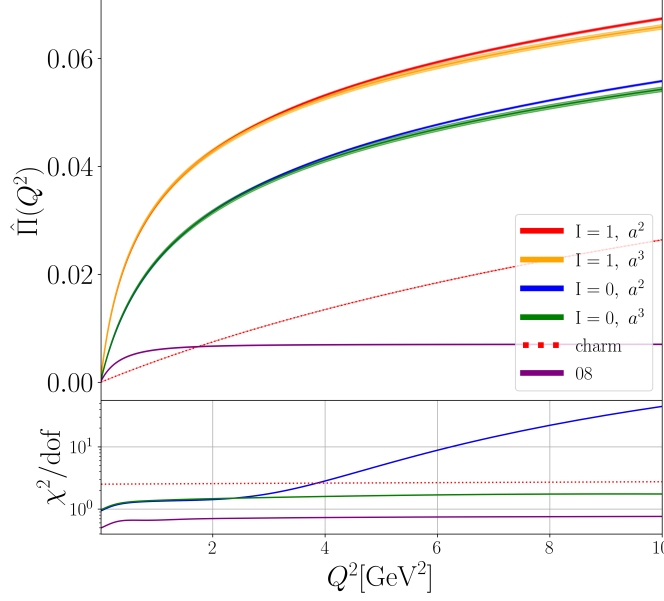


Figure 13.1: The upper panel shows the sVPF for the various $\hat{\Pi}$ components as a function of the space-like energy Q^2 , while the lower panel indicates the quality of the corresponding fit. For the isovector and isoscalar, we show the fit results using either the a^2 model of eq. (12.5) or the $a^2 + a^3$ function of eq. (12.6).

where $\hat{\Pi}_{a^2}$ uses eq. (12.5) for $\hat{\Pi}_{\text{lat}}(a; d)$, $\hat{\Pi}_{a^3}$ employs eq. (12.6), and

$$\Theta(Q^2) \equiv \frac{1}{2} \left(1 + \tanh \left(Q^2 - 2.5 \text{ GeV}^2 \right) \right). \quad (13.2)$$

Since we are in the continuum limit, eq. (13.2) no longer depends on the discretisation d .

13.2 Scale-setting uncertainty

In sections 12.1 to 12.3, we have not taken into account the uncertainty of the flow time $8t_0^{\text{phy}}$ for the continuum extrapolation. We do this to simplify the extrapolation to the physical point and, since the scale-setting is one of the most important sources of uncertainty, to give a detailed error budget that differentiates between statistics and scale-setting errors.

The scale-setting uncertainty mainly enters through three different quantities: $8t_0^{\text{phy}}Q^2$, ϕ_2^{phy} and ϕ_4^{phy} . That is, the scale is needed to define the physical point and compute $\hat{\Pi}$ at a particular momentum. We make use of the bootstrap sampling to estimate the uncertainty that these three quantities induce into $\hat{\Pi}$, $(\Delta\alpha)_{\text{had}}$ and $(\Delta\sin^2\theta_W)_{\text{had}}$, taking into account correlations. The latter stem from $8t_0^{\text{phy}}$, which has the dominant uncertainty and whose pseudo-bootstrap distribution is used for all three quantities $8t_0^{\text{phy}}Q^2$, ϕ_2^{phy} and ϕ_4^{phy} . For every isospin component, we compute the scale-setting error in two steps: First, we include the bootstrap distribution of ϕ_2^{phy} and ϕ_4^{phy} . Then, we estimate the error from

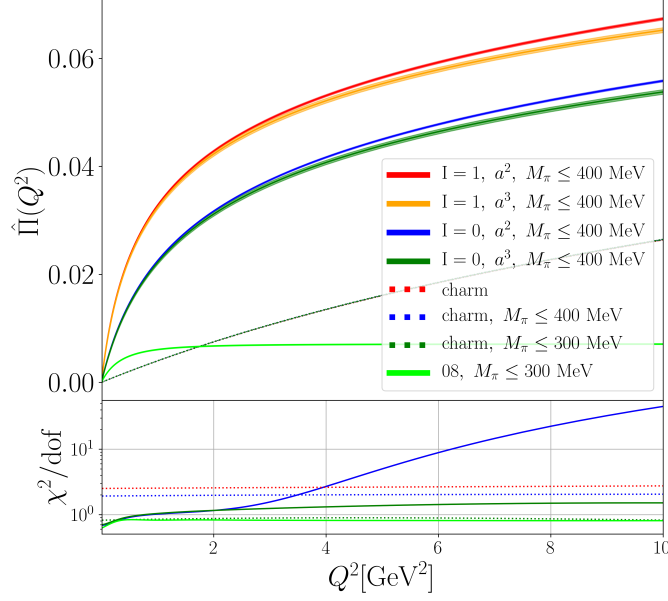


Figure 13.2: Same as fig. 13.1, but extrapolating to the physical point without including those ensembles with a pion mass heavier than 400 MeV. In the case of the charm quark, the number of data-points is enough to remove also every ensemble with $M_\pi > 300$ MeV.

$8t_0^{\text{phy}}Q^2$. Before describing the procedure, we introduce some notation. We differentiate between the bootstrap distribution of a quantity, A , its expectation value, $\text{Exp } A$, and a sample of its bootstrap distribution, A_s . Let us suppose that we want to compute the scale-setting error for the isovector component. Starting with ϕ_2^{phy} and ϕ_4^{phy} , we take the model in eq. (12.4), formed by the lattice and mass dependence on eqs. (12.6) and (12.7), and consider only the expectation value of the parameters obtained in the fit (we could have taken eq. (12.5) instead, but eq. (12.6) gives a more conservative estimate of the uncertainty for the entire range of momenta). Then, we evaluate the model at every bootstrap sample of ϕ_2^{phy} and ϕ_4^{phy} with $a = 0$. This produces a bootstrap distribution for $\hat{\Pi}_{33}^{\text{phy}}$ that reflects the uncertainty of $8t_0^{\text{phy}}$. The next step is to add the error from $8t_0^{\text{phy}}Q^2$ at a particular momentum Q_{target}^2 . First, we select all points $\{8t_0^{\text{phy}}Q^2, \hat{\Pi}_{33}^{\text{phy}}\}$ in an interval around Q_{target}^2 . We create a B-spline representation [281] for every bootstrap sample using $\{\text{Exp } 8t_0^{\text{phy}}Q^2, \hat{\Pi}_{33,s}^{\text{phy}}\}$. Then, we evaluate the B-spline on $(8t_0^{\text{phy}}Q_{\text{target}}^2)_s$. The result of this procedure is a bootstrap distribution for $\hat{\Pi}_{33}^{\text{phy}}$ whose spread or uncertainty is the scale-setting error. One can carry out similarly for the other isospins changing the fit model. Using eq. (6.40), one obtains the bootstrap distribution for $(\Delta\alpha)_{\text{had}}$ and $(\Delta\sin^2\theta_W)_{\text{had}}$ and their corresponding error.

The scale-setting uncertainty is the second error shown in tables 13.1 and 13.2. Here, we can realise the impact of a precise determination of the scale. The scale-setting error is as important as the statistical uncertainty for $\hat{\Pi}_{33}$, $\hat{\Pi}_{88}$ and the target quantities $(\Delta\alpha)_{\text{had}}$ and $(\Delta\sin^2\theta_W)_{\text{had}}$. In fact, it is the dominant error for the smaller components $\hat{\Pi}_{cc}$ and

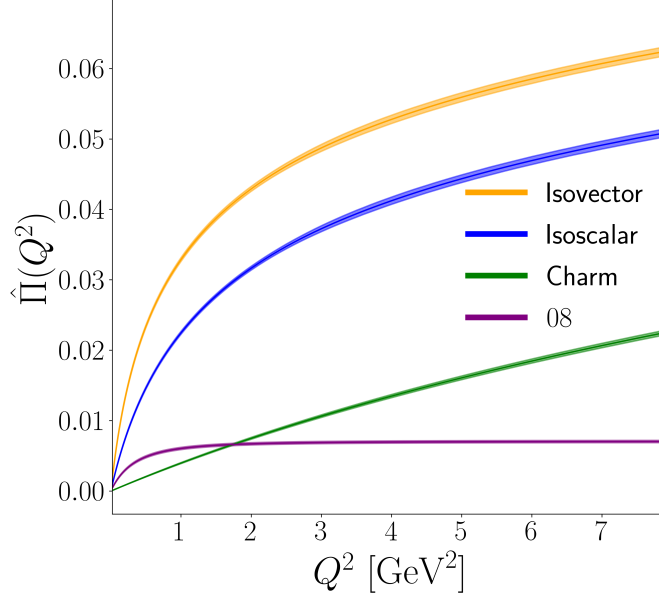


Figure 13.3: Components of $\hat{\Pi}$ as defined in eq. (6.38) after applying the step function Θ given in eq. (13.2) vs Q^2 . The error bands indicate the total uncertainty.

$\hat{\Pi}_{08}$. It is clear that any significant improvement of the precision requires an improved scale determination. In particular, $(8t_0^{\text{phy}})^{1/2} = 0.415(4)(2)$ fm [142] has a relative error of $\sim 1\%$, and this induces a relative error of $\sim 0.6\%$ in $(\Delta\alpha)_{\text{had}}$ and ~ 0.8 in $(\Delta\sin^2\theta_W)_{\text{had}}$ at $Q^2 = 1 \text{ GeV}^2$. Therefore, we find ourselves in a favourable position, where the uncertainty obtained for the scale has a slightly weakened influence in our target quantities.

13.3 Isospin-breaking effects

The CLS simulations employ exact isospin symmetry $\text{SU}(2)_V$ and neglect the effects of QED. The former implies $M_u = M_d = M_\ell$, which is a good approximation because the mass difference is much smaller than the QCD energy scale, $(M_d - M_u)/\Lambda_{\text{QCD}} \ll 1$. QED effects can also be neglected to a first approximation because its processes are scaled down by the QED coupling, whose typical size is $\alpha \sim 1/137$. However, at the current level of precision, one should start quantifying these IB effects because they might be sizeable.

To this end, the author of [57] employs the so-called RM123 approach [287, 288], which includes these effects via a perturbative expansion and Monte Carlo re-weighting [288, 289, 290, 291]. First, one considers the set of parameters $\epsilon = (M_u, M_d, M_s, \beta, e^2)$ [292, 293]. Choosing $\epsilon^{(0)} = (M_\ell^{(0)}, M_\ell^{(0)}, M_s^{(0)}, \beta^{(0)}, 0)$, we recover isospin-symmetric QCD, QCD_{iso} , with a free photon field. Second, one extends the action of the theory to [292, 293]

$$S[U, A, \psi, \bar{\psi}] = S_g[U] + S_\gamma[A] + S_q[U, A, \psi, \bar{\psi}], \quad (13.3)$$

where $S_\gamma[A]$ includes the dynamics of the photons, and $S_q[U, A, \psi, \bar{\psi}]$ the interactions

between quarks and gluons and photons. Then, one may expand in terms of $\Delta\epsilon = \epsilon - \epsilon^{(0)}$ around $\epsilon^{(0)}$. Now, it is possible to compute an expectation value in the full QCD+QED theory from QCD_{iso} configurations using re-weighting [293],

$$\begin{aligned}\langle O[U, A, \psi, \bar{\psi}] \rangle &= \frac{\langle R[U] \langle O[U, A, \psi, \bar{\psi}] \rangle_{q\gamma} \rangle_{\text{eff}}^{(0)}}{\langle R[U] \rangle_{\text{eff}}^{(0)}}, \\ R[U] &= \frac{\exp(-S_g[U]) Z_{q\gamma}[U]}{\exp(-S_g^{(0)}[U]) Z_q^{(0)}[U]},\end{aligned}\tag{13.4}$$

where $\langle \dots \rangle_{\text{eff}}^{(0)}$ is evaluated in the QCD_{iso} configurations and the subscript $q\gamma$ indicates the terms of eq. (13.3) included. The required Feynman rules are discussed in [293]. Operators that depend on QCD+QED gauge links are expanded in the form $O = O(e^0) + O(e) + O(e^2) + (e^3)$. The same boundary conditions apply for both, the photon and the QCD gauge fields [292].

To match QCD+QED with QCD_{iso}, reference [294] computes M_π^0 and $M_{K^+}^2 + M_{K^0}^2 - M_{\pi^+}^2$ in both theories and matches them. These two quantities serve as proxies for the average light and strange quark masses, respectively. The proxy for the light quark mass splitting, $M_{K^+}^2 - M_{K^0}^2 - M_{\pi^+}^2 + M_{\pi^0}^2$, is set to its physical value [294].

The author of [57] has computed the IB effects to $\mathcal{O}(e^2)$ for H102, N200 and D450 at every momentum Q^2 that we study. At the current level of precision, and with the current set of ensembles, it is not possible to distinguish any dependence with the lattice spacing or pion mass. Since the analysis of IB corrections is beyond the scope of this thesis, and an extrapolation to the physical point of the estimates presented in [57, 292, 293] is still not possible, we decide to include a preliminary estimate of IB in our error budget using D450's data because it shows the largest correction. We employ the ratio between the leading-order IB correction and the isospin-symmetric result for $\hat{\Pi}_{\gamma\gamma}$ to estimate the relative error due to missing IB corrections at the physical point.

Results for a subset of Q^2 appear in table 13.2. The fifth uncertainty of $(\Delta\alpha)_{\text{had}}$ and $(\Delta \sin^2 \theta_W)_{\text{had}}$ gives an estimate for the missing IB effects. One can see that the impact of this error in both quantities is similar and constant, around $\sim 0.3\%$ for the entire energy range. In principle, they are of the same magnitude as the scale-setting error, albeit systematically smaller. For $Q^2 < 2 \text{ GeV}^2$, they are also larger than the systematics for the extrapolation to the physical point. On the one hand, the very first estimate of isospin-breaking effects suggests that they are relatively small, and the use of QCD_{iso} is justified. On the other hand, it is still necessary to compute the IB corrections for all ensembles and make a prediction at the physical point to give a better estimate for this uncertainty, whose magnitude is no longer irrelevant. Any future determination of $(\Delta\alpha)_{\text{had}}$ and $(\Delta \sin^2 \theta_W)_{\text{had}}$ that reduces the statistical or systematic uncertainty with, for example, an improved scale setting, will need to address IB effects for all ensembles. Current progress by the Mainz group in this direction can be seen in [292, 293, 294] and the thesis [57].

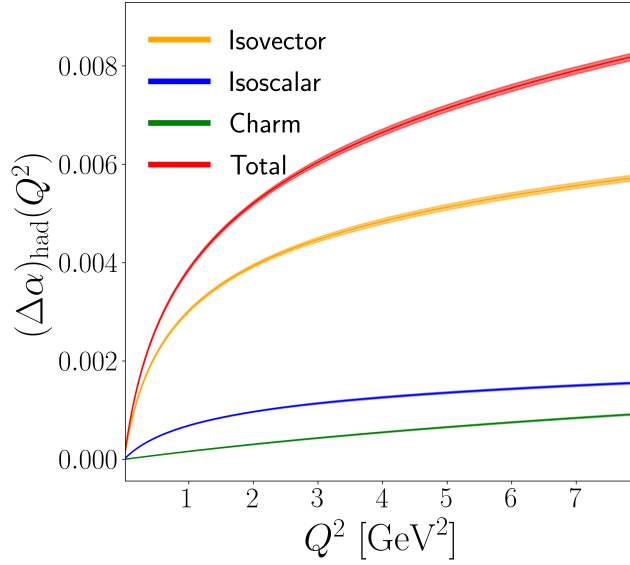


Figure 13.4: Running of the QED coupling.

13.4 $\hat{\Pi}$, $(\Delta\alpha)_{\text{had}}$ and $(\Delta \sin^2 \theta_W)_{\text{had}}$

Table 13.1 shows our estimate for the various components of $\hat{\Pi} \times 10^5$ at a representative set of momenta Q^2 . Together with the central value, we include a complete error budget. The first uncertainty represents statistics, the second stems from the scale-setting precision, and the third component is the systematic uncertainty of the extrapolation to the physical point. In square brackets, we add all these components in quadrature to obtain the total absolute error. The last number is the relative total error in percentage. We see that the two biggest contributions, $\hat{\Pi}_{33}$ and $\hat{\Pi}_{88}$, could be determined with $\sim 1\%$ accuracy; the charm component $\hat{\Pi}_{cc}$ shows a $\sim 2\%$ uncertainty; and $\hat{\Pi}_{08}$ reaches an error of $\sim 2.5\%$. One can also see that the relative uncertainty increases at lower momenta, although the absolute error is smaller. Figure 13.3 shows $\hat{\Pi}$ at the physical point given in eq. (12.1) for the various components $i = 33, 88, 08, cc$ as a function of Q^2 . The corresponding $(\Delta\alpha)_{\text{had}}$ and $(\Delta \sin^2 \theta_W)_{\text{had}}$ are plotted as a function of Q^2 in figs. 13.4 and 13.5, respectively. We also depict the different components including all pre-factors to underscore the dominance of the isovector contribution in the final result.

13.5 Comparison with previous results

In fig. 13.6, we compare our result for $(\Delta\alpha)_{\text{had}}$ with the lattice determination [173] by the Budapest-Marseille-Wuppertal (BMW) collaboration, and the phenomenological determinations by Davier-Hoecker-Malaescu-Zhang (DHMZ) [31], Jegerlehner [32] and Keshavarzi-Nomura-Teubner (KNT) [30]. For [173], we employ the results in their table S3 and add

Q^2 (GeV ²)	$\hat{\Pi}_{33} \times 10^5$	$\hat{\Pi}_{88} \times 10^5$
0.10	764 (10) (0) (3) (3) [11, 1.4]	403 (5) (3) (1) (0) [6, 1.5]
0.50	2340 (16) (13) (5) (5) [21, 0.9]	1465 (10) (14) (3) (1) [17, 1.2]
1.00	3289 (17) (22) (5) (5) [28, 0.9]	2248 (11) (19) (2) (1) [22, 1.0]
2.00	4292 (17) (29) (10) (5) [35, 0.8]	3165 (14) (24) (4) (1) [28, 0.9]
3.00	4874 (31) (32) (22) (5) [50, 1.0]	3726 (30) (26) (16) (1) [43, 1.1]
4.00	5279 (40) (34) (29) (5) [59, 1.1]	4123 (38) (27) (23) (1) [52, 1.3]
5.00	5594 (42) (35) (30) (5) [63, 1.1]	4436 (41) (28) (24) (1) [55, 1.2]
6.00	5853 (44) (36) (31) (5) [65, 1.1]	4694 (42) (29) (25) (1) [57, 1.2]
7.00	6072 (43) (36) (31) (5) [64, 1.1]	4914 (42) (29) (25) (1) [57, 1.2]

Q^2 (GeV ²)	$\hat{\Pi}_{cc} \times 10^5$	$\hat{\Pi}_{08} \times 10^5$
0.10	42 (0) (1) (0) [1, 2.2]	176 (5) (7) (0) [8, 4.7]
0.50	205 (1) (4) (0) [4, 2.1]	486 (7) (15) (1) [16, 3.4]
1.00	397 (2) (8) (1) [8, 2.0]	605 (7) (16) (1) [17, 2.9]
2.00	749 (3) (14) (1) [14, 1.9]	671 (8) (16) (2) [18, 2.6]
3.00	1064 (4) (19) (1) [20, 1.8]	689 (8) (15) (2) [17, 2.5]
4.00	1349 (5) (23) (2) [24, 1.8]	696 (8) (15) (2) [17, 2.5]
5.00	1608 (6) (26) (2) [27, 1.7]	700 (8) (15) (2) [17, 2.5]
6.00	1847 (6) (29) (2) [30, 1.6]	702 (8) (15) (2) [17, 2.5]
7.00	2067 (7) (32) (3) [32, 1.6]	703 (8) (15) (2) [17, 2.5]

Table 13.1: $\hat{\Pi} \times 10^5$ for the isovector, isoscalar, charm and 08 components at several Q^2 . The first uncertainty is statistical, the second is due to the scale-setting error, the third accounts for the systematic error of the extrapolation, and the fourth indicates the FSE systematic error. In square brackets, we indicate the absolute total error and the relative uncertainty in percentage.

Q^2 (GeV ²)	$(\Delta\alpha)_{\text{had}} \times 10^6$	$(\Delta \sin^2 \theta_W)_{\text{had}} \times 10^6$
0.10	841 (10) (1) (3) (3) (2) [11, 1.3]	−847 (11) (3) (3) (3) (3) [13, 1.5]
0.50	2678 (16) (15) (4) (5) (8) [24, 0.9]	−2710 (18) (22) (4) (5) (9) [31, 1.1]
1.00	3865 (17) (23) (4) (5) (12) [31, 0.8]	−3927 (19) (32) (5) (5) (13) [40, 1.0]
2.00	5208 (18) (28) (10) (5) (15) [39, 0.7]	−5299 (20) (40) (12) (6) (16) [49, 0.9]
3.00	6042 (36) (30) (25) (5) (17) [56, 0.9]	−6139 (40) (42) (28) (6) (19) [68, 1.1]
4.00	6651 (47) (30) (33) (5) (19) [67, 1.0]	−6743 (52) (43) (37) (6) (20) [80, 1.2]
5.00	7141 (51) (30) (34) (5) (20) [71, 1.0]	−7223 (55) (44) (39) (6) (22) [84, 1.2]
6.00	7554 (53) (29) (35) (5) (21) [73, 1.0]	−7624 (58) (44) (39) (6) (23) [86, 1.1]
7.00	7913 (51) (29) (35) (5) (22) [72, 0.9]	−7969 (56) (44) (40) (6) (24) [86, 1.1]

Table 13.2: $(\Delta\alpha)_{\text{had}} \times 10^6$ and $(\Delta \sin^2 \theta_W)_{\text{had}} \times 10^6$ for several virtualities. The first error is statistical, the second stems from the uncertainty of the scale setting, the third from the extrapolation to the physical point, the fourth from the FSE systematics and the fifth is an estimate of the IB effects missing in our main computation. In brackets, we show all uncertainties added in quadrature—giving the total error of the observables—, while the last number is the corresponding relative error in percentage.

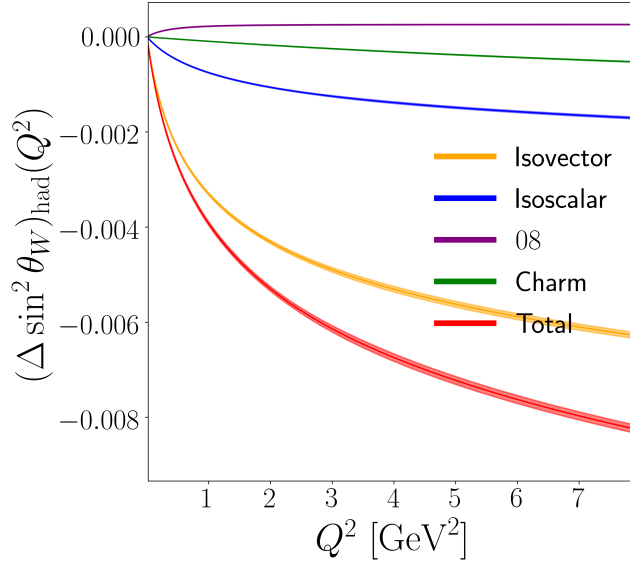


Figure 13.5: Running of the electroweak mixing angle.

the finite-size correction described in BMW’s work. The uncertainty of the latter is 100%, and we add it in quadrature to their error budget. Our results differ from BMW’s between one and two sigma, with less tension at higher momentum. Regarding the phenomenological determinations, the tension is much larger, especially at lower Q^2 . One can see the three phenomenological determinations agree well with each other and have smaller errors. However, both lattice determinations differ from phenomenology by several sigma. The situation that we find in fig. 13.6 is similar when one compares the Mainz determination of $(g-2)_\mu$ [218], which also uses the vector correlator, to the corresponding result by these groups —see for instance figure 44 in [38]. Regarding $(\Delta\sin^2\theta_W)_{\text{had}}$, there has been a previous lattice determination by [171] with $N_f = 2+1+1$ flavours of twisted mass fermions. However, their computation does not include the quark-disconnected contributions. With respect to [173], only the components to compute $(\Delta\alpha)_{\text{had}}$ are provided, so we miss their estimate of the 08 component.

13.6 Padé approximants

We have computed the running with Q^2 of $\hat{\Pi}_{\gamma\gamma}$ and $\hat{\Pi}_{Z\gamma}$ at 115 different points in the range $0.01 \text{ GeV}^2 \leq Q^2 \leq 10 \text{ GeV}^2$. Given the fit quality shown in fig. 13.1, which steadily deteriorates for larger Q^2 , we are confident to quote our estimates for $Q^2 \leq 7 \text{ GeV}^2$. The deterioration of the fit quality is likely caused by increasing lattice artefacts, which are no longer fully captured by the fit model given in section 12.1.1.

In order to present our results in a simple form, rather than a lengthy table, we use the fact that the sVPF can be expressed in terms of a positive spectral function through a

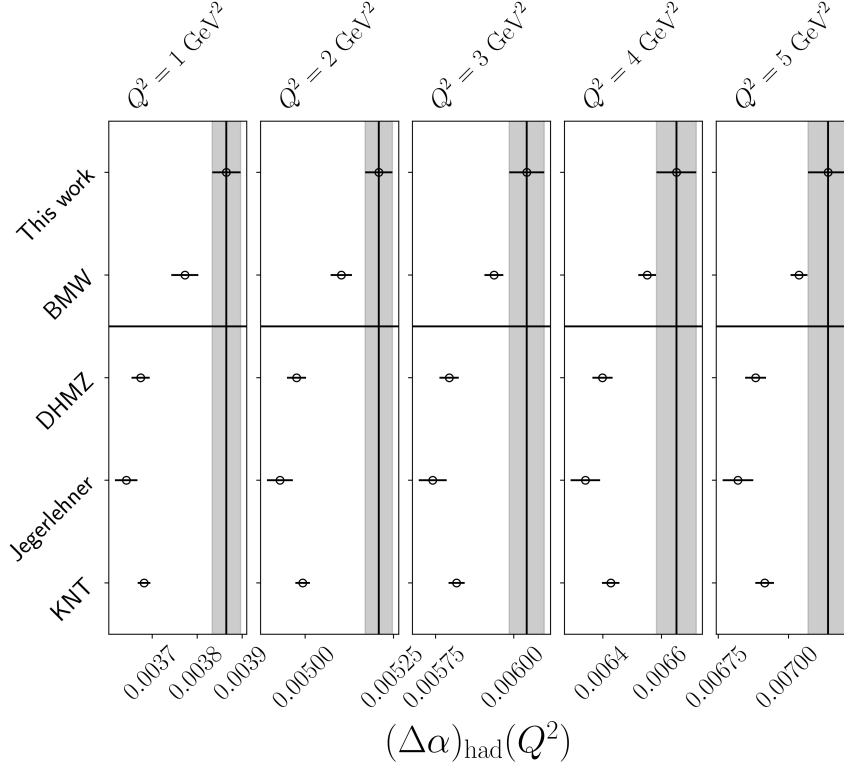


Figure 13.6: We compare the estimates of $(\Delta\alpha)_{\text{had}}$ obtained by BMW [173], DHMZ [31], Jegerlehner [32], KNT [30] and our work at several Q^2 . BMW is another lattice determination, while the others are phenomenological analysis.

dispersion relation [295, 296]. This, in turn, allows us to express $\hat{\Pi}$ in terms of convergent Padé approximants (PAs). First, we relate the sVPF with a Stieltjes function. Then, we quote the theorem that relates the Stieltjes function with a Padé approximant, and explain how to build the latter as a continued function. Finally, we present the explicit rational approximations that model the running with Q^2 of $\hat{\Pi}_{33}$, $\hat{\Pi}_{88}$, $\hat{\Pi}_{08}$, $\hat{\Pi}_{cc}$, $(\Delta\alpha)_{\text{had}}$ and $(\Delta\sin^2\theta_W)_{\text{had}}$. For this section, we have closely followed references [295, 296], which apply the general theory of PAs [297, 298] to compute the sVPF.

We start with the integral representation of a Stieltjes function $\Phi(z)$ [299, 296],

$$\Phi(z) = \int_0^{1/R} \frac{d\nu(\tau)}{1 + \tau z}, \quad (13.5)$$

where $\nu(z)$ is real, bounded, non-decreasing on the interval $[0, 1/R]$, and takes infinitely many values on that said interval. $\Phi(z)$ is analytic in the entire complex plane except on the cut $z \in (-\infty, -R]$, and decreases monotonically in the range $z \in (-R, \infty)$. If one takes

the particular choice [296]

$$\begin{aligned} \tau &= \frac{1}{s}, & d\nu(\tau) &= d\tau \rho(1/\tau), \\ R &= 4M_\pi^2, & \rho(1/\tau) &= \frac{1}{\pi} \text{Im}\Pi(1/\tau), \end{aligned} \quad (13.6)$$

one can express $\hat{\Pi}$ in terms of a Stieltjes function [296],

$$\hat{\Pi}(Q^2) = Q^2 \Phi(Q^2), \quad \Phi(Q^2) = \int_{4M_\pi^2}^{\infty} ds \frac{\rho(s)}{s(s+Q^2)}. \quad (13.7)$$

The spectral function $\rho(s)$ is non-negative in the integration range.

The next step is to approximate $\Phi(Q^2)$ using a PA. A rational or Padé approximant $R_M^N(Q^2)$ is the ratio of two polynomials of degrees N and M [297],

$$R_M^N(Q^2) = \frac{\sum_{n=0}^N a_n Q^{2n}}{1 + \sum_{m=1}^M b_m Q^{2m}}. \quad (13.8)$$

It is also common to name the Padé approximant as $[N, M]$ PA. To build PAs to describe $\Phi(Q^2)$, we employ the following theorem [297, 298]: Given P points $(Q_i^2, \Phi(Q_i^2))$, $i \in \{1, \dots, P\}$, a sequence of Padé approximants can be constructed converging to $\Phi(Q^2)$ in the limit $P \rightarrow \infty$ on any closed, bounded region of the complex plane, excluding the cut $Q^2 \in (-\infty, -4M_\pi^2]$. Then, the Stieltjes function $\Phi(Q^2)$ can be built as a continued fraction [297],

$$\Phi(Q^2) = \frac{\psi_1(Q_1^2)}{1 + \frac{(Q^2 - Q_1^2) \psi_2(Q_2^2)}{(Q^2 - Q_2^2) \psi_3(Q_3^2)} \dots 1 + (Q^2 - Q_{P-1}^2) \psi_P(Q_P^2)}. \quad (13.9)$$

The functions ψ_i can be constructed recursively using [300]

$$\psi_1 = \Phi(Q_1^2), \quad \psi_i(Q^2) = \frac{\psi_{i-1}(Q_{i-1}^2) - \psi_{i-1}(Q_i^2)}{(Q^2 - Q_{i-1}^2)\psi_{i-1}(Q^2)}, \quad i > 1. \quad (13.10)$$

Equation (13.9) can be brought to the more convenient form in eq. (13.8) via a simple *Mathematica* program [301]. By construction, our PA is exact at every point $(Q_i^2, \Phi(Q_i^2))$, and converges to $\Phi(Q^2)$. Regarding the degree of the polynomials in eq. (13.8), if the number of points Q_i^2 is even, $P = 2k$, we obtain a $[k-1, k]$ PA [297]. Since we need to find k a_n and k b_m coefficients, the system is completely determined; if the number of points is odd, $P = 2k+1$, we obtain a $[k, k]$ PA [297]. In this case, the numerator has $k+1$ parameters a_n , and the denominator k coefficients b_m . The number of parameters $a_n + b_m$ coincides with the number of points P used in the interpolation.

In practice, it is sufficient to give a handful of well chosen points to describe the entire range of results without increasing the uncertainty. The PAs for the various $\hat{\Pi}$ components in the range $0 \leq Q^2 \leq 7 \text{ GeV}^2$ are

$$\hat{\Pi}_{33}(Q^2) = Q^2 \frac{0.072694 + 0.065642 Q^2 + 0.000994 Q^4}{0.782073 + 2.45458 Q^2 + Q^4}, \quad (13.11)$$

$$\hat{\Pi}_{88}(Q^2) = Q^2 \frac{0.056471 + 0.054517 Q^2 + 0.000992 Q^4}{1.25582 + 2.72613 Q^2 + Q^4}, \quad (13.12)$$

$$\hat{\Pi}_{08}(Q^2) = Q^2 \frac{0.0101576 + 0.00699903 Q^2 + 0.00000377 Q^4}{0.468357 + 1.36725 Q^2 + Q^4}, \quad (13.13)$$

$$\hat{\Pi}_{cc}(Q^2) = Q^2 \frac{1.67802 + 0.0917093 Q^2}{395.517 + 48.7508 Q^2 + Q^4}. \quad (13.14)$$

Note the Q^2 prefactor is not part of the Padé approximant (see eq. (13.6)); therefore, it does not modify the power counting we explained earlier for the numerator and the denominator. The total uncertainty of $\hat{\Pi}$ can be reproduced in the same range using

$$\text{Err} [\hat{\Pi}_{33}] (Q^2) = Q^2 \frac{0.000272 + 0.000055 Q^2}{0.146502 + Q^2}, \quad (13.15)$$

$$\text{Err} [\hat{\Pi}_{88}] (Q^2) = Q^2 \frac{0.000235 + 0.000051 Q^2}{0.288976 + Q^2}, \quad (13.16)$$

$$\text{Err} [\hat{\Pi}_{08}] (Q^2) = Q^2 \frac{0.00012982 + 0.00016837 Q^2}{0.109516 + 0.580871 Q^2 + Q^4}, \quad (13.17)$$

$$\text{Err} [\hat{\Pi}_{cc}] (Q^2) = Q^2 \frac{0.00069196 - 0.00000338 Q^2}{7.46544 + Q^2}. \quad (13.18)$$

We have checked that the deviation between the original data and the interpolation is much smaller than the uncertainty for every Q^2 and, therefore, it does not change our error budget. It is remarkable that this is the case when we only use three, four or five points to describe the entire range of momenta $0 \leq Q^2 \leq 7 \text{ GeV}^2$. $(\Delta\alpha)_{\text{had}}$ and $(\Delta \sin^2 \theta_W)_{\text{had}}$ are given by the expressions

$$(\Delta\alpha)_{\text{had}}(Q^2) = 4\pi\alpha Q^2 \frac{0.111074 + 0.0941634 Q^2 + 0.00197788 Q^4}{1.0117 + 2.90494 Q^2 + Q^4}, \quad (13.19)$$

$$(\Delta \sin^2 \theta_W)_{\text{had}}(Q^2) = -\frac{4\pi\alpha}{\sin^2 \theta_W} Q^2 \frac{0.0230007 + 0.0225366 Q^2 + 0.000438037 Q^4}{0.871817 + 2.6288 Q^2 + Q^4}. \quad (13.20)$$

Equations (13.19) and (13.20) can be used to compute the QED coupling and the electroweak mixing angle in the space-like region through eqs. (4.8) and (5.9), respectively. The

uncertainty of $(\Delta\alpha)_{\text{had}}$ and $(\Delta\sin^2\theta_W)_{\text{had}}$ can be reproduced employing the interpolations

$$\text{Err}[(\Delta\alpha)_{\text{had}}](Q^2) = 4\pi\alpha Q^2 \frac{0.000333302 + 0.0000679074 Q^2}{0.171261 + Q^2}, \quad (13.21)$$

$$\text{Err}[(\Delta\sin^2\theta_W)_{\text{had}}](Q^2) = \frac{4\pi\alpha}{\sin^2\theta_W} Q^2 \frac{0.000111558 + 0.0000169117 Q^2}{0.224473 + Q^2}. \quad (13.22)$$

For the fine-structure constant, we use $\alpha = 0.0072973525693(11)$ [34], and for the weak-mixing angle in the $\overline{\text{MS}}$ scheme we use $\sin^2\theta_W = 0.23857(5)$ [34]. Alternatively, in the Heaviside-Lorentz system of units $e^2 = 4\pi\alpha$, so we could also use the corresponding value of the electric charge $e^2 = 0.091701236853(14)$ [34]. Regarding the low- and high-virtuality behaviour of the PAs, they vanish automatically at $Q^2 = 0$, but their high-virtuality is not well defined. This is not a problem, however, because eqs. (13.11) to (13.22) are only valid in the region $0 \leq Q^2 \leq 7 \text{ GeV}^2$. Also, it is important to note the different units of the coefficients. All quantities on the LHS of eqs. (13.11) to (13.22) are dimensionless. However, on the RHS, Q^2 must appear in GeV^2 , and the units of the various coefficients vary accordingly.

We have also explored a different method to describe the Stieltjes function. In [297, 298, 302], it was proven that $\Phi(Q^2)$ could also be written in the form

$$\hat{\Pi}(Q^2) = Q^2 \left(a_0 + \sum_{n=1}^{\lfloor P/2 \rfloor} \frac{a_n}{b_n + Q^2} \right), \quad (13.23)$$

where $\lfloor x \rfloor$ is the floor or integer part of x . Equation (13.23) gives a more convenient form to fit the data, as was done in [295, 296]. However, we found this method inferior to the interpolation of the data because we could not fit enough parameters to obtain a comparable level of precision. Another possibility to fit the data would be to use eq. (13.8) instead of eq. (13.23). Fitting the various observables would allow us to present the uncertainties in eqs. (13.15) to (13.18), (13.21) and (13.22) in the form of a covariance matrix; this would be useful if correlations between the various fit parameters were needed.

Chapter 14

Conclusions and Outlook

In the course of this thesis, we have studied the hadronic contribution to the running of the QED coupling and the electroweak mixing angle in the low-energy space-like region, employing the lattice regularisation to work with QCD in its confining phase.

As a result of our studies, we obtain both $(\Delta\alpha)_{\text{had}}$ and $(\Delta\sin^2\theta_W)_{\text{had}}$ as a function of the virtuality Q^2 in the range $0 \leq Q^2 \leq 7\text{GeV}^2$ with $\sim 1\%$ accuracy. The functional dependence of $\hat{\Pi}$, $(\Delta\alpha)_{\text{had}}$ and $(\Delta\sin^2\theta_W)_{\text{had}}$ is given in eqs. (13.11) to (13.22). These equations constitute our main result. Table 13.2 showcases results at a subset of Q^2 including a detailed error budget, and section 13.5 compares our results with other lattice and phenomenological determinations. We see that our central values tend to be larger, with better agreement with the other lattice determination by BMW [173], and that we are not yet at the level of precision of the phenomenological determinations by [31, 32, 30].

There are ways to reduce the uncertainty of our calculation and reach the sub-percent accuracy of the phenomenological determination.

Starting with the statistical error, it mainly stems from the signal-to-noise ratio problem, the extrapolation to the physical point and, unsurprisingly, finite statistics. First, to improve the signal, we need a dedicated and up-to-date analysis of the spectrum. Then, we could use the improved version of the bounding method, discussed in section 9.2. Although such analysis is already in progress, it requires huge resources on its own. Focusing efforts in the lightest-pion-mass ensembles would make the biggest impact. Second, including more ensembles in the immediate vicinity of the physical pion mass would allow us to neglect the curvature of the data at a local level and perform a linear interpolation in the meson masses, simplifying the fit model of the isovector and isoscalar contributions given in section 12.1. Moving to finer lattice spacings would delay the onset of the a^3 lattice artefacts discussed in section 12.1.4. Their corresponding fit parameter has a large impact on the accuracy of the extrapolation, as can be seen in table 13.2 when comparing the statistical error at low and high virtualities. Also, reducing the complexity of the fit model would reduce the systematic error of the extrapolation to the physical point, given separately as the third error in table 13.2. Third, increasing statistics on the more chiral and finer ensembles will have a greater impact on our final results, while the current statistics on the ensembles with heavier pion mass and coarser lattice spacing seem sufficient.

The scale-setting uncertainty is the largest contribution to the error budget alongside the statistical error, as shown in table 13.2. Therefore, we require an update of the scale-setting determination given in [142]. Aside of using the same or other techniques and observables, the current scale was determined using a smaller set of ensembles and statistics. It would make sense to have a CLS-wide computer script to estimate the scale automatically given a set of ensembles and statistics. This would allow to take correlations fully into account in any analysis, and always have an updated scale estimate.

Regarding the systematic error of the FSE, given in the fourth parenthesis of table 13.2, their contribution to the total error is negligible. The use of two different methods to estimate them, MLL and HP, explained in chapter 10, add a valuable cross-check. To keep this error small, it is necessary to have $M_\pi L > 4$ and close-to-physical pion masses.

Next, the IB effects, which are shown in the fifth parenthesis in table 13.2, have the same order of magnitude as the statistical and scale-setting errors. However, they are not determined at the physical point yet, and there is only a small subset of results available. Therefore, one needs to take their estimate with caution. Even though they appear sub-leading at our current $\sim 1\%$ accuracy, a future update will require to take them fully into account, or it risks to have an uncertainty dominated by these effects. Some first steps have already been taken in the Mainz group [57, 294, 292, 293, 303].

Finally, one main difference between our work and other determinations is the absence of a blinding procedure. The lattice community seems to be taking more interest in this topic recently [304], but no widely accepted procedure exists as of today.

Our results in eqs. (13.11) to (13.22) and table 13.2 can serve as a theoretical input to compute the five-flavour electromagnetic coupling at the Z -pole, $(\Delta\alpha)_{\text{had}}^{(5)}(M_Z^2)$, which enters the electroweak global fits [34]. To this end, first one needs to add the missing effects from the charm quark-disconnected diagrams and the charm sea-quark component, and the entire bottom-quark contribution. Nonetheless, the results from [173] suggest that the charm quark-disconnected component is negligible at our current level of precision, since it only contributes $\sim 1\%$ of the quark-disconnected component for $a_\mu^{\text{LO-HVP}}$. For an estimate of the bottom-quark component, one could follow [170]. Then, one can use the Euclidean split technique given in eq. (4.13) [169]

$$\begin{aligned}
(\Delta\alpha)_{\text{had}}^{(5)}(M_Z^2) &= (\Delta\alpha)_{\text{had}}^{(5)}(Q_0^2) \\
&+ \left[(\Delta\alpha)_{\text{had}}^{(5)}(-M_Z^2) - (\Delta\alpha)_{\text{had}}^{(5)}(Q_0^2) \right]^{\text{pQCD}} \\
&+ \left[(\Delta\alpha)_{\text{had}}^{(5)}(M_Z^2) - (\Delta\alpha)_{\text{had}}^{(5)}(-M_Z^2) \right]^{\text{pQCD}}, \quad (14.1)
\end{aligned}$$

where the first term corresponds with our lattice determination, and the other two terms can be evaluated with pQCD [48, 32] provided Q_0^2 is chosen high enough. This is an alternative approach, which does not depend on experimental results. In a similar fashion, one could use our results for the electroweak mixing angle together with the R-ratio determination to reduce the systematics due to flavour separation, or replace the data-driven approach with an *ab initio* determination to test for PBSM.

Acknowledgements

I want to thank everyone who contributed to this project. I start thanking my supervisor Hartmut Wittig, who accepted me as his PhD student, for his guidance and exciting discussions. Spending several years here in Germany and working on such a relevant topic was an incredible experience that I will never forget. Thank you for giving me the chance to study German, too; I enjoyed my time and learned a lot. I want to thank Harvey Meyer and Georg von Hippel for the valuable discussions about many topics. In particular, I want to thank Harvey for allowing me to be his assistant in the Numerical Methods course; I learned a lot myself. The contributions of Marco Cè, Antoine Gérardin and Kohtaroh Miura to this project have been invaluable. Thank you for all the informative discussions and joint effort. Besides, I want to thank Marco Cè, Antoine Gérardin, and Konstantin Ottnad for generating the data employed in this project and Andreas Risch. His work allowed us to give a better estimate of the isospin-breaking effects and compute the meson masses. Also, I want to thank Daniel Mohler and Dalibor Djukanovic for many valuable conversations and suggestions. Finally, I can not forget thanking Dalibor for his work managing the high-performance computing resources at the Helmholtz-Institut Mainz. This PhD would not have been the same without my fellow PhD students: En-Hung Chao, Andreas Risch, Tobias Schulz and Jonas Wilhelm. I am very grateful for all your help and the time we spent together. Besides the scientific group, I want to thank my German language teacher Eleni Kapnisti and all my fellow students of the German lessons for all the great experiences and time spent together. Finally, I would like to give my heartfelt thanks to my parents, who have educated me and supported me every step of the way. This thesis would not have been possible without you.

Bibliography

- [1] Chen-Ning Yang and Robert L. Mills. “Conservation of Isotopic Spin and Isotopic Gauge Invariance”. In: *Phys. Rev.* 96 (1954). Ed. by Jong-Ping Hsu and D. Fine, pp. 191–195. DOI: 10.1103/PhysRev.96.191.
- [2] H. Fritzsch, Murray Gell-Mann, and H. Leutwyler. “Advantages of the Color Octet Gluon Picture”. In: *Phys. Lett. B* 47 (1973), pp. 365–368. DOI: 10.1016/0370-2693(73)90625-4.
- [3] Sheldon L. Glashow. “Partial-symmetries of weak interactions”. In: *Nuclear Physics* 22.4 (1961), pp. 579–588. ISSN: 0029-5582. DOI: [https://doi.org/10.1016/0029-5582\(61\)90469-2](https://doi.org/10.1016/0029-5582(61)90469-2). URL: <https://www.sciencedirect.com/science/article/pii/0029558261904692>.
- [4] Abdus Salam and John Clive Ward. “Electromagnetic and weak interactions”. In: *Phys. Lett.* 13 (1964), pp. 168–171. DOI: 10.1016/0031-9163(64)90711-5.
- [5] Steven Weinberg. “A Model of Leptons”. In: *Phys. Rev. Lett.* 19 (1967), pp. 1264–1266. DOI: 10.1103/PhysRevLett.19.1264.
- [6] G. Arnison et al. “Experimental Observation of Isolated Large Transverse Energy Electrons with Associated Missing Energy at $\sqrt{s} = 540$ GeV”. In: *Phys. Lett. B* 122 (1983), pp. 103–116. DOI: 10.1016/0370-2693(83)91177-2.
- [7] M. Banner et al. “Observation of Single Isolated Electrons of High Transverse Momentum in Events with Missing Transverse Energy at the CERN anti-p p Collider”. In: *Phys. Lett. B* 122 (1983), pp. 476–485. DOI: 10.1016/0370-2693(83)91605-2.
- [8] G. Arnison et al. “Experimental Observation of Lepton Pairs of Invariant Mass Around 95-GeV/c**2 at the CERN SPS Collider”. In: *Phys. Lett. B* 126 (1983), pp. 398–410. DOI: 10.1016/0370-2693(83)90188-0.
- [9] P. Bagnaia et al. “Evidence for $Z^0 \rightarrow e^+e^-$ at the CERN $\bar{p}p$ Collider”. In: *Phys. Lett. B* 129 (1983), pp. 130–140. DOI: 10.1016/0370-2693(83)90744-X.
- [10] G. S. Guralnik, C. R. Hagen, and T. W. B. Kibble. “Global Conservation Laws and Massless Particles”. In: *Phys. Rev. Lett.* 13 (1964). Ed. by J. C. Taylor, pp. 585–587. DOI: 10.1103/PhysRevLett.13.585.
- [11] Peter W. Higgs. “Broken Symmetries and the Masses of Gauge Bosons”. In: *Phys. Rev. Lett.* 13 (1964). Ed. by J. C. Taylor, pp. 508–509. DOI: 10.1103/PhysRevLett.13.508.
- [12] F. Englert and R. Brout. “Broken Symmetry and the Mass of Gauge Vector Mesons”. In: *Phys. Rev. Lett.* 13 (1964). Ed. by J. C. Taylor, pp. 321–323. DOI: 10.1103/PhysRevLett.13.321.

- [13] Georges Aad et al. “Observation of a new particle in the search for the Standard Model Higgs boson with the ATLAS detector at the LHC”. In: *Phys. Lett. B* 716 (2012), pp. 1–29. DOI: 10.1016/j.physletb.2012.08.020. arXiv: 1207.7214 [hep-ex].
- [14] Serguei Chatrchyan et al. “Combined results of searches for the standard model Higgs boson in pp collisions at $\sqrt{s} = 7$ TeV”. In: *Phys. Lett. B* 710 (2012), pp. 26–48. DOI: 10.1016/j.physletb.2012.02.064. arXiv: 1202.1488 [hep-ex].
- [15] S. L. Glashow, J. Iliopoulos, and L. Maiani. “Weak Interactions with Lepton-Hadron Symmetry”. In: *Phys. Rev. D* 2 (7 Oct. 1970), pp. 1285–1292. DOI: 10.1103/PhysRevD.2.1285. URL: <https://link.aps.org/doi/10.1103/PhysRevD.2.1285>.
- [16] J. -E. Augustin et al. “Discovery of a Narrow Resonance in e^+e^- Annihilation”. In: *Phys. Rev. Lett.* 33 (23 Dec. 1974), pp. 1406–1408. DOI: 10.1103/PhysRevLett.33.1406. URL: <https://link.aps.org/doi/10.1103/PhysRevLett.33.1406>.
- [17] J. J. Aubert et al. “Experimental Observation of a Heavy Particle J ”. In: *Phys. Rev. Lett.* 33 (23 Dec. 1974), pp. 1404–1406. DOI: 10.1103/PhysRevLett.33.1404. URL: <https://link.aps.org/doi/10.1103/PhysRevLett.33.1404>.
- [18] Makoto Kobayashi and Toshihide Maskawa. “CP-Violation in the Renormalizable Theory of Weak Interaction”. In: *Progress of Theoretical Physics* 49.2 (Feb. 1973), pp. 652–657. ISSN: 0033-068X. DOI: 10.1143/PTP.49.652. eprint: <https://academic.oup.com/ptp/article-pdf/49/2/652/5257692/49-2-652.pdf>. URL: <https://doi.org/10.1143/PTP.49.652>.
- [19] S. W. Herb et al. “Observation of a Dimuon Resonance at 9.5 GeV in 400-GeV Proton-Nucleus Collisions”. In: *Phys. Rev. Lett.* 39 (5 Aug. 1977), pp. 252–255. DOI: 10.1103/PhysRevLett.39.252. URL: <https://link.aps.org/doi/10.1103/PhysRevLett.39.252>.
- [20] F. Abe et al. “Observation of Top Quark Production in $\bar{p}p$ Collisions with the Collider Detector at Fermilab”. In: *Phys. Rev. Lett.* 74 (14 Apr. 1995), pp. 2626–2631. DOI: 10.1103/PhysRevLett.74.2626. URL: <https://link.aps.org/doi/10.1103/PhysRevLett.74.2626>.
- [21] S. Abachi et al. “Observation of the Top Quark”. In: *Phys. Rev. Lett.* 74 (14 Apr. 1995), pp. 2632–2637. DOI: 10.1103/PhysRevLett.74.2632. URL: <https://link.aps.org/doi/10.1103/PhysRevLett.74.2632>.
- [22] Planck Collaboration et al. “Planck 2013 results. XVI. Cosmological parameters”. In: *A&A* 571 (2014), A16. DOI: 10.1051/0004-6361/201321591. URL: <https://doi.org/10.1051/0004-6361/201321591>.
- [23] S. Deser and P. van Nieuwenhuizen. “Nonrenormalizability of the Quantized Einstein-Maxwell System”. In: *Phys. Rev. Lett.* 32 (1974), pp. 245–247. DOI: 10.1103/PhysRevLett.32.245.
- [24] Gerard ’t Hooft and M. J. G. Veltman. “One loop divergencies in the theory of gravitation”. In: *Ann. Inst. H. Poincaré Phys. Theor. A* 20 (1974), pp. 69–94.

-
- [25] Y. Fukuda et al. “Evidence for oscillation of atmospheric neutrinos”. In: *Phys. Rev. Lett.* 81 (1998), pp. 1562–1567. DOI: 10.1103/PhysRevLett.81.1562. arXiv: hep-ex/9807003.
 - [26] Q. R. Ahmad et al. “Direct evidence for neutrino flavor transformation from neutral current interactions in the Sudbury Neutrino Observatory”. In: *Phys. Rev. Lett.* 89 (2002), p. 011301. DOI: 10.1103/PhysRevLett.89.011301. arXiv: nucl-ex/0204008.
 - [27] Michael E. Peskin and Daniel V. Schroeder. *An Introduction to quantum field theory*. Reading, USA: Addison-Wesley, 1995. ISBN: 978-0-201-50397-5.
 - [28] A. Zee. *Quantum field theory in a nutshell*. 2003. ISBN: 978-0-691-14034-6.
 - [29] Christian B. Lang Chritstof Gattringer. *Quantum Chromodynamics on the Lattice: An Introductory Presentation*. 2010.
 - [30] Alexander Keshavarzi, Daisuke Nomura, and Thomas Teubner. “ $g - 2$ of charged leptons, $\alpha(M_Z^2)$, and the hyperfine splitting of muonium”. In: *Phys. Rev. D* 101.1 (2020), p. 014029. DOI: 10.1103/PhysRevD.101.014029. arXiv: 1911.00367 [hep-ph].
 - [31] M. Davier et al. “A new evaluation of the hadronic vacuum polarisation contributions to the muon anomalous magnetic moment and to $\alpha(m_Z^2)$ ”. In: *Eur. Phys. J. C* 80.3 (2020). [Erratum: *Eur.Phys.J.C* 80, 410 (2020)], p. 241. DOI: 10.1140/epjc/s10052-020-7792-2. arXiv: 1908.00921 [hep-ph].
 - [32] F. Jegerlehner. “ $\alpha_{QED,eff}(s)$ for precision physics at the FCC-ee/ILC”. In: *CERN Yellow Reports: Monographs* 3 (2020). Ed. by A. Blondel et al., pp. 9–37. DOI: 10.23731/CYRM-2020-003.9.
 - [33] S. Bodenstein et al. “Hadronic contribution to the QED running coupling $\alpha(M_Z^2)$ ”. In: *Phys. Rev. D* 86 (2012), p. 093013. DOI: 10.1103/PhysRevD.86.093013. arXiv: 1209.4802 [hep-ph].
 - [34] P.A. Zyla et al. “Review of Particle Physics”. In: *PTEP* 2020.8 (2020), p. 083C01. DOI: 10.1093/ptep/ptaa104.
 - [35] Sergio Fanchiotti, Bernd A. Kniehl, and Alberto Sirlin. “Incorporation of QCD effects in basic corrections of the electroweak theory”. In: *Phys. Rev. D* 48 (1993), pp. 307–331. DOI: 10.1103/PhysRevD.48.307. arXiv: hep-ph/9212285.
 - [36] C. M. Carloni Calame et al. “A new approach to evaluate the leading hadronic corrections to the muon $g-2$ ”. In: *Phys. Lett. B* 746 (2015), pp. 325–329. DOI: 10.1016/j.physletb.2015.05.020. arXiv: 1504.02228 [hep-ph].
 - [37] Friedrich Jegerlehner. *The Anomalous Magnetic Moment of the Muon*. Vol. 274. Cham: Springer, 2017. DOI: 10.1007/978-3-319-63577-4.
 - [38] T. Aoyama et al. “The anomalous magnetic moment of the muon in the Standard Model”. In: *Phys. Rept.* 887 (2020), pp. 1–166. DOI: 10.1016/j.physrep.2020.07.006. arXiv: 2006.04822 [hep-ph].

- [39] B. Abi et al. “Measurement of the Positive Muon Anomalous Magnetic Moment to 0.46 ppm”. In: *Phys. Rev. Lett.* 126 (14 Apr. 2021), p. 141801. DOI: 10.1103/PhysRevLett.126.141801. URL: <https://link.aps.org/doi/10.1103/PhysRevLett.126.141801>.
- [40] G. W. Bennett et al. “Final Report of the Muon E821 Anomalous Magnetic Moment Measurement at BNL”. In: *Phys. Rev. D* 73 (2006), p. 072003. DOI: 10.1103/PhysRevD.73.072003. arXiv: hep-ex/0602035.
- [41] Morad Aaboud et al. “Measurement of the Higgs boson mass in the $H \rightarrow ZZ^* \rightarrow 4\ell$ and $H \rightarrow \gamma\gamma$ channels with $\sqrt{s} = 13$ TeV pp collisions using the ATLAS detector”. In: *Phys. Lett. B* 784 (2018), pp. 345–366. DOI: 10.1016/j.physletb.2018.07.050. arXiv: 1806.00242 [hep-ex].
- [42] Albert M Sirunyan et al. “A measurement of the Higgs boson mass in the diphoton decay channel”. In: *Phys. Lett. B* 805 (2020), p. 135425. DOI: 10.1016/j.physletb.2020.135425. arXiv: 2002.06398 [hep-ex].
- [43] M. Passera, W. J. Marciano, and A. Sirlin. “The Muon $g-2$ and the bounds on the Higgs boson mass”. In: *Phys. Rev. D* 78 (2008), p. 013009. DOI: 10.1103/PhysRevD.78.013009. arXiv: 0804.1142 [hep-ph].
- [44] D. Androić et al. “Precision measurement of the weak charge of the proton”. In: *Nature* 557.7704 (May 2018), pp. 207–211. DOI: 10.1038/s41586-018-0096-0. arXiv: 1905.08283 [nucl-ex].
- [45] J. Benesch et al. “The MOLLER Experiment: An Ultra-Precise Measurement of the Weak Mixing Angle Using Moller Scattering”. In: (Nov. 2014). arXiv: 1411.4088 [nucl-ex].
- [46] Y. X. Zhao. “Parity Violation in Deep Inelastic Scattering with the SoLID Spectrometer at JLab”. In: *22nd International Symposium on Spin Physics*. Jan. 2017. arXiv: 1701.02780 [nucl-ex].
- [47] Dominik Becker et al. “The P2 experiment”. In: *Eur. Phys. J. A* 54.11 (2018), p. 208. DOI: 10.1140/epja/i2018-12611-6. arXiv: 1802.04759 [nucl-ex].
- [48] F. Jegerlehner. “Hadronic Contributions to Electroweak Parameter Shifts: A Detailed Analysis”. In: *Z. Phys. C* 32 (1986), p. 195. DOI: 10.1007/BF01552495.
- [49] Fred Jegerlehner. “Electroweak effective couplings for future precision experiments”. In: *Nuovo Cim. C* 034S1 (2011), pp. 31–40. DOI: 10.1393/ncc/i2011-11011-0. arXiv: 1107.4683 [hep-ph].
- [50] Fred Jegerlehner. “Variations on Photon Vacuum Polarization”. In: *EPJ Web Conf.* 218 (2019). Ed. by A. Denig and C. -F. Redmer, p. 01003. DOI: 10.1051/epjconf/201921801003. arXiv: 1711.06089 [hep-ph].
- [51] Teseo San José et al. “The hadronic contribution to the running of the electromagnetic coupling and electroweak mixing angle”. In: *38th International Symposium on Lattice Field Theory*. Sept. 2021. arXiv: 2109.04537 [hep-lat].

-
- [52] Marco Cè et al. “The hadronic contribution to the running of the electromagnetic coupling and the electroweak mixing angle”. In: *PoS LATTICE2019* (2019), p. 010. DOI: 10.22323/1.363.0010. arXiv: 1910.09525 [hep-lat].
- [53] Hartmut Wittig et al. “Lattice calculation of the hadronic leading order contribution to the muon $g - 2$ ”. In: *EPJ Web Conf.* 234 (2020). Ed. by G. D’Ambrosio et al., p. 01016. DOI: 10.1051/epjconf/202023401016. arXiv: 1912.01950 [hep-lat].
- [54] M. Srednicki. *Quantum field theory*. Cambridge University Press, Jan. 2007. ISBN: 978-0-521-86449-7, 978-0-511-26720-8.
- [55] Vera Magdalena Gülpers. “Hadronic correlation functions with quark-disconnected contributions in lattice QCD”. eng. PhD thesis. Mainz, 2015. DOI: <http://doi.org/10.25358/openscience-1255>.
- [56] Jonas Wilhelm. “The strangeness form factors of the nucleon from lattice QCD”. eng. PhD thesis. Mainz, 2019. URL: <https://hds.hebis.de/ubmz/Record/HEB464591503>.
- [57] Andreas Risch. “Isospin breaking effects in hadronic matrix elements on the lattice”. eng. PhD thesis. Mainz, 2021. DOI: <http://doi.org/10.25358/openscience-6314>.
- [58] Gerard ’t Hooft. “Naturalness, chiral symmetry, and spontaneous chiral symmetry breaking”. In: *NATO Sci. Ser. B* 59 (1980). Ed. by Gerard ’t Hooft et al., pp. 135–157. DOI: 10.1007/978-1-4684-7571-5_9.
- [59] C. N. Yang and R. L. Mills. “Conservation of Isotopic Spin and Isotopic Gauge Invariance”. In: *Phys. Rev.* 96 (1 Oct. 1954), pp. 191–195. DOI: 10.1103/PhysRev.96.191. URL: <https://link.aps.org/doi/10.1103/PhysRev.96.191>.
- [60] C. A. Baker et al. “An Improved experimental limit on the electric dipole moment of the neutron”. In: *Phys. Rev. Lett.* 97 (2006), p. 131801. DOI: 10.1103/PhysRevLett.97.131801. arXiv: hep-ex/0602020.
- [61] R. D. Peccei and Helen R. Quinn. “CP Conservation in the Presence of Pseudoparticles”. In: *Phys. Rev. Lett.* 38 (25 June 1977), pp. 1440–1443. DOI: 10.1103/PhysRevLett.38.1440. URL: <https://link.aps.org/doi/10.1103/PhysRevLett.38.1440>.
- [62] R. D. Peccei and Helen R. Quinn. “Constraints imposed by CP conservation in the presence of pseudoparticles”. In: *Phys. Rev. D* 16 (6 Sept. 1977), pp. 1791–1797. DOI: 10.1103/PhysRevD.16.1791. URL: <https://link.aps.org/doi/10.1103/PhysRevD.16.1791>.
- [63] Steven Weinberg. “A New Light Boson?” In: *Phys. Rev. Lett.* 40 (4 Jan. 1978), pp. 223–226. DOI: 10.1103/PhysRevLett.40.223. URL: <https://link.aps.org/doi/10.1103/PhysRevLett.40.223>.
- [64] F. Wilczek. “Problem of Strong P and T Invariance in the Presence of Instantons”. In: *Phys. Rev. Lett.* 40 (5 Jan. 1978), pp. 279–282. DOI: 10.1103/PhysRevLett.40.279. URL: <https://link.aps.org/doi/10.1103/PhysRevLett.40.279>.

- [65] Laurie M Brown. *Feynman's Thesis — A New Approach to Quantum Theory*. WORLD SCIENTIFIC, 2005. DOI: 10.1142/5852. eprint: <https://www.worldscientific.com/doi/pdf/10.1142/5852>. URL: <https://www.worldscientific.com/doi/abs/10.1142/5852>.
- [66] Alexandre Deur, Stanley J. Brodsky, and Guy F. de Teramond. “The QCD Running Coupling”. In: *Nucl. Phys.* 90 (2016), p. 1. DOI: 10.1016/j.ppnp.2016.04.003. arXiv: 1604.08082 [hep-ph].
- [67] David J. Gross and Frank Wilczek. “Ultraviolet Behavior of Non-Abelian Gauge Theories”. In: *Phys. Rev. Lett.* 30 (26 June 1973), pp. 1343–1346. DOI: 10.1103/PhysRevLett.30.1343. URL: <https://link.aps.org/doi/10.1103/PhysRevLett.30.1343>.
- [68] H. David Politzer. “Reliable Perturbative Results for Strong Interactions?” In: *Phys. Rev. Lett.* 30 (26 June 1973), pp. 1346–1349. DOI: 10.1103/PhysRevLett.30.1346. URL: <https://link.aps.org/doi/10.1103/PhysRevLett.30.1346>.
- [69] William Celmaster and Richard J. Gonsalves. “Renormalization-prescription dependence of the quantum-chromodynamic coupling constant”. In: *Phys. Rev. D* 20 (6 Sept. 1979), pp. 1420–1434. DOI: 10.1103/PhysRevD.20.1420. URL: <https://link.aps.org/doi/10.1103/PhysRevD.20.1420>.
- [70] J.S. Bell and R. Jackiw. “A PCAC puzzle: $\pi^0 \rightarrow \gamma\gamma$ in the σ -model”. In: *Il Nuovo Cimento A* 60 (1969). DOI: 10.1007/BF02823296. URL: <https://doi.org/10.1007/BF02823296>.
- [71] Stephen L. Adler. “Axial vector vertex in spinor electrodynamics”. In: *Phys. Rev.* 177 (1969), pp. 2426–2438. DOI: 10.1103/PhysRev.177.2426.
- [72] Heinz J Rothe. *Lattice gauge theories: an introduction*. World Scientific Publishing Company, 2012.
- [73] Thomas DeGrand and Carleton DeTar. *Lattice Methods for Quantum Chromodynamics*. WORLD SCIENTIFIC, 2006. DOI: 10.1142/6065. eprint: <https://www.worldscientific.com/doi/pdf/10.1142/6065>. URL: <https://www.worldscientific.com/doi/abs/10.1142/6065>.
- [74] Rajan Gupta. “Introduction to lattice QCD: Course”. In: *Les Houches Summer School in Theoretical Physics, Session 68: Probing the Standard Model of Particle Interactions*. July 1997, pp. 83–219. arXiv: hep-lat/9807028.
- [75] Kenneth G. Wilson. “Confinement of Quarks”. In: *Phys. Rev. D* 10 (1974). Ed. by J. C. Taylor, pp. 2445–2459. DOI: 10.1103/PhysRevD.10.2445.
- [76] Kenneth G. Wilson. “Quarks and Strings on a Lattice”. In: *13th International School of Subnuclear Physics: New Phenomena in Subnuclear Physics*. Nov. 1975.
- [77] Holger Bech Nielsen and M. Ninomiya. “No Go Theorem for Regularizing Chiral Fermions”. In: *Phys. Lett. B* 105 (1981), pp. 219–223. DOI: 10.1016/0370-2693(81)91026-1.

-
- [78] Holger Bech Nielsen and M. Ninomiya. “Absence of Neutrinos on a Lattice. 1. Proof by Homotopy Theory”. In: *Nucl. Phys. B* 185 (1981). Ed. by J. Julve and M. Ramón-Medrano. [Erratum: Nucl.Phys.B 195, 541 (1982)], p. 20. DOI: 10.1016/0550-3213(82)90011-6.
- [79] Holger Bech Nielsen and M. Ninomiya. “Absence of Neutrinos on a Lattice. 2. Intuitive Topological Proof”. In: *Nucl. Phys. B* 193 (1981), pp. 173–194. DOI: 10.1016/0550-3213(81)90524-1.
- [80] K. Symanzik. “Continuum limit and improved action in lattice theories: (I). Principles and φ^4 theory”. In: *Nuclear Physics B* 226.1 (1983), pp. 187–204. ISSN: 0550-3213. DOI: [https://doi.org/10.1016/0550-3213\(83\)90468-6](https://doi.org/10.1016/0550-3213(83)90468-6). URL: <https://www.sciencedirect.com/science/article/pii/0550321383904686>.
- [81] K. Symanzik. “Continuum limit and improved action in lattice theories: (II). $O(N)$ non-linear sigma model in perturbation theory”. In: *Nuclear Physics B* 226.1 (1983), pp. 205–227. ISSN: 0550-3213. DOI: [https://doi.org/10.1016/0550-3213\(83\)90469-8](https://doi.org/10.1016/0550-3213(83)90469-8). URL: <https://www.sciencedirect.com/science/article/pii/0550321383904698>.
- [82] M. Luscher and P. Weisz. “On-Shell Improved Lattice Gauge Theories”. In: *Commun. Math. Phys.* 97 (1985). [Erratum: Commun.Math.Phys. 98, 433 (1985)], p. 59. DOI: 10.1007/BF01206178.
- [83] M. Lüscher and P. Weisz. “Erratum: “On-shell improved lattice gauge theories””. In: *Communications in Mathematical Physics* 98.3 (1985), pp. 433–433. DOI: [cmp/1103942448](https://doi.org/10.1007/BF01206178). URL: [https://doi.org/](https://doi.org/10.1007/BF01206178).
- [84] B. Sheikholeslami and R. Wohlert. “Improved Continuum Limit Lattice Action for QCD with Wilson Fermions”. In: *Nucl. Phys. B* 259 (1985), p. 572. DOI: 10.1016/0550-3213(85)90002-1.
- [85] John Bulava and Stefan Schaefer. “Improvement of $N_f = 3$ lattice QCD with Wilson fermions and tree-level improved gauge action”. In: *Nucl. Phys. B* 874 (2013), pp. 188–197. DOI: 10.1016/j.nuclphysb.2013.05.019. arXiv: 1304.7093 [hep-lat].
- [86] Paul H. Ginsparg and Kenneth G. Wilson. “A Remnant of Chiral Symmetry on the Lattice”. In: *Phys. Rev. D* 25 (1982), p. 2649. DOI: 10.1103/PhysRevD.25.2649.
- [87] P. Hasenfratz. “Prospects for perfect actions”. In: *Nucl. Phys. B Proc. Suppl.* 63 (1998). Ed. by C. T. H. Davies et al., pp. 53–58. DOI: 10.1016/S0920-5632(97)00696-8. arXiv: hep-lat/9709110.
- [88] Herbert Neuberger. “More about exactly massless quarks on the lattice”. In: *Phys. Lett. B* 427 (1998), pp. 353–355. DOI: 10.1016/S0370-2693(98)00355-4. arXiv: hep-lat/9801031.
- [89] Martin Luscher. “Exact chiral symmetry on the lattice and the Ginsparg-Wilson relation”. In: *Phys. Lett. B* 428 (1998), pp. 342–345. DOI: 10.1016/S0370-2693(98)00423-7. arXiv: hep-lat/9802011.
- [90] Herbert Neuberger. “Exactly massless quarks on the lattice”. In: *Phys. Lett. B* 417 (1998), pp. 141–144. DOI: 10.1016/S0370-2693(97)01368-3. arXiv: hep-lat/9707022.

- [91] Ivan Horvath. “Ginsparg-Wilson relation and ultralocality”. In: *Phys. Rev. Lett.* 81 (1998), pp. 4063–4066. DOI: 10.1103/PhysRevLett.81.4063. arXiv: hep-lat/9808002.
- [92] Pilar Hernandez, Karl Jansen, and Martin Luscher. “Locality properties of Neuberger’s lattice Dirac operator”. In: *Nucl. Phys. B* 552 (1999), pp. 363–378. DOI: 10.1016/S0550-3213(99)00213-8. arXiv: hep-lat/9808010.
- [93] Roberto Frezzotti et al. “A Local formulation of lattice QCD without unphysical fermion zero modes”. In: *Nucl. Phys. B Proc. Suppl.* 83 (2000). Ed. by M. Campostrini et al., pp. 941–946. DOI: 10.1016/S0920-5632(00)91852-8. arXiv: hep-lat/9909003.
- [94] Roberto Frezzotti et al. “Lattice QCD with a chirally twisted mass term”. In: *JHEP* 08 (2001), p. 058. DOI: 10.1088/1126-6708/2001/08/058. arXiv: hep-lat/0101001.
- [95] Roberto Frezzotti, Stefan Sint, and Peter Weisz. “O(a) improved twisted mass lattice QCD”. In: *JHEP* 07 (2001), p. 048. DOI: 10.1088/1126-6708/2001/07/048. arXiv: hep-lat/0104014.
- [96] R. Frezzotti and G. C. Rossi. “Twisted mass lattice QCD with mass nondegenerate quarks”. In: *Nucl. Phys. B Proc. Suppl.* 128 (2004). Ed. by A. C. Kalloniatis, D. B. Leinweber, and A. G. Williams, pp. 193–202. DOI: 10.1016/S0920-5632(03)02477-0. arXiv: hep-lat/0311008.
- [97] C Pena, S Sint, and A Vladikas. “Twisted mass QCD and lattice approaches to the $I = 1/2$ rule”. In: *Journal of High Energy Physics* 2004.09 (Oct. 2004), pp. 069–069. DOI: 10.1088/1126-6708/2004/09/069. URL: <https://doi.org/10.1088/1126-6708/2004/09/069>.
- [98] R. Frezzotti and G. C. Rossi. “Chirally improving Wilson fermions. 1. O(a) improvement”. In: *JHEP* 08 (2004), p. 007. DOI: 10.1088/1126-6708/2004/08/007. arXiv: hep-lat/0306014.
- [99] Florian Burger et al. “Four-Flavour Leading-Order Hadronic Contribution To The Muon Anomalous Magnetic Moment”. In: *JHEP* 02 (2014), p. 099. DOI: 10.1007/JHEP02(2014)099. arXiv: 1308.4327 [hep-lat].
- [100] D. Giusti, F. Sanfilippo, and S. Simula. “Light-quark contribution to the leading hadronic vacuum polarization term of the muon $g - 2$ from twisted-mass fermions”. In: *Phys. Rev. D* 98.11 (2018), p. 114504. DOI: 10.1103/PhysRevD.98.114504. arXiv: 1808.00887 [hep-lat].
- [101] D. Giusti and S. Simula. “Lepton anomalous magnetic moments in Lattice QCD+QED”. In: *PoS LATTICE2019* (2019), p. 104. DOI: 10.22323/1.363.0104. arXiv: 1910.03874 [hep-lat].
- [102] David B. Kaplan. “A Method for simulating chiral fermions on the lattice”. In: *Phys. Lett. B* 288 (1992), pp. 342–347. DOI: 10.1016/0370-2693(92)91112-M. arXiv: hep-lat/9206013.
- [103] Yigal Shamir. “Constraints on the existence of chiral fermions in interacting lattice theories”. In: *Phys. Rev. Lett.* 71 (1993), pp. 2691–2694. DOI: 10.1103/PhysRevLett.71.2691. arXiv: hep-lat/9306023.

-
- [104] Yigal Shamir. “Chiral fermions from lattice boundaries”. In: *Nucl. Phys. B* 406 (1993), pp. 90–106. DOI: 10.1016/0550-3213(93)90162-I. arXiv: hep-lat/9303005.
- [105] Vadim Furman and Yigal Shamir. “Axial symmetries in lattice QCD with Kaplan fermions”. In: *Nucl. Phys. B* 439 (1995), pp. 54–78. DOI: 10.1016/0550-3213(95)00031-M. arXiv: hep-lat/9405004.
- [106] C. Allton et al. “Physical Results from 2+1 Flavor Domain Wall QCD and SU(2) Chiral Perturbation Theory”. In: *Phys. Rev. D* 78 (2008), p. 114509. DOI: 10.1103/PhysRevD.78.114509. arXiv: 0804.0473 [hep-lat].
- [107] T. Blum et al. “Calculation of the hadronic vacuum polarization contribution to the muon anomalous magnetic moment”. In: *Phys. Rev. Lett.* 121.2 (2018), p. 022003. DOI: 10.1103/PhysRevLett.121.022003. arXiv: 1801.07224 [hep-lat].
- [108] John Kogut and Leonard Susskind. “Hamiltonian formulation of Wilson’s lattice gauge theories”. In: *Phys. Rev. D* 11 (2 Jan. 1975), pp. 395–408. DOI: 10.1103/PhysRevD.11.395. URL: <https://link.aps.org/doi/10.1103/PhysRevD.11.395>.
- [109] F. Gliozzi. “Spinor algebra of the one component lattice fermions”. In: *Nucl. Phys. B* 204 (1982), pp. 419–428. DOI: 10.1016/0550-3213(82)90199-7.
- [110] H. Kluberg-Stern et al. “Flavors of Lagrangian Susskind Fermions”. In: *Nucl. Phys. B* 220 (1983), pp. 447–470. DOI: 10.1016/0550-3213(83)90501-1.
- [111] Stephan Durr. “Theoretical issues with staggered fermion simulations”. In: *PoS LAT2005* (2006). Ed. by Christopher Michael, p. 021. DOI: 10.22323/1.020.0021. arXiv: hep-lat/0509026.
- [112] Stephen R. Sharpe. “Discretization errors in the spectrum of the Hermitian Wilson-Dirac operator”. In: *Phys. Rev. D* 74 (2006), p. 014512. DOI: 10.1103/PhysRevD.74.014512. arXiv: hep-lat/0606002.
- [113] Michael Creutz. “Chiral anomalies and rooted staggered fermions”. In: *Phys. Lett. B* 649 (2007), pp. 230–234. DOI: 10.1016/j.physletb.2007.03.065. arXiv: hep-lat/0701018.
- [114] Andreas S. Kronfeld. “Lattice Gauge Theory with Staggered Fermions: How, Where, and Why (Not)”. In: *PoS LATTICE2007* (2007). Ed. by Gunnar Bali et al., p. 016. DOI: 10.22323/1.042.0016. arXiv: 0711.0699 [hep-lat].
- [115] Silas R. Beane, Kostas Orginos, and Martin J. Savage. “Strong-isospin violation in the neutron-proton mass difference from fully-dynamical lattice QCD and PQQCD”. In: *Nucl. Phys. B* 768 (2007), pp. 38–50. DOI: 10.1016/j.nuclphysb.2006.12.023. arXiv: hep-lat/0605014.
- [116] A. Bazavov et al. “Nonperturbative QCD Simulations with 2+1 Flavors of Improved Staggered Quarks”. In: *Rev. Mod. Phys.* 82 (2010), pp. 1349–1417. DOI: 10.1103/RevModPhys.82.1349. arXiv: 0903.3598 [hep-lat].
- [117] Bipasha Chakraborty et al. “The hadronic vacuum polarization contribution to a_μ from full lattice QCD”. In: *Phys. Rev. D* 96.3 (2017), p. 034516. DOI: 10.1103/PhysRevD.96.034516. arXiv: 1601.03071 [hep-lat].

- [118] C. T. H. Davies et al. “Hadronic-vacuum-polarization contribution to the muon’s anomalous magnetic moment from four-flavor lattice QCD”. In: *Phys. Rev. D* 101.3 (2020), p. 034512. DOI: 10.1103/PhysRevD.101.034512. arXiv: 1902.04223 [hep-lat].
- [119] Kenneth G. Wilson. “Confinement of quarks”. In: *Phys. Rev. D* 10 (8 Oct. 1974), pp. 2445–2459. DOI: 10.1103/PhysRevD.10.2445. URL: <https://link.aps.org/doi/10.1103/PhysRevD.10.2445>.
- [120] G. P. Lepage. “Lattice QCD for novices”. In: *13th Annual HUGS AT CEBAF (HUGS 98)*. May 1998, pp. 49–90. arXiv: hep-lat/0506036.
- [121] G. Curci, P. Menotti, and G. Paffuti. “Symanzik’s Improved Lagrangian for Lattice Gauge Theory”. In: *Phys. Lett. B* 130 (1983). [Erratum: *Phys.Lett.B* 135, 516 (1984)], p. 205. DOI: 10.1016/0370-2693(83)91043-2.
- [122] Daniel Mohler, Stefan Schaefer, and Jakob Simeth. “CLS 2+1 flavor simulations at physical light- and strange-quark masses”. In: *EPJ Web Conf.* 175 (2018). Ed. by M. Della Morte et al., p. 02010. DOI: 10.1051/epjconf/201817502010. arXiv: 1712.04884 [hep-lat].
- [123] Simon Duane et al. “Hybrid Monte Carlo”. In: *Physics Letters B* 195.2 (1987), pp. 216–222. ISSN: 0370-2693. DOI: [https://doi.org/10.1016/0370-2693\(87\)91197-X](https://doi.org/10.1016/0370-2693(87)91197-X). URL: <https://www.sciencedirect.com/science/article/pii/037026938791197X>.
- [124] D.H. Weingarten and D.N. Petcher. “Monte Carlo integration for lattice gauge theories with fermions”. In: *Physics Letters B* 99.4 (1981), pp. 333–338. ISSN: 0370-2693. DOI: [https://doi.org/10.1016/0370-2693\(81\)90112-X](https://doi.org/10.1016/0370-2693(81)90112-X). URL: <https://www.sciencedirect.com/science/article/pii/037026938190112X>.
- [125] I.P. Omelyan, I.M. Mryglod, and R. Folk. “Symplectic analytically integrable decomposition algorithms: classification, derivation, and application to molecular dynamics, quantum and celestial mechanics simulations”. In: *Computer Physics Communications* 151.3 (2003), pp. 272–314. ISSN: 0010-4655. DOI: [https://doi.org/10.1016/S0010-4655\(02\)00754-3](https://doi.org/10.1016/S0010-4655(02)00754-3). URL: <https://www.sciencedirect.com/science/article/pii/S0010465502007543>.
- [126] Martin Luscher and Stefan Schaefer. “Lattice QCD with open boundary conditions and twisted-mass reweighting”. In: *Comput. Phys. Commun.* 184 (2013), pp. 519–528. DOI: 10.1016/j.cpc.2012.10.003. arXiv: 1206.2809 [hep-lat].
- [127] Martin Luscher and Filippo Palombi. “Fluctuations and reweighting of the quark determinant on large lattices”. In: *PoS LATTICE2008* (2008). Ed. by Christopher Aubin et al., p. 049. DOI: 10.22323/1.066.0049. arXiv: 0810.0946 [hep-lat].
- [128] Thomas A. DeGrand. “A conditioning technique for matrix inversion for Wilson fermions”. In: *Computer Physics Communications* 52.1 (1988), pp. 161–164. ISSN: 0010-4655. DOI: [https://doi.org/10.1016/0010-4655\(88\)90180-4](https://doi.org/10.1016/0010-4655(88)90180-4). URL: <https://www.sciencedirect.com/science/article/pii/0010465588901804>.

-
- [129] Martin Hasenbusch. “Speeding up the hybrid Monte Carlo algorithm for dynamical fermions”. In: *Phys. Lett. B* 519 (2001), pp. 177–182. DOI: 10.1016/S0370-2693(01)01102-9. arXiv: hep-lat/0107019.
- [130] Daniel Mohler and Stefan Schaefer. “Remarks on strange-quark simulations with Wilson fermions”. In: *Phys. Rev. D* 102.7 (2020), p. 074506. DOI: 10.1103/PhysRevD.102.074506. arXiv: 2003.13359 [hep-lat].
- [131] M. Hasenbusch and K. Jansen. “Speeding up lattice QCD simulations with clover improved Wilson fermions”. In: *Nucl. Phys. B* 659 (2003), pp. 299–320. DOI: 10.1016/S0550-3213(03)00227-X. arXiv: hep-lat/0211042.
- [132] Mattia Bruno et al. “Simulation of QCD with $N_f = 2 + 1$ flavors of non-perturbatively improved Wilson fermions”. In: *JHEP* 02 (2015), p. 043. DOI: 10.1007/JHEP02(2015)043. arXiv: 1411.3982 [hep-lat].
- [133] A. D. Kennedy, Ivan Horvath, and Stefan Sint. “A New exact method for dynamical fermion computations with nonlocal actions”. In: *Nucl. Phys. B Proc. Suppl.* 73 (1999). Ed. by Thomas A. DeGrand et al., pp. 834–836. DOI: 10.1016/S0920-5632(99)85217-7. arXiv: hep-lat/9809092.
- [134] M. A. Clark and A. D. Kennedy. “Accelerating dynamical fermion computations using the rational hybrid Monte Carlo (RHMC) algorithm with multiple pseudofermion fields”. In: *Phys. Rev. Lett.* 98 (2007), p. 051601. DOI: 10.1103/PhysRevLett.98.051601. arXiv: hep-lat/0608015.
- [135] Martin Luscher. “Computational Strategies in Lattice QCD”. In: *Les Houches Summer School: Session 93: Modern perspectives in lattice QCD: Quantum field theory and high performance computing*. Feb. 2010, pp. 331–399. arXiv: 1002.4232 [hep-lat].
- [136] N.I. Achiezer. *Theory of approximation*. 1992.
- [137] Luigi Del Debbio, Haralambos Panagopoulos, and Ettore Vicari. “theta dependence of SU(N) gauge theories”. In: *JHEP* 08 (2002), p. 044. DOI: 10.1088/1126-6708/2002/08/044. arXiv: hep-th/0204125.
- [138] Claude Bernard et al. “Topological susceptibility with the improved Asqtad action”. In: *Phys. Rev. D* 68 (2003), p. 114501. DOI: 10.1103/PhysRevD.68.114501. arXiv: hep-lat/0308019.
- [139] Stefan Schaefer, Rainer Sommer, and Francesco Virotta. “Critical slowing down and error analysis in lattice QCD simulations”. In: *Nucl. Phys. B* 845 (2011), pp. 93–119. DOI: 10.1016/j.nuclphysb.2010.11.020. arXiv: 1009.5228 [hep-lat].
- [140] Martin Luscher. “Topology, the Wilson flow and the HMC algorithm”. In: *PoS LATTICE2010* (2010). Ed. by Giancarlo Rossi, p. 015. DOI: 10.22323/1.105.0015. arXiv: 1009.5877 [hep-lat].
- [141] Martin Lüscher. “Properties and uses of the Wilson flow in lattice QCD”. In: *JHEP* 08 (2010). [Erratum: JHEP 03, 092 (2014)], p. 071. DOI: 10.1007/JHEP08(2010)071. arXiv: 1006.4518 [hep-lat].

- [142] Mattia Bruno, Tomasz Korzec, and Stefan Schaefer. “Setting the scale for the CLS $2 + 1$ flavor ensembles”. In: *Phys. Rev. D* 95.7 (2017), p. 074504. DOI: 10.1103/PhysRevD.95.074504. arXiv: 1608.08900 [hep-lat].
- [143] Maxwell T. Hansen and Agostino Patella. “Finite-volume and thermal effects in the leading-HVP contribution to muonic $(g - 2)$ ”. In: *JHEP* 2010.10 (Oct. 2020), p. 029. DOI: 10.1007/jhep10(2020)029. arXiv: 2004.03935 [hep-lat].
- [144] Martin Luscher and Peter Weisz. “Perturbative analysis of the gradient flow in non-abelian gauge theories”. In: *JHEP* 02 (2011), p. 051. DOI: 10.1007/JHEP02(2011)051. arXiv: 1101.0963 [hep-th].
- [145] R. Narayanan and H. Neuberger. “Infinite N phase transitions in continuum Wilson loop operators”. In: *JHEP* 03 (2006), p. 064. DOI: 10.1088/1126-6708/2006/03/064. arXiv: hep-th/0601210.
- [146] Doug Toussaint and C. T. H. Davies. “The Omega- and the strange quark mass”. In: *Nucl. Phys. B Proc. Suppl.* 140 (2005). Ed. by Geoffrey T. Bodwin et al., pp. 234–236. DOI: 10.1016/j.nuclphysbps.2004.11.129. arXiv: hep-lat/0409129.
- [147] C. T. H. Davies et al. “High precision lattice QCD confronts experiment”. In: *Phys. Rev. Lett.* 92 (2004), p. 022001. DOI: 10.1103/PhysRevLett.92.022001. arXiv: hep-lat/0304004.
- [148] R. Sommer. “A New way to set the energy scale in lattice gauge theories and its applications to the static force and alpha-s in SU(2) Yang-Mills theory”. In: *Nucl. Phys. B* 411 (1994), pp. 839–854. DOI: 10.1016/0550-3213(94)90473-1. arXiv: hep-lat/9310022.
- [149] Mattia Bruno and Rainer Sommer. “On the N_f -dependence of gluonic observables”. In: *PoS LATTICE2013* (2014), p. 321. DOI: 10.22323/1.187.0321. arXiv: 1311.5585 [hep-lat].
- [150] Szabolcs Borsanyi et al. “High-precision scale setting in lattice QCD”. In: *JHEP* 09 (2012), p. 010. DOI: 10.1007/JHEP09(2012)010. arXiv: 1203.4469 [hep-lat].
- [151] V. G. Bornyakov et al. “Wilson flow and scale setting from lattice QCD”. In: (Aug. 2015). arXiv: 1508.05916 [hep-lat].
- [152] T. Blum et al. “Domain wall QCD with physical quark masses”. In: *Phys. Rev. D* 93.7 (2016), p. 074505. DOI: 10.1103/PhysRevD.93.074505. arXiv: 1411.7017 [hep-lat].
- [153] A. Bazavov et al. “Gradient flow and scale setting on MILC HISQ ensembles”. In: *Phys. Rev. D* 93.9 (2016), p. 094510. DOI: 10.1103/PhysRevD.93.094510. arXiv: 1503.02769 [hep-lat].
- [154] R. J. Dowdall et al. “Vus from pi and K decay constants in full lattice QCD with physical u, d, s and c quarks”. In: *Phys. Rev. D* 88 (2013), p. 074504. DOI: 10.1103/PhysRevD.88.074504. arXiv: 1303.1670 [hep-lat].
- [155] Martin Luscher et al. “Chiral symmetry and O(a) improvement in lattice QCD”. In: *Nucl. Phys. B* 478 (1996), pp. 365–400. DOI: 10.1016/0550-3213(96)00378-1. arXiv: hep-lat/9605038.

-
- [156] Murray Gell-Mann, R. J. Oakes, and B. Renner. “Behavior of Current Divergences under $SU_3 \times SU_3$ ”. In: *Phys. Rev.* 175 (5 Nov. 1968), pp. 2195–2199. DOI: 10.1103/PhysRev.175.2195. URL: <https://link.aps.org/doi/10.1103/PhysRev.175.2195>.
 - [157] Oliver Bar and Maarten Golterman. “Chiral perturbation theory for gradient flow observables”. In: *Phys. Rev. D* 89.3 (2014). [Erratum: *Phys.Rev.D* 89, 099905 (2014)], p. 034505. DOI: 10.1103/PhysRevD.89.034505. arXiv: 1312.4999 [hep-lat].
 - [158] T. Blum et al. *Discussion: criteria for inclusion in WP update at the last g-2 theory initiative workshop, Wed 30/06 at 15:05 CEST*. 2021. URL: <https://agenda.hepl.phys.nagoya-u.ac.jp/indico/conferenceDisplay.py?ovw=True&confId=1691>.
 - [159] J. Gasser and H. Leutwyler. “Chiral perturbation theory: Expansions in the mass of the strange quark”. In: *Nuclear Physics B* 250.1 (1985), pp. 465–516. ISSN: 0550-3213. DOI: [https://doi.org/10.1016/0550-3213\(85\)90492-4](https://doi.org/10.1016/0550-3213(85)90492-4). URL: <https://www.sciencedirect.com/science/article/pii/0550321385904924>.
 - [160] Tatsumi Aoyama, Toichiro Kinoshita, and Makiko Nio. “Theory of the Anomalous Magnetic Moment of the Electron”. In: *Atoms* 7.1 (2019). ISSN: 2218-2004. DOI: 10.3390/atoms7010028. URL: <https://www.mdpi.com/2218-2004/7/1/28>.
 - [161] Peter J. Mohr, David B. Newell, and Barry N. Taylor. “CODATA Recommended Values of the Fundamental Physical Constants: 2014”. In: *Rev. Mod. Phys.* 88.3 (2016), p. 035009. DOI: 10.1103/RevModPhys.88.035009. arXiv: 1507.07956 [physics.atom-ph].
 - [162] Léo Morel et al. “Determination of the fine-structure constant with an accuracy of 81 parts per trillion”. In: *Nature* 588.7836 (Dec. 2020), pp. 61–65. DOI: 10.1038/s41586-020-2964-7.
 - [163] Jonathan Bagger, Konstantin T. Matchev, and Damien Pierce. “Precision corrections to supersymmetric unification”. In: *Phys. Lett. B* 348 (1995), pp. 443–450. DOI: 10.1016/0370-2693(95)00207-2. arXiv: hep-ph/9501277.
 - [164] Paul Langacker and Nir Polonsky. “The Strong coupling, unification, and recent data”. In: *Phys. Rev. D* 52 (1995), pp. 3081–3086. DOI: 10.1103/PhysRevD.52.3081. arXiv: hep-ph/9503214.
 - [165] Stephen L. Adler. “Some simple vacuum-polarization phenomenology: $e^+e^- \rightarrow$ hadrons; the muonic-atom x-ray discrepancy and $g_\mu - 2$ ”. In: *Phys. Rev. D* 10 (11 Dec. 1974), pp. 3714–3728. DOI: 10.1103/PhysRevD.10.3714. URL: <https://link.aps.org/doi/10.1103/PhysRevD.10.3714>.
 - [166] S. Eidelman et al. “Testing nonperturbative strong interaction effects via the Adler function”. In: *Phys. Lett. B* 454 (1999), pp. 369–380. DOI: 10.1016/S0370-2693(99)00389-5. arXiv: hep-ph/9812521.
 - [167] F. Jegerlehner. “Hadronic effects in $(g - 2)(\mu)$ and $\alpha(\text{QED})(M(Z))$: Status and perspectives”. In: *4th International Symposium on Radiative Corrections: Applications of Quantum Field Theory to Phenomenology*. Jan. 1999, pp. 75–89. arXiv: hep-ph/9901386.

- [168] F. Jegerlehner. “Hadronic vacuum polarization effects in $\alpha(\text{em})(M(Z))$ ”. In: *Mini-Workshop on Electroweak Precision Data and the Higgs Mass*. Aug. 2003, pp. 97–112. arXiv: hep-ph/0308117.
- [169] F. Jegerlehner. “The Running fine structure constant $\alpha(E)$ via the Adler function”. In: *Nucl. Phys. B Proc. Suppl.* 181-182 (2008). Ed. by Cesare Bini and Graziano Venanzoni, pp. 135–140. DOI: 10.1016/j.nuclphysbps.2008.09.010. arXiv: 0807.4206 [hep-ph].
- [170] B. Colquhoun et al. “ Υ and Υ' Leptonic Widths, a_μ^b and m_b from full lattice QCD”. In: *Phys. Rev. D* 91.7 (2015), p. 074514. DOI: 10.1103/PhysRevD.91.074514. arXiv: 1408.5768 [hep-lat].
- [171] Florian Burger et al. “Leading hadronic contributions to the running of the electroweak coupling constants from lattice QCD”. In: *JHEP* 11 (2015), p. 215. DOI: 10.1007/JHEP11(2015)215. arXiv: 1505.03283 [hep-lat].
- [172] Anthony Francis et al. “Study of the hadronic contributions to the running of the QED coupling and the weak mixing angle”. In: *PoS LATTICE2015* (2015), p. 110. arXiv: 1511.04751 [hep-lat].
- [173] Sz. Borsanyi et al. “Hadronic vacuum polarization contribution to the anomalous magnetic moments of leptons from first principles”. In: *Phys. Rev. Lett.* 121.2 (2018), p. 022002. DOI: 10.1103/PhysRevLett.121.022002. arXiv: 1711.04980 [hep-lat].
- [174] B.E. Lautrup, A. Peterman, and E. de Rafael. “Recent developments in the comparison between theory and experiments in quantum electrodynamics”. In: *Physics Reports* 3.4 (1972), pp. 193–259. ISSN: 0370-1573. DOI: [https://doi.org/10.1016/0370-1573\(72\)90011-7](https://doi.org/10.1016/0370-1573(72)90011-7). URL: <https://www.sciencedirect.com/science/article/pii/0370157372900117>.
- [175] Sz. Borsanyi et al. “Leading hadronic contribution to the muon magnetic moment from lattice QCD”. In: *Nature* 593.7857 (2021), pp. 51–55. DOI: 10.1038/s41586-021-03418-1. arXiv: 2002.12347 [hep-lat].
- [176] Steven Weinberg. “A Model of Leptons”. In: *Phys. Rev. Lett.* 19 (21 Nov. 1967), pp. 1264–1266. DOI: 10.1103/PhysRevLett.19.1264. URL: <https://link.aps.org/doi/10.1103/PhysRevLett.19.1264>.
- [177] Peter W. Higgs. “Broken symmetries, massless particles and gauge fields”. In: *Phys. Lett.* 12 (1964), pp. 132–133. DOI: 10.1016/0031-9163(64)91136-9.
- [178] Peter W. Higgs. “Broken Symmetries and the Masses of Gauge Bosons”. In: *Phys. Rev. Lett.* 13 (16 Oct. 1964), pp. 508–509. DOI: 10.1103/PhysRevLett.13.508. URL: <https://link.aps.org/doi/10.1103/PhysRevLett.13.508>.
- [179] Peter W. Higgs. “Spontaneous Symmetry Breakdown without Massless Bosons”. In: *Phys. Rev.* 145 (1966), pp. 1156–1163. DOI: 10.1103/PhysRev.145.1156.
- [180] K. S. Kumar et al. “Low Energy Measurements of the Weak Mixing Angle”. In: *Ann. Rev. Nucl. Part. Sci.* 63 (2013), pp. 237–267. DOI: 10.1146/annurev-nucl-102212-170556. arXiv: 1302.6263 [hep-ex].

-
- [181] Gerard 't Hooft. “Renormalizable Lagrangians for Massive Yang-Mills Fields”. In: *Nucl. Phys. B* 35 (1971). Ed. by J. C. Taylor, pp. 167–188. DOI: 10.1016/0550-3213(71)90139-8.
 - [182] A. Sirlin. “Radiative Corrections in the SU(2)-L x U(1) Theory: A Simple Renormalization Framework”. In: *Phys. Rev. D* 22 (1980), pp. 971–981. DOI: 10.1103/PhysRevD.22.971.
 - [183] W. J. Marciano and A. Sirlin. “Radiative Corrections to Neutrino Induced Neutral Current Phenomena in the SU(2)-L x U(1) Theory”. In: *Phys. Rev. D* 22 (1980). [Erratum: *Phys.Rev.D* 31, 213 (1985)], p. 2695. DOI: 10.1103/PhysRevD.22.2695.
 - [184] Giuseppe Degrossi and Alberto Sirlin. “Comparative analysis of electroweak corrections to $e^+ e^- \rightarrow f \text{ anti-}f$ in on-shell and (MS) frameworks”. In: *Nucl. Phys. B* 352 (1991), pp. 342–366. DOI: 10.1016/0550-3213(91)90446-5.
 - [185] Paolo Gambino and Alberto Sirlin. “Relation between $\sin^2 \Theta_w(m(z))$ and $\sin^2 \Theta_{\text{effective}}(\text{leptonic})$ ”. In: *Phys. Rev. D* 49 (1994), pp. 1160–1162. DOI: 10.1103/PhysRevD.49.R1160. arXiv: hep-ph/9309326.
 - [186] W. J. Marciano and A. Sirlin. “Precise SU(5) Predictions for $\sin^2 \Theta(W)$, $m(W)$ and $m(Z)$ ”. In: *Phys. Rev. Lett.* 46 (1981), p. 163. DOI: 10.1103/PhysRevLett.46.163.
 - [187] W. J. Marciano and A. Sirlin. “SU(5) THEORY versus EXPERIMENT”. In: *Conf. Proc. C* 810424 (1981). Ed. by J. P. Leveille, L. R. Sulak, and D. G. Unger, p. 151.
 - [188] Andrzej Czarnecki and William J. Marciano. “Electroweak radiative corrections to polarized Moller scattering asymmetries”. In: *Phys. Rev. D* 53 (1996), pp. 1066–1072. DOI: 10.1103/PhysRevD.53.1066. arXiv: hep-ph/9507420.
 - [189] Andrzej Czarnecki and William J. Marciano. “Polarized Moller scattering asymmetries”. In: *Int. J. Mod. Phys. A* 15 (2000). Ed. by C. A. Heusch, pp. 2365–2376. DOI: 10.1016/S0217-751X(00)00243-0. arXiv: hep-ph/0003049.
 - [190] Fred Jegerlehner. “The Standard model as a low-energy effective theory: what is triggering the Higgs mechanism?” In: *Acta Phys. Polon. B* 45.6 (2014), p. 1167. DOI: 10.5506/APhysPolB.45.1167. arXiv: 1304.7813 [hep-ph].
 - [191] R. R. Akhmetshin et al. “Reanalysis of hadronic cross-section measurements at CMD-2”. In: *Phys. Lett. B* 578 (2004), pp. 285–289. DOI: 10.1016/j.physletb.2003.10.108. arXiv: hep-ex/0308008.
 - [192] Jens Erler and Michael J. Ramsey-Musolf. “Low energy tests of the weak interaction”. In: *Prog. Part. Nucl. Phys.* 54 (2005), pp. 351–442. DOI: 10.1016/j.ppnp.2004.08.001. arXiv: hep-ph/0404291.
 - [193] C. Y. Prescott et al. “Parity Nonconservation in Inelastic Electron Scattering”. In: *Phys. Lett. B* 77 (1978), pp. 347–352. DOI: 10.1016/0370-2693(78)90722-0.
 - [194] Jens Erler et al. “Weak Polarized Electron Scattering”. In: *Ann. Rev. Nucl. Part. Sci.* 64 (2014), pp. 269–298. DOI: 10.1146/annurev-nucl-102313-025520. arXiv: 1401.6199 [hep-ph].

- [195] D. Wang et al. “Measurement of Parity-Violating Asymmetry in Electron-Deuteron Inelastic Scattering”. In: *Phys. Rev. C* 91.4 (2015), p. 045506. DOI: 10.1103/PhysRevC.91.045506. arXiv: 1411.3200 [nucl-ex].
- [196] D. Wang et al. “Measurement of parity violation in electron-quark scattering”. In: *Nature* 506.7486 (2014), pp. 67–70. DOI: 10.1038/nature12964.
- [197] C. S. Wu et al. “Experimental Test of Parity Conservation in β Decay”. In: *Phys. Rev.* 105 (1957), pp. 1413–1414. DOI: 10.1103/PhysRev.105.1413.
- [198] M. A. Bouchiat and C. C. Bouchiat. “Weak Neutral Currents in Atomic Physics”. In: *Phys. Lett. B* 48 (1974), pp. 111–114. DOI: 10.1016/0370-2693(74)90656-X.
- [199] M. S. Safronova et al. “Search for New Physics with Atoms and Molecules”. In: *Rev. Mod. Phys.* 90.2 (2018), p. 025008. DOI: 10.1103/RevModPhys.90.025008. arXiv: 1710.01833 [physics.atom-ph].
- [200] C. S. Wood et al. “Measurement of parity nonconservation and an anapole moment in cesium”. In: *Science* 275 (1997), pp. 1759–1763. DOI: 10.1126/science.275.5307.1759.
- [201] J. Guena, M. Lintz, and M. A. Bouchiat. “Measurement of the parity violating 6S-7S transition amplitude in cesium achieved within 2×10^{-13} atomic-unit accuracy by stimulated-emission detection”. In: *Phys. Rev. A* 71 (2005), p. 042108. DOI: 10.1103/PhysRevA.71.042108. arXiv: physics/0412017.
- [202] N. H. Edwards et al. “Precise Measurement of Parity Nonconserving Optical Rotation in Atomic Thallium”. In: *Phys. Rev. Lett.* 74 (1995), pp. 2654–2657. DOI: 10.1103/PhysRevLett.74.2654.
- [203] P. A. Vetter et al. “Precise test of electroweak theory from a new measurement of parity nonconservation in atomic thallium”. In: *Phys. Rev. Lett.* 74 (1995), pp. 2658–2661. DOI: 10.1103/PhysRevLett.74.2658.
- [204] D. M. Meekhof et al. “High-precision measurement of parity nonconserving optical rotation in atomic lead”. In: *Phys. Rev. Lett.* 71 (1993), pp. 3442–3445. DOI: 10.1103/PhysRevLett.71.3442.
- [205] M. J. D. Macpherson et al. “Precise measurement of parity nonconserving optical rotation at 876 nm in atomic bismuth”. In: *Phys. Rev. Lett.* 67.20 (1991), p. 2784. DOI: 10.1103/PhysRevLett.67.2784.
- [206] J. A. Formaggio and G. P. Zeller. “From eV to EeV: Neutrino Cross Sections Across Energy Scales”. In: *Rev. Mod. Phys.* 84 (2012), pp. 1307–1341. DOI: 10.1103/RevModPhys.84.1307. arXiv: 1305.7513 [hep-ex].
- [207] J. Dorenbosch et al. “EXPERIMENTAL RESULTS ON NEUTRINO - ELECTRON SCATTERING”. In: *Z. Phys. C* 41 (1989). [Erratum: *Z.Phys.C* 51, 142 (1991)], p. 567. DOI: 10.1007/BF01564701.
- [208] L. A. Ahrens et al. “Determination of electroweak parameters from the elastic scattering of muon-neutrinos and anti-neutrinos on electrons”. In: *Phys. Rev. D* 41 (1990). Ed. by A. K. Mann et al., pp. 3297–3316. DOI: 10.1103/PhysRevD.41.3297.

-
- [209] P. Vilain et al. “Precision measurement of electroweak parameters from the scattering of muon-neutrinos on electrons”. In: *Phys. Lett. B* 335 (1994), pp. 246–252. DOI: 10.1016/0370-2693(94)91421-4.
 - [210] Vera Gülpers et al. “The leading hadronic contribution to γ - Z mixing”. In: *PoS LATTICE2015* (2016), p. 263. DOI: 10.22323/1.251.0263.
 - [211] Marco Cè et al. “The leading hadronic contribution to the running of the Weinberg angle using covariant coordinate-space methods”. In: *PoS LATTICE2018* (2018), p. 137. DOI: 10.22323/1.334.0137. arXiv: 1811.08669 [hep-lat].
 - [212] Antoine Gerardin, Tim Harris, and Harvey B. Meyer. “Nonperturbative renormalization and $O(a)$ -improvement of the nonsinglet vector current with $N_f = 2 + 1$ Wilson fermions and tree-level Symanzik improved gauge action”. In: *Phys. Rev. D* 99.1 (2019), p. 014519. DOI: 10.1103/PhysRevD.99.014519. arXiv: 1811.08209 [hep-lat].
 - [213] Tanmoy Bhattacharya et al. “Improved bilinears in lattice QCD with non-degenerate quarks”. In: *Phys. Rev. D* 73 (2006), p. 034504. DOI: 10.1103/PhysRevD.73.034504. arXiv: hep-lat/0511014.
 - [214] T. Bakeyev et al. “Nonperturbative renormalization and improvement of the local vector current for quenched and unquenched Wilson fermions”. In: *Phys. Lett. B* 580 (2004), pp. 197–208. DOI: 10.1016/j.physletb.2003.11.050. arXiv: hep-lat/0305014.
 - [215] Stefan Sint and Rainer Sommer. “The Running coupling from the QCD Schrodinger functional: A One loop analysis”. In: *Nucl. Phys. B* 465 (1996), pp. 71–98. DOI: 10.1016/0550-3213(96)00020-X. arXiv: hep-lat/9508012.
 - [216] Sinya Aoki, Roberto Frezzotti, and Peter Weisz. “Computation of the improvement coefficient $c(\text{SW})$ to one loop with improved gluon actions”. In: *Nucl. Phys. B* 540 (1999), pp. 501–519. DOI: 10.1016/S0550-3213(98)00742-1. arXiv: hep-lat/9808007.
 - [217] Yusuke Taniguchi and Akira Ukawa. “Perturbative calculation of improvement coefficients to $O(g^2a)$ for bilinear quark operators in lattice QCD”. In: *Phys. Rev. D* 58 (1998), p. 114503. DOI: 10.1103/PhysRevD.58.114503. arXiv: hep-lat/9806015.
 - [218] Antoine Gerardin et al. “The leading hadronic contribution to $(g - 2)_\mu$ from lattice QCD with $N_f = 2 + 1$ flavours of $O(a)$ improved Wilson quarks”. In: *Phys. Rev. D* 100.1 (2019), p. 014510. DOI: 10.1103/PhysRevD.100.014510. arXiv: 1904.03120 [hep-lat].
 - [219] Franz Mandl and Graham Shaw. *QUANTUM FIELD THEORY*. 1985.
 - [220] David Bernecker and Harvey B. Meyer. “Vector Correlators in Lattice QCD: Methods and applications”. In: *Eur. Phys. J. A* 47 (2011), p. 148. DOI: 10.1140/epja/i2011-11148-6. arXiv: 1107.4388 [hep-lat].
 - [221] Anthony Francis et al. “A new representation of the Adler function for lattice QCD”. In: *Phys. Rev. D* 88 (2013), p. 054502. DOI: 10.1103/PhysRevD.88.054502. arXiv: 1306.2532 [hep-lat].
 - [222] Martin Luscher. “Deflation acceleration of lattice QCD simulations”. In: *JHEP* 12 (2007), p. 011. DOI: 10.1088/1126-6708/2007/12/011. arXiv: 0710.5417 [hep-lat].

- [223] Martin Luscher. “Local coherence and deflation of the low quark modes in lattice QCD”. In: *JHEP* 07 (2007), p. 081. DOI: 10.1088/1126-6708/2007/07/081. arXiv: 0706.2298 [hep-lat].
- [224] Martin Luscher. “Solution of the Dirac equation in lattice QCD using a domain decomposition method”. In: *Comput. Phys. Commun.* 156 (2004), pp. 209–220. DOI: 10.1016/S0010-4655(03)00486-7. arXiv: hep-lat/0310048.
- [225] E. Endress, A. Juttner, and H. Wittig. “On the efficiency of stochastic volume sources for the determination of light meson masses”. In: (Nov. 2011). arXiv: 1111.5988 [hep-lat].
- [226] Shao-Jing Dong and Keh-Fei Liu. “Stochastic estimation with Z(2) noise”. In: *Phys. Lett. B* 328 (1994), pp. 130–136. DOI: 10.1016/0370-2693(94)90440-5. arXiv: hep-lat/9308015.
- [227] M. Foster and Christopher Michael. “Quark mass dependence of hadron masses from lattice QCD”. In: *Phys. Rev. D* 59 (1999), p. 074503. DOI: 10.1103/PhysRevD.59.074503. arXiv: hep-lat/9810021.
- [228] John Bulava, Robert Edwards, and Colin Morningstar. “Stochastic All-to-All Propagators for Baryon Correlators”. In: *PoS LATTICE2008* (2008). Ed. by Christopher Aubin et al., p. 124. DOI: 10.22323/1.066.0124. arXiv: 0810.1469 [hep-lat].
- [229] C. McNeile and Christopher Michael. “Decay width of light quark hybrid meson from the lattice”. In: *Phys. Rev. D* 73 (2006), p. 074506. DOI: 10.1103/PhysRevD.73.074506. arXiv: hep-lat/0603007.
- [230] Philippe Boucaud et al. “Dynamical Twisted Mass Fermions with Light Quarks: Simulation and Analysis Details”. In: *Comput. Phys. Commun.* 179 (2008), pp. 695–715. DOI: 10.1016/j.cpc.2008.06.013. arXiv: 0803.0224 [hep-lat].
- [231] P. A. Boyle et al. “Use of stochastic sources for the lattice determination of light quark physics”. In: *JHEP* 08 (2008), p. 086. DOI: 10.1088/1126-6708/2008/08/086. arXiv: 0804.1501 [hep-lat].
- [232] Justin Foley et al. “Practical all-to-all propagators for lattice QCD”. In: *Comput. Phys. Commun.* 172 (2005), pp. 145–162. DOI: 10.1016/j.cpc.2005.06.008. arXiv: hep-lat/0505023.
- [233] Leonardo Giusti et al. “Frequency-splitting estimators of single-propagator traces”. In: *Eur. Phys. J. C* 79.7 (2019), p. 586. DOI: 10.1140/epjc/s10052-019-7049-0. arXiv: 1903.10447 [hep-lat].
- [234] Marco Cè et al. “The hadronic running of the electromagnetic coupling and the electroweak mixing angle from lattice QCD”. In: *To be published* (2022).
- [235] K. Jansen, Christopher Michael, and C. Urbach. “The eta-prime meson from lattice QCD”. In: *Eur. Phys. J. C* 58 (2008), pp. 261–269. DOI: 10.1140/epjc/s10052-008-0764-6. arXiv: 0804.3871 [hep-lat].

-
- [236] Vera Gülpers, Georg von Hippel, and Hartmut Wittig. “Scalar pion form factor in two-flavor lattice QCD”. In: *Phys. Rev. D* 89.9 (2014), p. 094503. DOI: 10.1103/PhysRevD.89.094503. arXiv: 1309.2104 [**hep-lat**].
 - [237] Andreas Stathopoulos, Jesse Laeuchli, and Kostas Orginos. “Hierarchical probing for estimating the trace of the matrix inverse on toroidal lattices”. In: (Feb. 2013). arXiv: 1302.4018 [**hep-lat**].
 - [238] C. Thron et al. “Pade - $Z(2)$ estimator of determinants”. In: *Phys. Rev. D* 57 (1998), pp. 1642–1653. DOI: 10.1103/PhysRevD.57.1642. arXiv: hep-lat/9707001.
 - [239] Craig McNeile and Christopher Michael. “Mixing of scalar glueballs and flavor singlet scalar mesons”. In: *Phys. Rev. D* 63 (2001), p. 114503. DOI: 10.1103/PhysRevD.63.114503. arXiv: hep-lat/0010019.
 - [240] Gunnar S. Bali, Sara Collins, and Andreas Schafer. “Effective noise reduction techniques for disconnected loops in Lattice QCD”. In: *Comput. Phys. Commun.* 181 (2010), pp. 1570–1583. DOI: 10.1016/j.cpc.2010.05.008. arXiv: 0910.3970 [**hep-lat**].
 - [241] Mattia Bruno et al. “Effects of Heavy Sea Quarks at Low Energies”. In: *Phys. Rev. Lett.* 114.10 (2015), p. 102001. DOI: 10.1103/PhysRevLett.114.102001. arXiv: 1410.8374 [**hep-lat**].
 - [242] Maarten Golterman, Kim Maltman, and Santiago Peris. “Chiral extrapolation of the leading hadronic contribution to the muon anomalous magnetic moment”. In: *Phys. Rev. D* 95 (7 Apr. 2017), p. 074509. DOI: 10.1103/PhysRevD.95.074509. URL: <https://link.aps.org/doi/10.1103/PhysRevD.95.074509>.
 - [243] S. Aoki et al. “FLAG Review 2019: Flavour Lattice Averaging Group (FLAG)”. In: *Eur. Phys. J. C* 80.2 (2020), p. 113. DOI: 10.1140/epjc/s10052-019-7354-7. arXiv: 1902.08191 [**hep-lat**].
 - [244] Maxwell T. Hansen and Agostino Patella. “Finite-volume effects in $(g - 2)_\mu^{\text{HVP,LO}}$ ”. In: *Phys. Rev. Lett.* 123 (2019), p. 172001. DOI: 10.1103/PhysRevLett.123.172001. arXiv: 1904.10010 [**hep-lat**].
 - [245] Harvey B. Meyer. “Lattice QCD and the Timelike Pion Form Factor”. In: *Phys. Rev. Lett.* 107 (2011), p. 072002. DOI: 10.1103/PhysRevLett.107.072002. arXiv: 1105.1892 [**hep-lat**].
 - [246] Laurent Lellouch and Martin Lüscher. “Weak transition matrix elements from finite volume correlation functions”. In: *Commun. Math. Phys.* 219 (2001), pp. 31–44. DOI: 10.1007/s002200100410. arXiv: hep-lat/0003023.
 - [247] Ulli Wolff. “Monte Carlo errors with less errors”. In: *Comput. Phys. Commun.* 156 (2004). [Erratum: *Comput. Phys. Commun.* 176, 383 (2007)], pp. 143–153. DOI: 10.1016/S0010-4655(03)00467-3. arXiv: hep-lat/0306017.
 - [248] Neal Madras and Alan D. Sokal. “The Pivot algorithm: a highly efficient Monte Carlo method for selfavoiding walk”. In: *J. Statist. Phys.* 50 (1988), pp. 109–186. DOI: 10.1007/BF01022990.

- [249] A. Sokal. “Monte Carlo Methods in Statistical Mechanics: Foundations and New Algorithms”. In: *Functional Integration: Basics and Applications*. Ed. by Cecile DeWitt-Morette, Pierre Cartier, and Antoine Folacci. Boston, MA: Springer US, 1997, pp. 131–192. ISBN: 978-1-4899-0319-8. DOI: 10.1007/978-1-4899-0319-8_6. URL: https://doi.org/10.1007/978-1-4899-0319-8_6.
- [250] Barbara De Palma et al. “A Python program for the implementation of the Γ -method for Monte Carlo simulations”. In: *Comput. Phys. Commun.* 234 (2019), pp. 294–301. DOI: 10.1016/j.cpc.2018.07.004. arXiv: 1703.02766 [hep-lat].
- [251] Christopher Kelly and Tianle Wang. “Update on the improved lattice calculation of direct CP-violation in K decays”. In: *PoS LATTICE2019* (2019), p. 129. DOI: 10.22323/1.363.0129. arXiv: 1911.04582 [hep-lat].
- [252] Bradley Efron and Robert J Tibshirani. *An introduction to the bootstrap*. CRC press, 1994.
- [253] B. Efron. “Bootstrap Methods: Another Look at the Jackknife”. In: *The Annals of Statistics* 7.1 (1979), pp. 1–26. ISSN: 00905364. URL: <http://www.jstor.org/stable/2958830>.
- [254] Bradley Efron. “Nonparametric Standard Errors and Confidence Intervals”. In: *The Canadian Journal of Statistics / La Revue Canadienne de Statistique* 9.2 (1981), pp. 139–158. ISSN: 03195724. URL: <http://www.jstor.org/stable/3314608>.
- [255] BRADLEY EFRON. “Nonparametric estimates of standard error: The jackknife, the bootstrap and other methods”. In: *Biometrika* 68.3 (Dec. 1981), pp. 589–599. ISSN: 0006-3444. DOI: 10.1093/biomet/68.3.589. eprint: <https://academic.oup.com/biomet/article-pdf/68/3/589/581658/68-3-589.pdf>. URL: <https://doi.org/10.1093/biomet/68.3.589>.
- [256] Bradley. Efron, Society for Industrial, and Applied Mathematics. *The jackknife, the bootstrap, and other resampling plans / Bradley Efron*. English. Society for Industrial and Applied Mathematics Philadelphia, Pa, 1982, vii, 92 p. : ISBN: 0898711797. URL: <http://www.loc.gov/catdir/enhancements/fy0726/81084708-t.html>.
- [257] G. P. Lepage et al. “Constrained curve fitting”. In: *Nucl. Phys. B Proc. Suppl.* 106 (2002). Ed. by M. Muller-Preussker et al., pp. 12–20. DOI: 10.1016/S0920-5632(01)01638-3. arXiv: hep-lat/0110175.
- [258] Ying Chen et al. “The Sequential empirical bayes method: An Adaptive constrained-curve fitting algorithm for lattice QCD”. In: (May 2004). arXiv: hep-lat/0405001.
- [259] M. Asakawa, Y. Nakahara, and T. Hatsuda. “Maximum entropy analysis of the spectral functions in lattice QCD”. In: *Progress in Particle and Nuclear Physics* 46.2 (2001), pp. 459–508. ISSN: 0146-6410. DOI: [https://doi.org/10.1016/S0146-6410\(01\)00150-8](https://doi.org/10.1016/S0146-6410(01)00150-8). URL: <https://www.sciencedirect.com/science/article/pii/S0146641001001508>.

-
- [260] K. Sasaki et al. “Excited nucleon spectrum from lattice QCD with maximum entropy method”. In: *Nuclear Physics B - Proceedings Supplements* 129-130 (2004). Lattice 2003, pp. 212–214. ISSN: 0920-5632. DOI: [https://doi.org/10.1016/S0920-5632\(03\)02533-7](https://doi.org/10.1016/S0920-5632(03)02533-7). URL: <https://www.sciencedirect.com/science/article/pii/S0920563203025337>.
 - [261] Benoit Blossier et al. “On the generalized eigenvalue method for energies and matrix elements in lattice field theory”. In: *JHEP* 04 (2009), p. 094. DOI: 10.1088/1126-6708/2009/04/094. arXiv: 0902.1265 [hep-lat].
 - [262] Christian Andersen et al. “The $I = 1$ pion-pion scattering amplitude and timelike pion form factor from $N_f = 2 + 1$ lattice QCD”. In: *Nuclear Physics B* 939 (Feb. 2019), pp. 145–173. DOI: 10.1016/j.nuclphysb.2018.12.018. arXiv: 1808.05007 [hep-lat].
 - [263] Maxwell T. Hansen, Fernando Romero-López, and Stephen R. Sharpe. “Generalizing the relativistic quantization condition to include all three-pion isospin channels”. In: *arXiv e-prints*, arXiv:2003.10974 (Mar. 2020), arXiv:2003.10974. arXiv: 2003.10974 [hep-lat].
 - [264] A. Francis et al. “New representation of the Adler function for lattice QCD”. In: *prd* 88.5, 054502 (Sept. 2013), p. 054502. DOI: 10.1103/PhysRevD.88.054502. arXiv: 1306.2532 [hep-lat].
 - [265] M. Della Morte et al. “The hadronic vacuum polarization contribution to the muon $g-2$ from lattice QCD”. In: *ArXiv e-prints* (May 2017). arXiv: 1705.01775 [hep-lat].
 - [266] Fred Jegerlehner and Andreas Nyffeler. “The Muon $g-2$ ”. In: *Phys. Rept.* 477 (2009), pp. 1–110. DOI: 10.1016/j.physrep.2009.04.003. arXiv: 0902.3360 [hep-ph].
 - [267] Martin Lüscher. “Two particle states on a torus and their relation to the scattering matrix”. In: *Nucl. Phys.* B354 (1991), pp. 531–578. DOI: 10.1016/0550-3213(91)90366-6.
 - [268] Martin Lüscher. “Signatures of unstable particles in finite volume”. In: *Nucl. Phys. B* 364 (1991), pp. 237–251. DOI: 10.1016/0550-3213(91)90584-K.
 - [269] Laurent Lellouch. “Flavor physics and lattice quantum chromodynamics”. In: *Modern perspectives in lattice QCD: Quantum field theory and high performance computing. Proceedings, International School, 93rd Session, Les Houches, France, August 3-28, 2009*. 2011, pp. 629–698. arXiv: 1104.5484 [hep-lat]. URL: <http://inspirehep.net/record/897440/files/arXiv:1104.5484.pdf>.
 - [270] Yoichiro Nambu and J. J. Sakurai. “Rare Decay Modes of the omega (eta) Meson”. In: *Phys. Rev. Lett.* 8 (1962), pp. 79–81. DOI: 10.1103/PhysRevLett.8.79.
 - [271] G. J. Gounaris and J. J. Sakurai. “Finite-Width Corrections to the Vector-Meson-Dominance Prediction for $\rho \rightarrow e^+e^-$ ”. In: *Phys. Rev. Lett.* 21 (4 July 1968), pp. 244–247. DOI: 10.1103/PhysRevLett.21.244. URL: <https://link.aps.org/doi/10.1103/PhysRevLett.21.244>.

- [272] Christian Andersen et al. “The $I = 1$ pion-pion scattering amplitude and timelike pion form factor from $N_f = 2 + 1$ lattice QCD”. In: *Nucl. Phys. B* 939 (2019), pp. 145–173. DOI: 10.1016/j.nuclphysb.2018.12.018. arXiv: 1808.05007 [hep-lat].
- [273] Felix Erben et al. “Rho resonance, timelike pion form factor, and implications for lattice studies of the hadronic vacuum polarization”. In: *Phys. Rev. D* 101.5 (2020), p. 054504. DOI: 10.1103/PhysRevD.101.054504. arXiv: 1910.01083 [hep-lat].
- [274] Geoffrey F. Chew and Stanley Mandelstam. “Theory of the Low-Energy Pion-Pion Interaction”. In: *Phys. Rev.* 119 (1 July 1960), pp. 467–477. DOI: 10.1103/PhysRev.119.467. URL: <https://link.aps.org/doi/10.1103/PhysRev.119.467>.
- [275] Alan Jeffrey. “2 - Functions and Identities”. In: *Handbook of Mathematical Formulas and Integrals (Third Edition)*. Ed. by Alan Jeffrey. Third Edition. Burlington: Academic Press, 2004, pp. 101–137. ISBN: 978-0-12-382256-7. DOI: <https://doi.org/10.1016/B978-012382256-7/50005-1>. URL: <http://www.sciencedirect.com/science/article/pii/B9780123822567500051>.
- [276] D. Brömmel et al. “The Pion form-factor from lattice QCD with two dynamical flavours”. In: *Eur. Phys. J. C* 51 (2007), pp. 335–345. DOI: 10.1140/epjc/s10052-007-0295-6. arXiv: hep-lat/0608021.
- [277] *NIST Digital Library of Mathematical Functions*. <http://dlmf.nist.gov/>, Release 1.1.3 of 2021-09-15. F. W. J. Olver, A. B. Olde Daalhuis, D. W. Lozier, B. I. Schneider, R. F. Boisvert, C. W. Clark, B. R. Miller, B. V. Saunders, H. S. Cohl, and M. A. McClain, eds. URL: <http://dlmf.nist.gov/>.
- [278] Marco Cè et al. “Vacuum correlators at short distances from lattice QCD”. In: (June 2021). arXiv: 2106.15293 [hep-lat].
- [279] Ivan Markovsky and Sabine Van Huffel. “Overview of total least-squares methods”. In: *Signal Processing* 87.10 (2007). Special Section: Total Least Squares and Errors-in-Variables Modeling, pp. 2283–2302. ISSN: 0165-1684. DOI: <https://doi.org/10.1016/j.sigpro.2007.04.004>. URL: <https://www.sciencedirect.com/science/article/pii/S0165168407001405>.
- [280] Gene H. Golub and Charles F. Van Loan. “An Analysis of the Total Least Squares Problem”. In: *SIAM Journal on Numerical Analysis* 17.6 (1980), pp. 883–893. ISSN: 00361429. URL: <http://www.jstor.org/stable/2156807>.
- [281] Pauli Virtanen et al. “SciPy 1.0: Fundamental Algorithms for Scientific Computing in Python”. In: *Nature Methods* 17 (2020), pp. 261–272. DOI: 10.1038/s41592-019-0686-2.
- [282] Ananth Ranganathan. “The levenberg-marquardt algorithm”. In: *Tutorial on LM algorithm* 11.1 (2004), pp. 101–110.
- [283] Darrell A. Turkington. “New Matrix Calculus Results”. In: *Generalized Vectorization, Cross-Products, and Matrix Calculus*. Cambridge University Press, 2013, pp. 164–213. DOI: 10.1017/CBO9781139424400.006.

-
- [284] Olivier Ledoit and Michael Wolf. “Improved estimation of the covariance matrix of stock returns with an application to portfolio selection”. In: *Journal of Empirical Finance* 10.5 (2003), pp. 603–621. ISSN: 0927-5398. DOI: [https://doi.org/10.1016/S0927-5398\(03\)00007-0](https://doi.org/10.1016/S0927-5398(03)00007-0). URL: <https://www.sciencedirect.com/science/article/pii/S0927539803000070>.
- [285] Olivier Ledoit and Michael Wolf. “A well-conditioned estimator for large-dimensional covariance matrices”. In: *Journal of Multivariate Analysis* 88.2 (2004), pp. 365–411. ISSN: 0047-259X. DOI: [https://doi.org/10.1016/S0047-259X\(03\)00096-4](https://doi.org/10.1016/S0047-259X(03)00096-4). URL: <https://www.sciencedirect.com/science/article/pii/S0047259X03000964>.
- [286] F. Pedregosa et al. “Scikit-learn: Machine Learning in Python”. In: *Journal of Machine Learning Research* 12 (2011), pp. 2825–2830.
- [287] G. M. de Divitiis et al. “Isospin breaking effects due to the up-down mass difference in Lattice QCD”. In: *JHEP* 04 (2012), p. 124. DOI: 10.1007/JHEP04(2012)124. arXiv: 1110.6294 [hep-lat].
- [288] G. M. de Divitiis et al. “Leading isospin breaking effects on the lattice”. In: *Phys. Rev. D* 87.11 (2013), p. 114505. DOI: 10.1103/PhysRevD.87.114505. arXiv: 1303.4896 [hep-lat].
- [289] Alan M. Ferrenberg and Robert H. Swendsen. “New Monte Carlo technique for studying phase transitions”. In: *Phys. Rev. Lett.* 61 (23 Dec. 1988), pp. 2635–2638. DOI: 10.1103/PhysRevLett.61.2635. URL: <https://link.aps.org/doi/10.1103/PhysRevLett.61.2635>.
- [290] A. Duncan, E. Eichten, and R. Sedgewick. “Computing electromagnetic effects in fully unquenched QCD”. In: *Phys. Rev. D* 71 (2005), p. 094509. DOI: 10.1103/PhysRevD.71.094509. arXiv: hep-lat/0405014.
- [291] Jacob Finkenrath, Francesco Knechtli, and Björn Leder. “One flavor mass reweighting in lattice QCD”. In: *Nucl. Phys. B* 877 (2013). [Erratum: Nucl.Phys.B 880, 574–575 (2014)], pp. 441–456. DOI: 10.1016/j.nuclphysb.2013.10.019. arXiv: 1306.3962 [hep-lat].
- [292] Andreas Risch and Hartmut Wittig. “Leading isospin breaking effects in the hadronic vacuum polarisation with open boundaries”. In: *PoS LATTICE2019* (2019), p. 296. DOI: 10.22323/1.363.0296. arXiv: 1911.04230 [hep-lat].
- [293] Andreas Risch and Hartmut Wittig. “Towards leading isospin breaking effects in mesonic masses with open boundaries”. In: *PoS LATTICE2018* (2018), p. 059. DOI: 10.22323/1.334.0059. arXiv: 1811.00895 [hep-lat].
- [294] Andreas Risch and Hartmut Wittig. “Leading isospin breaking effects in the HVP contribution to a_μ and the running of α ”. In: *PoS LATTICE2021* (2021), p. 296.
- [295] Christopher Aubin et al. “Pade approximants and g-2 for the muon”. In: *PoS LATTICE2012* (2012). Ed. by Derek Leinweber et al., p. 176. DOI: 10.22323/1.164.0176. arXiv: 1210.7611 [hep-lat].

- [296] Christopher Aubin et al. “Model-independent parametrization of the hadronic vacuum polarization and $g-2$ for the muon on the lattice”. In: *Phys. Rev. D* 86 (2012), p. 054509. DOI: 10.1103/PhysRevD.86.054509. arXiv: 1205.3695 [hep-lat].
- [297] Michael Barnsley. “The bounding properties of the multipoint Padé approximant to a series of Stieltjes on the real line”. In: *Journal of Mathematical Physics* 14.3 (1973), pp. 299–313. DOI: 10.1063/1.1666314. eprint: <https://doi.org/10.1063/1.1666314>. URL: <https://doi.org/10.1063/1.1666314>.
- [298] George A. Baker. “Best Error Bounds for Padé Approximants to Convergent Series of Stieltjes”. In: *Journal of Mathematical Physics* 10.5 (1969), pp. 814–820. DOI: 10.1063/1.1664911. eprint: <https://doi.org/10.1063/1.1664911>. URL: <https://doi.org/10.1063/1.1664911>.
- [299] Jacques Hadamard. *Essai sur l’étude des fonctions, données par leur développement de Taylor*. Gauthier-Villars, 1892.
- [300] G. A. Baker. “Best error bounds for pade approximants to convergent series of stieltjes”. In: *J. Math. Phys.* 10 (1969), pp. 814–820. DOI: 10.1063/1.1664911.
- [301] Wolfram Research Inc. *Mathematica, Version 12.3.1*. Champaign, IL, 2021. URL: <https://www.wolfram.com/mathematica>.
- [302] G.A. Baker et al. *Pade Approximants: Encyclopedia of Mathematics and It’s Applications, Vol. 59 George A. Baker, Jr., Peter Graves-Morris*. Encyclopedia of Mathematics and its Applications. Cambridge University Press, 1996. ISBN: 9780521450072. URL: <https://books.google.es/books?id=Vkk4JNLKbLoC>.
- [303] Andreas Risch and Hartmut Wittig. “Towards leading isospin breaking effects in mesonic masses with $O(a)$ improved Wilson fermions”. In: *EPJ Web Conf.* 175 (2018). Ed. by M. Della Morte et al., p. 14019. DOI: 10.1051/epjconf/201817514019. arXiv: 1710.06801 [hep-lat].
- [304] Vera Gülpers. “Recent Developments of Muon $g-2$ from Lattice QCD”. In: *PoS LATTICE2019* (2020), p. 224. DOI: 10.22323/1.363.0224. arXiv: 2001.11898 [hep-lat].